UNIVERSITY *of the*
WESTERN CAPE

GEOCHRONOLOGY, PETROGENESIS AND ISOTOPIC CHARACTERISTICS OF THE PALAEOPROTEROZOIC GLADKOP SUITE, NORTH-WESTERN PORTION OF THE NAMAQUA SECTOR, NAMAQUA-NATAL METAMORPHIC COMPLEX, SOUTH AFRICA.

by

ANSAHMBOM YONG NKE

A thesis submitted in fulfilment of the requirements for the degree of Magister Scientiae in the Department of Earth Sciences, University of the Western Cape.

Supervisor: Dr Russell Bailie

Co-supervisor: Prof Dirk Frei

July 2019

ABSTRACT

The Gladkop Suite (GS) granitic gneisses in the Bushmanland Domain (BD) represent one of the oldest rock units in the Namaqua-Natal Metamorphic Province (NNMP), and are located adjacent to the northern Richtersveld Magmatic Arc (RMA). This study represents results of a series of studies on the granitic gneisses which make up the GS, aiming to characterize them, explain their petrogenesis and understand their role in the development of the NNMP. The GS rocks preserved evidence of the ~1.0 Ga Namaqua Orogeny, with evidence of an older tectonic event preserved only in metasedimentary xenoliths. The GS is made up of three distinct gneisses, namely: the Steinkopf (STK) Gneiss, the Brandewynsbank (BWB) Gneiss and the Noenoemaasberg (NNM) Gneiss. Petrographically, these rocks range from granites to granodiorites. Quartz, plagioclase and K-feldspar are the principal phases, accompanied by minor amounts of biotite, hornblende, sericite, chlorite ± clinopyroxene and accessory minerals. Geochemically, the granitoids are silica-rich, magnesian, metaluminous to weakly peraluminous with a calcic to calc-alkalic characteristic and were generated in a high-K calc-alkaline series. These rocks invariably show enrichment in light rare earth elements (LREE) and significant negative Eu anomalies. All the granitic gneisses show characteristic negative anomalies in Ba, Ti, Nb, P, Sr and Eu, and a positive anomaly in Pb in the multi-element trace element plot (spider-diagram).

The emplacement of the GS rocks took place between 1793 ± 23 and 1825 ± 10 Ma (weighted mean ~1813 ± 48) as revealed by U-Pb zircon data, with the tight range in age variation suggesting that the constituent gneisses intruded simultaneously. $^{87}Sr/^{86}Sr$, $\varepsilon_{Nd(t)}$, $\varepsilon_{Hf(t)}$ and T_{DM} (~ 2.29-2.68 Ga) values are consistent with magmas produced by partial melting of slightly enriched pre-existing crust. These magmas were possibly generated from K-rich orthogneisses, granodiorites or andesitic rocks. Despite the overlap in some isotopic provenance indicators and REE patterns between the Palaeoproterozoic Vioolsdrif Suite (VS) of the RMA, and the adjacent GS, their chemical signatures are different, and define two distinct liquid-lines-of-descent, suggesting they formed at different times and in differing tectonic settings. The GS rocks possibly intruded during the Orange River Orogeny, as a resulting of crustal melting of the earlier VS phases. Geotectonic plots suggest that the GS magmas were emplaced in a transitional collision to within-plate setting. The Palaeoproterozoic GS gneisses represent a basement complex in the NNMP as revealed by detrital zircon and sedimentation ages.

Geochemical data suggest that the GS rocks are highly fractionated high-K I-type granites. Fractionation of feldspars and biotite was the principal process of magmatic differentiation and responsible for the major element variation. The gneisses which make-up the GS represent fractional crystallization products of differing amounts of plagioclase, K-feldspar, biotite and accessory minerals, likely from a similar magma source emplaced in three separate pulses. Feldspar separation was responsible for the concentrations of Rb, Sr and Ba, whereas the REEs were fractionated by accessory minerals such as allanite, hornblende and zircon. Peritectic assemblage entrainment (PAE) seems to have played a significant role, with the dominant entrained phases being clinopyroxene and ilmenite.

Keywords: Gladkop Suite; Granitic gneiss; Petrography; Amphibolite facies; Geochemistry; I-type granite; U-Pb zircon Geochronology; Isotope; Petrogenesis; Fractional crystallization; Peritectic assemblage entrainment.

DECLARATION:

I declare that *Geochronology, petrogenesis and isotopic characteristics of the Palaeoproterozoic Gladkop Suite, north-western portion of the Namaqua Sector, Namaqua-Natal Metamorphic Complex,* apart from the contributions of Dr Russell Bailie, is my own work, that it has not been submitted for any degree or examination in any other university, and that all the sources I have used or quoted have been indicated and acknowledged by complete references.

Ansahmbom Yong Nke July 2019

Signed: .....

Acknowledgements

I would like to say thank you to my patient, kind and funny supervisor, Dr Russell Bailie (Senior lecturer: Earth Science Department, University of the Western Cape). I knew I had succeeded already, when he accepted to supervise my MSc research because of his dedication and attention to detail. I have learned so much from him, and I hope that he continues to inspire others the way he has inspired me.

I would also like to thank the owners and staff of Bossa Nova, especially Pikkie Malan, who gave me the opportunity to raise the funds I needed to cover my debt at the University of the Western Cape, so that I could return and complete my studies. And to Yafah Williams (University of the Western Cape) who made a seemingly complicated return to the university, after a forced gap-year, much easier.

I would like to say thank you to Prof Dirk Frei (University of the Western Cape), Dr Juergen Reinhardt (University of the Western Cape), Richard Harrison (University of the Western Cape) and Ms. Janine Becorney (University of the western Cape), for providing the required analytical data and technical assistance throughout my research.

To my cousins here in South Africa, Ruth Mukong and Claudia Mukong, and the rest of my family back home, I would like to say thank you for all your moral and emotional support throughout this project. Special thanks goes to my mother who, despite all the difficulties it caused her, made sure that I achieved my dream of becoming a graduate geologist.

List of abbreviations

Minerals and geochemical abbreviations

Ap - Apatite

ASI - Aluminium saturation index

Bt - Biotite

Cpx - Clinopyroxene

Chl - Chlorite

Di - Diopside

En - Enstatite

Eu/Eu* - Europium anomaly

Hbl - Hornblende

HFS - High field strength

Kfs - Potassium feldspar

LOI - Loss of ignition

LFS - Low field strength

MALI - Modified alkali-lime index

Mg# - Magnesium number

Mag - Magnetite

Opx - Orthopyroxene

Orth - Orthoclase

Plag - Plagioclase

Qtz - Quartz

REE - Rare Earth Elements; LREE, MREE, HREE:Light, medium, heavy REE

Zr – Zircon

Tt – Titanite

General

CHUR - Chondritic Uniform Reservoir

Ga - 10^9 years

GS - Gladkop Suite

IBM - International Business Machines Corporation

IUGS - International Union of Geological Sciences

LA ICP-MS – Laser Ablation Inductively Coupled Plasma-Mass Spectrometry

Ma - 10^6 years

BD - Bushmanland Domain

PD - Pella Domain

ppm - Parts per million

RMA - Richtersveld Magmatic Arc

SPSS - Statistical Package for the Social Sciences

VD - Vioolsdrif Domain

VS - Vioolsdrif Suite

XRF - X-Ray Fluorescence Spectrometry

Wt. % - weight percentage

Table of Contents

List of figures

List of tables

CHAPTER 1

INTRODUCTION

The Mesoproterozoic Namaqua-Natal Metamorphic Province (NNMP) represents a fold and thrust belt whose outcrops flank the western, southwestern and southeastern Kaapvaal Craton (Blignault et al., 1983; Cornell et al., 2006; Jacobs et al., 2008). Outcrops of the NNMP which occur to the west of the Kaapvaal Craton, at the border region between South Africa and Namibia, and into the northwestern parts of South Africa are referred to as the Namaqua Sector (Fig. 1.1; Blignault et al., 1983). The Namaqua Sector consists of tectono-stratigraphic domains/terranes and subprovinces recognized from various geological, geophysical and geochronological studies (e.g. De Beer and Meyer, 1984; Pitts et al., 1992). In age, the domains of the Namaqua Sector range from Palaeoproterozoic to Neoproterozoic (Eglington, 2006). The rocks in this sector formed as a result of two major tectonic events, these being the ~2.1-1.8 Ga Orange River Orogeny (possibly associated with the assembly and break-up of the Supercontinent Columbia/Nuna; Rogers and Santosh, 2002), and the 1.2-1.0 Ga Namaqua Orogeny (possibly associated with the assembly of the Supercontinent Rodinia) (Reid, 1982; Blignault et al., 1983; Cornell et al., 1998, 2006; Jacobs et al., 2008; Li et al., 2008; Thomas et al., 1994). Magmatism in the Namaqua Sector was generated between 2.0 and 1.7 Ga (Barton, 1983; Rogers and Santosh, 2002), as well as during and after the Namaqua Orogeny (Eglington, 2006). Reid (1977) suggested that the Palaeoproterozoic Gladkop Suite (GS), a migmatitic suite of orthogneisses, and the calc-alkaline Vioolsdrif Suite (VS) represent the oldest granitoid plutons in the Namaqua Sector. Barton (1983) and Blignault et al. (1983) further suggested that the GS is temporally and compositionally related to the younger phases of the VS, but the exact nature of the relationship is yet to be established. Although the VS has been extensively studied (e.g. Macey et al., 2017), very few geochemical studies have investigated the potential sources and genetic relationships of the GS.

The term ‘terrane’ was used in Colliston and Schoch (2013) and Colliston et al. (2014), but in this study the non-genetic term ‘domain’ is used in place of the genetic term ‘terrane’ which has a precise definition related to accretionary tectonics (Coney et al., 1980). For the purposes of this study, the tectonostratigraphic subdivision of the NNMP, as described by Hartnady et al. (1984) and Thomas et al. (1994), is largely followed. The term ‘tectonic event’, as applied to pre-, syn- or post-tectonic in this study refers to the 1.2-1.0 Ga Namaqua tectonic events.

1.1. Location of the study area; the Gladkop Suite (GS)

The Namaqua Sector is made up of tectonically distinct easterly trending domains which amalgamated during the Namaqua Orogeny and are subdivided based on marked changes in the lithostratigraphy across structural discontinuities (Blignault et al., 1983).

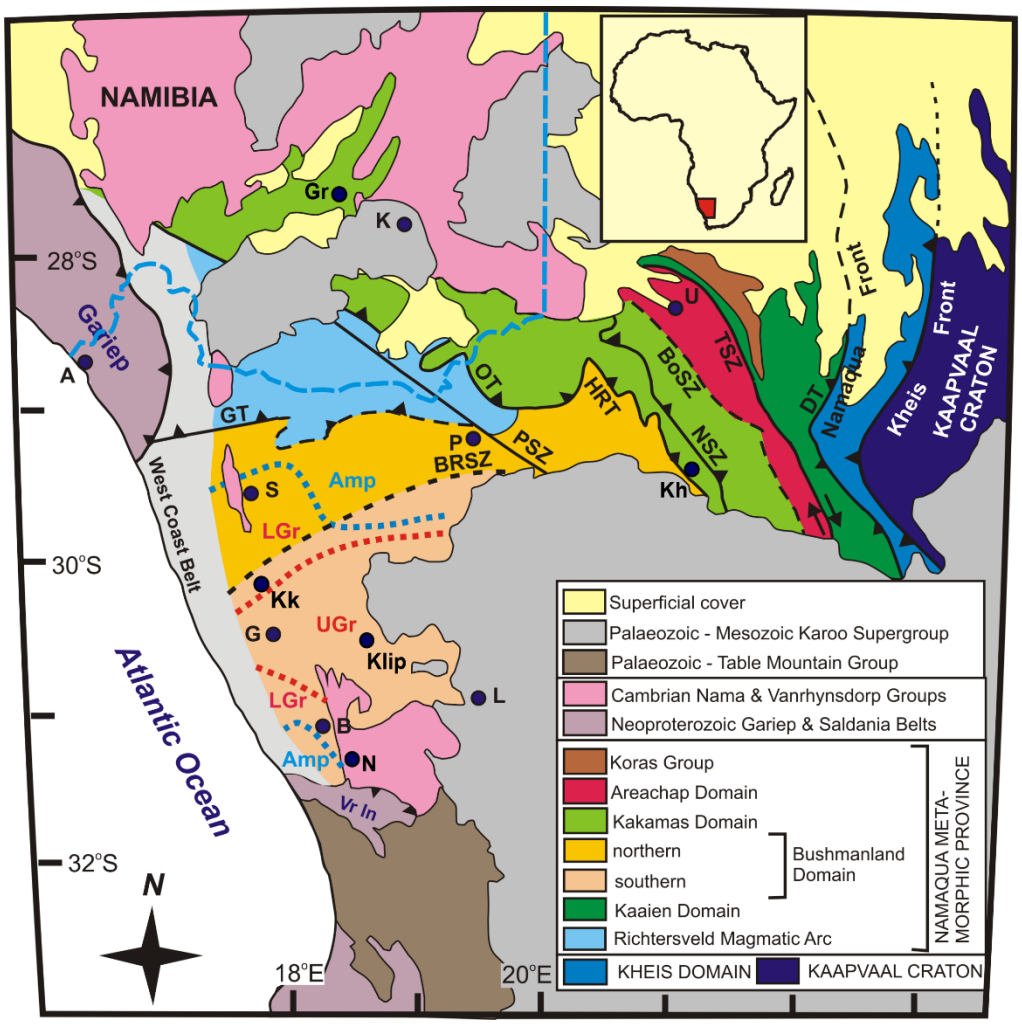

Fig. 1.1. *Tectonostratigraphic position of the Bushmanland Domain of the Namaqua Sector of the NNMP (modified after Macey et al., 2015). Gr - Grünau, K - Karasburg, Kh - Kenhardt, Kk - Kamieskroon, U - Upington, S - Springbok, P - Pofadder, G - Garies, Klip - Kliprand, L - Loriesfontein, B - Bitterfontein, N - Nuwerus, GT - Groothoek Thrust, BRSZ - Buffels River Shear Zone, PSZ - Pofadder Shear Zone, HRT - Hartbees River Thrust, OT - Onseepkans Thrust, NSZ - Neusberg Shear Zone, BoSZ - Boven Rugzeer Shear Zone, TSZ - Trooilapspan Shear Zone, DT - Dabep Thrust, Amp - Amphibolite facies, LGr - Lower granulite facies, UGr - Upper granulite facies, Vr In - Van Rhynsdorp inlier.*

The Bushmanland Domain (BD) forms a crustal block in the western parts of the Namaqua Sector (Fig. 1.1). It is separated from the adjacent Richtersveld Magmatic Arc (RMA) by the Groothoek Thrust, and is bounded to the east by the Kakamas Domain (Cornell et al., 2006). According to Moore et al. (1990), the BD is made up of rocks of three distinctive age groups, and includes: (1) granitic rocks of Palaeoproterozoic age (2.0-1.7 Ga), (2) supracrustal sequences of sedimentary and volcanic origins spanning the Palaeoproterozoic and Mesoproterozoic Eras (1.9, 1.6 and 1.2 Ga), and (3) intrusive granitic to charnockitic rocks of Namaquan age (1.2-1.0 Ga).

The extensive suite of pink-grey Palaeoproterozoic orthogneisses (the GS) whose outcrops are exposed in the northwestern BD (Figs. 1.1, 1.2; Blignault et al., 1983) is one of the oldest plutons in the BD (Reid, 1977; Reid and Barton, 1983). The GS orthogneisses are overlain by the Cambrian Nama Group (Figs. 1.1, 1.2), a major lithostratigraphic unit in southwestern

Gondwana which crops out in southern Namibia and adjacent northwestern South Africa (Gresse et al., 2006; Blanco et al., 2011). The study area (the GS) is located between the Nama Group in the west, and longitude 18°E in the east, and is bordered to the south by the Ratelpoort Synform. The northern border to the study area is latitude -29.250S (29°15'0" S; Fig. 1.2). The study area is cross-cut by the N7 highway, which connects Cape Town to the Northern Cape through to Namibia. The GS is composed mostly of Palaeoproterozoic granitic gneisses, with slivers of supracrustal, syn- and post-tectonic intrusive (mafic and felsic) rocks, as well as Neoproterozoic pegmatites (Reid and Barton, 1983; Robb et al., 1988; Doggart, 2019).

1.2. Background and rationale

The GS forms an extensive suite of grey–pink orthogneisses developed in the northern end of the BD adjacent to the poorly defined boundary with the RMA (Fig. 1.2). The migmatitic orthogneisses are inferred to have intruded during the 2.0 to 1.7 Ga Orange River Orogeny (Barton, 1983; Blignault et al., 1983; Colliston et al., 1991, 2017; Colliston and Schoch, 1996, 1998). At least three lithologically distinct orthogneisses are recognized, namely: (1) the fine- to medium-grained granodioritic Steinkopf (STK) Gneiss, (2) the K-feldspar megacrystic Brandewynsbank (BWB) Gneiss, and (3) the pink leucocratic Noenoemaasberg (NNM) Gneiss. Van Aswegen (1983) identified an intimately associated intrusive relationship between these three lithologically distinct orthogneisses of the GS. He observed that the STK Gneiss is intruded by the BWB Gneiss, which are both intruded by the NNM Gneiss, making the STK Gneiss the oldest granitic gneiss lithology in the GS. Van Aswegen (1983) suggested that the GS gneisses are igneous in origin, hence orthogneisses, and that the well-developed banding in these gneisses are of secondary origin which formed through processes such as mechanical flattening. Based on the recognition of xenoliths of metasedimentary rocks which show evidence of assimilation and contamination at the contacts with the GS gneisses, Van Aswegen (1983) identified an intrusive relationship into surrounding metasedimentary rocks, the Eenriet Subgroup. Although Van Aswegen (1983) suggested that the STK Gneiss is the oldest and the NNM Gneiss is the youngest, there has not been substantial geochronological data to support this observation.

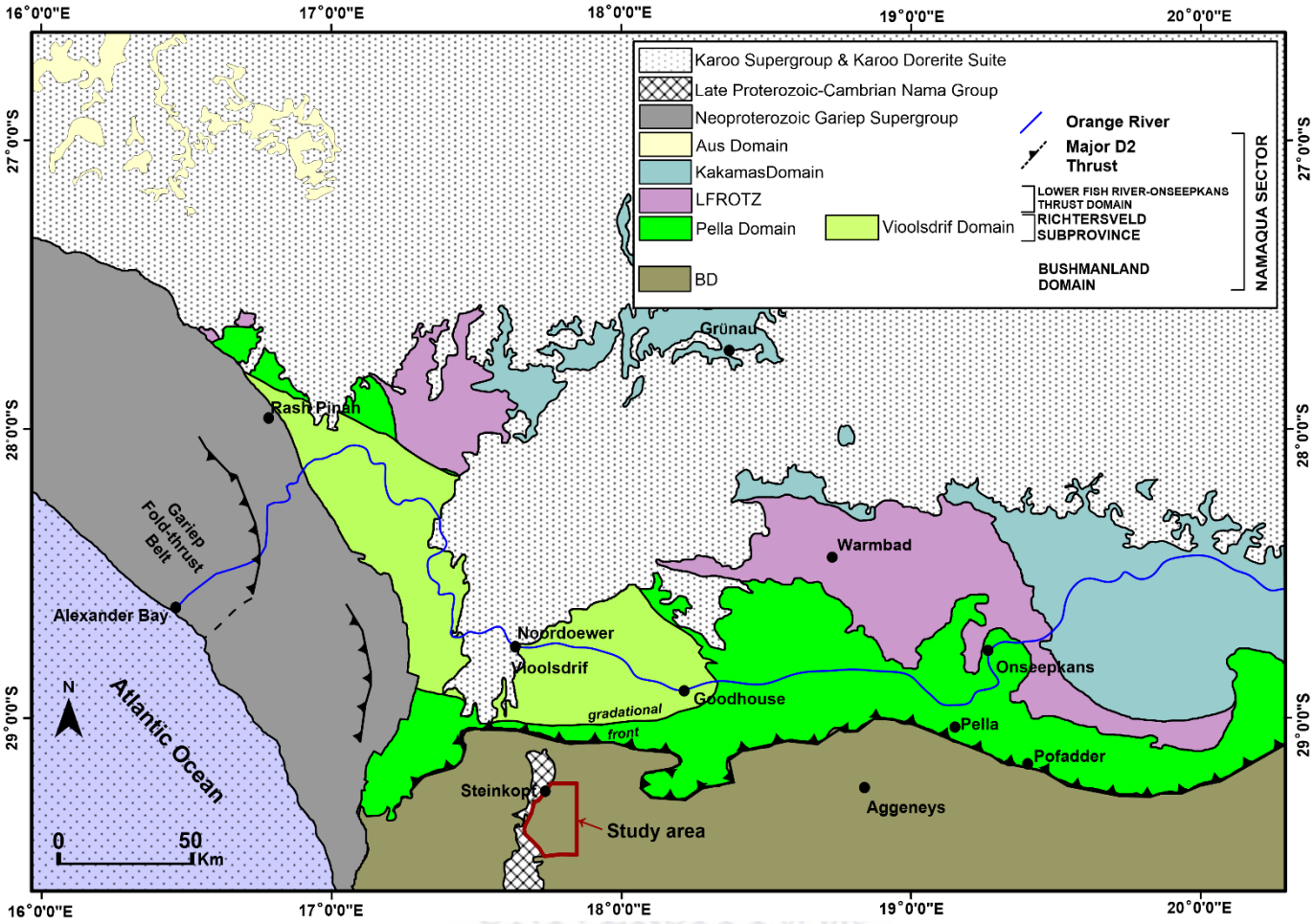

Fig. 1.2. *Simplified map showing the regional context of the study area (the Gladkop Suite) in relation to the Richtersveld Magmatic Arc (modified from Macey et al., 2017). The position of the Groothoek Thrust is shown, which separates the Bushmanland Domain from the Richtersveld Magmatic Arc.*

Barton (1983) carried out isotopic investigations in the NNMP and obtained Rb-Sr and Pb-Pb isotope ages of the gneiss lithologies of the GS, suggesting that the emplacement of the GS gneisses was one of the major occurrences of the Palaeoproterozoic Orange River event. While Rb-Sr regression data for the STK Gneiss produced mean errorchron ages of about 1.8 Ga, no reasonable ages could be obtained from the BWB Gneiss due to the limited variation in Rb-Sr ratios in the analysed BWB Gneiss samples. As a result of this, and due to the intimate spatial association between the STK and BWB gneisses, Barton (1983) combined the data from both the STK and BWB samples to obtain an average errorchron Rb-Sr age of about 1.82 Ga. Very little variation was also observed in Pb-Pb ratios, and combining the results for both the BWB and STK samples yielded an average Pb-Pb isochron age of about 1.77 Ga. Barton (1983) then suggested that the mean age of 1.8 Ga represents the age of emplacement of the GS gneisses. Robb et al. (1999) provided magmatic and metamorphic Pb-Pb zircon ages for the BWB Gneiss, but could not obtain any relevant ages from the NNM samples. They dated one sample each of the BWB and NNM gneisses (twelve BWB and eleven NNM zircons) and obtained Palaeoproterozoic magmatic

Pb-Pb zircon ages of 1.83 Ga for the BWB Gneiss, using U-Pb zircon Sensitive High-Resolution Ion Microprobe (SHRIMP) dating. The average Pb-Pb zircon age of ~1.0 Ga obtained from zircon rims was taken as the age of metamorphism. However, no useful data could be obtained from the eleven analyzed zircons of the NNM sample. Robb et al. (1999) arrived at this conclusion after noticing a wide range in age shown by plotting $^{206}Pb/^{238}U$ vs. $^{207}Pb/^{235}U$ ratios (concordia plot), and, as a result, concluded that 1.83 Ga is the age of emplacement of the GS rocks. They also noticed that zircons collected from the NNM sample were characterized by very high U contents and discordant U-Pb isotopic ratios. Previous studies have provided no meaningful geochronological data specifically for the NNM Gneiss. The fact that the ages of the individual GS orthogneisses are yet to be obtained in order to support the age relationships based on field relationships (Van Aswegen, 1983) provides the basis for updated geochronological data on the GS gneisses.

The Palaeoproterozoic age obtained for the GS gneisses is similar to ages obtained for the VS which intruded the Orange River Group of the RMA, during the Orange River Orogeny (e.g. Reid and Barton, 1983). Van Aswegen (1983) identified another possible correlation between the GS and the RMA from evidence which suggests that both the VS and the GS intruded the Eenriet Subgroup metasedimentary rocks. Barton (1983) suggested that, because the emplacement of the GS gneisses occurred during the Palaeoproterozoic Orange River event, the Suite is temporally and compositionally related to the younger phases of the VS. However, the GS was emplaced into pelites and calc-silicate rocks (Blignault et al., 1983), and is more deformed, while the less deformed VS was mostly emplaced into calc-alkaline volcanic rocks (Reid and Barton, 1983; Van Aswegen, 1983; Macey et al., 2017). Van der Merwe and Botha (1989) observed that the boundary between the GS and the adjacent RMA is obscured by the Groothoek thrust zone (Figs. 1.1, 1.2), posing a question as to the exact nature of the boundary. The non-foliated granitoids of the RMA (the Vioolsdrif Domain; Fig. 1.2) become gneissic towards the northern and southern margins (Blignault et al., 1983; Macey et al., 2017). Blignault et al. (1983) pointed out that because the younger phases of the VS can be correlated both in time and space to the GS, there is a relationship between them which is yet to be established. However, they differ in their environment of intrusion and the amount of deformation they have experienced. This suggests a complex relationship between the two intrusive suites which is yet to be unraveled clearly. Recent studies by Macey et al. (2017) provide grounds for a new comparison between the GS and the RMA VS.

Reid and Barton (1983) characterized the GS as peraluminous S-type granites. They attributed the S-type characteristics of these gneisses to the assimilation of sedimentary material by the granitoid magmas as well as tectonic admixing during the tectono-thermal events which produced these gneisses.

A number of studies (Barton, 1983; Robb et al., 1999) have provided emplacement ages for the GS granitic gneisses as predating the 1.2-1.0 Ga Namaqua Orogeny. The relatively older age (Palaeoproterozoic) of the GS compared to the formation of the Namaqua Sector, in addition to the location of the GS on the NNMP suggests that the GS had a role to play in the formation of the NNMP. Joubert (1971) and Blignault et al. (1983) suggested that the complex structural nature of the GS is consistent with an older basement in the BD on which supracrustal successions were deposited. As a result, Moore (1989) suggested that similar megacrystic gneisses in the central and southern BD, overlain by supracrustal successions should represent similar basements. This is, however, not the case as evident from dating, thus putting a question mark on the extent and nature of the basement complex in the BD. This project will therefore investigate whether the GS represents a basement complex (as suggested by Cornell et al., 2006) and whether it is genetically

related to the RMA. Consequently, petrogenetic studies of the GS can reveal the role of the granitic gneisses in the evolution of the NNMP.

In addition to the fact that there has been no published data characterizing the GS based on petrographic observations, an examination of the petrological processes (using trace element chemistry) which produced the GS gneisses is also required. Although Rb-Sr isotope dating remains an invaluable tool in isotope dating, the reliability of data obtained from Rb-Sr dating of metamorphosed and altered rocks is suspect. The reason for this is that Rb and Sr are both mobile, with Rb more so than Sr, and can both be removed or added to rock systems by fluids (DePaolo, 1988; Dickin, 1995). Furthermore, some K-bearing minerals, such as micas, are comparatively reactive, in the sense that some or much of the Rb may be present in exchangeable sites (DePaolo, 1988; Rollinson, 1993). Sm and Nd, by contrast, are generally immobile (except in high-grade metamorphic conditions) and are not easily removed from or added to the isotopic system (Dickin, 1995). This author further suggests that Rb-Sr dating and Sm-Nd dating complement each other and should thus be used together rather than in isolation. Barton (1983) used radiogenic isotope data to determine the emplacement ages of the GS migmatitic gneisses, with no real connection to petrogenetic processes or sources of these rocks.

All these points highlighted above, and the fact that the most recent data on the GS was documented about 35 years ago reveal the gap in the present understanding of the origin and formation (petrogenesis) of the GS. The most recent explanation of the petrogenesis of this suite was provided by Reid and Barton (1983), and was based mostly on trace element chemistry, without any input from radiogenic isotope data. Tectonic, metamorphic and geochronological relationships between the VS and the GS have been mentioned (e.g. Reid and Barton, 1983), but the exact nature of their relationship remains unclear. Unanswered questions which need to be addressed include: what is the source of the GS plutons and what caused the variation in the granitic magmas? Is the GS a basement complex in the BD? Is the GS genetically related to the RMA?

1.3. Petrogenesis and source characteristics of granitic rocks

The upper continental crust (UCC) is dominated by rocks of granitic composition. The geochemical differentiation in the UCC is directly related to the processes which produce magmas of granitic composition. Granitic melts are products of melting of crustal rocks (Clemens, 1990; Stevens and Clemens, 1993; Johannes and Holtz, 1996; Clemens and Watkins, 2001). Various models have been suggested to explain the processes which affect granitic magmas from partial melting of the source rock, through to the formation of granitic rocks (petrogenesis). These models are based on theories such as peritectic phase entrainment (Stevens et al., 2007; Villaros et al., 2009; Clemens et al., 2011; Clemens and Stevens, 2012), magma mixing at depth (e.g. Zorpi et al., 1989; Chappell, 1996; Vernon, 2007; Karsli et al., 2010), assimilation/contamination and fractional crystallization at depth (e.g. Soesoo, 2000). These models which control variation in granitic magmas are tested and modelled by making use of the correlation between selected appropriate elements.

Igneous petrologists have carried out several studies in order to attempt an explanation for the variation in geochemical compositions exhibited by granitic rocks (of the same suite) which make up most of the earth's crust. These studies have shown that there is no particularly dominant process responsible for this geochemical diversity in suites of granitoid rocks of similar magmatic

origin, but several processes work either in isolation or together. This is evident in the several hypotheses put forward by researchers (e.g. Chappell, 1996; Soesoo, 2000; Stevens et al., 2007; Karsli et al., 2010). Two main types of hypotheses have been put forward to try and explain the compositional variation observed in granitic rocks. The first hypothesis covers theories which attribute the variation to processes such as crystal-liquid fractionation, assimilation of country rock and mixing between magmas from different sources as magmas rise to their level of emplacement (e.g. Chappell, 1996; Soesoo, 200; Karsli et al., 2010). The second hypothesis, on the other hand, attributes the variation in chemical composition of magmas to the chemical composition of the source rock. This second hypothesis encompasses the set of ideas which suggest that the chemical variability in granitic magmas emerges from the source rock chemistry and the manner in which melting is achieved (e.g. White and Chappell, 1977; Chappell et al., 1987; Skjerlie and Johnston, 1992; Stevens et al., 2007; Clemens et al., 2011). In line with the second hypothesis, White and Chappell (1977) attributed the variation in chemical composition observed in (the mafic component of) granitic rocks from felsic sources to the ratio of unmelted residual fraction of the source (restite) to partial melt during entrainment by the partial melt. Stevens et al. (2007) opposed the aforementioned theory, and rather attributed the formation of more mafic rocks in granitic series to the entrainment of peritectic assemblages produced by the melting reaction. Clemens et al. (2011) observed a strong positive correlation between Ca, Mg-number, Ti, Zr and Fe + Mg (maficity) in S- and I-type granites, and then determined that this relationship in granitic rocks was caused by the entrainment of peritectic clinopyroxene, ilmenite and plagioclase. Clemens and Stevens (2012) further provided evidence which suggests that the entrainment of peritectic mineral assemblages is one of the major factors which contribute to the geochemical variability in granitic rocks.

The two different factors proposed to influence geochemical variation in granitic rocks will be tested for the GS rocks in this study.

1.4. Outline, aims and objectives of this study

The Palaeoproterozoic granitic gneisses of the GS have been subjected to very few investigations (such as Barton, 1983; Reid and Barton, 1983; Van Aswegen, 1983; Robb et al., 1999) which have focused on only certain aspects of their lithological and field description, time of emplacement and geochemical characterization. This study comprises investigations which include: the origin of the GS granitic magmas, their evolution through time and also characterizes the compositional variation of these gneisses. It is aimed at applying our present understanding of deep crustal processes and their development through time to understand and/or explain the origin (protolith nature) and evolution of the GS magmas.

In its simplest form, this study sets out to characterise the granitic gneisses of the GS in terms of their mineralogy, emplacement age and geochemical characteristics. It also seeks to determine the relative magmatic and radiogenic isotopic signatures of the component orthogneisses of the GS, all with an aim to characterise their compositional variation and provide a petrogenetic interpretation of the GS. The obtained results will be compared to previous whole-rock geochemical studies (Barton, 1983; Reid and Barton, 1983). This study will also compare the geochemical and isotopic characteristics of the GS to those of the Palaeoproterozoic VS of the Richtersveld Magmatic Arc (Macey et al., 2017) to investigate any relationship in their magma

sources. U-Pb isotopic data will be used to determine the role of the GS rocks in the evolution of the Namaqua Sector. As such, this study of the GS orthogneisses is subdivided as follows:

Chapter 1 is an introductory section in which general information about this research project is given, including previous work in the area, the aims and objectives of the research project, the location of the study area and a summary on the origin and formation (petrogenesis) of granites.

Chapter 2 outlines the geological history of the study area, as well as the adjacent RMA.

Chapter 3 describes the methods used to meet the aims and objectives of this research project.

Chapter 4 presents the lithological characteristics of the GS granitic gneisses, based on field relationships, hand samples and thin sections. The lithological characteristics of other lithologies (country rocks and intrusions) intercalated with the GS orthogneisses are also described. The chapter ends with a description of the structural characteristics of the GS and compares the observations to the existing structural history of the Namaqua Sector.

Chapter 5 presents whole-rock major and trace element geochemical characteristics and relationships within the GS. Elemental distributions are investigated while interpreting their associations with whole-rock geochemical compositions (major-, trace- and rare-earth-elements). The geochemical data is used to compare and contrast the GS orthogneisses. This chapter also shows a comparison between the geochemical data from literature (Van Aswegen, 1983; Reid and Barton, 1983) and the geochemical data of this study. In addition, the geochemical characteristics of the GS gneisses are compared to those of the VS rocks.

Chapter 6 presents Rb-Sr and Sm-Nd isotopic analyses. The isotopic signatures of the GS orthogneisses are used to constrain the source of the GS magmas. Zircon U-Pb and Lu-Hf isotopic data for the GS orthogneisses is also presented here. The relative age relationships as described by Van Aswegen (1983) are further tested in this chapter.

Chapter 7 is an overall discussion (and conclusion) of the work presented throughout this dissertation and communicates lithological and petrographic relationships, geochemical characteristics, as well as geochronological ages and the isotopic significance which are all tied together in order to infer the petrogenesis of the GS.

CHAPTER 2

GEOLOGICAL SETTING

2.1. Regional geological setting

The 1400-400 km wide NNMP is a fold and thrust belt which flanks the western and southwestern margin of the Kaapvaal Craton (Blignault et al., 1983; Cornell et al., 2006; Jacobs et al., 2008). It is made up of the Namaqua Sector (NS) (Figs. 1.1, 1.2), defined by outcrops in the Northern Cape Province, South Africa, and the Natal Sector, defined by outcrops in KwaZulu-Natal. The NNMP consists of tectono-stratigraphic domains recognized from various geological, geophysical and geochronological studies (De Beer and Meyer, 1983; Joubert, 1986; Thomas et al., 1994; Cornell et al., 2006; Eglington, 2006; Miller, 2012; Colliston and Schoch, 2013; Colliston et al., 2014). Based on its age, it has been suggested that the NNMP formed along the southern margin of the Archean-Proterozoic proto-Kalahari Craton, during the ~ 1.2-1.0 Ga Namaqua Orogeny, through the accretion of micro-continents and island arcs (e.g. Hartnady et al., 1985; Jacobs et al., 2008). Magmatism in the Namaqua Sector was generated during two main periods, between ~2.0 and 1.7 Ga (Rogers and Santosh, 2002), as well as during and after the Namaqua Orogeny (Eglington, 2006). During the Namaqua Orogeny, three main lithostratigraphic components were assembled in the NNMP, and include: (1) preserved and reworked Palaeoproterozoic (~ 2.0 Ga) crust believed to have formed during the Orange River Orogeny (Blignault et al., 1983); (2) juvenile supracrustal and plutonic material, and (3) voluminous pre-, syn- and post-tectonic granitoids formed between 1.2 and 1.0 Ga. In addition, a number of scattered small mafic/ultramafic intrusions also occur. Cornell et al. (2006) suggested that juvenile material formed during the rifting, ocean spreading and subduction phases of the Namaqua Orogeny, and was assembled (and deformed) during the later stages.

2.1.1. Tectonostratigraphy of the Namaqua Sector

The western Namaqua Sector of the NNMP has been conventionally subdivided into different domains based on major tectonic boundaries such as large-scale shear zones (e.g. the Buffels River Shear zone, the Groothoek Thrust), or as determined from changes in lithostratigraphy, tectonic history and metamorphic grade (Figs. 1.1, 1.2; Hartnady et al., 1985; Thomas et al., 1994; Macey et al., 2011; Colliston and Schoch, 2013; Colliston et al., 2014). Different workers in the Namaqua Sector (e.g. Joubert, 1986; Thomas et al., 1994; Cornell et al., 2006; Colliston et al., 2015) made use of different tectonostratigraphic terminologies and subdivisions, but the subdivisions of the Namaqua Sector by Hartnady et al. (1985) and Thomas et al. (1994) have been adopted in this project. The domains which make up the Namaqua Sector, from west to east include: the Richtersveld Magmatic Arc (RMA), the Bushmanland Domain (BD), the Kakamas Domain, the Areachap Domain, the Kaaien Domain and the Koras Group (Fig. 1.1). The Namaqua Sector is separated from the Kaapvaal Craton by the Kheis Domain (Fig. 1.1),

characterized by supracrustal rocks with ages spanning the Palaeoproterozoic to Mesoproterozoic Eras, and with the pervasive Namaqua fabric (Cornell et al., 2006). The northwest-trending tectonostratigraphic domains of the eastern part of the Namaqua Sector are interpreted as major southwest-verging thrust sheets (Colliston and Schoch, 2000, 2002) juxtaposed and reworked during the polyphase Namaqua Orogeny (Clifford et al., 2004; Eglington, 2006; Colliston et al., 2015; Macey et al., 2015). The resulting high-grade metamorphism (granulite to upper amphibolite facies) has been extensively investigated and recorded in the Steinkopf and surrounding areas of the BD (Fig. 1.1; Albat, 1979, 1983, 1984; Waters, 1986, 1988, 1989, 1990; Raith and Harley, 1998). The focus of this study is the GS of the BD, and the similarities/differences between its origin and that of the VS (RMA). As a result, the geological settings of both the BD and the RMA will be described in more detail.

2.1.2. The Richtersveld Magmatic Arc (RMA)

The RMA extends from southern Namibia into the northern parts of South Africa (Fig. 1.1). It forms a tectonically-bound wedge-shaped crustal block which encloses the Orange River in the western parts of the NNMP (Figs. 1.1, 1.2; Blignault et al., 1983; Macey et al., 2017), enveloped by the high-grade BD to the south and the Kakamas Domain to the north (Figs. 1.1, 1.2; Hartnady et al., 1985). Its boundary with the BD is proposed to be the Groothoek Thrust (Van Aswegen et al., 1987; Colliston and Schoch, 1996), while the boundary with the Kakamas Domain is defined by the Lower Fish River-Onseepkans Thrust Zone (LFROTZ) (Fig. 1.2; Macey et al., 2015). The RMA, much less affected by the Namaqua orogeny than the other Namaqua Sector domains, is predominantly made up of volcano-sedimentary rocks of the Orange River Group (ORG) and voluminous plutonic rocks of the VS, and their metamorphosed equivalents (Blignault, 1977; Reid, 1977, 1997; Reid et al., 1987, Macey et al., 2017). The ORG is mostly composed of ~1.9 Ga low- to medium-grade supracrustal rocks (Macey et al., 2017). Rocks in the west of the RMA are covered by outcrops of the Pan-African Gariep Fold Belt, superimposed by younger thrusts and shear zones (Cornell et al., 2006).

The RMA is composed of rocks initially generated in a Palaeoproterozoic island-arc setting (Reid, 1977, 1997; Macey et al., 2017), with the magmatic period lasting between 1.91 and 1.86 Ga (Macey et al., 2017). The crystallization ages for the ORG and VS has recently been provided as ~1.9 Ga (Moen and Toogood, 2007; Macey et al., 2017). Based on field observation and geochronology, Cornell et al. (2006) and Macey et al. (2017) suggested that the ORG rocks exhibit low-grade metamorphic conditions as a result of the Orange River Orogeny, roughly synchronous with the intrusion of the VS. The RMA is composed of two distinct parts, a western Vioolsdrif Domain and an eastern Pella Domain (Fig. 1.2; Blignault, 1974; Macey et al., 2017). Rocks in the relatively undeformed Vioolsdrif Domain and their highly deformed equivalents in the Pella Domain demonstrate overlapping ages and geochemical characteristics (Macey et al., 2017).

The Vioolsdrif Domain, which is composed of Palaeoproterozoic rocks of greenschist facies conditions, was only slightly reworked during the main phases of the Mesoproterozoic Namaqua Orogeny. Deformation in the low-grade Vioolsdrif Domain is limited to Palaeoproterozoic D_1 deformation of the volcanic belts, late-Namaqua (D_4) shear zones and, in the west, it has been overprinted and reworked by the Gariep Orogenic event during Cambrian (Pan-African) times (Macey et al., 2015). The Vioolsdrif Domain is made up of both ORG and VS

rocks. The ORG rocks in the Vioolsdrif Domain (Table 2.1) are composed of volcanic rocks of calc-alkaline composition which cover the complete spectrum from basaltic to rhyolitic compositions (Reid, 1977, 1997; Reid et al., 1987). These rocks mostly exhibit aphanitic to porphyritic textures, but pyroclastic and volcanoclastic varieties are also present. Minor quartzites and conglomerates occur as minor components of the ORG (Gresse et al., 2016). The VS, which intrudes the ORG rocks in the Vioolsdrif Domain, is made up of voluminous plutonic rocks with minor hypabyssal and intrusive migmatite components (Table 2.2). It forms a calc-alkaline magma series of mafic to felsic rocks (Macey et al., 2017). The rocks of the VS are traditionally subdivided into a number of units on the basis of their relative intrusive age relationships (Table 2.2; Macey et al., 2017).

The Pella Domain is made up of Palaeoproterozoic rocks (Table 2.2), including rocks typically found in the VS, which were extensively reworked to gneisses during the main phases of the Namaqua Orogeny, as evident in a pervasive amphibolite facies Namaqua imprint (Macey et al., 2017). The boundary between the Pella and Vioolsdrif Domains was termed the Front Zone (Namaqua front; Beukes, 1973) by Blignault (1977) and Blignault et al. (1983) (Fig. 1.2). The stratigraphic subdivision of the highly deformed and extensively intruded ORG rocks in the Pella Domain are those described by Strydom et al. (1987) and Macey et al. (2017).

Table 2.1. *Lithostratigraphy of the ~1.9 Ga Orange River Group in the Vioolsdrif Domain (Macey et al., 2017).*

VIOOLSDRIF DOMAIN					
Western parts (McMillan, 1968; Blignault, 1974; Ritter, 1980; Minnaar, 2012; Cornell et al., 2006; Miller, 2008; Gresse et al., 2006)			**Eastern parts (Blignault, 1974, 1977; Reid, 1977; Blignault et al., 1983; Macey et al., 2015; Shifotoka et al., 2016)**		
Subgroup	**Formation**	**Description**	**Subgroup**	**Formation**	**Description**
De Hoop Subgroup	Kuams River	f.g. mafic lava, f.g.-c.g. qtz porphyry, tuff (<1 500 m)	**Haib Subgroup**	Nous	Mainly andesitic lava and pyroclastic rocks with minor dacite to rhyolite lava and pyroclastic rocks, volcanoclastic rocks (<3000m)
	Kook River	Ignimbritic qtz-fsp porphyry (<1 400 m)		Tsams	f.g. mafic to felsic, fsp-qtz and fsp porphyry, volcanoclastic rocks (<5000m)
	Abiekwa River	Alternating sequence of felsic pyroclastic rocks/tuff, mafic to felsic lavas, volcanoclastic rocks, phyllite (<4000 m)			
	Windvlakte	Mixed volcanic rocks			
	Paradys River	Tuff, felsic lava, conglomerate and minor other volcanic rocks			
	Klipneus	Vesicular and f.g. lava interbedded with quartzite, volcanoclastic rocks, conglomerate (>3 000 m)			

Abbreviations: f.g. - fine-grained, c.g. - coarse-grained, qtz - quartz

The intense deformation of the ORG rocks makes determination of the relative ages between units impossible (Macey et al., 2017). However, these authors subdivided the ORG into four lithodemic units: the Guadom, Umeis, Gaidip and Hom gneisses. The Guadom Gneiss is a heterogeneous succession of meta-volcanic and subordinate meta-sedimentary rocks forming a roughly east-west belt across the southern and eastern parts of the Pella Domain. It is dominated by biotite-hornblende gneiss with andesitic, dacitic and rhyolitic compositions with subordinate layers of quartzite, amphibolite, meta-agglomerate and rare pelitic schist. The Umeis Gneiss comprises a variety of banded, commonly strongly migmatitic grey hornblende-biotite-quartz-feldspar gneisses. Compositional banding, typically at centimeter and decimeter scales, is defined

by variations in mineralogy and grain size and the presence of stromatic leucosomes. The succession also includes quartz-feldspar gneiss, anthophyllite-bearing gneiss, biotite schist, amphibolite, calc-silicate gneiss and rare aluminous garnet-sillimanite-bearing layers. The Gaidip Gneiss is dominated by a leucocratic quartzofeldspathic gneiss considered to represent meta-rhyolite (e.g. Cilliers, 1989), whereas the Hom Gneiss consists of intercalated quartzo-feldspathic and biotite-hornblende gneisses.

***Table 2.2**. Lithostratigraphy of the ~1.9 Ga Vioolsdrif Suite in the Richtersveld Magmatic Arc (see Macey et al., 2017 and references therein).*

PELLA DOMAIN	**Vioolsdrif Suite**	Pipeline Gneiss		Bt-hbl equigranular granitic to tonalitic gneiss
		Ramansdrif Alkali Granite Gneiss		Fine-medium grained alkali granite gneiss (Lower Houms River-type)
				Coarse-grained alkali granite gneiss
		Goodhouse Subsuite		Interlayered bt granite augen gneiss and leucogranite gneiss (Coboop-type)
				Bt-hbl augen orthogneiss (Noudap-type)
				Leucogranite augen gneiss
				Bt ± hbl granite augen gneiss
		Aluminous paragneiss		Foliation-parallel, often stringer-like, layers of sillimanite-biotite-muscovite-quartz ± cordierite schist/gneiss and sillimanite-muscovite-quartz nodule gneiss occur as inclusions in the orthogneisses
		Goabis Meta-diorite		Foliated coarse-grained equigranular diorite
		Vuurdood Meta-gabbro		Strongly foliated coarse-grained gabbro and gabbronorite
VIOOLSDRIF DOMAIN	**Vioolsdrif Suite**	Ramansdrif Alkali Granite		Leucocratic pink granite dominated by plutons of coarse-grained to porphyritic K-feldspar granite and alkali granite but locally forms stockworks of fine-grained aplitic dykes and veins. Intrudes all members of the Vioolsdrif Suite.
		Goodhouse Subsuite	Gaarseep Granodiorite	Relatively heterogeneous with composition ranging from quartz diorite to granite, but granodiorite is dominant. Textures vary from medium- to coarse- grained (3 mm) to very coarse- grained (5 mm) equigranular to porphyritic. Widespread presence of ovoid mafic enclaves. Dominant lithology in the Vioolsdrif Suite.
			Xaminkaip River Granodiorite	Relatively homogeneous, dominated by medium-grained equigranular granodiorite. Widespread presence of ovoid mafic enclaves.
		Khoromus Porphyry		Subvolcanic feldspar ± quartz porphyries of dioritic to granitic composition typically characterised by small outcrops which occur as black weathering hills.
		Blokwerf Intrusive Migmatite Complex		Occurs along a contact between the ORG and the Vioolsdrif Suite in the west of the Vioolsdrif Domain. Comprises blocks of the ORG and hypabyssal rocks intruded partially by networks of Vioolsdrif Suite intrusive rocks.
		Goabis Diorite		Coarse-grained equigranular diorite.
		Vuurdood Gabbro		Weakly foliated coarse-grained gabbro and gabbronorite, but also includes peridotite, pyroxenite and troctolite. Form numerous isolated bodies of limited extent (<3 km^2) closely associated with, or hosted within the Goabis Diorite.

In the Pella Domain, the D_1 structures and fabrics were obliterated by the pervasive, polyphase D_2 Namaqua thrust tectonics (~1.2-1.1 Ga) which were associated with coeval magmatism (Macey et al., 2015). D_1 structures are, however, preserved in the Vioolsdrif Domain (Macey et al., 2017). They are only preserved in belts of ORG rocks (and the earlier more mafic phases of the VS) as large-scale, open to isoclinal, upright to recumbent F_1 folds of S_0 bedding. Macey et al. (2017) suggest that the timing of the D_1 Orange River Orogeny is tightly constrained between the age of extrusion of the ORG (~1889 ± 12 Ma) and the intrusion of the early phases of the VS (~1885 ± 12 Ma) which occurred soon after. The main phases of the Namaqua Orogeny are absent from the Vioolsdrif Domain, but produced intense deformation and medium-grade metamorphism in the Pella Domain. The D_2 deformation was associated with isoclinal folding, the formation of an intense regional penetrative S_2 gneissosity and NE-plunging L_2 stretching lineations (Joubert, 1986). The principal D_2 fabrics were refolded by mega-scale F_3 structures and

subsequently reoriented and mylonitised by late-Namaqua transcurrent D_4 shear zones (~1.0-0.96 Ga; Toogood, 1976; Melcher et al., 2008; Lambert, 2013). The D_3 event produced upright, NE-plunging anticlinoria and synclinoria (Macey et al., 2017). Both the Pella Domain and the Vioolsdrif Domain are cross-cut by late-Namaqua (D_4) dextral shear zones, characterized by sub-vertical mylonitic, phyllonitic and cataclastic foliations and subhorizontal and near down-dip lineations (Toogood, 1976; Macey et al., 2015).

2.1.3. The Bushmanland Domain (BD)

The BD is the crustal block (approximately 60 000 km^2) which is separated from the overlying RMA by the Groothoek Thrust and from the Kakamas Domain to the east by the Hartbees River Thrust (Figs. 1.1, 1.2). The BD makes up most of the Namaqua Sector, occupying up to 60 percent of the total area (Fig. 1.1; Cornell et al., 2006). Predominantly it comprises late Mesoproterozoic (1.2 to 1.0 Ga) granitoids, but Palaeoproterozoic granitic gneisses (e.g. the GS orthogneisses) and early Mesoproterozoic amphibolite- to granulite-facies supracrustal rocks are also present (Robb et al., 1999; Cornell et al., 2006; Eglington, 2006). The rocks along the southern boundary are covered by the younger Vanrhynsdorp Group and Karoo Supergroup sediments, while the rocks to the west are affected by the thermal and deformational effects of the Pan-African Gariep orogeny (Figs. 1.1, 1.2; Cornell et al., 2006). The 1.2-1.0 Ga Namaqua magmatism formed most of the granitoids exposed in the BD (Barton, 1983; Robb et al., 1999; Clifford et al., 2004; Macey et al., 2018). Development of new crust in the BD was largely achieved by reworking of Palaeoproterozoic crust (Eglington, 2006). The rocks of the BD are subdivided based on lithology, age and relationship towards the main regional Namaqua deformation (D_2). Some researchers (e.g. Waters, 1986, 1988, 1989; Raith and Harley, 1998) working in the BD have proposed that the domain can be further subdivided into a northern lower granulite domain and a southern upper granulite domain, separated by the Buffels River Shear Zone (BRSZ) (Fig. 1.1). However, recent work by Bailie et al. (2019) suggests that the BRSZ is not a terrane boundary, but represents a long-lived shear zone which probably juxtaposes slightly different levels of continental crust, based on similar Sm-Nd ratios and a continuum in Palaeoproterozoic heritage from the northern to the southern BD. According to Moore et al. (1990), the BD is made up of rocks of three distinctive age groups and include: (1) granitic rocks of Palaeoproterozoic age (2.0-1.7 Ga) which they believed to be a basement complex; (2) supracrustal sequences of sedimentary and volcanic origins spanning the Palaeoproterozoic to Mesoproterozoic Eras (1.9, 1.6 and 1.2 Ga), and (3) syn- and late- tectonic intrusive granitic to charnokitic rocks of Namaquan age (1.2-1.0 Ga).

a. Granitic gneisses

Dating has revealed that the GS granitic gneisses in the Steinkopf area represent the oldest (Palaeoproterozoic) rocks in the BD, and are exposed along the northern boundary, adjacent to the RMA (Fig. 1.2). Colliston et al. (2017) suggests that these rocks, similarly to the oldest rocks in the RMA are products of the Columbian orogenic cycle (Rogers and Santosh, 2002). As mentioned above, the GS consists of the STK Gneiss, the BWB Gneiss and the NNM Gneiss (Van Aswegen, 1983; Reid and Barton, 1983). The STK Gneiss is typically a fine- to medium-grained and heterogeneous gneiss with a characteristic migmatitic nature. The BWB gneiss is generally medium-grained and homogeneous on a mesoscale, while the NNM Gneiss is a typical medium-

grained leucocratic pink gneiss (Van Aswegen, 1983). Xenoliths of amphibolite, calc-silicate rock and quartzite are typically found in the gneisses, and were interpreted by Van Aswegen (1983) and Watkeys (1986) as remnants of an older supracrustal succession. Reid and Barton (1983) characterized the GS gneisses as peraluminous S-type granites, and attributed the S-type character to assimilation of the older sedimentary material by the Gladkop magmas.

Studies show that the VS rocks (~1.9 Ga) are slightly older than the GS granitic gneisses (Robb et al., 1999; Macey et al., 2017). Ages for the BWB Gneiss were obtained as 1822 ± 36 Ma and 1824 ± 70 Ma, by Robb et al. (1999) and Reid and Barton (1983), respectively. While Robb et al. (1999) used ion-probe zircon Pb-Pb dating, Reid and Barton (1983) used Rb-Sr whole-rock dating. Although Reid and Barton (1983) suggested that the BWB Gneiss underwent high-grade metamorphism immediately after intrusion, Robb et al. (1999) did not find any metamorphic overgrowths around zircons from the BWB Gneiss to support this idea. The GS has a very complex structure which is in line with the interpretations of Joubert (1971) and Blignault et al. (1983) as an older basement on which various supracrustal sequences were deposited.

b. Supracrustal belts

Supracrustals occur in several discontinuous east-west trending belts within the BD, increasing in abundance towards the south in the vicinity of Garies (Fig. 1.1) (Moore, 1989; Cornell et al., 2006). Correlation of these supracrustal units has been made difficult by nature of their heterogeneity, as well as disruptions caused by thrust-related deformation and massive granitoid intrusions (Cornell et al., 2006). However, Moore (1989) suggested a broad subdivision into a northern succession (the Springbok-Steinkopf-Pofadder area; Fig. 1.2), which he called the Bushmanland Group, and a southern succession (Bitterfontein-Kamieskroon area; Fig. 1.1). The southern succession of Moore (1989) is comprised of basal quartzofeldspathic gneisses and overlying feldspathic quartzites as well as garnet-cordierite gneisses. The northern succession is composed of basal leucocratic gneisses and overlying quartzites and mica–sillimanite schists.

Marais et al. (2001) further grouped the supracrustals of the Namaqua Sector into the ORG of the RMA and the Bushmanland Group of the BD. The Bushmanland Group is made up of units of metaquartzites, metapelites, schists and conglomerates, interbanded with mafic and calc-silicate rocks (Blignault et al., 1980; De Beer et al., 2002). Metapelites from the north of the BD are lower in plagioclase and mafic minerals and higher in K-feldspar than those in the south. This allowed De Beer (2001) and De Beer et al. (2002) to group the less evolved supracrustal rocks to the south into the Kamiesberg Subgroup of the Bushmanland Group. The Kamiesberg, Aggeneys, Haib and Enriet Subgroups together make-up the Bushmanland Group (Blignault et al., 1980; De Beer et al., 2002). While pre-Namaqua ages (~1.9 Ga; Reid, 1997; Macey et al., 2017) have been accurately constrained for the ORG supracrustals, detrital zircon core ages of the Bushmanland Group supracrustals reveal derivation from two main age groups, 1150-1300 and 1600-2000 Ma, although the age of deposition still remains a debate (Raith et al., 2003; McClung, 2006). Moore (1989) observed that the supracrustal belts in the BD are dominated by leucocratic and biotite-bearing quartzofeldspathic gneisses, metavolcanic rocks of rhyolite to dacite composition, feldspathic and glassy quartzite, interpreted as arkose and quartzose sandstone respectively, and mica-sillimanite schist or cordierite-rich gneisses, interpreted as metapelite (shale) and psammite (sandy) clastic sediments (Moore, 1989). Minor rock types include amphibolite and basic granulite, interpreted as basic volcanic rocks of tholeiitic composition (Reid

et al., 1987; Moore, 1989), calc-silicate and rare marble, metaconglomerate, iron-formation, and magnesium-rich cordierite-anthophyllite ± orthopyroxene ± phlogopite rocks. Unusual rock types, mainly concentrated in the Aggeneys-Pofadder area (Fig. 1.2), include sillimanite-rich rocks (± corundum, sapphirine, topaz; Willner et al., 1990), tourmalinite and sulphide-, gahnite- and barite-rich rocks (Rozendaal and Stumpfl, 1984; Ryan et al., 1986). Metaquartzite becomes less abundant eastwards from Pofadder towards Kenhardt (Fig. 1.1, 1.2), whereas quartz-rich calc-silicate rocks become more abundant.

Sedimentation in the BD has been dated between ~1.64 and 1.2 Ga (Bailie et al., 2007a; Cornell et al., 2009). Palaeoproterozoic ages (~2.0 Ga) for metavolcanic and metasedimentary supracrustal rocks have also been identified in the RMA (Reid, 1997). Based on these ages, Eglington (2006) suggested that the supracrustal lithologies in the Namaqua Sector were likely deposited during at least three intervals (~2.0, 1.65 and 1.2 Ga).

c. Intrusive rocks

The pre- to syn- tectonic Little Namaqualand Suite (LNS) and the late- to post-tectonic Spektakel Suite (SS) are the main Namaquan intrusive units found in the BD (Thomas et al., 1994; Robb et al., 1999; Clifford et al., 2004; Macey et al., 2011, 2018). However, pegmatites and the mafic Koperberg Suite (KS) (Clifford et al., 1995) are also present in the BD, in only small outcrop exposures. The KS typically occurs as a series of noritoids which intruded along fabric planes.

The LNS generally occurs as granite to quartz-monzonite sheet-like bodies and are characterized by quartz-microcline-biotite K-feldspar augen gneisses with plagioclase, magnetite and garnet ± hypersthene ± clinopyroxene occurring in the southern portions where the metamorphic grade is high (Reid and Barton, 1983). The LNS is made up of the Nababeep Granite Gneiss and Granite together with the Modderfontein Granite Gneiss (Lombaard et al., 1986). There is a gneissic fabric present in the LNS, characterized by the strongly recrystallized elongate K-feldspar augen porphyroclasts and the preferred alignment of platy minerals (especially biotite) which define the S_2 fabric (Macey, 2001). In general, the feldspar porphyroclasts within the LNS augen gneisses show symmetrical tails, indicating a strong component of non-rotational pure shear flattening strain during the main D_2 deformation (Jackson, 1998; Macey, 2001). Field relationships suggest the Modderfontein Gneiss intrudes the Nababeep Gneiss, although the two appear to be related by fractional crystallization (Reid and Barton, 1983). The ion probe Pb-Pb zircon ages calculated by Robb et al. (1999) for both gneisses gave an age of 1212 ± 11 Ma, whereas a Rb-Sr whole-rock age of 1154 ± 40 Ma was determined by Reid and Barton (1983).

The SS is the group of relatively undeformed coarse-grained, megacrystic, locally charnockitic 'Rietberg-type' granitoids (Macey et al., 2018). They intruded the BD gneisses of the Namaqua Sector during the late- to post-tectonic phase of the main (D_2) Namaqua tectonic event. The older varieties have stronger tectonic alignment of megacrysts suggesting intrusion into a waning stress field. These Rietberg-type plutons have been subdivided into twenty-two individually mapped plutons which intruded over a prolonged period of more than 60 m.y., between 1.09 and 1.03 Ga. The suite intrudes much of the central BD between Nuwerus and Springbok but is particularly concentrated in the upper granulite facies region around Garies and Kliprand. Broadly speaking, the oldest plutons are found in the south and the youngest in the north. Based on geochemical data, Macey et al. (2018) suggests that the SS granites were derived from a variety of crustal source regions with significant mantle input.

Mafic rocks of the post-tectonic KS occur as layers and lenses throughout the BD (Kisters et al., 1994). Lombaard et al. (1986) characterised the KS as irregular east-west-trending dykes, which may be 60-100 m wide and up to 1 km along strike. These intrusions are commonly multi-phase pulses (Schoch and Conradie, 1990) and may include anorthosite, jotunite, biotite diorite, and hypersthene-bearing rocks ranging from leuconorite to hypersthenite. The sequence of intrusion has been clearly established as being from felsic to mafic. The KS is inferred to have intruded the BD rocks during a short period of time (< 10 m.y.), at ~1030 Ma (Clifford et al., 2004).

2.2. Tectono-metamorphic evolution of the NNMP

2.2.1. The Orange River Orogeny

Rogers and Santosh (2002) proposed that the Columbian orogenic cycle involved three main periods which include: (1) an early period (~2.5-2.0 Ga), (2) a middle period (~2.0-1.7 Ga), and (3) a break-up period (~1.6-1.4 Ga). The Orange River Orogeny (2.0-1.7 Ga) has been correlated by several authors (e.g. Joubert, 1971, 1986; Blignault et al., 1983) to the Palaeoproterozoic Eburnean Orogeny in west Africa (Bonhomme, 1962), and would place these events in the early to mid-Columbian orogenic cycle. These observations are supported by SHRIMP data (Robb et al., 1988). The Palaeoproterozoic orogenic event was accompanied by the emplacement of granitoid rocks. Colliston et al. (2017) suggested that these granitic rocks were emplaced in the Steinkopf and surrounding areas (and probably part of the Congo Craton), which possibly form basement complexes in the NNMP. Evidences for the Orange River Orogeny have been described by researchers such as Joubert (1971, 1986), Blignault et al. (1983), Moore (1989), Colliston et al. (1991), Colliston and Schoch (1996, 1998, 2000), Macey et al. (2015, 2017), etc. The ~1.9 Ga rocks in the Vioolsdrif Domain of the RMA, and supracrustal xenoliths in the BD preserve evidence of a D_1 deformation event which accompanied the Orange River Orogeny (Joubert, 1971, 1986; Blignault et al., 1983). The deformation created large scale, SW-trending isoclinal folds in supracrustal rocks and a localized weak fabric, S_1 (Joubert, 1971; Colliston and Schoch, 2013; Macey et al., 2015), with associated NW-dipping axial planar foliation and lineations (Blignault, 1977; Macey et al., 2017). The Orange River area is made up of rocks that were assembled during the ~1.2-1.0 Ga Namaqua Orogeny (Blignault et al., 1983; Macey et al., 2015). Although the Namaqua Orogeny has since obliterated most evidence of the early deformation in the BD, the existence of older deformation is, however, preserved in the Steinkopf, Grünau and Pofadder areas (Figs. 1.1, 1.2) (Colliston and Schoch, 2000).

2.2.2. The Namaqua Orogeny

It has been suggested that the formation of the Mesoproterozoic NNMP occurred during the assembly of the Supercontinent Rodinia (e.g. Hoffman, 1991; Jacobs et al., 1993; Thomas et al., 1994; Dalziel et al., 2000; Karlstrom et al., 2001). Waters (1990) and Thomas et al. (1994) suggested that, at the onset of the Namaqua Orogeny, the BD was located in an extensional back-arc environment, overriding a N-dipping subduction zone. Although Jacobs et al. (1993), Thomas et al. (1994), etc. proposed a Wilson cycle-related collisional tectonics in the evolution of the NS,

more recent work (e.g. Bial et al., 2015a, 2015b, 2016) have suggested that the tectonic setting and orogenic evolution of the NS most likely took place in a continental back-arc setting. The evidence for this tectonic setting is based on the repeated and long-standing high-temperature conditions at almost constant pressures, observed in several domains which make up the NS, which cannot be accounted for by Wilson cycle-related collisional tectonics (Bial et al., 2015a and b, 2016).

Table 2.3. *Summary of the major deformational and tectonic events in the western part of the Namaqua Sector, following Joubert (1986) and Macey et al. (2015).*

Deformation episode	Structures	Metamorphism	Timing	Orogenic event
D_5	SE-directed thrusting of Gariep over RMA associated with shear zones in the footwall and faulting in hinterland	Lower amphibolite to greenschist	~540-500 Ma	GARIEP-PAN AFRICAN
D_4	Dextral transcurrent shear zones	Amphibolite to greenschist	~1000-960 Ma	NAMAQUA
D_3	Regional scale folds	Amphibolite	Age poorly constrained	
D_2	Polyphase SW-directed thrusting and associated ductile fabrics	Amphibolite/Granulite	~1120-1090 Ma	NAMAQUA
D_1	Folds, localized weak fabrics	Greenschist	~1900 Ma	

The ~ 1.2-1.0 Ga Namaqua Orogeny involved the juxtaposition of several tectonic domains which now make-up the NNMP (Bachmann et al., 2015; Bial et al., 2016; Macey et al., 2015, 2017). This series of tectonic events were accompanied by intense ductile deformation (D_2-D_4; Joubert, 1986; Colliston and Schoch, 2013; Macey et al., 2015) and amphibolite to granulite facies metamorphism. The D_2 deformational event in the BD is characterized by very strong subhorizontal heterogeneous fabrics (generally east-west S_2 fabrics) and associated east-northeast oriented mineral and augen lineations (Joubert, 1971, 1986). Colliston and Schoch (2013) and Macey et al. (2015) attributed the D_2 deformational event to intra-terrane thrusting and folding with associated macro-scale sheath folds. The timing of the D_2 event has been constrained by making use of the timing of various intrusive events in the BD. The ~1.2 Ga LNS and older gneisses show strong S_2 fabrics, which are absent in the 1.06 Ga SS, suggesting that the D_2 event ended prior to the SS intrusion (at ~1.097 Ga; Macey et al., 2018). The main Namaqua deformation (D_2) in the BD comprises at least two phases of compressional tectonics at ~1.2 and ~1.11 Ga, separated by a period of extension (Macey et al., 2018). The minimum age of sedimentation in the NS, as determined from detrital zircon studies (~ 1.16 Ga; Cornell et al., 2009), provides evidence for a period of uplift, erosion and sedimentation within an extensional regime (Macey et al., 2015, 2018). The D_3 deformation is associated with mega- and macroscopic sheath F_3 folds with coaxial fold axes and mineral stretching lineations (Macey et al., 2011; Colliston and Schoch, 2013). The D_3 structures formed from folding and deformation of the S_2 fabric into km-scale open dome and basin structures with a locally developed S_3 fabric. These D_3 structures also produced steep structures which host the ~1.03 Ga Cu-bearing KS in the BD (Clifford et al., 2004). After the main phases of the Namaqua Orogeny (D_2-D_3), a D_4 event, which is assumed to be the continuation of an extended shear deformation event, deformed the D_1-D_3 fabrics (Colliston and Schoch, 2013). The D_4 event, which also involved re-activation and dextral strike-slip faulting along pre-existing major regional shear zones and faults, ended with the intrusion of pegmatites into F_4 folds (Macey et al., 2015; Doggart, 2019). By about 0.95 Ga, the Namaqua-Natal rocks were uplifted and as a result cooled down to temperatures of about 350ºC. However, the Gariep belt (Frimmel et al.,

2001) in the west of the Namaqua Sector is evidence of the Pan-African event in this area and was accompanied by an intrusion with a very low-grade effect. Macey et al. (2015) added a post-Namaquan, Pan-African deformation (D_5; Table 2.3) affecting the western part of the NNMP.

The NNMP encompasses both the Palaeoproterozoic Orange River extrusive supracrustal gneisses and the Mesoproterozoic Namaquan intrusives (Eglington, 2006). Eglington (2006) and Macey et al. (2018) suggested that regional igneous intrusion during the Namaquan orogeny occurred during two main periods, which include 1.21-1.18 and 1.09-1.03 Ga. The 1.21-1.18 Ga intrusion is associated with the LNS intrusion in the BD while the Spektakel, Koperberg, Oribi Gorge and Keimoes suites are associated with the 1.11-1.03 Ga intrusions. Pegmatites, which occur as roughly east-west trending intrusions in the NS, were emplaced at ~1.038 - 0.96 Ga (Melcher et al., 2015) and marked the end of the Namaqua Orogeny (Macey et al., 2015; Doggart, 2019).

2.2.3. Metamorphism and geochronology

Waters (1986, 1989) and Raith and Harley (1998) described a symmetric low pressure-high temperature metamorphic distribution in the BD, with an upper granulite facies (830ºC, 5-7 kbar) central zone (Garies and Kliprand area; Fig. 1.1), symmetrically surrounded in the north and south by lower granulite and upper amphibolite facies (650-700ºC, 4 kbar) zones (Fig. 1.1; Waters, 1986; Robb et al., 1999; Macey, 2001). Based on prograde reaction textures and a pseudomorphous replacement of andalusite by sillimanite, Waters (1986) and Raith and Harley (1998) suggested an anti-clockwise P-T path for the Namaquan metamorphism. The anticlockwise P-T path and amphibolite to granulite facies conditions determined for the BD are attributed to P-T gradients associated with crustal thickening conditions such as those observed in island arc environments (Wells, 1980; Harley, 1989; Waters, 1989). Miller (2012), Bial et al. (2015a), etc. argue, however, that the pressures at which the high-temperature metamorphism took place do not support the presence of thickened continental crust. Bial et al. (2015a, b) went on to suggest crustal development in the NS as a response to long-lasting steady heat transfer from the mantle into thinned lithosphere in a continental back-arc mobile belt setting. This is further supported by Bailie et al. (2017) and Macey et al. (2018).

Although there is still a debate as to the exact time and duration of the metamorphic events in the BD, evidences for these metamorphic events in the Namaqua Sector have been provided at ~1.2 Ga and again between ~1.1 and 1.0 Ga (Robb et al., 1999; Eglington, 2006; Cornell et al., 2009; Bial et al., 2015a, b). While peak metamorphism in the BD is dated as ~1.03 Ga (Robb et al., 1999; Raith et al., 2003) and coincides with the ~1.03 to 1.09 Ga intrusion of the SS, evidence suggests that the regional S_2 penetrative fabric formed before these events (Macey et al., 2018). Raith et al. (2003) also dated an ~1.19 Ga metamorphic event in the southern amphibolite domain which might not be obvious because of an overprint of the 1.03 Ga metamorphism in the granulite domains.

Robb et al. (1999) suggest a metamorphic grade from lower granulite facies to upper amphibolite facies in the Steinkopf area (Fig. 1.1). The dominant mineral assemblage in the metapelites of the Steinkopf area were identified by Van Aswegen (1983) as quartz + K-feldspar + sillimanite ± muscovite, suggesting upper amphibolite facies metamorphism for the rocks of the study area. Van Aswegen (1983) determined that the dominant S_2 fabric in the Steinkopf area formed during the Namaqua orogeny. This was based on the observation that the dominant

metamorphic conditions in the Steinkopf area coincided with the pressure and temperature conditions of the Namaqua orogeny.

CHAPTER 3

ANALYTICAL TECHNIQUES AND METHODOLOGY

3.1. Introduction

Several techniques were employed in order to obtain the required quantitative and qualitative data from the granitic gneisses of the GS.

Owing to time and logistical constraints, the location of the detailed map (the southern portion of the GS; Fig. 4.2) was chosen so as to closely investigate and record, in detail, the nature of the intermingled relationships between the various gneisses of the GS. However, extensive mapping of the entire GS (Appendix G) was provided by Blignault et al. (1980). The scales used in photographs, during field mapping, were oriented in the North direction and these orientations were used to add North arrows onto the field photographs in the lithological description section (Chapter 4). Sampling of the GS was carried out during field mapping of outcrops which are exposed in the Steinkopf area, and does not include the proposed GS outcrops to the west of the Nama Group (Fig. 1.2). In addition to the thirty-one (31) gneiss samples which were collected to adequately represent each of the granitic gneiss units, samples of other lithologies encountered within the GS were also collected. Samples were collected at several locations around the Steinkopf area, with the main criteria being their suitability for analysis and an appropriate representation of the GS gneisses and associated intrusive and supracrustal lithologies. Sampling sites are shown in Figs. 4.2, 5.1 and 6.1. Effort was taken to collect fresh samples. However, some samples collected were unavoidably weathered.

In addition to fieldwork and hand sample investigations, other investigations carried out include: petrographic analyses by transmitted light microscopy to investigate the mineral composition of the gneisses, whole-rock geochemical analyses (XRF and LA-ICPMS) to determine major and trace element compositions respectively, isotopic analysis (Rb-Sr and Sm-Nd isotopes) and U-Pb zircon geochronology with the aid of LA-ICP-MS.

3.2. Analytical methods

3.2.1. Petrography

Petrographic thin sections were prepared for thirty-one (31) GS granitic gneiss samples plus eleven (11) samples of associated supracrustal (mostly) and intrusive lithologies (amphibolites, metasedimentary gneisses, metaquartzite and anorthosite) encountered in the study area. Gneiss samples were chosen to adequately represent the three (3) units which make up the GS. Rock samples were cut and mounted on surfaces perpendicular to the planar fabric (regional S_2 foliation) in order to investigate mineral lineations. Thin section preparation was achieved using standard techniques as described by Humphries (1992). In summary, thin rock slices were cut and mounted on thin section glass. The mounted blocks were then reduced, first using a discoplan-TS, and then manually to a thickness of about 30 µm, using a 600grit silicon carbide powder on a glass plate. The thin section analyses were performed using transmitted light microscopy, with the aid

of a Leica DMLP polarizing microscope. The photomicrographs which accompany the petrographic observations were taken using a Leica DFC295 camera with a resolution of 2048x1536 pixels (3 Megapixels), mounted on the viewing microscope.

3.2.2. Major and trace element geochemistry

All 31 gneiss samples were analyzed for major and trace element data. Samples for geochemical analyses were prepared at the University of the Western Cape (UWC). A representative part of each sample was crushed using a jaw crusher, cleaning with quartz after every sample. The crushed samples were then milled for up to 5 minutes using a TS 250-disc mill equipped with tungsten carbide steel rings, to pulverize samples. In between each sample the steel rings were cleaned using soap water, quartz and then ethanol. Geochemical analyses were performed at the Central Analytical Facilities (CAF), Stellenbosch University. The whole-rock data recalculations were performed using the GeoChemical Data ToolKIT (GCDkit) computer programme (Janoušek et al., 2006), and other programmes, such as the Tectonic Discrimination for Intermediate and Acid magmas (TecDIA) computer programme (Verma et al., 2012, 2013; Verma and Verma, 2013; Verma, 2015) and IBM SPSS.

Loss of ignition (LOI)

The LOI was calculated by heating 1g of powder in a porcelain crucible for 2 hours at 1000ºC. LOI includes the total of the volatile content of the rock (including the water combined to the lattice of silicate minerals) and the gain on ignition related to the oxidation of the rock (mostly due to Fe). In this case, LOI represents the weight loss or gain at 1000ºC.

X-Ray Fluorescence (XRF) spectrometry

XRF spectrometry was used to obtain whole-rock major element geochemical data for the thirty-one (31) gneiss samples. Discs were prepared from powdered samples and analysed using XRF as described by Taylor et al. (2014). XRF analyses were carried out by a PANalytical Axios Wavelength Dispersive spectrometer with an X-ray tube mounted with rhodium (Rh) and operated at 3 kW. Control standards that were used in the calibration process for major element analyses were BE-N (Basalt Reference values), JB-1 (Basalt (depleted) Reference values), SY-3 (Syenite Reference values), SY-2 (Syenite Reference values), NIM-S (Syenite Reference values), BHVO-1 (Basalt Reference values), JG-1 (Granodiorite Reference values), NIM-G (Granite Reference values), WITS-G (Granite Reference values), WITS-B (Basalt Reference values), DISKO-1 (Basalt Reference values).

Laser-Ablation Inductively Coupled Plasma Mass Spectrometry (LA-ICPMS)

LA-ICPMS was used to obtain trace element data for the thirty-one (31) gneiss samples. Fused glass discs were prepared by an automatic Claisse M4 Gas Fusion instrument using ultrapure Claisse Flux (66.67 % $Li_2B_4O_7$; 32.83 % $LiBO_2$; 0.50 % LiI) and a sample to flux ratio of 1:10 (Taylor et al., 2014). The fused glass discs were analysed for trace element concentrations using a

Resonetics 193 nm Excimer laser connected to an Agilent 7700ce ICP-MS (Taylor et al., 2014). Operating conditions for the laser were 10 Hz frequency through which two spots of 100 μm each, per sample, were created during the laser ablation analysis at 5.6 J/cm^2. Ablation was performed in Helium gas at a flow rate of 0.35 L/min and mixed with Argon (and nitrogen) before introduction into the ICP plasma (Taylor et al., 2014). Certified reference standards BCR and BHVO, both basaltic glass (Jochum et al., 2005) and powder (Jochum et al., 2016) were used. A fusion control standard from certified basaltic reference material (BCR) was analyzed at the beginning of each sequence to verify the effective ablation of the fused material (Taylor et al., 2014). The data was processed using the Glitter software distributed by Access Macquarie Ltd. (Taylor et al., 2014). Each sample was analyzed twice and an arithmetic mean of both readings used as the final concentration values.

3.2.3. Isotope Geochemistry

a. Radiogenic Rb-Sr isotope analysis

Radiogenic Sr-isotope whole-rock analysis was performed on the seven samples (GS 04, GS 14, GS 20, GS 22, GS 28B, GS 30 and GS 37B) which were dated by U-Pb zircon geochronology. A Nu instruments NuPlasma HR mass spectrometer in the AEON EarthLAB, Department of Geological Sciences, at the University of Cape Town (UCT) was used to obtain the Sr-isotope data. Chemical separation was achieved using standard techniques as described by Miková and Denková (2007). Sr-isotopes were analyzed as 200 ppb 0.2 % HNO_3 solutions using NIST SRM987 as a reference standard. A value of 0.710225 was used to normalize the $^{87}Sr/^{86}Sr$ data. All Sr-isotope data were corrected for Rb interference and instrumental mass fractionation using the exponential law and an $^{86}Sr/^{88}Sr$ value of 0.1194.

b. Radiogenic Sm-Nd isotope analysis

Radiogenic Nd-isotope whole-rock analysis was performed on the seven samples analyzed for Rb-Sr. The Nd-isotope data was obtained using the same instrument as for the radiogenic Sr-isotope, following the chemical separation procedures described by Miková and Denková (2007). Nd-isotopes were analyzed as 50 ppb 2 % HNO_3 solutions using the Nu Instruments DSN-100 desolvating nebuliser. The Nd-isotope values were normalized to a value of 0.512115 (JNdi-1) after Tanaka et al. (2000). All Nd-isotope data was corrected for Sm and Ce interference, as well as instrumental mass fractionation, using the exponential law and a $^{146}Nd/^{144}Nd$ value of 0.7219. Radiogenic isotope analyses were performed using the GeoChemical Data ToolKIT (GCDkit) computer programme (Janoušek et al., 2006).

3.2.4. Geochronological methods

a. Laser ablation zircon U-Pb geochronology

About 5kg of each sample (eight samples in total) was used for U-Pb zircon dating. Heavy minerals were carefully separated using standard techniques as described by Frei and Gerdes (2009). In summary, samples were crushed and milled (in a swing mill equipped with tungsten carbide steel rings) to medium- to coarse-grained samples at the University of the Western Cape (UWC). The resulting samples were then sieved and minerals with sizes between 100-300 μm selected for heavy mineral separation as this fraction usually contains the highest zircon population. The selected fraction was washed to remove clay particles and a wet shaking table was then used to separate the heavier minerals from the lighter ones. After drying the heavier fraction obtained from the wet shaking table, the sample was subjected to magnetic separation, first with a hand magnet and then a Frantz magnetic separator. A heavy liquid density separation then followed, separating out the heaviest minerals (the fraction which contains zircon crystals and very few other minerals) based on their density. Zircon grains of different forms and roundness were then handpicked. The extracted zircon grains were mounted in epoxy and polished. A scanning electron microscope (SEM) was used to identify the internal structures of the mounted zircons and thus isolate specific target areas for U-Pb isotope analyses. Individual zircon grains were subjected to U–Pb isotopic analyses using a laser ablation single collector-magnetic sector field-inductively coupled plasma-mass spectrometry (LA-SF-ICP-MS). The LA-ICP-MS uses an ASI Resolution M-50-SE Excimer laser coupled to a Thermo Element 2 SF-SC ICP-MS (Taylor et al., 2014). All age data presented here were obtained by single spot analyses with a spot diameter of 30 μm and a crater depth of ~15-20 μm (Taylor et al., 2014). The methods employed for analyses and data processing are described in detail by Gerdes and Zeh (2006) and Frei and Gerdes (2009). The calculation of weighted mean and concordia ages, as well as plotting of concordia diagrams were performed using Isoplot/Ex. 3.0 (Ludwig, 2003).

b. Laser ablation zircon Hf isotopes

Lu-Hf isotopic analyses were only performed on the two samples (RTB027 and RTB028) provided by P. Macey (pers. comm., 2018). The zircon spots which provided near concordance (>95 % concordant) from the U-Pb analyses were further analysed for their Lu-Hf isotopic compositions. The analyses were carried out using a Thermo Scientific Neptune Plus MC-ICP-MS coupled to a New Wave Research UP193UC excimer laser ablation system and a TwoVol2 ablation cell at Curtin University, Australia. The carrier gas used through the ablation cell was Helium, while Argon sourced from a Cetac Aridus II desolvating nebuliser was connected via a T-piece. During the ablation analyses, the nebuliser was aspirating air, and the masses measured include: ^{172}Yb, ^{173}Yb, ^{175}Lu, ^{176}Hf+Yb+Lu, ^{177}Hf, ^{178}Hf, ^{179}Hf and ^{180}Hf. These masses were measured at the same time using a 1 s integration time during a static, 30 s ablation analysis utilizing a 35 μm diameter spot and a fluence of 8-10 J/cm^2 (after Spencer et al., 2015).

The precision and accuracy of internally corrected Hf-isotope ratios and instrumental drift with respect to the Lu/Hf ratio were monitored using a standard-sample-standard bracketing technique, utilizing zircons Mudtank and 91500 as reference materials. Normalization of the laser ablation Hf-isotope data was achieved during analytical sessions by analyzing Hf reference solution JMC475 (both doped with 2 ppb Yb and undoped) during each session. A ^{176}Yb/^{173}Yb

ratio, calibrated for Hf mass bias using Yb-doped JMC475 solutions was used to correct for ^{176}Yb on the ^{176}Hf peak (Nowell and Parrish, 2001). In addition, the accuracy of the Hf ratio normalization and Yb ratio correction were assessed by analyzing Plešovice and Yb-doped synthetic zircons (Zr141 and Zr142; Fisher et al., 2011), respectively. In order to correct the ^{176}Lu interference on the ^{176}Hf peak, the ^{176}Lu/^{175}Lu value, assumed to be 0.02653 (after Nowell and Parish, 2001), and the measured ^{175}Lu were used. Systematic uncertainties of Hf- and Lu-isotope ratios were propagated using quadratic addition incorporated with the external variance of the reference materials utilized. The complete methodology can be found in Spencer et al. (2015).

CHAPTER 4

LITHOLOGICAL DESCRIPTIONS AND MICROSCOPIC OBSERVATIONS

4.1. Introduction

This chapter deals with the macroscopic and mesoscopic field observations of the GS, as well as the microscopic (thin section) observations. It includes lithological observations of the GS gneisses (Figs. 4.1, 4.2) made during field mapping and sampling exercises. In addition to making lithological observations of the various GS lithologies, the aim of the mapping exercise was to use field relationships in determining, if any, relative age relationships between the gneiss units of the GS and to record evidence of tectonic deformation, as well as for structural analysis. The characteristics used during field mapping to recognize and classify the various gneiss units of the lithologically monotonous GS are secondary characteristics based on those described by Van Aswegen (1983). These secondary characteristics are defined by textural and compositional appearances at a mesoscopic scale, as well as deformation structures such as penetrative banding and metamorphic or anatectic differentiation. The S_2 and S_3 fabrics in the grey gneisses tend towards parallelism along the margins of ductile shear zones in the grey gneisses, as they are pulled along the shear zone.

Alternating light and dark layers produced by the alignment of mafic minerals imparts a gneissic appearance to the GS rocks. The gneisses are characterized by a mineralogical assemblage dominated by quartz and feldspars (plagioclase and K-feldspar), while biotite, hornblende, sericite, chlorite ± clinopyroxene and accessory minerals collectively make up less than 20 %. The gneiss units of the GS are leucocratic to mesocratic and can be broadly divided into pink (NNM Gneiss) and grey gneisses (STK and BWB gneisses). The grey varieties are generally well foliated and lineated, characterized by alternating distinct micaceous and quartzofeldspathic bands. The pink gneiss, which is less micaceous and so not really having the mineralogical make-up to develop a well-defined fabric, is weakly foliated. The GS gneisses show grain sizes which vary from medium to fine, and a porphyritic texture is commonly developed in the BWB Gneiss having relatively coarse augen-shaped grains of feldspar. The difference in the colour of the rocks does not indicate a significant difference in their mineralogical and chemical composition. Occurrences of orbicular (spheroidal) granites are uncommon, but one such occurrence was encountered during field mapping in the Steinkopf locality (Fig. 4.2) and is described here.

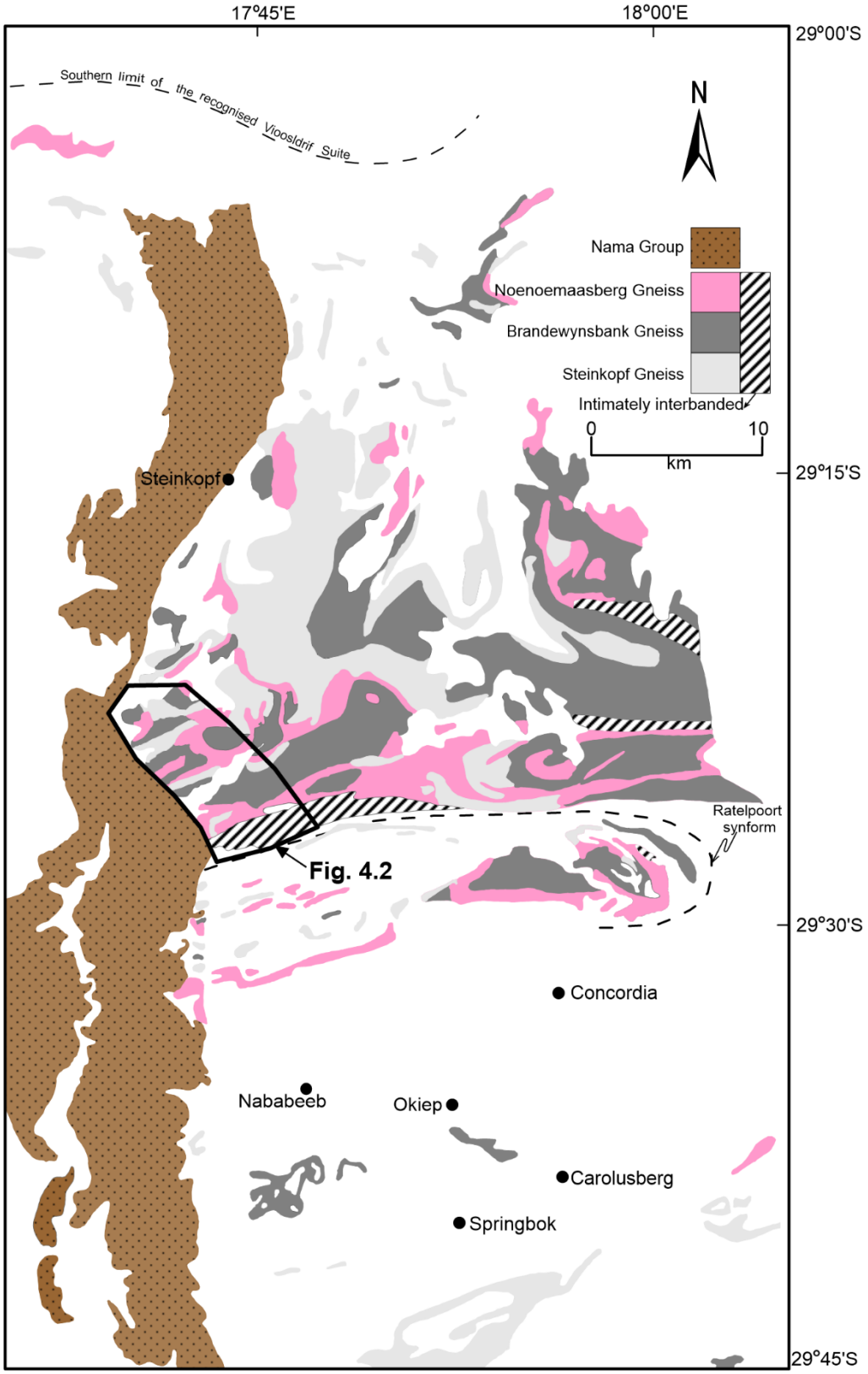

Fig. 4.1. *Distribution of the Gladkop Suite lithologies after Van Aswegen (1983), including the location of the area mapped for this study (Fig. 4.2).*

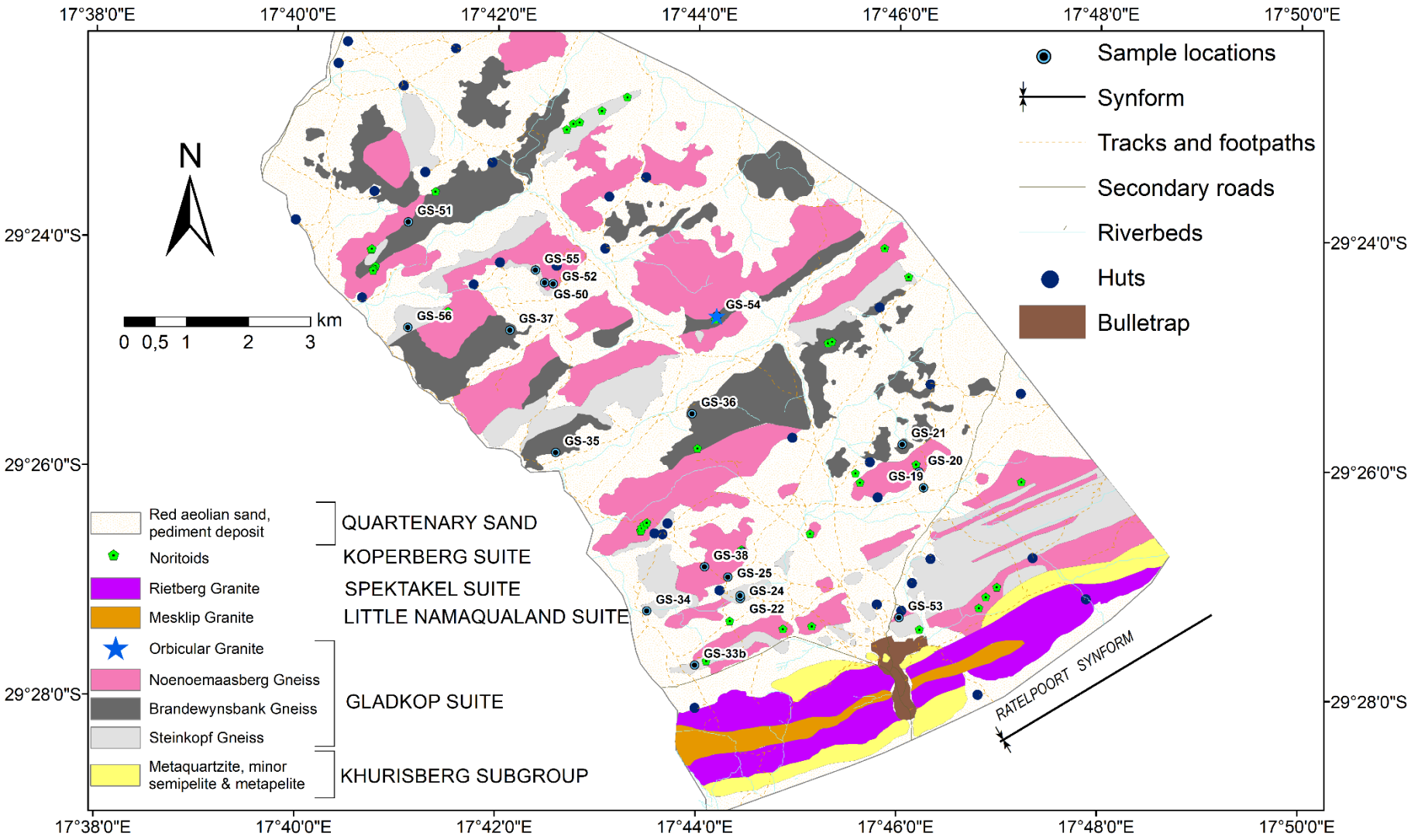

Fig. 4.2. *Geological map showing the distribution and intimate field relationships of the Gladkop Suite lithologies south of Steinkopf (this study). Locations of Koperberg Suite intrusive bodies are shown, as well as sample locations.*

Metasedimentary supracrustal rocks commonly occur as xenoliths in the GS gneisses throughout the study area, while Mesoproterozoic intrusive granitoids (late- to post-tectonic SS and pre- to syn-tectonic LNS; Joubert, 1986; Macey et al., 2018) outcrop at the southern end of the study area (Fig. 4.2). Supracrustal rocks in the GS include: amphibolite layers alternating with quartzofeldspathic sedimentary bands/layers (para-amphibolite), metapelites and metaquartzites. Xenoliths in the study area tend to be slightly flattened, thus exhibiting evidence of tectonic shearing. The group of post-tectonic mafic to intermediate rocks of the KS (Kisters et al., 1994; Clifford et al., 1995, 2004) occur as chains of small intrusive bodies throughout the study area (Fig. 4.2). The boundaries between these lithologies and the GS orthogneisses tend to be subparallel to the pervasive S_2 fabric observed in the orthogneisses. Dykes of leucocratic, metre-wide pegmatites cut into the GS gneisses. The sedimentary Nama Group overlies the GS (Fig. 4.1).

4.2. Steinkopf (STK) Gneiss

4.2.1. Description and field relationships

The STK Gneiss appears compositionally homogeneous at a macroscale, with a grey appearance. At a mesoscale, however, the STK Gneiss is a medium-grained (±1 mm) grey biotite migmatitic gneiss with a granitic to granodioritic composition (Fig. 4.3). The outcrops typically demonstrate dome-shaped weathering (Fig. 4.3b). Generally, mineral abundances tend to vary at different outcrops. Based on the visited outcrops, quartz varies between 30-40 %, plagioclase between 20-40 %, K-feldspars between 15-30 %, while biotite concentrations are usually more consistent at about 10 %. The STK Gneiss is equigranular, revealing a compositional heterogeneity imparted by a well-developed penetrative secondary banding generally consistent with the E-W oriented D_2 Namaqua fabric (Fig. 4.3b, c and d). This banding is defined by thin (0.5-1 cm) alternating leucocratic and melanocratic layers. The leucocratic layer comprises quartz, K-feldspar and plagioclase, with limited biotite. The melanocratic layer, on the other hand, is defined predominantly by biotite (and hornblende in places). The biotite content in the leucocratic layers increases towards the boundary between the melanocratic layer and the former. The STK Gneiss developed very distinct secondary structural features such as ptygmatic folding of leucocratic layers (Fig. 4.3c), as well as metamorphic features such as the partial or complete replacement of biotite by hornblende, which distinguishes it from the other GS units. However, the metamorphic replacement of biotite by hornblende is localized, making biotite the dominant mafic mineral. Leucocratic and mesocratic grey gneiss subunits (Fig. 4.3d, e and f) which display fine banding (0.5-2 cm) were considered as minor components of the STK Gneiss during mapping. Polyphase

deformation is evident in places where the D_2 fabric has been folded, forming a D_3 fabric (Fig. 4.3g).

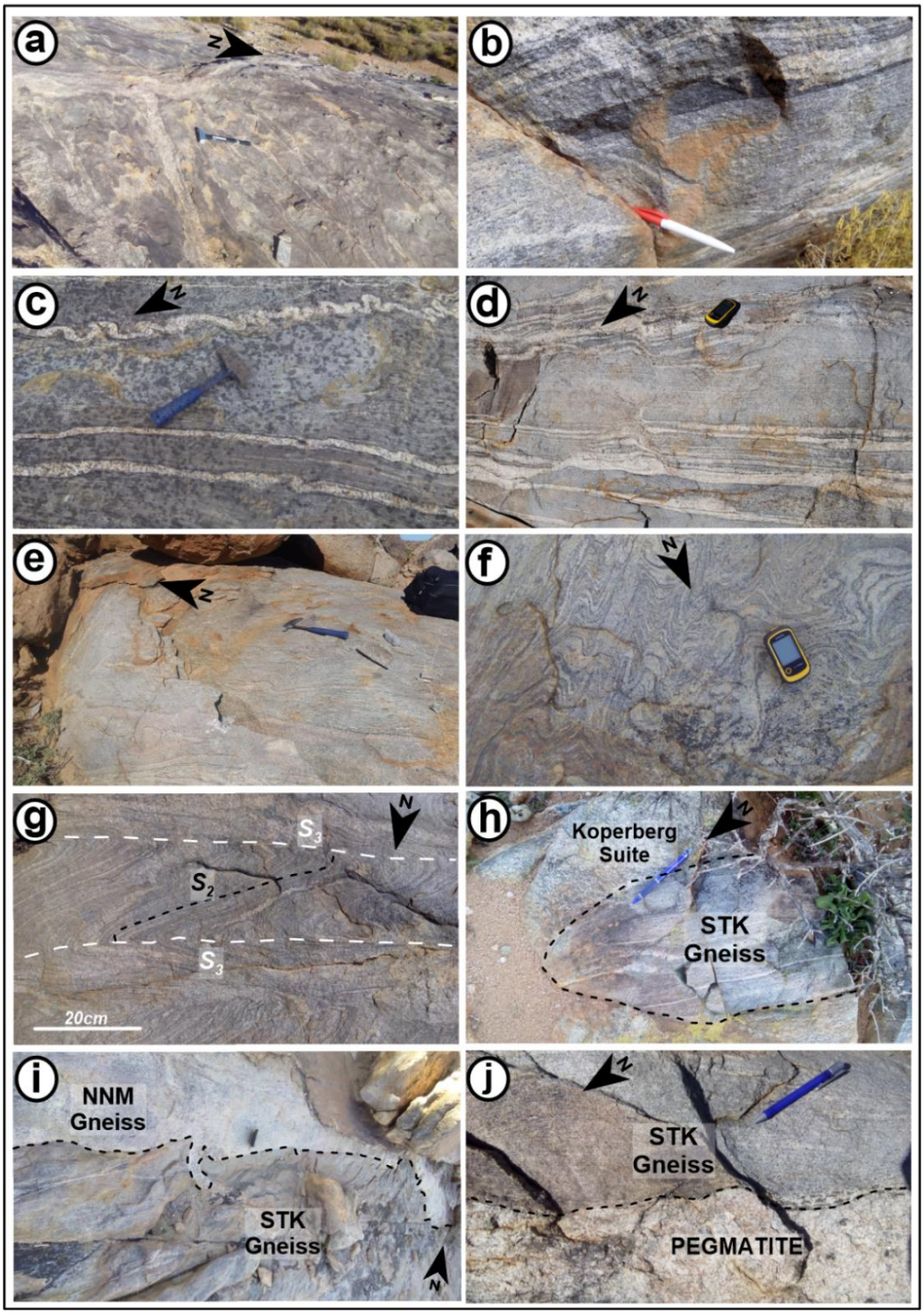

Fig. 4.3. *Field photographs of rocks of the STK Gneiss lithology. North arrow is shown.* ***(a)*** *Migmatitic character;* ***(b)*** *Thin penetrative S_2 fabric and thicker alternating bands of leucocratic and melanocratic layering. The north arrow points out of page, as shown by the pen;* ***(c)*** *Ptygmatic folding of leucocratic layers (dark spots represent rain droplets);* ***(d)*** *Folding of leucocratic layers;* ***(e)*** *Leucocratic subunit;* ***(f)*** *Mesocratic subunit;* ***(g)*** *S_2 crenulation, forming S_3;* ***(h)*** *Xenolith in Koperberg Suite intrusion;* ***(i)*** *Sharp contact with NNM Gneiss;* ***(j)*** *Sharp contact with pegmatite. For scale: Pens=15 cm; geological hammer=35 cm; Estwing hammer=40 cm; sledge hammer=60 cm; garmin GPS=10 cm.*

The STK Gneiss consistently forms sharp contacts with the BWB and NNM gneisses (e.g. Fig. 4.3i), as well as with intrusive lithologies such as pegmatites (Fig. 4.3j). Although the STK Gneiss is differentiated from the BWB Gneiss based on textural (e.g. compositional heterogeneity) and structural grounds (e.g. amount of strain), transitional types do exist.

4.2.2. Microscopic observations

The STK Gneiss is made up of 0.1-1 mm grains and is predominantly characterized by a mineral assemblage of quartz (25-35 %), microcline (15-30 %), plagioclase (10-25 %), orthoclase (5-15 %), biotite (10-15 %) ± hornblende (up to 5 % in some samples) and chlorite (up to 3 %) with accessory phases including zircon, titanite, allanite, apatite and magnetite (Fig. 4.4a-i). The mineral grains are generally bounded by straight to slightly curved grain boundaries (defining a granoblastic fabric), and are generally strain-free.

Quartz occurs mostly as equidimensional grains with regular to irregular boundaries, except at the boundaries between small newly formed grains and larger older grains where the boundary tends to be seriate (Fig. 4.4a-d and g-i). The grain sizes fall in two main ranges and include: (1) very fine sub-rounded grains (0.1-0.25 mm) which commonly occur as inclusions in plagioclase, orthoclase and microcline; and (2) fine grains (0.5-1mm), slightly elongate in places, occurring both interstitially (to the feldspars and biotite) and freely. When it occurs freely, quartz (2) usually contains inclusions of accessory zircon as well as fine grains of microcline, orthoclase, biotite and smaller hetero-oriented quartz grains. Fine grains of quartz are also observed at boundaries between larger quartz grains and either plagioclase and/or K-feldspars (myrmekite).

Biotite is the most common ferromagnesian mineral in this gneiss unit. It varies slightly in size and in abundance, measuring from 0.05 x 0.2 mm to 0.5 x 1.0 mm, and varying in concentration from 10-15 %. It occurs as fine grains to stumpy flakes with irregular edges along their width. Biotite grains usually show moderate alignment, with 50-75 % of the grains defining the alignment (Fig. 4.4h). Biotite occurs as oblong brown (to green) grains in the STK Gneiss and are pleochroic from light brown to deep brown (or light green to dark green or not pleochroic, respectively). These grains are generally interstitial between quartz and feldspar grains. The chlorite which forms coronas around biotite (Fig. 4.4f) is the product of alteration. Another feature commonly observed in biotite grains is inclusions of needle-like rutile grains intersecting at 60º.

Plagioclase commonly occurs as subhedral grains which are either interstitial or free. These grains present a fairly regular fine grain size, measuring from 0.5-1.0 mm. In areas of abundant alteration, plagioclase develops highly irregular boundaries. Typical albite and pericline twins are deformed in places, as seen from uneven spacing between them, as well as tapering ends and kinking.

Microcline occurs as subhedral grains with irregular to regular grain boundaries. They vary in size from 0.05-0.25 mm and from 0.5-1.0 mm. Most grains show cross-hatched twinning throughout the entire grain or in parts of the grain.

Where present, hornblende varies in length from 0.25 to 1 mm, with an amoeboid shape. These grains are generally pleochroic, varying from light yellow green to green to dark green. Hornblende partially replaces biotite but also shows complete replacement in a few samples, where its abundance varies up to 10 %. They commonly occur in clusters which tend to be aligned, also defining foliation (Fig. 4.4b and c).

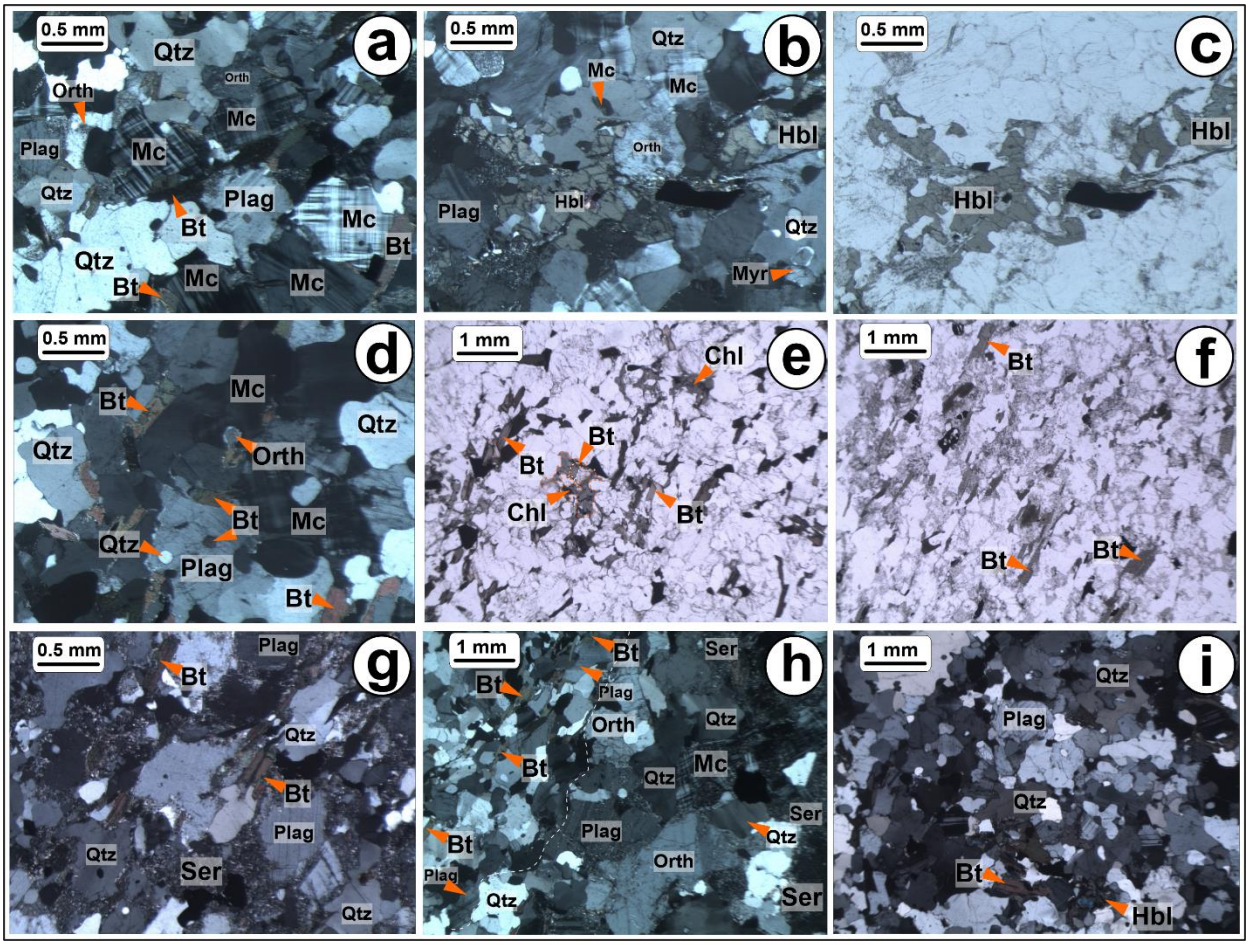

Fig. 4.4. *Photomicrographs for STK Gneiss samples from the study area.* ***(a)*** *Typical medium-grained STK Gneiss mineralogy in cross-polarized light (XPL). Biotite (Bt) grain at the bottom left of the photomicrograph is kinked.* ***(b)*** *and* ***(c)*** *Sample showing 1-2 mm hornblende crystals; (b) in crossed-polarized light (XPL) and (c) in plan-polarized light (PPL).* ***(d)****. Typical STK Gneiss mineralogy in XPL. An orthoclase (orth) inclusion in microcline (mc) is shown, as well as quartz (qtz) and bt inclusions in plagioclase (plag).* ***(e)*** *Sample shows chlorite (chl) forming coronas around bt grains resulting in an aggregate which defines the* S_2 *fabric in the STK Gneiss. White outline represents bt while orange outline represents chlorite (chl). (PPL).* ***(f)*** *Aggregate of sericite (ser) alteration, and aligned biotite. (PPL).* ***(g)*** *Aggregate of sericite (ser) alteration, quartz and aligned biotite. Extensive alteration to sericite alters plag grain boundaries. Owing to the dominance of the mica lanes, some of the quartz grains tend to be elongate parallel to the fabric caused by the biotite grains (XPL).* ***(h)*** *Sample shows the boundary (dashed line) between a bt-rich fine-grained band (left) and a bt-poor medium-grained band (right), in XPL. The qtz grain in the center of this image partly replaces a microcline grain.* ***(i)*** *Typical STK Gneiss sample showing a granoblastic texture in XPL.*

Orthoclase exhibits an almost consistent fine grain size, varying between 0.5 and 1.0 mm, with their abundances varying between 10-15 %. Orthoclase grains are usually subhedral, occurring as inclusions (in quartz mostly) or interstitially and do not show simple twinning (possibly suggesting they are metamorphic in origin).

The STK Gneiss is generally fine-grained, with a high biotite content and a granoblastic fabric. The samples typically show a rough gneissic foliation defined by partial alignment of biotite grains (which locally occur as aggregates with chlorite and hornblende). A variation of the STK Gneiss forms alternating thicker bands, defined by plagioclase-rich bands which are generally more altered (composed predominantly of plagioclase, microcline and quartz; Fig. 4.4h), alternating with plagioclase-poor bands. A transition from the characteristic STK Gneiss

mineralogy/fabric to the felsic bands is accompanied by a general increase in grain size and alteration, and a decrease in biotite content (Fig. 4.4h). Intragranular structures such as curved cleavages in micas (biotite specifically) and distorted twin lamellae in plagioclase are locally present. Intergrowths such as myrmekite are also present. Reaction rims of unaltered sodic plagioclase (albite), which formed around plagioclase, separating it from quartz, are present. Quartz, plagioclase and microcline may occur as porphyroblasts, with inclusions of small newly formed quartz grains. The K-feldspars (microcline and orthoclase) are the dominant feldspars in the STK Gneiss.

4.3. Brandewynsbank (BWB) Gneiss

4.3.1. Description and field relationships

The BWB Gneiss is a phaneritic, equigranular and compositionally homogeneous grey biotite gneiss. The homogeneity of this lithological variety is reflected on both a macro- and mesoscale. It is a grey medium- grained (±2 mm) granitic gneiss which is differentiated from the STK Gneiss by its relatively larger grain size, as well as its relatively less mafic composition. Based on textural features, the BWB Gneiss is divided into a non-megacrystic (Fig. 4.5a and b) and a megacrystic subunit (Fig. 4.5c, d and f). The non-megacrystic BWB Gneiss is the more common subunit, which is medium-grained equigranular and forms monotonous dome-shaped outcrops. This subunit is consistently composed of approximately equal amounts of quartz and K-feldspar (35-45 %), with lesser amounts of plagioclase (10-20 %) and a relatively low biotite content (about 5 %). The biotite distribution follows an anastomosing pattern resulting in distinct domainal fabrics. The megacrystic subunit is characterized by discrete K-feldspar megacrysts (about 0.3x0.8 mm) and is generally more mafic (up to 12 % biotite) than the non-megacrystic subunit. In some localities, the frequency and size of the megacrysts increase and the rocks grade into an augen gneiss in which the K-feldspars (up to 10mm in length) are set in a fine-grained biotite-rich matrix. The augen gneiss is characterized by a higher biotite content, local sites where hornblende replaces biotite, and variable sizes of augen, ranging from very small (just above matrix size) up to 10 mm in length. Outcrops of the megacrystic BWB Gneiss typically form L-S tectonites (Fig. 4.5e). Xenoliths of the mafic (megacrystic) BWB subunit occur locally in the outcrops of the common (non-megacrystic) BWB Gneiss. These xenoliths tend to vary in size, up to 1x2 m and occur over distances of about 20 m. Contamination of the BWB Gneiss commonly occurs at the point of contact between it and the metasedimentary minor bands. A rare example is seen in the case where a BWB Gneiss, which is in contact with a calc-silicate, experiences a replacement of biotite by hornblende and an enrichment of plagioclase relative to K-feldspar, changing the composition from a normal granitic type towards that of a calc-silicate. The contacts between the BWB Gneiss and the metasedimentary bands tend to be parallel to the regional S_2 tectonic fabric. This gneiss variety forms a sharp contact with the NNM Gneiss, where the biotite content in the latter becomes significantly reduced, imparting a sugary texture. The contact with the STK Gneiss tends to be gradational over about 100 cm. The S_2 fabric in the Steinkopf gneisses is cross-cut by an intrusive biotite-hornblende granite in a few localities (Fig. 4.5h).

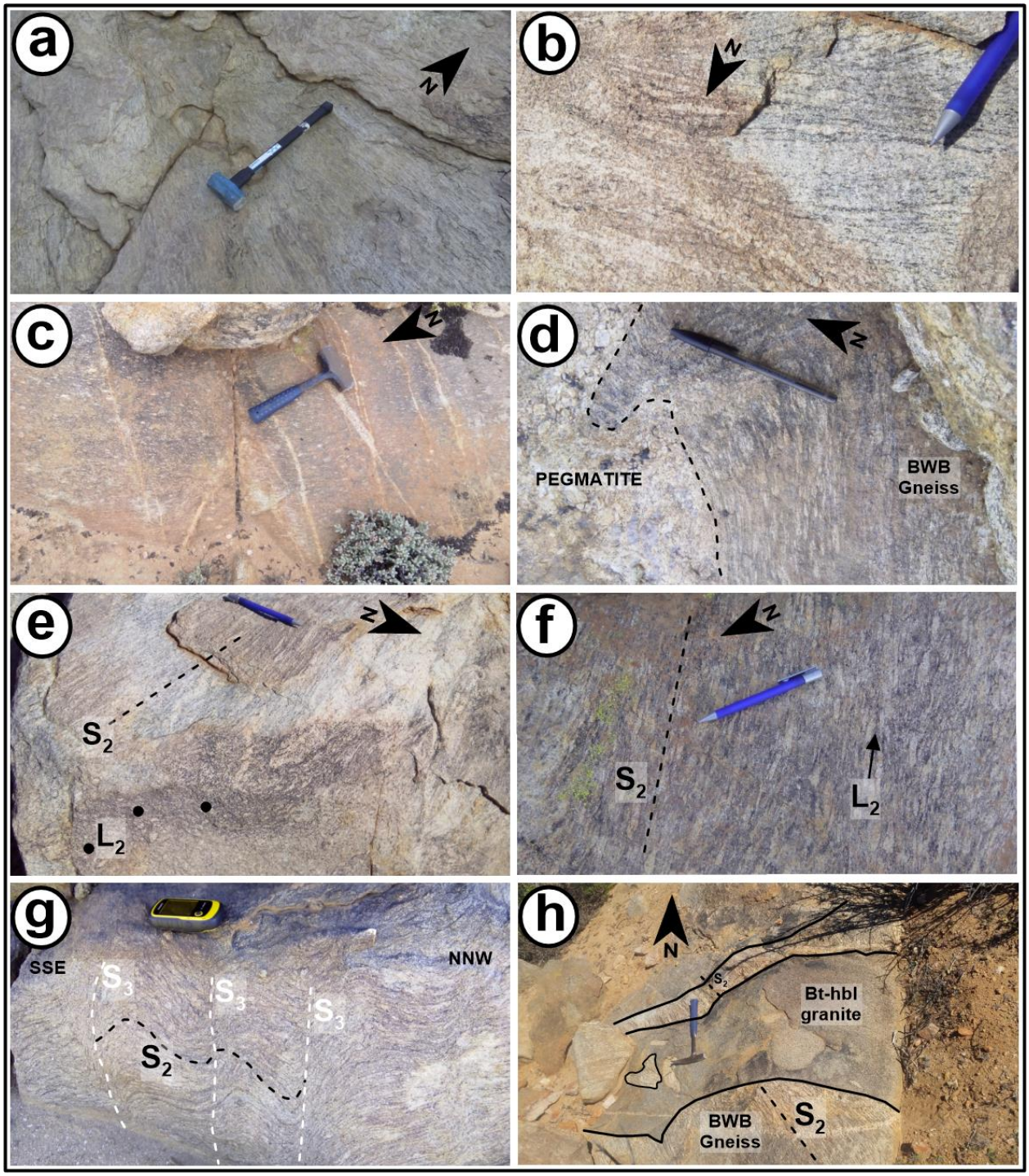

Fig. 4.5. *Field photographs of the rocks of the BWB Gneiss lithology. North arrow is shown. Scales the same as in Fig. 4.3.* ***(a)*** *Equigranular (non-megacrystic) biotite-granite BWB Gneiss;* ***(b)*** *Non-megacrystic BWB Gneiss;* ***(c)*** *Megacrystic (mafic) BWB Gneiss;* ***(d)*** *Pegmatite (left side) in megacrystic BWB Gneiss;* ***(e)*** *L-S tectonites. S (and dotted line) represent the fabric (foliation) on the horizontal plane while the black dots and L represent K-feldspar lineations on the vertical plane;* ***(f)*** *K-feldspar augen are aligned (direction shown by black arrow) subparallel to the S_2 fabric in the BWB Gneiss;* ***(g)*** *S_2 fabric crenulation producing the S_3 fabric;* ***(h)*** *Dyke of biotite-hornblende granite cross-cutting the fabric in the BWB Gneiss. Solid lines define the boundary between the two lithologies, while dashed lines represent the S_2 fabric. The polygon in the bottom left indicates a BWB Gneiss xenolith in the biotite-hornblende granite.*

4.3.2. Microscopic observations

The BWB Gneiss is typically medium-grained (1-2 mm) and predominantly characterized by a mineral assemblage of quartz (30-35 %), microcline (10-20 %), plagioclase (10-15 %), orthoclase (5-15 %), biotite (5-10 %) ± hornblende (up to 3 % in some samples) and clinopyroxene (up to 3 %) with accessory phases including zircon, apatite, allanite and magnetite (Fig. 4.6). The mineral grains are generally bounded by straight to slightly curved grain boundaries (defining a granoblastic fabric), and are generally strain-free.

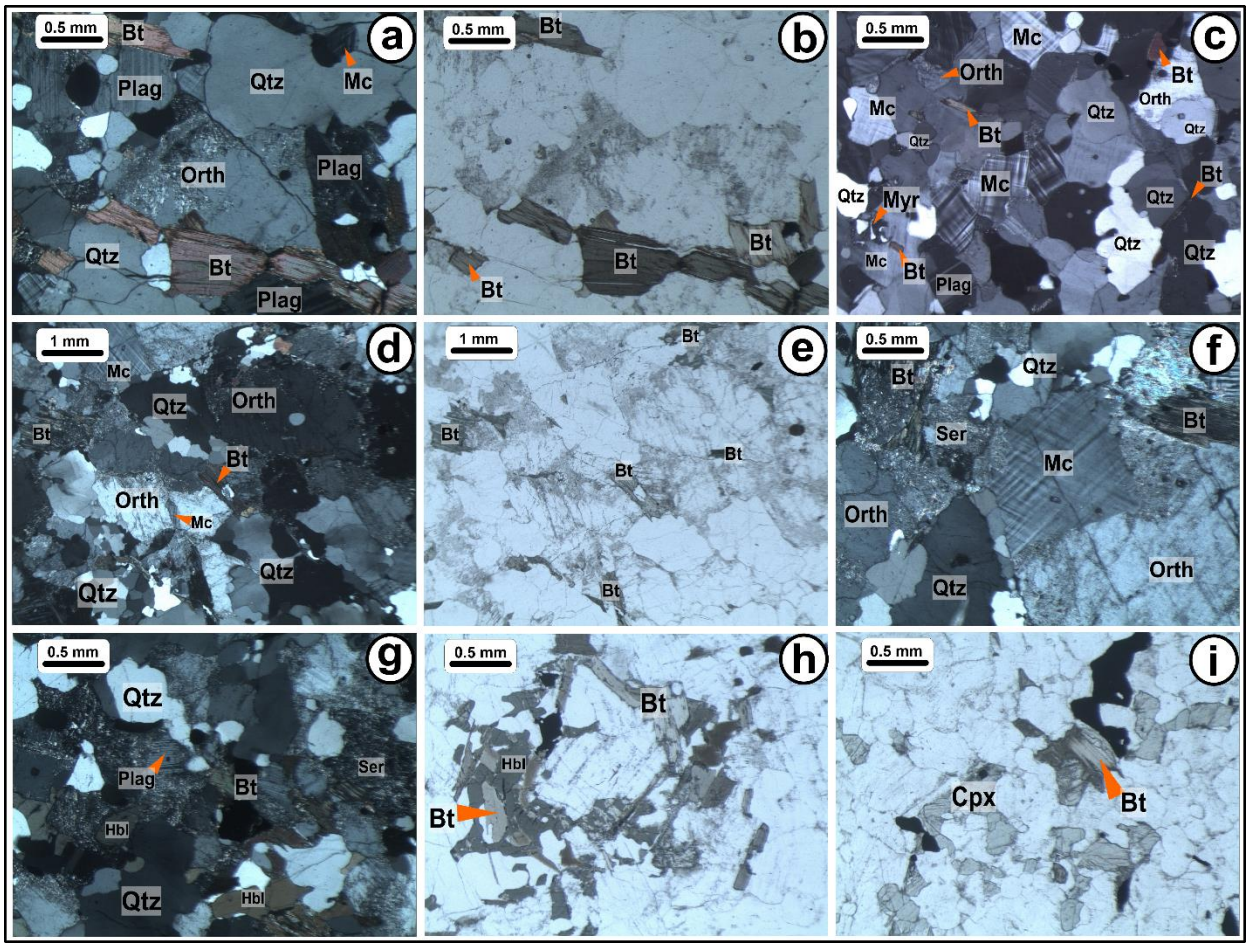

Fig. 4.6. *Photomicrographs for BWB Gneiss samples from the study area.* ***(a)*** *Aggregate of quartz, plagioclase, orthoclase and biotite in the BWB Gneiss. Image is in XPL.* ***(b)*** *Same image as (a), but in PPL.* ***(c)*** *Aggregate of quartz and feldspar with minor biotite in the BWB Gneiss (XPL). Although the quartz and feldspar form polygonal aggregates, interfaces between these minerals meet biotite planes at right angles (bottom right) or attach to the ends of biotite grains (top right).* ***(d)*** *K-feldspars (Mc and Orth) and recrystallized quartz (Qtz) in the BWB Gneiss (XPL). The large orthoclase grain in the top right hand corner has a round quartz inclusion.* ***(e)*** *Same image as in (d), but in PPL.* ***(f)*** *Aggregate of K-feldspars (Mc and Orth) and recrystallized quartz in XPL. Biotite grains (top left and top right) are altered to muscovite.* ***(g)*** *Abundant sericite alteration in the BWB Gneiss (XPL).* ***(h)*** *An aggregate of hornblende and biotite (PPL).* ***(i)*** *Sample showing clinopyroxene grains (high relief) which locally surround biotite (center). Image is in PPL.*

Quartz makes up about 30-35 % of the rock and occurs as anhedral grains with regular to irregular boundaries. Irregular boundaries are commonly formed between older quartz grains and

newly formed finer quartz grains. Quartz grains were grouped based on grain sizes and occurrence: the first group consists of small, sub-rounded grains (0.1-0.25 mm) which commonly occur as inclusions in plagioclase, orthoclase and microcline showing different optical orientation; the second group occurs as slightly elongate 1-2 mm grains, are interstitial and contain inclusions of minute particles such as biotite, sericite and K-feldspars; and the third group constitutes recrystallized grains along grain boundaries of other minerals notably feldspars (Fig. 4.6d). Plagioclase (10-15 %) occurs as subhedral grains, measuring from 0.5x0.75 mm to 1.0x2.0 mm. Microcline occurs as subhedral grains with irregular to regular grain boundaries and varies in size from 0.1 mm to 0.5x1.0 mm to 1.0x3.0 mm.

Biotite is the most common ferromagnesian mineral in these rocks. It varies in abundance from 5-10 % and in size from 0.1-0.5 mm, with irregular terminations (Fig. 4.6a and b). The grains mostly occur interstitially or as inclusions and are mostly brown and pleochroic (Fig. 4.6b, e and f). Orthoclase exhibits an almost consistent medium grain size, varying between 1.0-2.0 mm. Their abundances vary between 10-15 %.

The BWB Gneiss is medium-grained, with a relatively low biotite content. The biotite content is however higher than in the NNM Gneiss. Biotite grains are slightly aligned, defining a rough gneissic foliation with a general elongation of the quartz and feldspar grains (Fig. 4.6a, b, g and h), while quartz and feldspar aggregates show a mosaic (granoblastic) fabric (Fig. 4.6c). The BWB Gneiss is commonly altered, especially evident in minerals such as plagioclase (by sericite and clay minerals), and orthoclase (by sericite and clay minerals), with biotite less commonly altered to muscovite and chlorite. Intragranular structures, such as curved cleavages in micas and distorted twin lamellae in plagioclase, are present in some places. Intergrowths, such as myrmekite, are also present. Reaction rims of unaltered sodic plagioclase (albite) formed around plagioclase separating it from quartz are also present. Plagioclase and microcline may occur as porphyroblasts, with inclusions of quartz. K-feldspars (microcline and orthoclase) tend to be the dominant feldspar. Feldspars and quartz commonly host zircon grains.

4.4. Noenoemaasberg (NNM) Gneiss

4.4.1. Description and field relationships

The NNM Gneiss is typically a medium-grained (±2 mm) leucogranitic gneiss which weathers reddish-brown (Fig. 4.7a), with light grey to white fresh surfaces. The rock typically has a pink appearance and is compositionally homogeneous on all scales, with a rare penetrative anastomosing fabric. Texturally, this gneiss unit can be divided into a banded and a non-banded subunit.

The typical leucogneiss of the Steinkopf locality (the non-banded subunit) is medium-grained and characterized by about 4% biotite content (Fig. 4.7a, b). It is texturally and compositionally homogeneous on both meso- and macro-scales. The leucogneiss typically shows a blocky style of weathering (Fig. 4.7a). Typical outcrops reveal an anastomosing distribution pattern displayed by the arrangement of leucocratic and mesocratic minerals, defining a penetrative gneissic fabric. The leucocratic bands (about 3 cm wide) are dominated by equidimensional quartz and feldspar crystals (±2 mm). The shapes of these bands (formed by anastomosing foliation) are determined by the amount of strain which affected the area, with low strain resulting in thinner bands (about 1 cm wide). Such fabrics are clearly visible on weathered surfaces with relatively

high biotite content, which are perpendicular to the regional stretching lineation. Wherever a contact between this leucogneiss lithology and the BWB Gneiss is exposed, the boundary between the two is sharp (Fig. 4.7g).

Small inclusions of the BWB and STK gneisses are fairly common in the leucogneiss units, mostly in the form of thick bands (10 to 20 cm wide), but variable shapes are also present (Fig. 4.7h). At the boundaries between the leucogneiss and the grey gneisses (the BWB and STK gneisses), the biotite content in the leucogneisses is significantly reduced to about 1-2 % and occurs over a distance of a few centimeters.

The leucogneiss, however, demonstrates noticeable banding in some locations (referred to as the banded subunit; Fig. 4.7e, f). The banding in this subunit is characterized by alternating leucocratic and melanocratic bands, which are parallel to the regional gneissic fabric. The leucocratic bands are composed of approximately equal amounts of K-feldspar, plagioclase and quartz, while the intervening slightly darker bands consist of K-feldspar, quartz and minor amounts of biotite. The change from the non-banded to the banded leucogneiss is characterized by the overall reduction of characteristic textural sizes and shapes, and is gradational over a few centimeters.

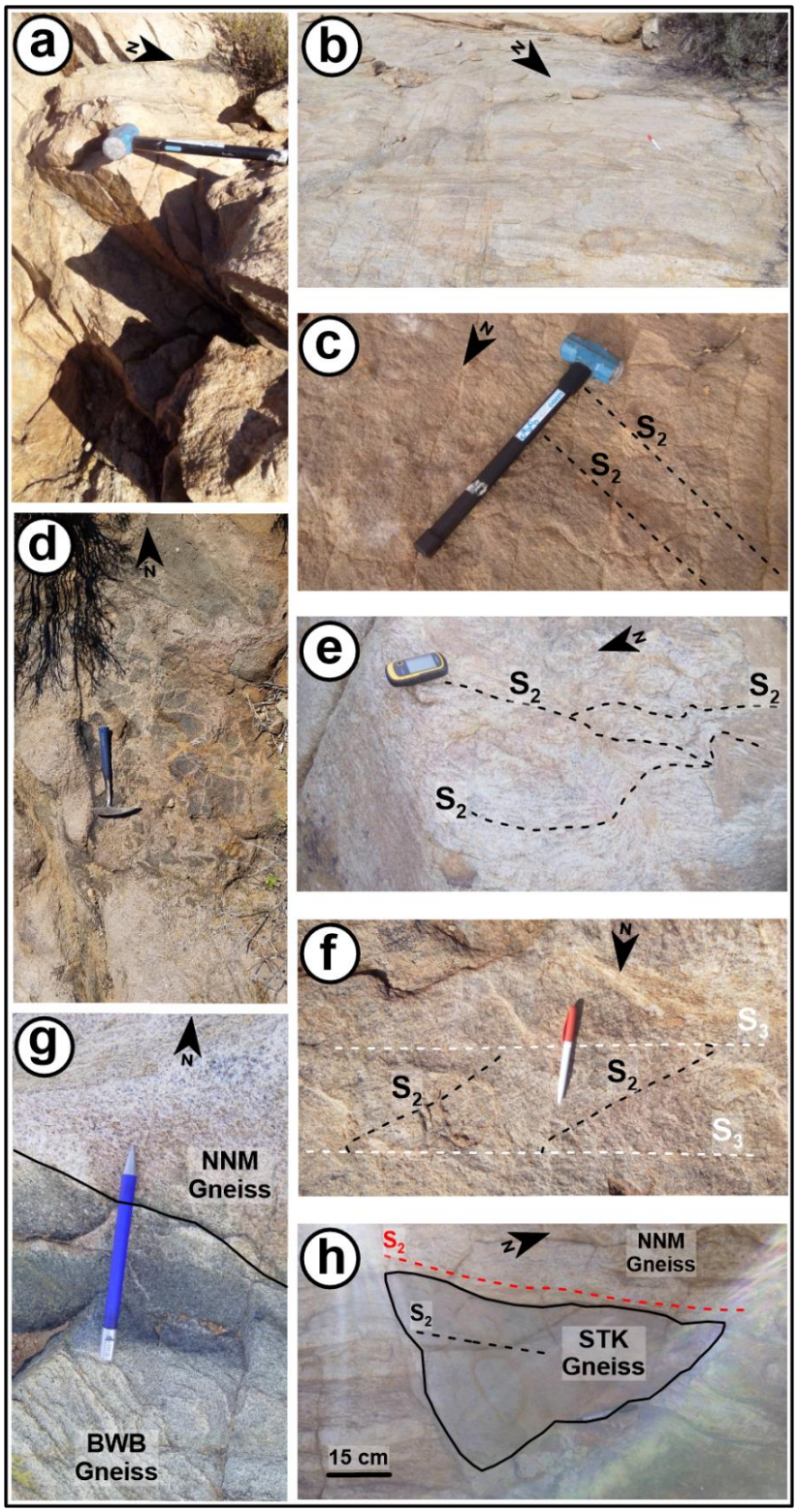

Fig. 4.7. *Field photographs of the rocks of the NNM Gneiss lithology. The North arrow is shown. Scales is the same as in Fig. 4.3.* ***(a)*** *Blocky nature of the pink gneiss, as a result of its very quartzofeldspathic composition;* ***(b)*** *Non-banded subunit;* ***(c)*** *S_2 fabric (dashed lines) in the pink gneiss;* ***(d)*** *Blocky intrusive magmatic mega-breccia;* ***(e)*** *Anastomosing fabric. Dashed lines represent the S_2 fabric;* ***(f)*** *S_2 fabric crenulation producing the S_3 fabric;* ***(g)*** *Sharp contact between the BWB and NNM gneiss lithologies;* ***(h)*** *STK Gneiss xenolith in the NNM Gneiss. The black solid line represents the contact between the two gneisses and the dashed lines represent the S_2 fabric in both gneisses, red for the NNM Gneiss and black for the STK Gneiss.*

4.4.2. Microscopic observations

The NNM leucogneiss is typically medium-grained (1-3 mm), with a biotite content ranging from 3 to 5 %, and is characterized by a granoblastic fabric (Fig. 4.8a-l). They are predominantly characterized by a mineralogical assemblage of quartz (40-50 %), microcline (20-30 %), orthoclase (15-20 %), plagioclase (5-10 %) and biotite (3-5 %), with accessory minerals including magnetite, zircon, titanite and allanite. The NNM Gneiss minerals (mostly feldspars) are highly altered, to sericite and clay minerals, with very little deformation. K-feldspars (microcline mostly) are the dominant feldspars. Mineralogical banding is rare to absent in the NNM Gneiss samples.

Quartz occurs as xenoblastic grains with regular boundaries (with feldspars; Fig. 4.8b, d-h) to irregular boundaries (with newly formed quartz grains; Fig. 4.8a, d), as well as in finer polygonal aggregates (Fig. 4.8a, d and l). The polygonal quartz aggregates suggest extensive recrystallization of quartz. Intergrowths of fine grains of quartz with microcline and plagioclase (myrmekite) are present. Quartz generally shows replacement textures, typically overgrowing biotite (Fig. 4.8b, c). Plagioclase occurs as xenoblastic grains, mostly measuring from 1-2 mm, but smaller grains are present (0.1-0.25 mm; Fig. 4.8k). They are usually interstitial and free. Most grains are altered to sericite but a few samples show very little alteration. Both for altered and unaltered grains, a 'clear rim' on plagioclase forms at contacts with microcline (probably due to a decrease in Ca content) (Fig. 4.8k). Unaltered grains show characteristic albite and pericline twinning, and are highly deformed, evident from tapering twins. Myrmekitic intergrowths with quartz are present particularly where plagioclase is associated with microcline (Fig. 4.8g). Plagioclase grains are rarely antiperthitic and forms clear rims at contacts with microcline (Fig. 4.8g).

Microcline occurs as xenoblasts with irregular to slightly regular grain boundaries. Irregular boundaries are prominent at contacts with plagioclase, and hetero-oriented microcline. They vary in size from 0.1 to 0.5 mm by 1.0 to 3.0 mm. Most grains show cross-hatched (tartan) twinning in the entire grain or in parts of the grain (Fig. 4.8). Worm-like intergrowths of myrmekitic quartz replace microcline in places (Fig. 4.8g, l). Microcline is commonly perthitic (Fig. 4.8b). Exsolved albite is altered to sericite and clay minerals. Alteration is rare in microcline, but where present alteration to clay minerals gives a cloudy appearance. Inclusions of altered biotite (to muscovite), plagioclase and quartz occur in large porphyroblasts of microcline. Intergrowths such as myrmekite and perthite are also present. Plagioclase and microcline may occur as porphyroblasts, with inclusions of quartz. Generally, samples do not show any foliation, but samples of the banded subunit are foliated (defined by biotite alignment; Fig. 4.8h and i). Biotite is the most common ferromagnesian mineral in these rocks. The grains are mostly interstitial and also occur as inclusions in quartz, microcline and plagioclase (Fig. 4.8g). It varies in size, measuring from 0.05x0.2 mm to 0.5x1.0 mm and occurs as fine grains to oblong flakes with irregular terminations. The mineral is commonly green and pleochroic, but clear to pale brown varieties are also present. Pleochroic haloes are developed around inclusions of zircon and titanite. Biotite grains are consistently overgrown, especially by quartz (Fig. 4.8b, c). Some biotite grains tend to be sagenitic. Orthoclase is rare, but where present shows a very limited occurrence (3-5 %) and vary in size between 0.5 and 2 mm. They tend to be highly altered to sericite and twins are rare, but are present (Fig. 4.8j).

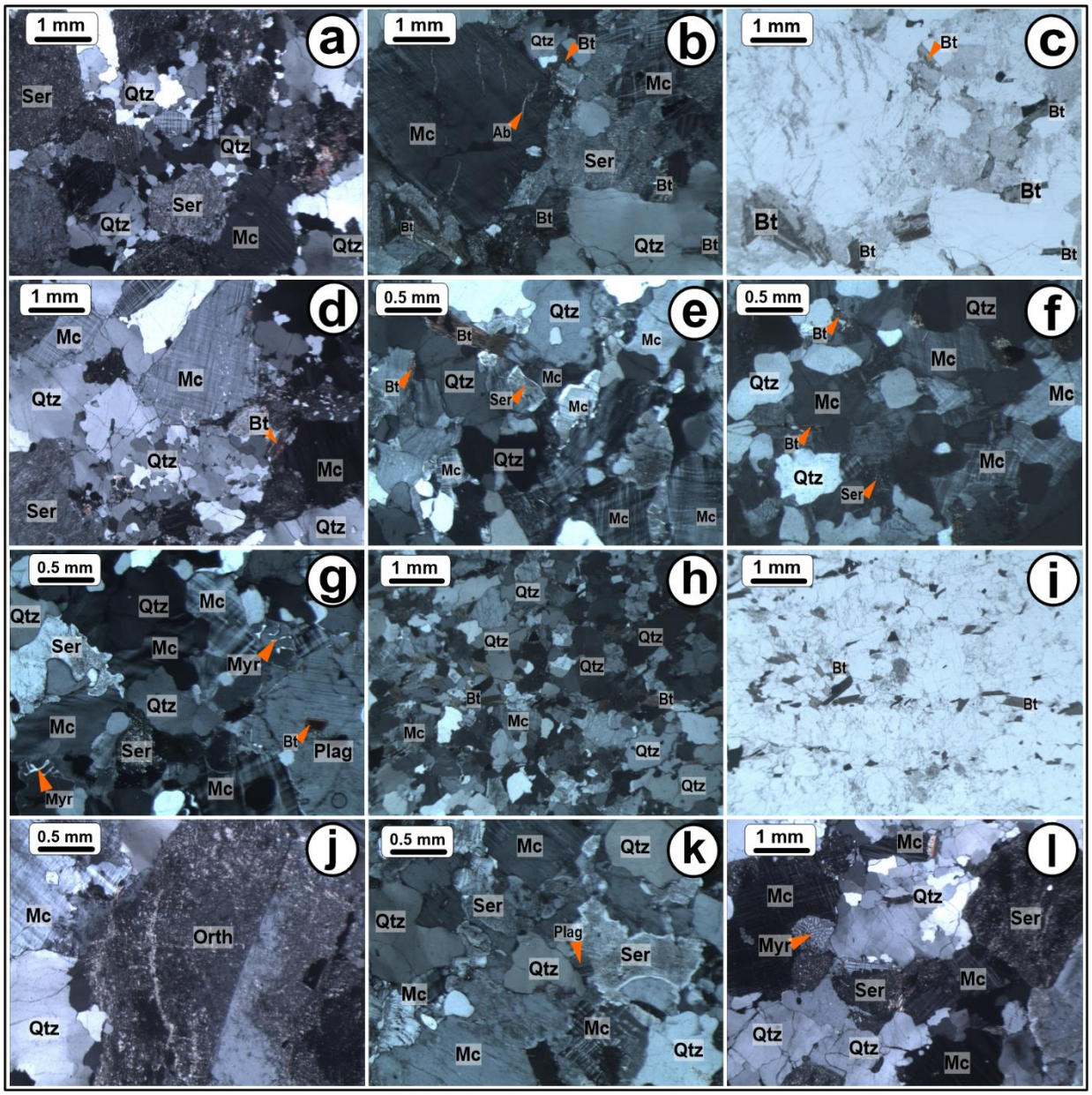

Fig. 4.8. *Photomicrographs of the NNM Gneiss samples.* ***(a)*** *Extensive alteration of feldspars to sericite and recrystallization of quartz grains producing finer polygonal quartz aggregates. Irregular boundaries typically occur between new and old quartz grains (e.g. bottom right corner) (XPL).* ***(b)*** *Microcline perthite grain in the NNM Gneiss (left side). The exsolved albite (Ab) lamellae anastomose and are of various widths. The large quartz grain in the bottom right corner overgrows the adjacent biotite grains (XPL).* ***(c)*** *Same photo as (b), but in PPL. Biotite has a pale-green colour, probably due to alteration.* ***(d)*** *Extensive quartz recrystallization producing finer polygonal quartz grains (bottom). Regular boundaries are formed between larger quartz grains and microcline (XPL).* ***(e)*** *Limited alteration in the NNM Gneiss. A clear rim is formed between two hetero-oriented microcline grains (center) (XPL).* ***(f)*** *Quartz and microcline aggregate (XPL).* ***(g)*** *Myrmekite (Myr) replacing microcline (Mc) in the NNM Gneiss (bottom left, top right). There is a clear rim formed between the plagioclase and microcline grains in contact (bottom right) (XPL).* ***(h)*** *NNM Gneiss sample with an unusually high biotite (Bt) content. Biotite rains are aligned, defining the fabric in the rock (XPL).* ***(i)*** *Same as in (h), but in PPL.* ***(j)*** *Extensively altered orthoclase (orth) grain showing simple twinning (XPL).* ***(k)*** *Patchy tartan twinning in microcline (top and bottom). Grain boundaries are irregular between feldspars, but regular between feldspars and quartz. A 'clear rim' is present around an altered grain (right). Multiple twinning characteristic of plagioclase grains is preserved in the altered grain (XPL).* ***(l)*** *Quartz grain (center) is extensively recrystallized. Myrmekite replaces microcline (left) (XPL).*

4.5. Orbicular granite

These are granitic rocks characterized by large concentrically layered spheroidal to ellipsoidal structures generally referred to as orbicules (Fig. 4.9). Orbicular granites, although generally uncommon, have been found to coincide with margins of intrusive plutonic complexes as ten- to hundred-metre diameter bodies (Decrite et al., 2002). Previous studies (e.g. Elliston, 1984; Fernandez and Castro, 1999; Abdallah et al., 2007; Grosse et al., 2010) have associated the formation of orbicular bodies to magma fractures, crystallization fronts or magma-host rock interactions. The formation of these orbicular bodies has also been linked to nucleation around a seed grain in a dynamic fluid-rich super-cooled magma chamber (Kobe, 1983, 1988). Elliston (1984) noted that the spheroidal to ellipsoidal orbicules are composed of a core and one or several rings with radially and/or concentrically arranged granitic minerals (shell).

4.5.1. Description and field relationships

The body of orbicular granite occurs in a very small area with a radius of ~2 m, at a boundary between the BWB and NNM gneisses (Figs. 4.2, 4.10a-d). The orbicular granite is characterized by spheroidal to ellipsoidal orbicules hosted in a medium- to coarse-grained granitic to granodioritic matrix (composed of plagioclase, quartz, hornblende, biotite, K-feldspar ± clinopyroxene). The contact relationship between the orbicular granite and the BWB/NNM gneisses is generally 'diffuse' and difficult to pinpoint exactly.

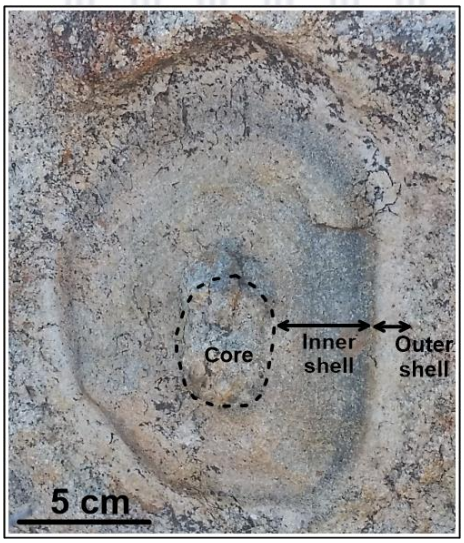

Fig. 4.9. *Image showing the zones (core, inner shell and outer shell) of an orbicule in the Gladkop Suite. The light-grey core is coarse-grained and composed of Qtz, Kfs, Plag and minor amounts of Mag and Bt. The inner shell is fine- to medium-grained and is characterized by alternating light and dark layers (see text for mineralogy). The outer shell is medium-grained and composed of Qtz, Kfs and Plag.*

The ellipsoidal to globular orbicules, which vary in size from ~10x15 cm up to ~15x20 cm, are composed of concentrically arranged components/layers (Figs. 4.9 and 4.10). The

orbicules (Fig. 4.9) are mainly characterized by a light-grey, medium- to coarse-grained core, surrounded by thin alternating light and dark layers (inner shell). The inner shell is enclosed by an outermost 1-2 cm quartzofeldspathic layer (outer shell). Although the orbicule shells maintain a constant width of 2-5 cm, the external shapes and sizes of the orbicules generally mimic the shapes of the cores. The distance between orbicules is random, and the orbicules may appear plastically deformed against each other (Fig. 4.10a, c). The orbicules make up about 60 % of the orbicular body.

The orbicular core (3-5 cm in diameter) is compose of K-feldspar and quartz, with minor plagioclase, biotite and magnetite. It is characterized by its light-grey colour, with an average grain size varying from 1 to 2 mm. The inner shell is composed of K-feldspar, quartz, magnetite, plagioclase and biotite, and shows an average grain size ranging from 0.1 to 0.7 mm. It is composed of concentrically alternating 1 to 2 cm thick leucocratic and melanocratic bands. The leucocratic bands are made up of K-feldspar and quartz (70-80 %), with minor plagioclase, magnetite and biotite (20-30 %). The melanocratic bands are made up of K-feldspar, magnetite and biotite (80-90 %), with minor quartz and plagioclase (10-20 %). The outer shell has an average grain size of 1 mm, and is composed of K-feldspar and quartz (90 %), with minor plagioclase and biotite (10 %).

4.5.2. Orbicule microscopic observations

The observations described here pertain to the inner shell (Figs. 4.9 and 4.10) of the orbicule. The orbicule shells are typically made up of grains whose sizes vary from 0.1 to 0.7 mm (Fig. 4.10e-h). They are predominantly characterized by a mineralogical assemblage of microcline (40-50 %), orthoclase (15-20 %), magnetite (10-20 %), quartz (10-15 %), plagioclase (5-10 %) and biotite (1-2 %). K-feldspars are the dominant feldspars (Fig. 4.10e-h). The orbicule shells are characterized by concentrically alternating melanocratic and leucocratic layers. A transition from the melanocratic layer to the leucocratic layer is accompanied by a general increase in grain size, an increase in the abundance (and grain size) of quartz, a decrease in amount of magnetite and an increase in alteration of feldspars to sericite (Fig. 4.10g, h).

Microcline occurs as 0.4 to 0.7 mm grains with fairly regular grain boundaries (Fig. 4.10e-g). Most grains show cross-hatch twinning in the entire grain or in parts of the grain. Alteration is rare in microcline, but where present alteration to clay minerals gives a cloudy appearance. Inclusions of magnetite, altered orthoclase and quartz occur in large microcline grains (Fig. 4.10e, f). Reaction rims of unaltered sodic plagioclase (albite) formed around altered (to sericite) plagioclase and orthoclase grains, separating it from microcline (Fig. 4.10f, g), are present. Quartz occurs mostly as 0.1-0.25 mm grains, but up to 0.5 mm in felsic bands (Fig. 4.10e, f). It generally forms regular boundaries with feldspars. Quartz commonly occurs as inclusions (in sericitized orthoclase and microcline; Fig. 4.10e, f and g), interstitially and freely. Plagioclase has a slightly more consistent grain size of about 0.25 mm and shows characteristic albite and pericline twinning. Worm-like intergrowths of myrmekitic quartz with feldspars are rare but present, particularly where orthoclase is associated with microcline. Orthoclase and (mostly) plagioclase, where present, show a very limited occurrence but are significantly altered, with no twins present in the former.

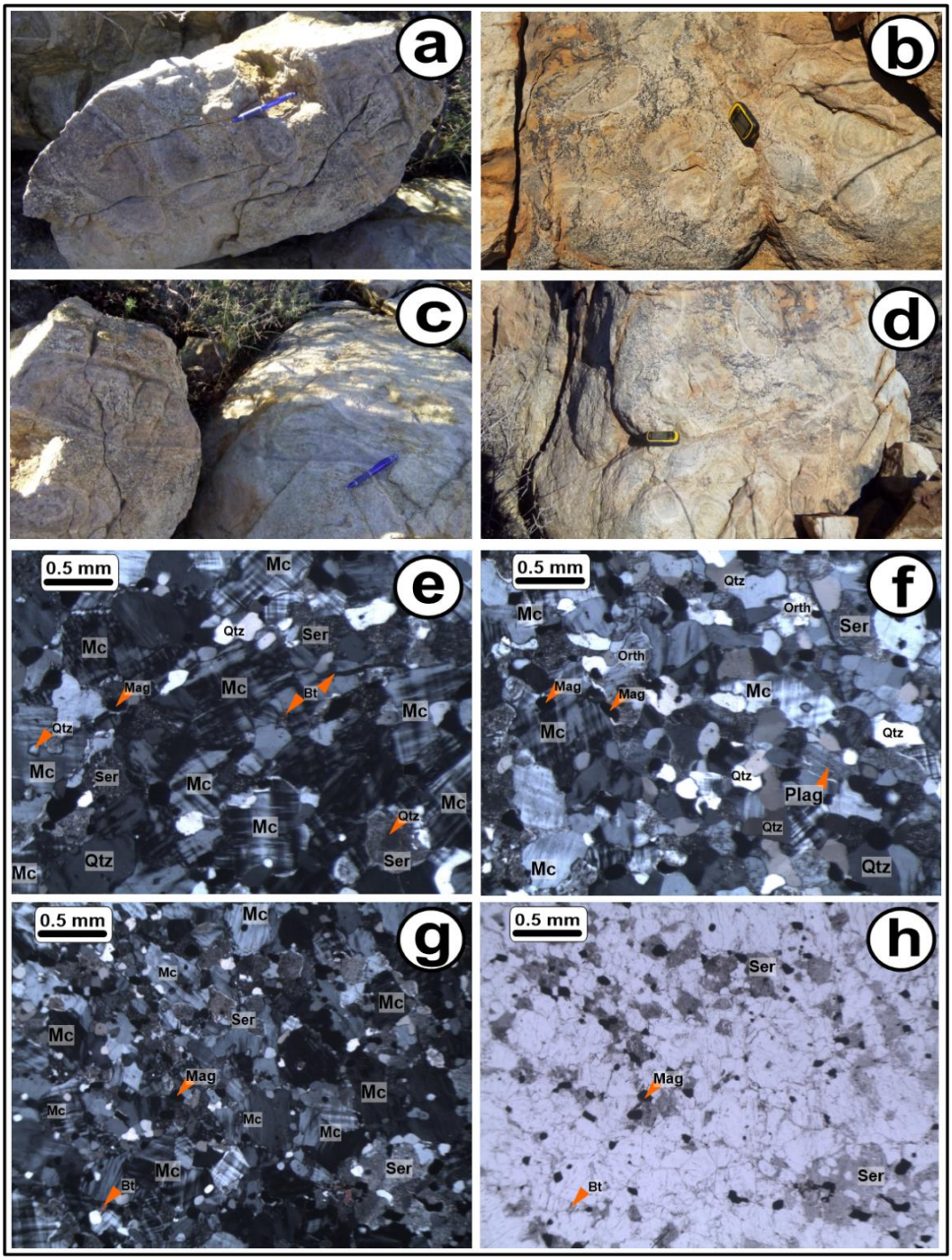

Fig. 4.10. Field photographs (a-d), and photomicrographs representing the orbicule inner shell region (e-h) of the orbicular granite (OG) samples from the study area. **(a)** Plastically deformed orbicules characterized by a triangular shape with rounded corners. The pen is 15 cm long. **(b)** The orbicular granite is characterized by a high density of spheroidal to ellipsoidal orbicules. The garmin GPS is 10 cm in length. **(c)** Ellipsoidal orbicules with an average size of 15 to 20 cm for the short axis and 25 to 30 cm for the long axis. **(d)** A high density of spheroidal to ellipsoidal-shaped orbicules in a granitic to granodioritic matrix. **(e)** Equigranular medium-grained texture of the felsic band in the inner shell. Qtz is scarce, and occurs mostly as inclusions in sericitized orthoclase (bottom right) and microcline (left), although a relatively large grain is present (bottom left). Rounded black grains of magnetite (Mag) occur interstitially. Photograph is in XPL. **(f)** Photomicrograph of a felsic band in the inner shell of an orbicule. Photograph is in XPL. **(g)** Photomicrograph of the inner shell, in XPL, showing a transition from a Magnetite-rich, finer grained mafic band (left) to a coarser-grained felsic band (right). Notice the slight increase in grain size from left to right. **(h)** Same image as in (g), in PPL.

Magnetite (0.1-0.25 mm) is the most abundant ferromagnesian mineral in these orbicules (Fig. 4.10e-h). Biotite is, however, present as elongated grains up to 1 mm long. The mineral is commonly altered to muscovite (Fig. 4.10g, h).

4.6. Intrusive rocks

The intrusive rocks encountered in the study area include: the post-tectonic Koperberg Suite (KS), the pre-tectonic Little Namaqualand Suite (LNS), and the late- to post-tectonic Spektakel Suite (SS). Pegmatites, presumed to be products of the late-stage Namaqua Orogeny (~1.0 - 0.95 Ga; Doggart, 2019) were also encountered in the study area.

4.6.1. Koperberg Suite (KS)

a. Description and field relationships

Outcrops of the KS occur throughout the GS (and the Namaqua Sector; Conradie and Schoch, 1986; Schoch and Conradie, 1990; Clifford et al., 1995) as mafic to intermediate (light- to dark-green) small bodies of intrusive rocks; they are preserved as chains of anorthositic to noritic rocks. Their compositions vary based on the proportions of plagioclase, orthopyroxene and biotite (Conradie and Schoch, 1986; Schoch and Conradie, 1990). These small bodies of the KS are assumed to have intruded through D_3-related high-strain zones, termed 'steep structures' (Conradie and Schoch, 1986; Kisters et al., 1998). The gneissic fabric is rare to absent in these intrusive bodies, suggesting a post-tectonic timing of emplacement. Outcrops of the KS which were encountered during field mapping of the study area are very small and hence are presented as points on the lithological map (Fig. 4.2).

The most encountered KS rocks in the GS are coarse-grained (1-5 mm) and have a light-green appearance, with a massive (homogeneous) texture (Fig. 4.11b-d). These outcrops typically occur as 20 to 80 m wide bodies and along strike dimensions of less than 1 km. Their mineralogical assemblage is dominated by plagioclase (80-90 %) with minor biotite (5-10 %). Due to the abundance of plagioclase, these rocks are classified as anorthosite. Locally, the KS rocks are seen to host xenoliths of the STK Gneiss (Fig. 4.3h). The contact with the grey gneisses of the GS (the STK and BWB gneisses) is typically sharp (Figs. 4.3h and 4.11c).

b. Microscopic observations

The KS outcrops encountered in the study area (anorthosite) are coarse-grained and defined by a mineralogical assemblage of plagioclase (80-90 %) with minor biotite (5-10 %) and no pyroxenes. Plagioclase grains (1-5 mm) are typically characterized by pericline and albite twins (Fig. 4.12), although most of the grains are extensively altered to clay minerals. Biotite (0.5-1 mm) typically occurs as dark-brown grains, but Mg-rich (phlogopitic) grains with a pale-brown to colourless appearance are also present (Fig. 4.12b and c). Biotite is weakly pleochroic, from brown to yellow to colourless and tends to occur in clusters (Fig. 4.12d). Some biotite grains are either

completely or partially altered to muscovite (Fig. 4.12e and f). Accessory minerals typically include zircon, magnetite and ilmenite.

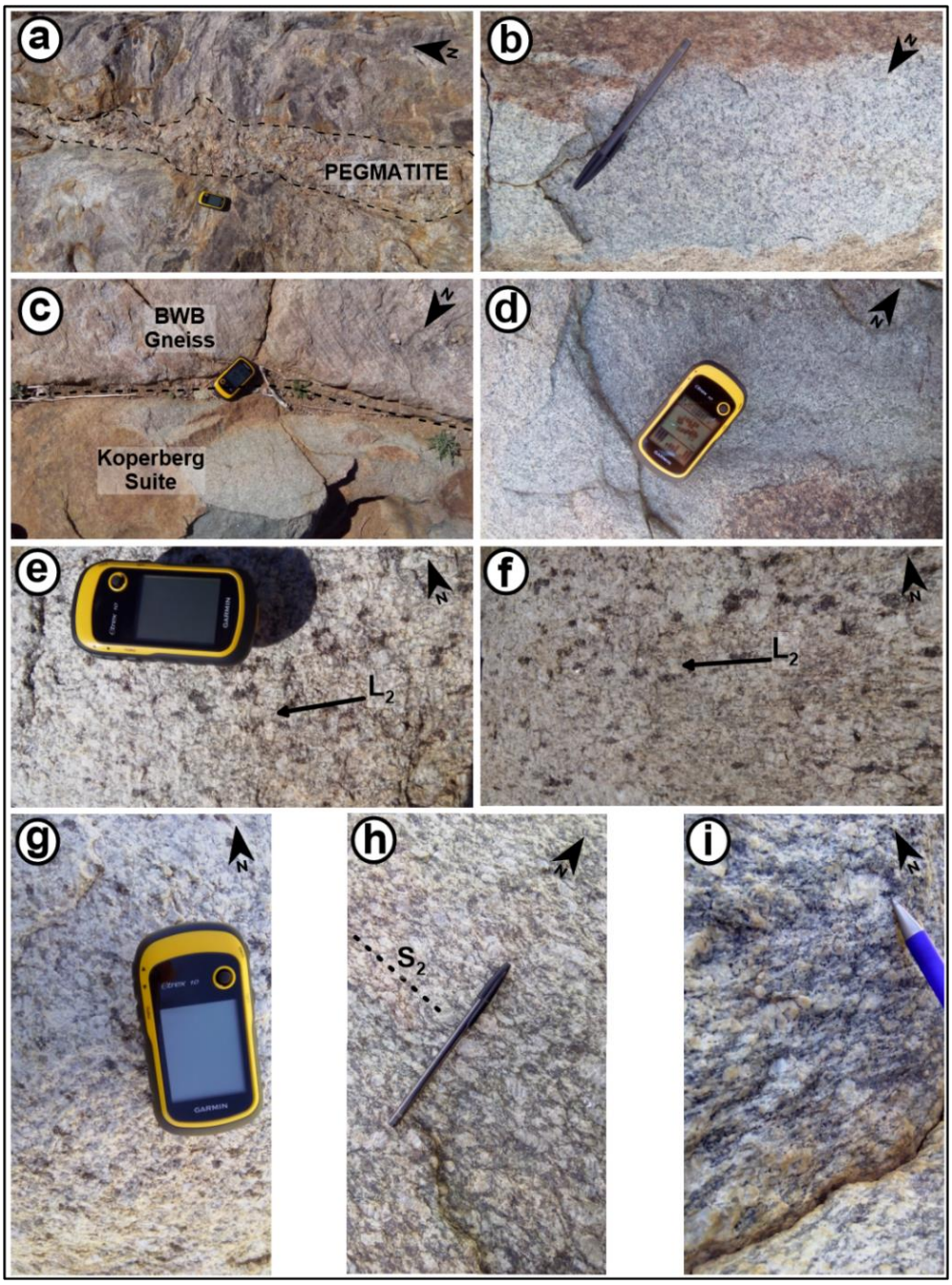

Fig. 4.11. *Field photographs of the intrusive lithologies in the study area.* ***(a)*** *Pegmatite intrusion;* ***(b)*** *Massive Koperberg Suite intrusion;* ***(c)*** *Sharp contact between a Koperberg Suite rock and the BWB Gneiss;* ***(d)*** *Koperberg Suite intrusion;* ***(e)*** *to* ***(g)*** *Quartzofeldspathic garnet-rich granites of the Spektakel Suite Rietberg granite (at contact with pelitic gneisses). The field of view in (f) is ~25 cm across. The arrows in (e) and (f) indicate the direction of mineral alignment;* ***(h)*** *and* ***(i)*** *Mesklip granite-gneiss of the Little Namaqualand Suite. The dotted line in (h) indicates the orientation of the* S_2 *fabric defined by Kfs augen and Bt. The scales are the same as in Fig. 4.10.*

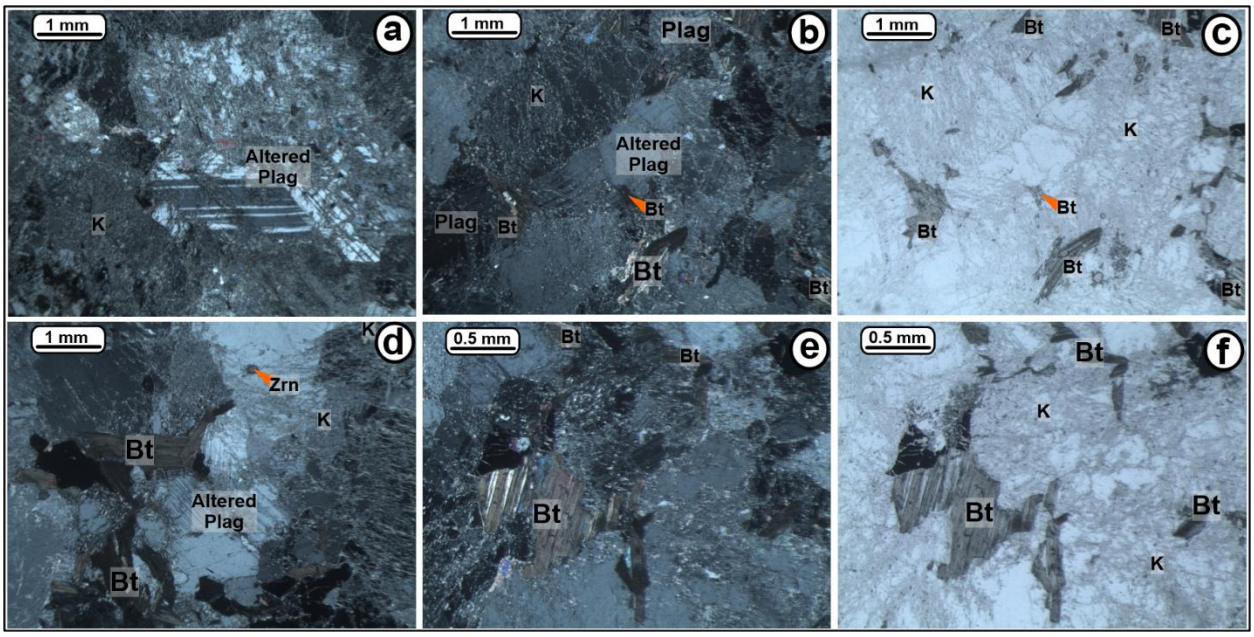

Fig. 4.12. *Photomicrographs of the Koperberg Suite anorthosite encountered in the study area.* ***(a)*** *Plagioclase is extensively altered to clay minerals (K). Image is in XPL.* ***(b)*** *and* ***(c)*** *Assemblage of extensively altered plagioclase with associated biotite; (b) in XPL and (c) in PPL.* ***(d)*** *Extensively altered plagioclase with associated biotite aggregates in XPL. Zircon (Zrn) occurring as an inclusion in altered plagioclase (to clay minerals) is shown.* ***(e)*** *and* ***(f)*** *Biotite grain (left) is partially altered to muscovite, occurring as thin bands in the biotite grain, which show a high interference in (e) but are colourless in (f). (e) is in XPL, while (f) is in PPL.*

4.6.2. Little Namaqualand Suite (LNS)

Description and field relationships

The LNS granitoids which occur in the GS are generally leucocratic to mesocratic granites, typically composed of K-feldspar (40-50 %), quartz (30-40 %), plagioclase (~10 %), biotite (~5 %) and hornblende (~5 %). The elongate K-feldspar crystals in these coarse-grained (1-4 mm) granitoids are completely recrystallized and occur as augen (0.5-1.5 cm long) wrapped in a quartz-plagioclase-biotite matrix (Fig. 4.11h). These augen impart a penetrative streaky gneiss fabric. However, the K-feldspar porphyroclasts occur as phenocrysts in areas of low strain (Fig. 4.11i). These gneisses show the typical D_2 Namaqua fabric of the BD (defined by east-west-oriented biotite and K-feldspar augen alignment; Fig. 4.11h), and garnet is present locally. These characteristics are consistent with the Mesklip granite gneiss (Macey, 2001). In the GS, these gneisses are only encountered along the southern boundary (Fig. 4.2). The L_2 mineral elongation (ESE-WNW trending) is particularly well developed in the LNS gneisses, where the feldspar porphyroclasts occur locally as sub-horizontal strongly elongated rod-shaped augen and the mafic minerals (mostly biotite) occur as elongate flattened ellipsoids (Fig. 4.11h).

4.6.3. Spektakel Suite (SS) - Rietberg Granite

Description and field relationships

These granites are typically grey, mostly undeformed, and are composed of K-feldspar (30-40 %), plagioclase (30-35 %), quartz (20-30 %) and biotite (5-10 %). The K-feldspar occur as megacrysts (0.5 x 2.0 cm) which are locally twinned, show perthite exsolution and are surrounded by a coarse-grained matrix made up of quartz (3-5 mm), plagioclase (2-5 mm) and biotite (1-2 mm), in order of decreasing abundances. The megacrysts are weakly aligned, generally subparallel to the D_2 fabric in the older gneisses of the GS. Based on Macey et al. (2018), these characteristics suggest that these granites form part of the Rietberg Granite plutons of the SS. These outcrops of the Rietberg Granite are only encountered along the southern boundary of the GS, surrounding the older LNS gneisses (Fig. 4.2). They tend to be homogeneous with a broadly consistent fabric and mineralogy (Fig. 4.11e-g). The contact between the megacrystic granite and the augen granites of the LNS is subparallel to the Namaqua fabric (D_2) in the augen gneisses. Older gneisses with prominent D_2 Namaqua fabric occur as xenoliths within the megacrystic granite. Locally, the quartzofeldspathic Rietberg Granite in contact with a pelitic gneiss is garnet-rich, with garnet crystals aligned subparallel to the megacryst alignment (Figs. 4.11e-g and 4.16a).

4.6.4. Bleskop Suite (Pegmatites)

Description and field relationships

Pegmatite intrusions encountered in the GS are largely oriented E-W to ENE-SSW and occur mostly small isolated bodies, although few larger intrusions are also present. The pegmatite bodies generally vary in width from ~10 cm up to a few tens of metres, with shapes varying between elongate, rounded and irregular. They mostly comprise reddish to pink K-feldspar (about 40-50 %) and white quartz (about 35-45 %) (Fig. 4.11a), with subordinate amounts of muscovite (about 5 %). Most of these bodies occur along shear zones in the grey gneiss units of the GS (Fig. 4.22d) and some are variably deformed. Melcher et al. (2008), Lambert (2013) and Doggart (2019) used the timing of pegmatite emplacement, and their variably deformed characteristics within shear zones in the Namaqua Sector, to suggest that multiple pulse intrusions of granitic magmas were possibly trapped in D_4 structural features.

4.7. Metasedimentary supracrustals

Outcrops of supracrustal rocks, such as metapelites, aluminous rocks, metaquartzites, calc-silicates, amphibolites, metaconglomerates and mafic gneisses have been identified in many areas within the Namaqua Sector (Moore, 1988; McStay, 1991; De Beer et al., 2002; Raith et al., 2003; Cornell et al. 2009). Supracrustal lithologies encountered in the study area include amphibolite, metaquartzite, metapelite (or simply pelite) and semi-pelite, which occur as lenses and supracrustal rafts in the GS.

4.7.1. Amphibolite

a. Description and field relationships

The amphibolite outcrops encountered in the study area commonly occur in spatial association with quartzofeldspathic rocks, forming sharp boundaries (Fig. 4.13a-d). Amphibolite typically occurs as lenses and fairly extensive lateral bands/rafts (up to 5m wide) within the GS gneisses, although a few xenolith occurrences were found (Fig. 4.13a-d). These amphibolites are fine-grained (0.5-1 mm) with a typical gneissic fabric, and are generally composed of about 60-70 % hornblende and 25 % plagioclase, with minor quartz and biotite (~5 %) (Fig. 4.13a-d). Some outcrops reveal interference folding, suggesting multiple phases of deformation.

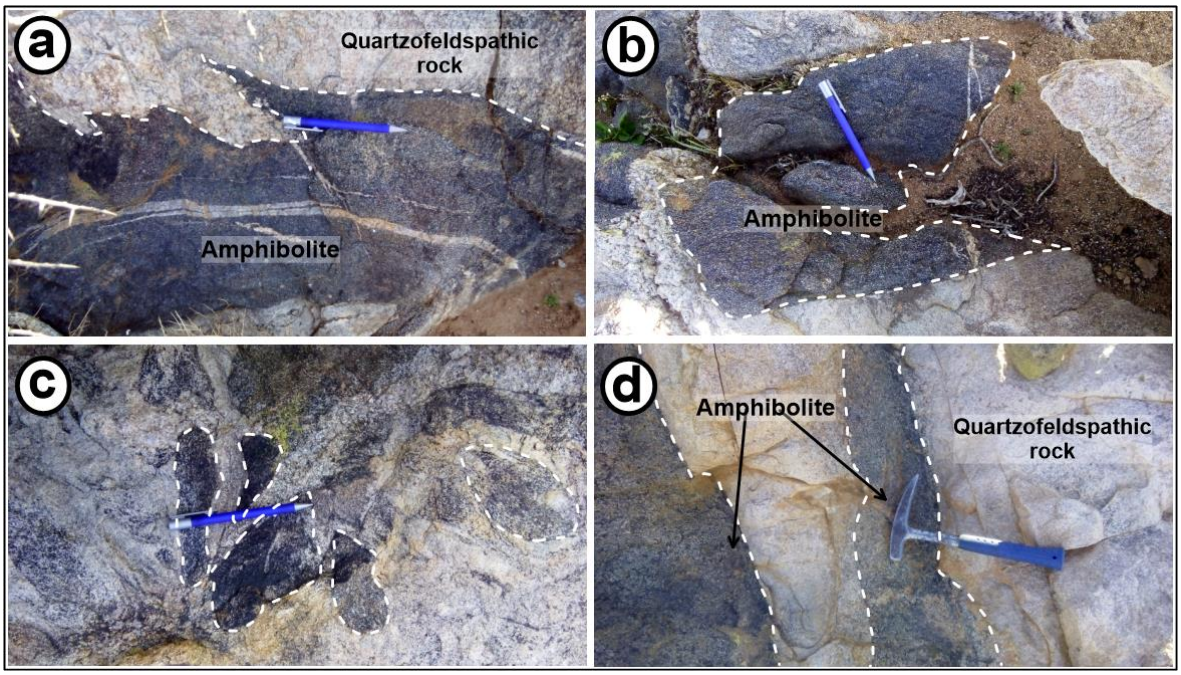

Fig. 4.13. *Field photographs of amphibolites in the Gladkop Suite.* ***(a)*** *Sharp contact between a quartzofeldspathic rock (top) and an amphibolite (bottom).* ***(b)*** *Amphibolite xenolith in a quartzofeldspathic rock.* ***(c)*** *Plastically deformed amphibolite xenoliths.* ***(d)*** *Amphibolite bands in quartzofeldspathic rock. Hammer=40 cm and pen=15 cm.*

b. Microscopic observations

The amphibolite in the study area is characterized by a mineral assemblage of hornblende (60-70 %), plagioclase (20-30 %), biotite (5-10 %) and quartz (1-5 %). In some cases, clinopyroxene is present, slightly changing the mineral assemblage as follows: hornblende (~60 %), plagioclase (~25 %), clinopyroxene (5-10 %) and quartz (1-5 %) (Fig. 4.14c-f). The hornblende grains are characteristically euhedral and green, with characteristic polygonal textures (Fig. 4.14c). They are pleochroic from dark green to light green to light brown (Fig. 4.14d-f).

Quartz (0.1-0.25 mm) occurs mostly interstitially and as inclusions (Fig. 4.14c). Accessory minerals commonly include titanite and apatite (Fig. 4.14c and d).

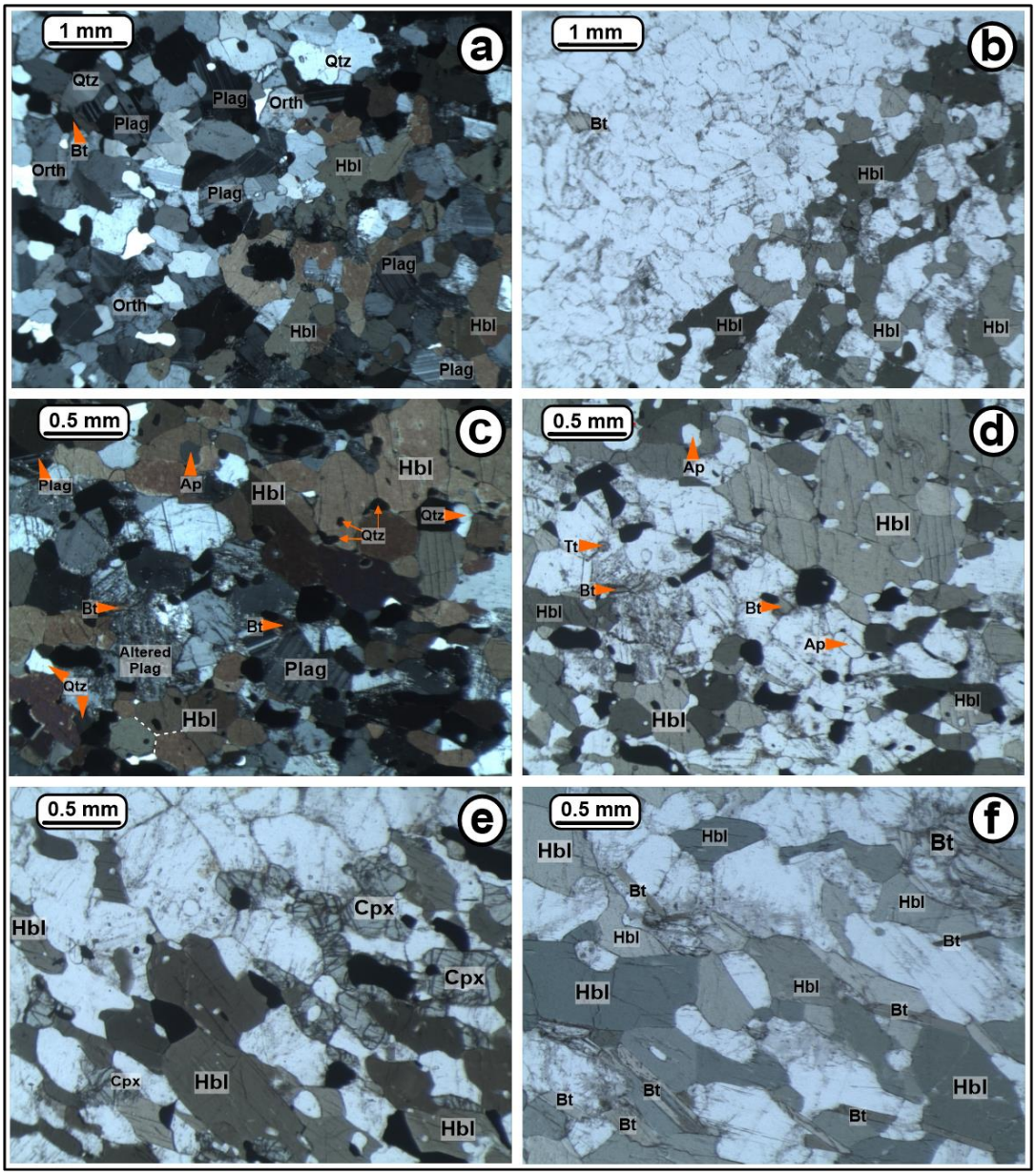

Fig. 4.14. *Photomicrographs of amphibolite samples from the study area.* ***(a)*** *and* ***(b)*** *Petrography at the contact between a quartzofeldspathic sedimentary rock (left) and an amphibolite (right); (a) in XPL and (b) in PPL.* ***(c)*** *and* ***(d)*** *Petrography of amphibolite dominated by hornblende and plagioclase; (c) in XPL and (d) in PPL. Dotted lines (bottom left) show hornblende crystals with polygonal texture. Titanite (Tt) and apatite (Ap) are also shown.* ***(e)*** *Hornblende associated with (relict?) clinopyroxene in PPL.* ***(f)*** *Hornblende and plagioclase associated with biotite in PPL.*

4.7.2. Metaquartzites

a. Description and field relationships

Metaquartzites are relatively rare in the study area, but where present occur as discontinuous rafts/bands parallel to the regional fabric. Outcrops of metaquartzites generally occur as ridges, due to the high resistance of such outcrops. Both a granular feldspathic metaquartzite and a ferruginous metaquartzite were encountered in the GS.

The medium- to coarse-grained (1-2 mm) equigranular feldspathic metaquartzite is the most common subunit. The outcrops have a granoblastic fabric and are made up of quartz (60-70 %), K-feldspars (10-20 %), plagioclase (5-10 %), and minor biotite (~5 %). Where present, biotite is completely oxidized. Thin compositional banding, defined by alternating quartz-rich and quartz-feldspar layers, defines a penetrative fabric. Outcrops of the feldspathic metaquartzite typically have a white color. This subunit was notably found close to the Ratelpoort Synform. These form prominent ridges which can be seen from aerial photographs. A typical example is found 5.5 km SE of Steinkopf at -29.2772S; 017.7904E.

The ferruginous metaquartzite is a melanocratic (dark grey) foliated metaquartzite. These outcrops are characterized by a mineral assemblage of quartz (75-85 %), with hematite, magnetite and ilmenite making up the remaining 15 %. These metaquartzites are foliated in places as a result of discrete millimeter- to centimeter-scale banding, defined by quartz and iron-oxide layers. The rocks are medium- to coarse-grained (1-10 mm) crystalline rocks, with a sparkly translucent appearance on the surface. Ferruginous quartzites were notably observed 1.6 km east of Steinkopf at -29.2557S; 017.7514E, where they occur between the GS granitic gneisses as 20-30 m wide and 15-20 m high ridges.

b. Microscopic observations

The granular feldspathic metaquartzite consists of quartz (60-70 %), orthoclase (10-20 %), plagioclase (5-10 %) and biotite (1-5 %). Where present, the elongated biotite minerals are randomly oriented and locally interstitial. Quartz, which occurs as 1-2 mm grains, is by far the most abundant mineral (60-70 %) and is typically recrystallized, forming very fine-grained (0.1-0.25 mm) polygonal aggregates around older larger quartz and orthoclase grains. The newly formed quartz grains form slightly seriate grain boundaries with the older quartz grains (Fig. 4.15c and d). The larger grains typically show undulose extinction, in contrast to the newly formed equant subgrains (Fig. 4.15c). The presence of properly formed subgrains is evidence that the metaquartzites have been extensively deformed. Orthoclase typically occurs as subhedral 1-2 mm grains, and are extensively altered to clay minerals (Fig. 4.15a-d). Plagioclase occurs as subhedral 1-2 mm grains. In places where they are not completely altered (to clay minerals), typical albite twinning is present (Fig. 4.15b). Biotite occurs as 0.1 mm interstitial grains between quartz-quartz boundaries and quartz-feldspar boundaries. The biotite grains are typically altered completely to muscovite (Fig. 4.15a).

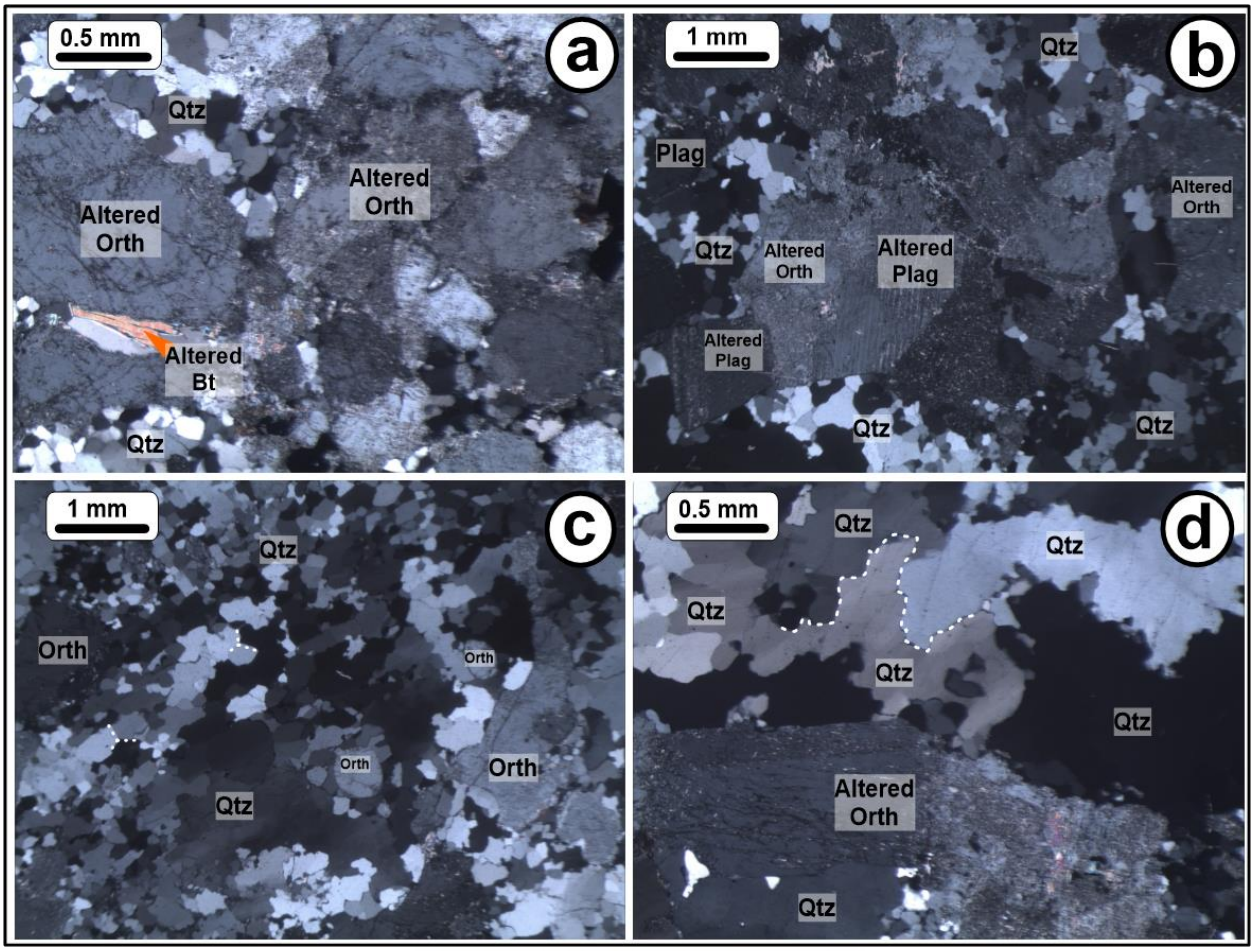

Fig. 4.15. *Photomicrographs of the granular feldspathic metaquartzites in the Gladkop Suite.* ***(a)*** *Orthoclase is extensively altered to clay minerals and biotite to muscovite. XPL.* ***(b)*** *An aggregate of recrystallized quartz with plagioclase and orthoclase altered to clay minerals. XPL.* ***(c)*** *Equant subgrains forming polygonal textures (white dashed lines on the left) and new (recrystallized) grains. The subgrains occur in the darker areas, and show very small misorientations, whereas the new grains have seriate boundaries and marked misorientations between themselves and the areas of subgrains. The new grains are larger than most of the subgrains, as is common in recrystallization by subgrain rotation. XPL.* ***(d)*** *Deeply sutured boundaries (e.g. white dashed line) of quartz formed by grain-boundary bulging. XPL.*

4.7.3. Metapelitic (pelitic) and Semi-pelitic gneisses

a. Description and field relationships

The division between the semi-pelitic and pelitic gneisses has been based mainly on the presence of significant amounts (more than 10 %) of the aluminous minerals cordierite, sillimanite and garnet in the pelitic rocks. Both the pelitic and semi-pelitic gneisses are only exposed as small xenolithic rafts (1-10 m wide) within the late-tectonic granites (SS) at the southern boundary of the study area, close to the Ratelpoort Synform. Locally, these pelitic gneisses are found as pockets along the S_3 fabric.

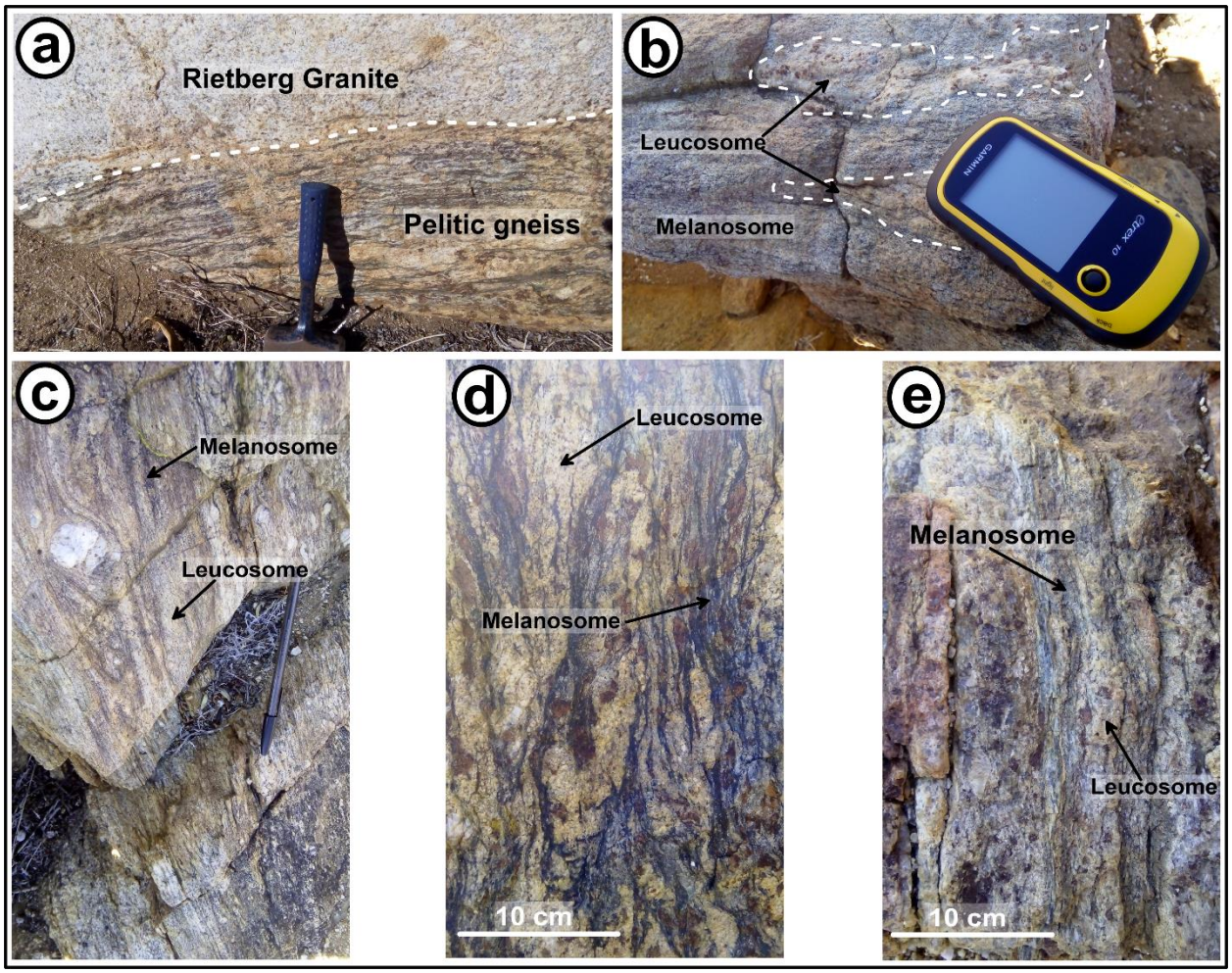

Fig. 4.16. *Field photographs of the pelitic rocks in the Gladkop Suite.* ***(a)*** *Contact between garnet-rich quartzofeldspathic Rietberg Granite (top) and pelitic gneiss.* ***(b)*** *and* ***(c)*** *Semi-pelitic gneiss.* ***(d)*** *and* ***(e)*** *Metapelitic gneiss. Hammer=40 cm, Pen=15 cm and garmin GPS=10 cm.*

The migmatitic pelitic gneisses (up to 30 % aluminous minerals) occur as elongate regional fabric-parallel bodies in association with most of the other supracrustal units, especially metaquartzites and semipelitic gneisses. The fine- to medium-grained pelites have varying

appearances mainly due to their grain size and mineral textures. They are typically characterized by compositional banding defined by alternating millimeter- to centimeter-thick bands of biotite-cordierite-sillimanite-rich melanosomes interlayered with centimeter-thick granoblastic garnet-rich quartzofeldspathic leucosomes (Fig. 4.16d, e). The abundant wavy-edged concordant felsic leucosomes contribute to the strongly banded appearance of these rocks (Fig. 4.16d, e). The compositional and migmatitic banding, together with the alignment of sillimanite needles, garnet augen, and locally biotite, defines a strong planar gneissic fabric. Garnet, which typically reaches a maximum size of 4 cm, is bright red, suggesting they are almandine garnets. The melanosome of the metapelites is typified mainly by the mineral assemblage K-feldspar + cordierite + plagioclase + garnet + sillimanite + biotite with a low abundance of quartz. The leucosome is largely composed of K-feldspar (~35-40 %) + quartz (30-40 %) + subhedral to euhedral garnet poikiloblasts (5-30 %) + plagioclase (less than 10 %). K-feldspar is more abundant than plagioclase and its relative proportion to plagioclase increases significantly in the leucosomes. Sillimanite occurs as euhedral needle-shaped centimeter-sized crystals. The pelitic gneisses are massive, partially or well banded. The massive gneisses typically have a spotted texture and consist of disseminated poikiloblastic spots (~1 cm) of garnet set in a massive medium-grained equigranular textured blue-grey matrix (70-80 %) consisting predominantly of quartz, feldspars, cordierite, biotite and sillimanite. Locally, the pelitic gneiss forms a sharp contact with the adjacent quartzofeldspathic granite (Fig. 4.16a). The granite at the boundary tends to be garnet-rich, the amount of garnet in the quartzofeldspathic granite increasing toward the contact.

Banded migmatitic semi-pelitic gneisses (Fig. 4.16b, c) are commonly interlayered with the pelitic gneisses, and in places, are intruded by concordant sheets of equigranular granite. The gneisses consist predominantly of K-feldspar, plagioclase, quartz and biotite, together with less than 10 % garnet ± sillimanite ± hornblende, but the proportions of the mafic and aluminosilicate minerals vary considerably. The semi-pelitic gneisses are typically medium-grained (0.5-1 mm), with an equigranular texture, and are characterized by a 0.5-5 m-thick, regional foliation-parallel compositional (largely a function of percentage biotite) and migmatitic banding. As with the pelitic gneisses, the semi-pelitic gneisses characteristically contain both concordant and discordant leucosomes (quartz-feldspar ± garnet) (Fig. 4.16b, c). The development of these garnet-bearing anatectic melt layers, patches and veins represents typical dehydration melting products of sedimentary material (e.g. greywackes) (Waters, 1986). The semi-pelitic rocks generally weather to an orange-brown or grey color and usually occur as flaggy outcrops owing to the presence of the strong regional fabric.

4.8. Structures

This section includes a description of the fabrics encountered in the study area (the GS), formed as a result of the deformation events which affected the BD (Namaqua Sector). The prevalent fabric in the GS is the S_2 fabric (product of the D_2 deformation), with the S_3 fabric (produced from the crenulation of the S_2 fabric) secondary in extent but present nonetheless (Fig. 4.17). Other structures encountered include: shear zones and lineations (formed by augen and phenocrysts). Both brittle and ductile deformation mechanisms are evident, as well as features of both low-grade and high-grade metamorphic conditions.

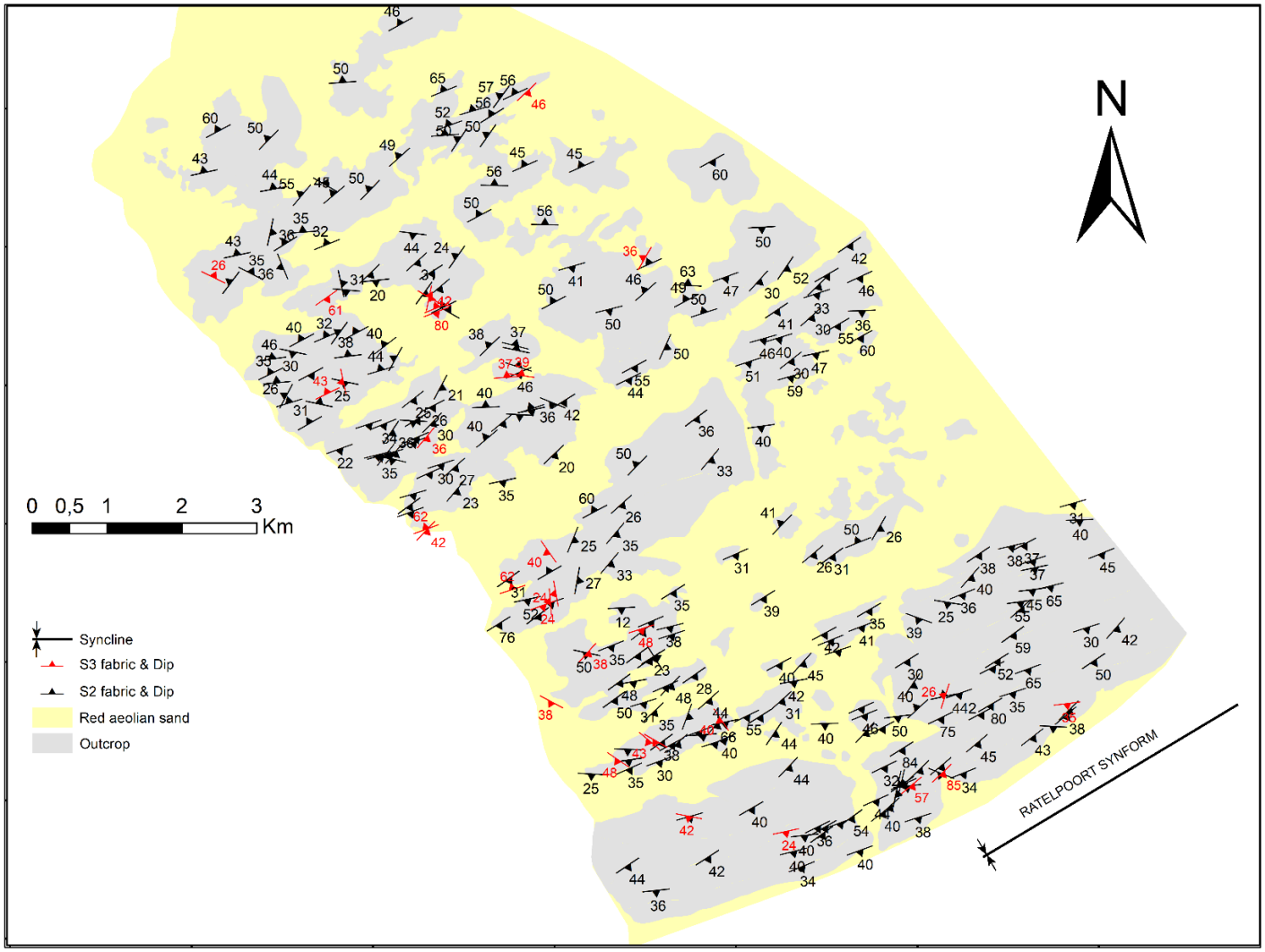

Fig. 4.17. *Orientations of S_2 and S_3 fabrics in the Gladkop Suite rocks, south of Steinkopf (this study). Map symbols are in line with the Federal Geographic Data Committee (FGDC) Digital Cartographic Standard for Geologic Map Symbolization.*

Joubert (1971, 1986) described four main deformation components (D_{1-4}) in the Namaqua rocks. The earliest, D_1, is Palaeoproterozoic in age (related to the Orange River Orogeny) and D_2-

D_4 are Mesoproterozoic to earliest Neoproterozoic (related to the ~1.2-1.0 Ga Namaqua Orogeny). These components are dominated by ductile fabrics (foliations), melt veins, interference folds and ductile shear zones. The D_2 and D_3 deformation events have been identified as the main deformation phases of the Namaqua Orogeny (Joubert, 1986). This scheme has been largely followed since, except for a few modifications (e.g. Colliston and Schoch, 2013 and Macey et al., 2015). Macey et al. (2015) identified the structural markers of a D_5 event as products of the regional ~550 Ma Pan-African Orogeny. The GS lies within the SE region of the Gariep Orogen (Figs. 1.1, 1.2) and, as a result, shows some evidence of this younger deformation event.

4.8.1. D_1

Joubert (1971) observed gneissic banding, which he termed S_1 (of unknown origin), in Palaeoproterozoic supracrustal rocks, which had been almost completely reworked (folded) by the main regional D_2 deformation into rootless isoclinal intrafolial folds (Joubert, 1971; Albat, 1984). He described the gneissic banding as products of a D_1 event, possibly related to the Orange River orogeny. The GS orthogneisses are intercalated with intrusive (LNS and SS) and sedimentary rocks (as described in Section 4.7). During this project, metaquartzites were the most encountered sedimentary rocks, with only minor amphibolite, quartzofeldspathic sedimentary xenoliths and metapelites. These rocks, together with the GS orthogneisses have been extensively reworked and metamorphosed, with the existing fabric becoming isoclinally folded (Fig. 4.18), and transposed subparallel to the more recent S_2 fabric. Most evidence for the D_1 deformation is, however, obliterated.

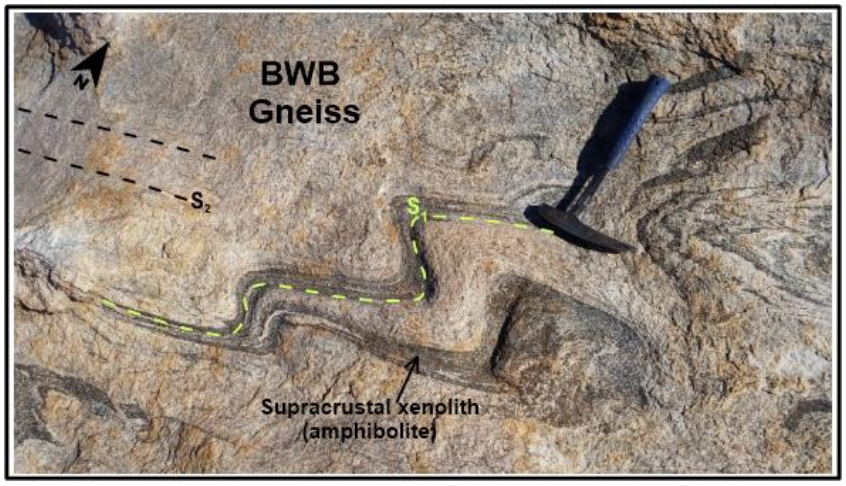

Fig. 4.18. *Isoclinal folding of S_1 fabric in amphibolite xenolith within a Brandewynsbank Gneiss by the D_2 deformation event.*

4.8.2. D_2

The main deformation phase of the Namaqua Orogeny produced penetrative intense ductile deformation (D_2), forming a new S_2 gneissic fabric (Joubert, 1986; Waters, 1986). The D_2 deformation was associated with large scale ESE/WNW-trending isoclinal folding (F_2). In the GS, this deformation is evident in the intense regional penetrative subparallel axial planar S_2 cleavage

(gneissosity), dipping NNW (to SSE) and with NNW- to WNW-plunging L_2 stretching lineations (Figs. 4.17, 4.23).

The S_2 gneissic banding (Fig. 4.19) observed in the GS is present in all the orthogneiss varieties. The fabric is generally oriented ENE-WSW (Fig. 4.17) and is characterized by the preferred planar orientation of platy minerals such as biotite (and hornblende locally). In the mapped area, the S_2 fabric generally dips towards the SSE in the southern portion of the map area, while the fabric in the northern portion generally dips towards the NNW (Fig. 4.17). The S_2 fabric and stretching L_2 lineation (Fig. 4.19) are also observed in the ~1.2-1.18 Ga LNS intrusives in the southern portions of the study area.

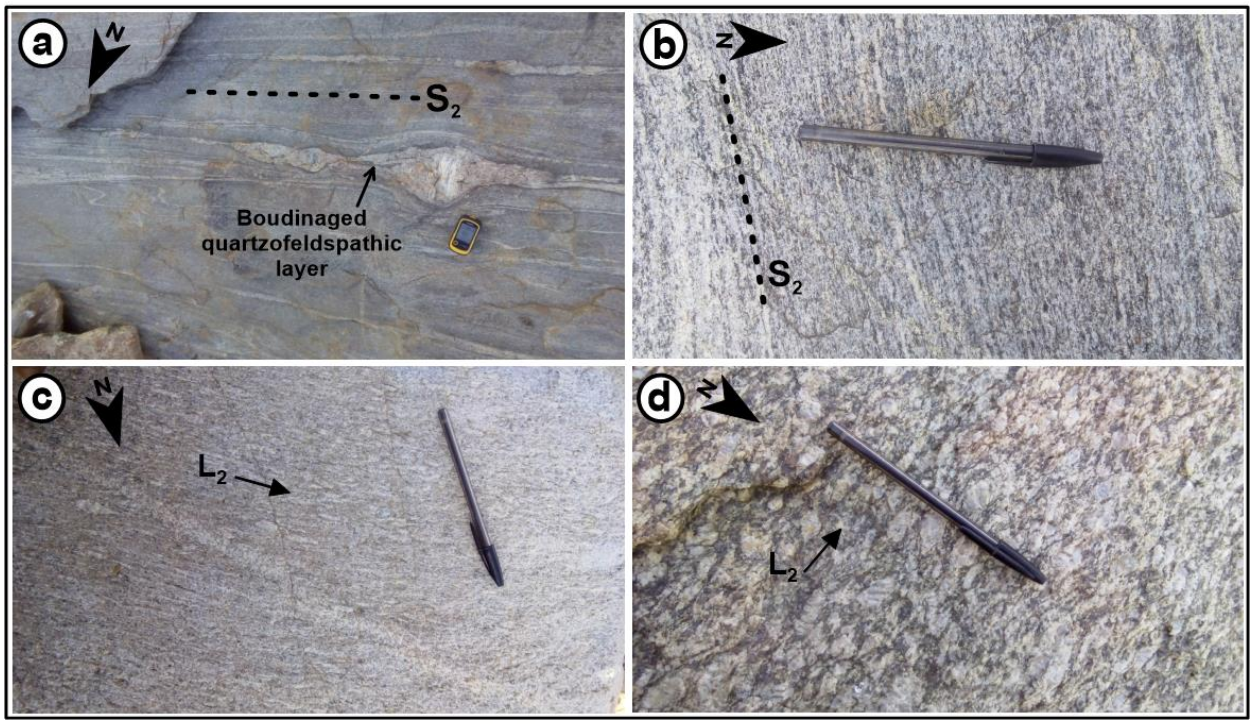

Fig. 4.19. *D_2 deformation fabrics observed in the study area.* ***(a)*** *and* ***(b)*** *Ductile ENE-WSW-oriented S_2 fabric present in the Gladkop Suite gneisses.* ***(c)*** *and* ***(d)*** *L_2 lineation in the Spektakel and Little Namaqualand Suites, respectively. Black arrows show lineation plunging direction. North arrows are shown. The garmin GPS is 10cm in length. Pen is 15cm in length.*

It appears that the S_2 fabric has been re-oriented by the subsequent megascopic F_3 and F_4 folding, and therefore exhibits variable attitudes within the study area, which is in line with observations made by Macey et al. (2011) working in the southern parts of the BD. Despite this, the S_2 fabric in the southern portion of the map area (towards the Ratelpoort Synform) is dominantly shallow to moderately S to SE dipping (10-50°), but NNW-dipping fabrics were recorded in the northern portion (Figs. 4.17, 4.20). This is in contrast to the southern parts of the BD, where the S_2 fabric has a moderate to steep dip (Macey et al., 2011).

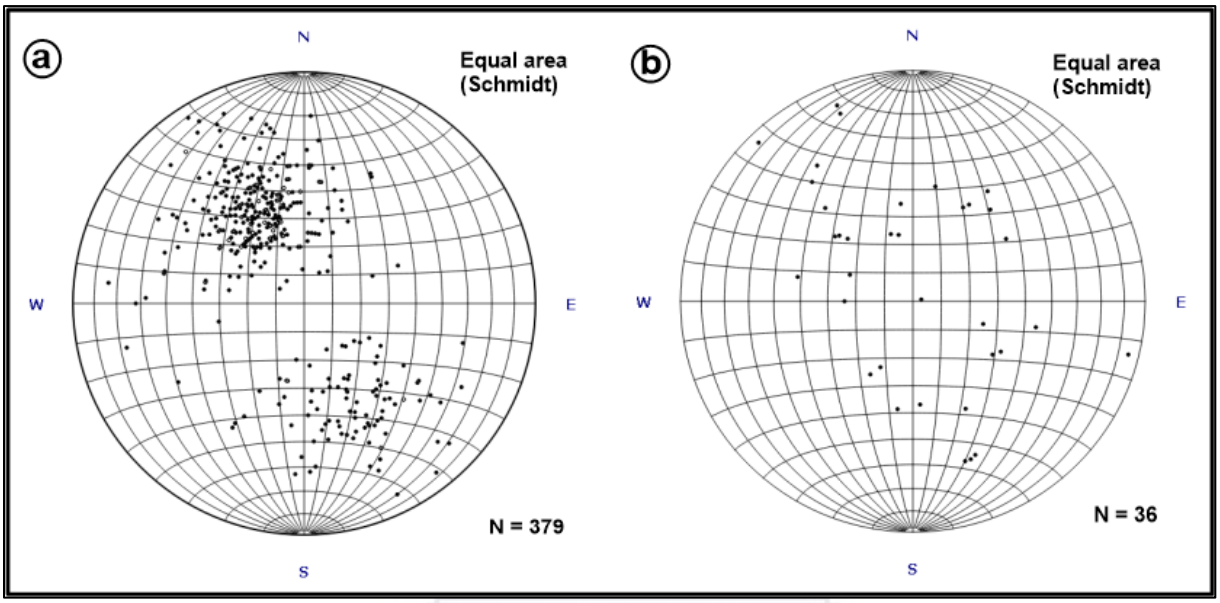

Fig. 4.20. *Orientations of the poles to all measured fabric in the study area.* ***(a)*** *Poles to S_2 fabric.* ***(b)*** *Poles to S_3 fabric.*

Joubert (1971, 1986) suggested that the F_2 folds developed as large-scale near recumbent NW-trending structures associated with a S to SW tectonic transport direction. Joubert (1971, 1986) argued, however, that the present orientation of the S_2 fabrics and the L_1 and L_2 stretching lineations cannot be regarded as primary, but rather that the fabrics have been re-oriented during the subsequent D_3 and D_4 events. In this model, the S_2 fabric and L_2 lineations were rotated from NW-trending attitudes to generally E-W-trending orientations during the large-scale open F_3 folding; and the L_2 lineations were rotated into their ENE- and WNW-trending orientations as a result of gentle mega-scale warping during the D_4 deformation (Joubert, 1971; 1986). In the GS, this can be seen by the fact that the S_2 poles to plane in Fig. 4.20 form quite a wide spread in the equal area projection rather than being concentrated in one (or two) orientations. These then have been rotated during D_3, which may actually be related (and within the same overall deformation phase) to D_2. The same also holds true for the S_3 foliation which has likely been modified during D_4.

4.8.3. D_3

During the D_3 phase, kilometer-scale ESE-WNW folding (F_3) of the S_2 fabrics and thrust structures formed open folds, with upright to inclined NE-dipping axial planes, and an S_3 fabric in the western Namaqua Sector (Macey et al., 2011). No new metamorphic fabrics were formed during this deformation event. The S_3 fabric formed as a non-penetrative, sub-vertical planar cleavage (Fig. 4.21a, b), locally filled with thin white to cream-coloured quartz-feldspar-garnet leucosomes, as was also observed by Macey et al. (2011) working in the southern BD. Macey et al. (2001) suggested that the formation of the S_3 fabric occurred by shearing along the limbs of the minor parasitic F_3 folds, with the gneissic S_2 fabric adjacent to the planar structures being drawn into parallelism with the spaced cleavage.

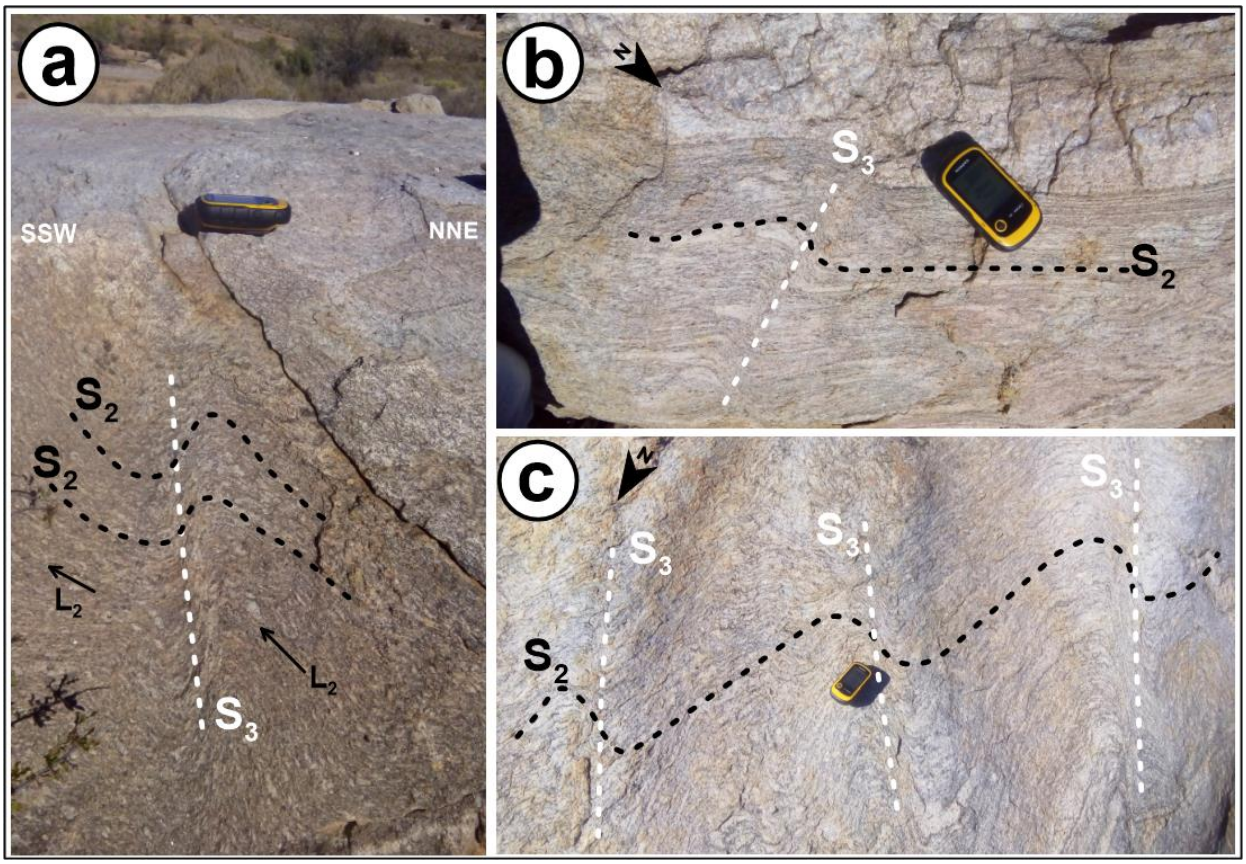

Fig. 4.21. (a) *Crenulation of the S_2 fabric during D_3 deformation to produce the S_3 fabric. Notice that the L_2 lineation, defined by augen alignment (black arrow), is also folded.* ***(b)*** *S_3 fabric is produced by crenulation of the S_2 fabric.* ***(c)*** *S_3 fabric occurring between 50 and 60 cm apart. Garmin GPS is 10cm in length.*

The S_3 fabric in the study area was recognized from crenulation of the S_2 fabric. Where encountered in the study area, the S_3 fabric occurred 10 to 100 cm apart (Fig. 4.21c). The S_3 fabric was mostly identified on flat surfaces, and could hardly be traced on 3D surfaces, making orientation measurements difficult. However, some measurements were made. In the south of the study area, the S_3 fabric dips shallowly towards the SSE but the dip direction changes to SSW in

the middle portion and changes again to a NNW direction in the north (Fig. 4.17). The change in dip direction occurs in a clockwise pattern.

4.8.4. D_4

Colliston and Schoch (2013) identified the D_4 deformation event in the western part of the Namaqua Sector as the occurrence of transcurrent shearing and the formation of open folds, with Macey et al. (2015) specifying a dextral sense of shear. Colliston and Schoch (2013) suggested that the D_4 event ended with the intrusion of the KS into F_4 folds, although Macey et al. (2015) argues that the D_4 event post-dates the intrusion, having been associated with the emplacement of extensive pegmatites at ~1000-950 Ma.

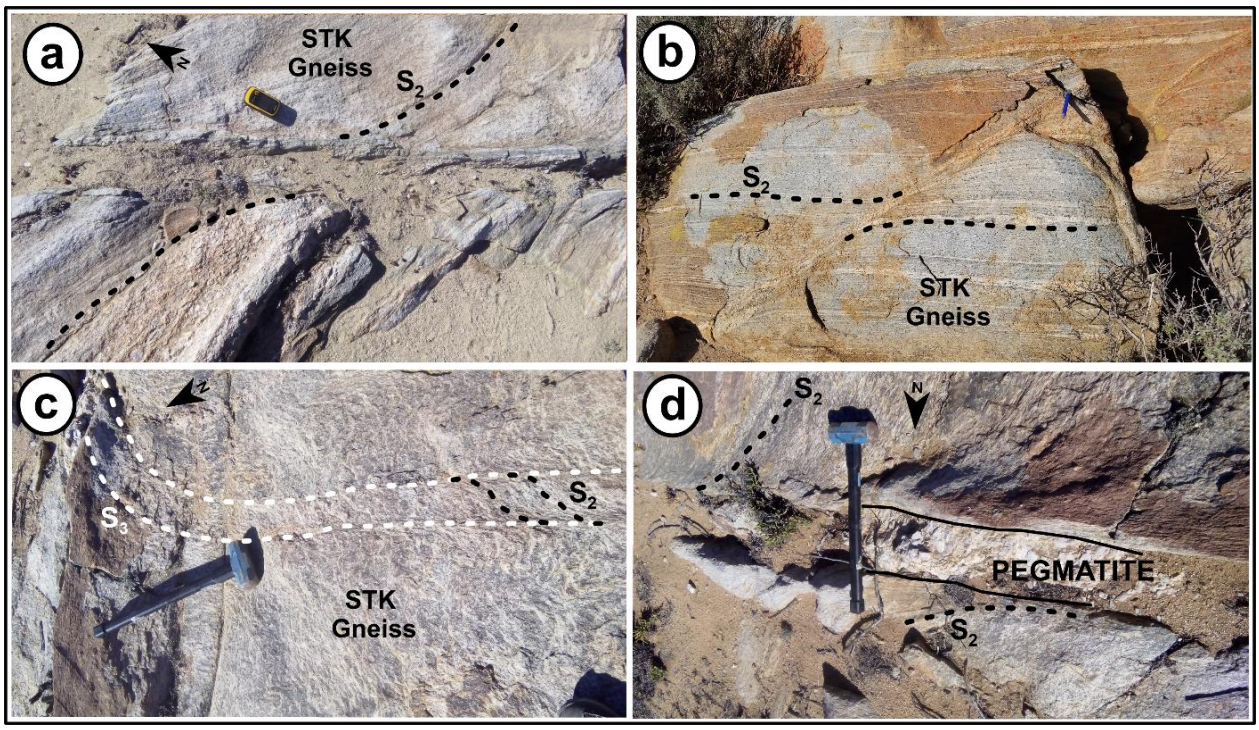

Fig. 4.22. (a) *Dextral shearing in the STK Gneiss.* ***(b)*** *Sinistral shearing in the STK Gneiss. The pen points north.* ***(c)*** *Dextral shearing (left edge of photo), dragging both S_2 and S_3 fabrics in the shear direction.* ***(d)*** *E-W oriented pegmatite body along dextral shear zone in the STK Gneiss. Garmin GPS is 10 cm in length. Pen is 15 cm in length. Sledge hammer is 60 cm.*

In the study area, both dextral and sinistral shearing were encountered. Both the STK and BWB gneisses are cross-cut by late Namaqua (D_4) dextral and sinistral shear zones, characterized by sub-vertical mylonitic, phyllonitic and cataclastic foliations (Fig. 4.22a, b). The NNM Gneiss, however, because of its quartzofeldspathic nature tends to be more brittle, as evident in zones with a large amount of fractures and is interpreted as a response to high stress, and is not cross-cut by these shear zones. The observed shear zones are generally trending NNE (to ENE), subparallel to the S_2 fabric locally, but their orientations vary slightly as shown on Fig. 4.23. Locally, the shear zones postdate the deformation fabrics in the area, clearly dragging along the S_2 and S_3 fabrics (Fig. 4.22c). The D_4 shear zones were identified in the field by intense refoliation of the gneissic fabric and a mylonitic appearance.

Fig. 4.23. *Locations of lineations and shear zones in the Gladkop Suite, south of Steinkopf (this study). The S-shaped symbols are oriented to indicate the linear trend of shear zones. Map symbols are in line with the Federal Geographic Data Committee (FGDC) Digital Cartographic Standard for Geologic Map Symbolization.*

CHAPTER 5

WHOLE-ROCK GEOCHEMISTRY

5.1. Introduction

The main objectives of the whole-rock major and trace element geochemical analyses are to: (1) characterize/classify and contrast the main plutonic units of the GS; (2) test for any geological/petrogenetic processes which might have been responsible for the observed compositional variations in the GS gneisses. In addition to these, previously published geochemical data on the GS is compared with the data generated for this study. A comparison is also made between the GS and the RMA VS geochemical datasets to determine any relationship between the two suites.

The major element composition data was acquired using XRF spectrometry, while LA-ICPMS was used to obtain trace element compositions, as described in Chapter 3. The major element concentrations are reported in weight percent (wt. %) oxides, and the oxides measured include: SiO_2, TiO_2, Al_2O_3, $Fe_2O_3^T$, MnO, MgO, CaO, Na_2O, P_2O_5, Cr_2O_3 and LOI. The total Fe in the samples is represented as $Fe_2O_3^T$. The trace element concentrations are reported in parts per million (ppm), and elements measured include: (1) the transition metals (Sc, V, Cr, Co, Ni, Cu, Zn and Mo); (2) the Rare Earth Elements (REE) (La, Ce, Pr, Nd, Sm, Eu, Gd, Tb, Dy, Ho, Er, Tm, Yb, and Lu); (3) High Field Strength (HFS) elements (Y, Zr, Nb, Hf, Ta, Pb, Th and U); and (3) Low Field Strength (LFS) elements, also termed Large Ion lithophile (LIL) elements (Rb, Sr, Cs, Ba). Covariance matrices for the GS geochemical compositions were generated using the IBM SPSS 19 statistical software package although data management, recalculation, plotting and statistical evaluation were mostly performed using the GeoChemical Data ToolKIT (GCDkit) computer program (Janoušek et al., 2006). Due to the complex tectonic history of the GS rocks, the Tectonic Discrimination for Intermediate and Acid magmas (TecDIA) computer program (Verma et al., 2012, 2013; Verma and Verma, 2013; Verma, 2015) is used to determine the geotectonic settings in which the GS magmas were generated. Where applied: (1) molar (cationic) concentration (M) is calculated as [wt. % oxide / molecular weight oxide] x No. of cations (De la Roche and Leterrier, 1973; De la Roche et al., 1980) and is represented in units of mol/100 g; (2) Magnesium number (or magnesium-iron ratio; Mg#) is calculated as [100 x Mg / (Mg + Fe)] and reported in units of mol %, with Fe and Mg representing molar concentrations of $Fe_2O_3^T$ and MgO respectively.

The variations in element compositions between rocks of the same lithology, as well as between rocks of the different lithologies of the GS indicate that statistical analyses are necessary to comprehend the pattern of major oxides and trace element compositions in these gneisses. The major element data has been used in characterizing/classifying the GS gneisses as well as in combination with trace element data to determine the tectonic settings from which the GS magmas were generated. Both major and trace elements are also used to identify possible markers of petrogenetic processes such as fractional crystallization, magma assimilation, contamination, magma mixing and/or mingling, partial melting, source mixing and source character, as well as peritectic assemblage entrainment. Cr_2O_3 has not been included in any plots due to a possible

contamination from preparing powdered samples for geochemical analyses with a swing mill, as mentioned in Chapter 3.

This chapter is divided into different subsections. Section 5.1 is an introductory section, while Section 5.2 presents statistical analyses of the whole-rock major and trace element geochemical data of the GS. These are followed by analyses of element mobility in the GS (Section 5.3), and then by the properties of the GS major element compositions (Section 5.4). The next section (5.5) presents the properties of the trace element data, and is followed by an evaluation of the geotectonic settings in which the GS magmas were potentially generated (Section 5.6). An overall summary is provided in Section 5.7. The GS data from this study is reported in comparison with the VS data (and literature data on the GS) throughout this chapter. The VS samples/lithologies include the Khoromus (dioritic to granitic) porphyry, the Goabis Diorite, the Weisserquartzkuppe Granite, an undifferentiated group of VS rocks and the Gaarseep Granodiorite (Macey et al., 2017).

5.2. Statistics

Thirty-one samples representative of the various GS lithologies were collected from several locations around the Steinkopf area (Fig. 5.1). The collected samples were analyzed for eleven (11) major oxide and thirty-four (34) trace element compositions (Tables 5.1-5.3). Tables 5.1-5.3 display summary statistics of the major oxide and trace element (transition metals, REE, HFS and LFS) geochemical data of the GS (the complete geochemical data set is shown in Appendix B, Tables B1 and B2). Out of the thirty-one samples analyzed for major and trace element data, fourteen were sampled from the BWB Gneiss, eight from the NNM Gneiss and the remaining nine from the STK Gneiss. The GS gneisses display a range of silica (SiO_2) values between 60 and 79 wt. % and most of the samples are relatively felsic, with more than 80 % having SiO_2 values greater than 68 wt. % (Table 5.1; Figs. 5.3, 5.5a).

The NNM Gneiss has the highest average SiO_2 content (75.44 wt. %), while the STK Gneiss shows the least average SiO_2 content (69.19 wt. %) (Table 5.1). The VS rocks have a range of SiO_2 values between 52.95 and 78.94 wt. % (Table B3). The GS gneisses are K-rich (mean K_2O/Na_2O >1; Table 5.1). The NNM Gneiss has the highest mean ratio while the STK Gneiss has the lowest. The GS samples show low MgO concentrations (0.31-1.5 wt. %), and, while the NNM samples show a wide range in Mg# (defined as 100 x Mg / [Mg + Fe]) values (14.45 - 46.43), the BWB and STK samples vary between 23.58-39.70 and 25.35-37.00 respectively (Table 5.1). The VS rocks have relatively higher Mg#, ranging between 21.31 and 81.86 (mean 51.48), and mean K_2O/Na_2O ratios ranging between 1.1 and 1.5.

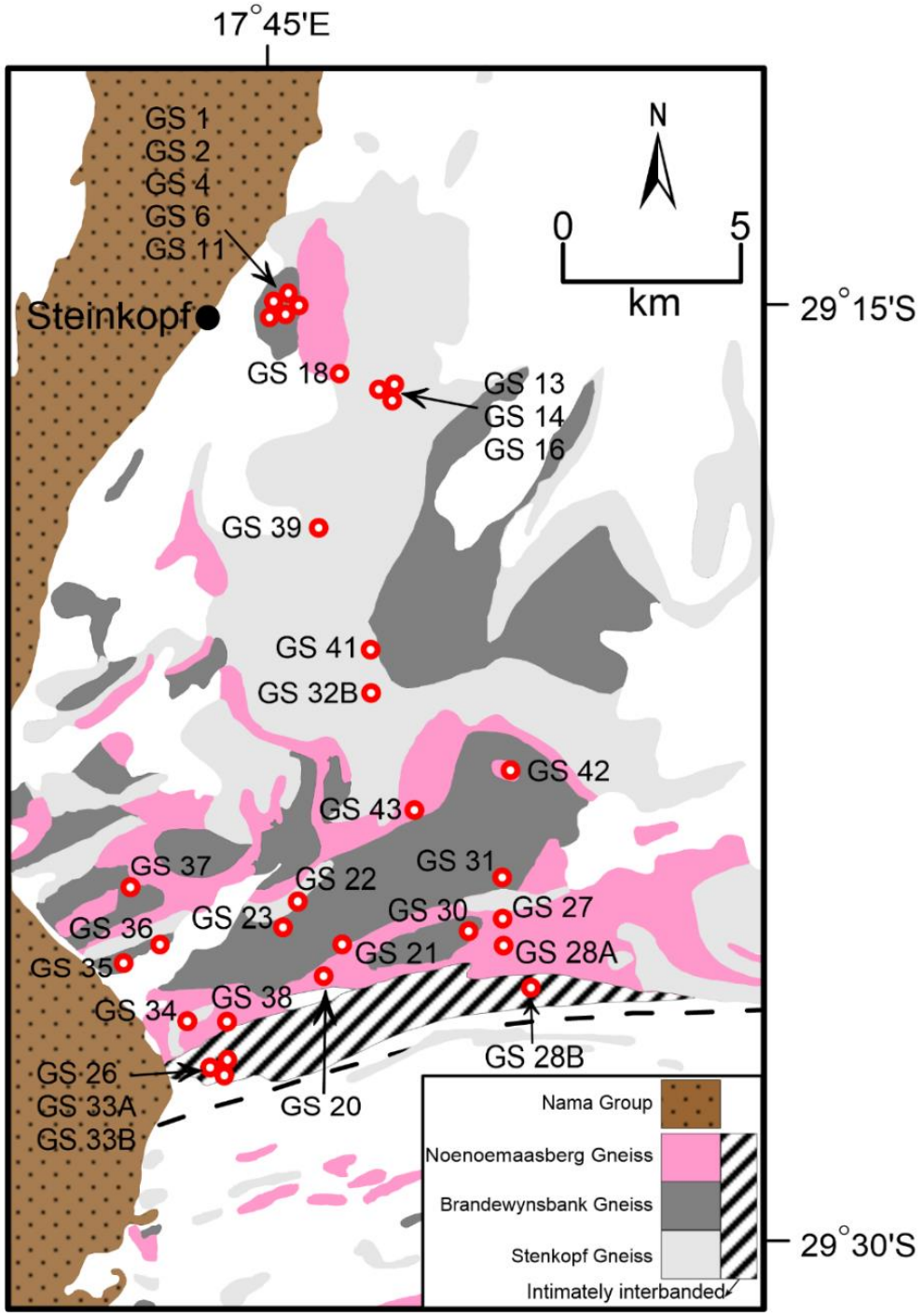

Fig. 5.1. *Distribution of the Gladkop Suite gneisses showing the locations of the samples used for geochemical analyses (this study).*

The inter-relationship (association) between major and trace element pairs in each of the GS gneisses, is highlighted, based on covariance. The nature of element associations is generally linked to specific petrogenetic processes. Centered log-ratio covariance matrices are used with the intention of eliminating spurious correlations introduced by the 'closure problem' which arises from using composition data (Aitchison, 1986). This method involves transforming (major and

trace element) compositions to natural log-ratios using the geometric mean (g) of all components as a common divisor, and calculating a centered log-ratio covariance matrix (Table 5.4; Appendix C, Tables C2, C3, C4; Aitchison, 1986). Butler and Woronow (1986) suggested that, because this method of calculating the covariance matrices between elements does not single out one element as the divisor (as opposed to the log-ratio and variance matrices), it is advantageous to the geochemist. Transforming data this way allows correlation to produce geologically meaningful results (Aitchison, 1986; Rollinson, 1992). Aitchison (1986) emphasizes the structure of the matrix rather than the correlation of the log-ratios themselves. He supports the use of element ratios by emphasizing that studying compositions is based on relative magnitudes of the components, rather than absolute values and goes on to say that the covariance nature of log-ratios frees up the data, eliminating the problems of negative bias and spurious correlations introduced by percentage (composition) data (Aitchison, 1986; Rollinson, 1992).

Following the method of Aitchison (1986), the major and trace element compositions are recalculated as natural log-ratios and the centered covariance matrices for the GS lithologies are presented in Tables 5.4a-c (and Appendix C, Tables C2, C3 and C4). The covariance matrices were generated using the statistical software package IBM SPSS 19. Centered log-ratio covariance matrices for the STK Gneiss indicate that the greatest positive covariances occur between the pairs Fe-Mg, Fe-Mn, Fe-P, Fe-Ca, Mg-Ca, Mg-P, Mn-Mg, and Mn-P and negative covariances occur between the pairs K-Fe, K-Mn, K-Mg, K-Ca and K-P (Table 5.4a). Very strong positive covariances also occur between the pairs Ni-Fe, Ni-Mg, Ni-Zn and Ni-Mn (Appendix C). This could be accounted for by elements such as Ni, Zn, Mg and/or Mn substituting for Fe^{2+} in magnetite or other ferromagnesian minerals, such as olivine or the pyroxenes. Si and Al show covariances close to 0 (lowest), while Na also shows low covariances (Table 5.4a). The positive covariances above support the association/coexistence of the elements Fe-Mg-Mn-P-Ca, suggesting a mineral assemblage of major ferromagnesian minerals and accessory phases (such as apatite) is controlling the composition of the STK Gneiss. This positive association, together with the negative covariances with K, indicate an inverse relationship between a potassic phase (such as K-feldspars) and Fe, Mg, Mn, P and Ca. The significant positive covariance between the pairs Ca-P, Ni-Fe, Ni-Mg and Ni-Mn, together with the negative covariance between P and Ce, La and Th (Appendix C) possibly suggests the importance of apatite and magnetite as the main accessory phases controlling the chemistry of the STK Gneiss, and rules out monazite as a possibility.

In the BWB Gneiss, the greatest positive covariance relationships occur between the pairs Ti-Mg, Ti-P, Ti-Fe, Ti-Ca, Mg-P, Fe-Mg, Fe-P, Fe-Ca, Mg-Ca and Ca-P (Table 5.4b). The greatest negative covariances, indicating the greatest variability between the elements, occur between the pairs formed by K, Th and U, with P, Ca, Fe, Ti, Mn and Mg (Table 5.4b and Appendix C). Na, Si and Al form covariances close to 0 (Table 5.4b). These observations similarly suggest an inverse relationship between a potassic phase (such as K-feldspars) and Fe, Mg, Mn, Ti, P and Ca, again possibly highlighting the role of ferromagnesian phases (and possibly accessory phases). The significant covariances of Ti could possibly highlight the importance of magnetite or titanite. Significant negative covariances between Th and P (Appendix C) possibly eliminates any importance of apatite in the chemistry of the BWB Gneiss.

Centered log-ratio covariance matrices for the NNM Gneiss indicate that the greatest positive covariances occur between the element pairs Mg-Ca, Mg-Mn, Mg-P, Mn-Ca, and Ba-Sr (Table 5.4c and Appendix C). The greatest negative covariances occur between the element pairs K-Mn, K-Mg and K-Ca. Element associations with Si, Na and K show the lowest covariances (Table 5.4c). The association between Ba and Sr is stronger in the NNM Gneiss relative to the

BWB and STK gneisses, the latter showing the least association, possibly suggesting a greater influence of feldspars in the NNM Gneiss chemistry.

The strength in element association (covariances) generally increases from the STK Gneiss to the BWB Gneiss, and is strongest in the NNM Gneiss. The consistent significant positive covariance between Ca and Mg in all of the GS lithologies suggests the importance of hornblende and/or pyroxenes (notably clinopyroxene) in the melt residue. The inverse and positive relationships between the elements described above, as observed in the chemistry of the GS gneisses, suggest the importance of accessory minerals (such as apatite, magnetite and/or titanite), ferromagnesian minerals and/or iron-titanium oxides as variables contributing to the observed rock chemistry. The covariance between Ba and Sr is strongest in the NNM Gneiss, and less through the BWB Gneiss to the STK Gneiss, possibly indicating a greater influence of feldspar fractionation in the formation of the NNM Gneiss.

Table 5.1. *Summary statistics of the Gladkop Suite major element whole-rock geochemical data.*

Lithology	**Brandewynsbank Gneiss**				**Noenoemaasberg Gneiss**				**Steinkopf Gneiss**				**Brandewynsbank Gneiss**				**Noenoemaasberg Gneiss**				**Steinkopf Gneiss**			
No. of samples	**14**				**8**				**9**				**5**				**13**				**11**			
Source	**This study**				**This study**				**This study**				**Reid and Barton (1983)**				**Van Aswegen (1983)**				**Reid and Barton (1983)**			
Major (wt. %)	**Mean***	**Std**	**Min**	**Max**	**Mean***	**Std**	**Min**	**Max**	**Mean***	**Std**	**Min**	**Max**	**Mean***	**Std**	**Min**	**Max**	**Mean***	**Std**	**Min**	**Max**	**Mean***	**Std**	**Min**	**Max**
SiO_2	72.23	3.70	64.64	76.51	75.44	2.63	72.01	78.93	69.19	2.45	65.29	72.28	71.45	5.53	61.57	74.26	75.66	2.04	71.00	78.34	70.39	4.57	60.03	76.55
TiO_2	0.41	0.18	0.24	0.79	0.25	0.07	0.17	0.34	0.56	0.11	0.41	0.75	0.35	0.07	0.30	0.47	0.25	0.16	0.13	0.74	0.50	0.23	0.25	1.05
Al_2O_3	13.27	1.15	11.66	15.52	12.21	1.09	10.69	13.91	14.45	0.68	13.47	15.33	14.86	3.21	13.05	20.59	12.56	1.27	11.12	15.32	14.45	1.23	12.70	17.11
$Fe_2O_3^t$	2.68	1.19	1.54	5.26	1.59	0.46	0.82	2.16	3.64	1.02	2.17	4.90	2.07	0.46	1.73	2.88	0.71	0.90	0.22	3.63	3.11	1.82	1.34	7.67
MnO	0.06	0.02	0.04	0.10	0.03	0.04	0.01	0.14	0.09	0.03	0.05	0.13	0.06	0.02	0.03	0.08	0.02	0.01	0.01	0.04	0.08	0.04	0.01	0.15
MgO	0.61	0.39	0.31	1.53	0.28	0.31	0.11	1.05	0.85	0.33	0.52	1.50	0.55	0.12	0.47	0.76	0.48	0.24	0.15	0.85	0.84	0.43	0.27	1.65
CaO	2.06	0.97	1.11	4.58	0.84	0.86	0.35	2.87	2.74	0.71	1.92	3.82	2.11	0.55	1.77	3.09	0.94	0.31	0.43	1.53	2.35	1.06	1.08	4.14
Na_2O	3.05	0.40	2.45	3.79	2.65	0.47	2.15	3.59	3.35	0.43	2.88	4.13	2.81	0.51	2.48	3.70	2.76	0.26	2.34	3.32	2.88	0.81	1.50	4.17
K_2O	3.67	0.95	1.54	5.65	4.90	1.28	2.76	6.91	3.17	1.01	1.76	4.69	4.52	0.59	4.02	5.53	4.73	0.58	3.81	5.77	4.00	0.93	2.07	5.05
P_2O_5	0.09	0.05	0.04	0.19	0.04	0.03	0.02	0.09	0.13	0.03	0.09	0.18	0.08	0.05	0.05	0.17	0.08	0.14	0.01	0.52	0.11	0.05	0.03	0.20
LOI	0.57	0.20	0.20	0.93	0.49	0.27	0.25	0.93	0.62	0.25	0.23	1.01	No measured data				0.44	0.03	0.42	0.48	No measured data			
C	0.38	0.29	0.00	1.00	0.58	0.42	0.00	1.36	0.58	0.34	0.00	1.14	1.69	0.91	1.09	3.31	1.47	1.20	0.00	3.83	1.41	1.08	0.00	3.61
Mg#	31.07	3.88	23.58	39.70	26.92	10.48	14.45	46.43	31.67	3.48	25.35	37.00	32.02	0.96	31.03	33.58	58.48	16.18	25.87	86.07	32.54	4.27	26.42	38.97
ASI	1.02	0.03	0.96	1.08	1.04	0.05	0.95	1.10	1.03	0.03	0.95	1.07	1.12	0.04	1.09	1.18	1.12	0.11	0.91	1.32	1.10	0.10	0.96	1.31
MALI	4.64	1.51	0.75	6.99	6.66	1.64	3.48	8.48	3.87	1.33	2.03	5.65	5.21	0.55	4.68	6.14	6.55	0.8	5.56	7.84	4.54	1.97	1.75	7.46
K_2O/Na_2O	1.29	0.46	0.41	2.31	1.99	0.73	0.77	2.94	1.03	0.40	0.46	1.63	1.62	0.13	1.49	1.78	1.72	0.24	1.32	2.25	1.54	0.72	0.53	3.35
$Fe_2O_3^T$ + MgO	3.58	1.70	2.05	7.38	2.03	0.79	1.03	3.45	4.69	1.42	2.95	6.95	2.81	0.57	2.41	3.96	1.04	1.05	0.45	4.74	3.77	2.32	1.76	10.17

* - mean calculated is geometric, rather than arithmetic (same as for Tables 5.2 and 5.3). Abbreviations: C - Normative corundum; Min - Minimum; Max - Maximum; Std: Standard deviation

Geometric mean = $(X_1 \times X_2 \times X_3 \ldots X_n)^{1/n}$; where X = variable and n = number of variables

Mg#: Magnesium number or magnesium-iron ratio = [100 x Mg / (Mg + Fe)]

MALI: Modified Alkali lime index = $Na_2O + K_2O$ - CaO after Frost et al. (2001)

ASI: Aluminium saturation index = Al_2O_3 / ($Na_2O + K_2O$ + CaO - $1.67P_2O_5$) after Frost et al. (2001)

Table 5.2. *Summary statistics of the Gladkop Suite trace element whole-rock geochemical data.*

Lithology	**Brandewynsbank Gneiss**				**Noenoemaasberg Gneiss**				**Steinkopf Gneiss**				**Brandewynsbank Gneiss**				**Noenoemaasberg Gneiss**				**Steinkopf Gneiss**			
No. of samples	**14**				**8**				**9**				**5**				**13**				**11**			
Source	**This study**				**This study**				**This study**				**Reid and Barton (1983)**				**Van Aswegen (1983)**				**Reid and Barton (1983)**			
Trace (ppm)	**Mean***	**Std**	**Min**	**Max**	**Mean***	**Std**	**Min**	**Max**	**Mean***	**Std**	**Min**	**Max**	**Mean***	**Std**	**Min**	**Max**	**Mean***	**Std**	**Min**	**Max**	**Mean***	**Std**	**Min**	**Max**
Sc	13.79	4.05	8.84	21.36	11.43	4.25	8.77	21.99	16.53	3.21	12.58	20.48	5.20	1.10	4.00	7.00					10.89	6.55	3.00	27.00
V	62.57	24.88	34.20	119.15	45.52	12.55	22.41	60.60	86.74	27.00	54.95	135.45	20.40	4.98	17.00	29.00					41.45	34.06	11.00	126.00
Cr	324.10	106.67	162.55	506.80	354.75	135.26	172.45	593.50	367.71	87.87	263.30	505.65	5.64	1.32	4.20	7.60					11.72	5.69	4.00	23.00
Co	4.43	3.13	2.30	12.07	2.17	1.34	1.04	4.56	7.15	2.98	4.13	12.87	3.58	0.28	3.30	4.00					6.84	4.85	2.20	17.00
Ni	12.91	4.64	7.65	25.70	13.12	3.44	8.80	18.35	15.89	6.44	9.00	27.60	1.98	0.41	1.50	2.50					4.69	2.36	2.30	9.20
Cu	51.60	95.23	20.43	385.25	33.30	26.08	11.08	96.15	50.72	64.62	19.76	194.50	2.84	1.35	1.60	4.90					5.64	7.58	0.80	27.00
Zn	61.75	60.77	26.55	242.10	24.66	16.49	12.55	65.05	64.42	32.10	38.95	146.65	34.20	11.12	25.00	53.00					52.18	28.66	16.00	110.00
Rb	141.52	36.24	58.77	219.25	178.71	49.31	98.65	249.60	147.35	31.32	116.75	210.45	174.60	24.63	159.00	218.00					162.00	17.74	138.00	195.00
Sr	176.79	54.73	117.05	298.80	87.26	85.12	33.50	283.60	222.12	51.84	162.83	332.00	189.00	30.83	173.00	244.00					239.64	79.01	149.00	423.00
Y	29.55	17.33	10.36	72.14	20.91	20.24	8.62	65.12	31.04	7.70	22.55	50.22	32.20	6.76	26.00	43.00					30.55	6.90	22.00	43.00
Zr	199.10	65.07	108.40	297.70	126.62	24.99	96.20	162.10	248.30	16.16	209.40	268.20	156.40	26.25	140.00	203.00	No measured data				210.73	47.92	123.00	263.00
Nb	12.07	3.59	6.18	21.18	10.81	4.35	4.22	18.27	13.00	1.14	11.66	15.34	14.60	2.30	13.00	18.00					12.19	3.17	6.80	18.00
Mo	20.09	6.86	9.72	31.90	22.38	8.81	10.78	37.50	23.19	5.77	16.47	31.98	1.40	0.00	1.40	1.40					1.58	0.54	1.00	3.10
Cs	1.00	0.25	0.59	1.51	0.80	0.32	0.35	1.29	1.74	1.02	0.76	3.46	No measured data								No measured data			
Ba	762.31	350.10	310.85	1441.50	476.21	579.72	179.50	1878.50	1030.26	304.98	695.95	1518.50	886.00	43.40	813.00	918.00					1012.82	281.70	605.00	1420.00
Hf	5.90	1.56	3.82	8.30	4.13	0.72	2.61	4.87	6.76	0.45	6.04	7.26	No measured data								No measured data			
Ta	0.70	0.36	0.22	1.40	0.56	0.39	0.20	1.29	0.82	0.23	0.47	1.30												
Pb	23.29	6.84	14.99	43.17	24.73	13.58	15.71	57.74	22.29	5.07	15.36	31.34	22.20	4.97	19.00	31.00					23.64	6.45	13.00	36.00
Th	18.51	12.45	6.85	58.23	22.85	4.32	17.10	28.87	15.68	2.94	11.72	20.72	19.00	7.55	14.00	32.00					15.64	4.57	6.00	24.00
U	1.15	0.99	0.52	4.23	1.47	0.51	0.67	2.16	1.36	0.52	0.86	2.59	2.00	0.00	2.00	2.00					2.46	0.56	2.00	3.40
Rb/Sr	0.87	0.34	0.28	1.49	3.19	3.01	0.74	7.45	0.70	0.24	0.38	1.13	0.93	0.03	0.89	0.97					0.70	0.27	0.39	1.31
Sr/Y	7.16	4.49	2.05	16.76	7.27	8.94	1.21	25.50	7.58	2.56	3.54	11.14	5.91	1.79	4.07	9.38					7.67	2.90	4.44	14.10
K/Rb	215.60	14.47	181.04	241	229.10	29.11	174.27	273.61	183.35	41.34	174.27	273.61	215.00	3.97	209.88	218.95					200.27	37.35	102.90	25.03

* - mean calculated is geometric, rather than arithmetic

Table 5.3. *Summary statistics of the Gladkop Suite Rare Earth Element (REE) whole-rock geochemical data.*

Lithology	**Brandewynsbank Gneiss**				**Noenoemaasberg Gneiss**				**Steinkopf Gneiss**				**Brandewynsbank Gneiss**				**Noenoemaasberg Gneiss**				**Steinkopf Gneiss**			
No. of samples	**14**				**8**				**9**				**5**				**13**				**11**			
Source	**This study**				**This study**				**This study**				**Reid and Barton (1983)**				**Van Aswegen (1983)**				**Reid and Barton (1983)**			
REE (ppm)	**Mean***	**Std**	**Min**	**Max**	**Mean***	**Std**	**Min**	**Max**	**Mean***	**Std**	**Min**	**Max**	**Mean***	**Std**	**Min**	**Max**	**Mean***	**Std**	**Min**	**Max**	**Mean***	**Std**	**Min**	**Max**
La	55.60	24.78	34.66	117.80	44.08	6.53	34.21	52.47	56.04	22.59	41.64	117.20	67.40	20.22	54.00	103.00					52.45	12.11	35.00	71.00
Ce	112.88	49.30	68.23	239.60	90.50	11.42	71.31	107.45	111.05	31.08	84.70	192.50	119.00	32.23	99.00	176.00					95.55	22.08	59.00	126.00
Pr	12.58	4.98	7.38	24.91	10.05	1.23	8.09	11.66	12.58	4.45	9.52	24.58	No measured data								No measured data			
Nd	45.72	16.83	25.24	83.50	36.31	4.53	29.05	42.40	47.00	14.80	36.50	86.65	49.00	13.21	38.00	72.00					43.73	10.14	28.00	57.00
Sm	8.35	2.80	4.67	13.34	6.99	0.80	5.56	6.12	8.44	2.31	6.95	14.66	8.64	1.93	6.20	11.00					7.59	2.01	4.10	11.00
Eu	1.37	0.36	0.91	1.99	0.88	0.49	0.41	1.70	1.74	0.19	1.49	2.03												
Gd	6.86	2.49	3.98	12.48	5.53	1.40	4.39	8.01	7.02	1.67	6.01	11.39												
Tb	0.93	0.43	0.50	2.06	0.75	0.28	0.53	1.29	0.96	0.22	0.79	1.53					No measured data							
Dy	5.58	2.99	2.51	13.46	4.33	2.43	2.53	9.09	5.80	1.34	4.40	9.14												
Ho	1.07	0.62	0.41	2.68	0.77	0.63	0.34	2.08	1.13	0.27	0.82	1.77												
Er	3.06	2.00	0.89	8.26	2.03	2.24	0.70	6.97	3.31	0.85	2.16	5.28	No measured data								No measured data			
Tm	0.41	0.28	0.10	1.11	0.27	0.37	0.07	1.12	0.47	0.14	0.28	0.80												
Yb	2.67	1.92	0.57	7.30	1.74	2.80	0.53	8.56	3.05	0.86	1.94	5.05												
Lu	0.39	0.25	0.07	0.95	0.25	0.45	0.06	1.35	0.44	0.14	0.26	0.77												
Eu/Eu*	**0.57**	0.13	0.34	0.79	**0.48**	0.22	0.25	0.83	**0.70**	0.10	0.47	0.81												
$(La/Yb)_N$	**21.54**	24.05	3.85	82.23	**27.41**	23.73	2.72	63.22	**12.91**	3.7	8.97	21.13												
$(Gd/Yb)_N$	**2.49**	1.79	1.09	6.41	**3.55**	2.81	0.76	7.52	**1.89**	0.34	1.49	2.73												
$(La/Sm)_N$	**4.31**	1.04	2.29	5.89	**3.99**	0.57	2.64	4.39	**4.18**	0.5	3.6	5.01												
Mean ∑REE	275.69				209.00				267.30															

$_N$ - Elements are normalized with respect to the primitive mantle (after Sun and McDonough, 1989).

* - mean calculated is geometric, rather than arithmetic, except for Eu/Eu*

$Eu/Eu^* = Eu_N/[(Sm_N)(Gd_N)]^{1/2}$

Table 5.4. *Centered log-ratio covariance matrices for the GS gneisses calculated after the methods of Aitchison (1986), where SiO_2/g, etc. represents (natural) log [SiO_2 wt. % / g], etc. and where g is the geometric mean of the oxide. Numbers in* ***bold*** *indicate significant covariances.*

a. Centered log-ratio covariance matrix of the Steinkopf Gneiss.

	SiO_2/g	TiO_2/g	Al_2O_3/g	$Fe_2O_3^T$/g	MnO/g	MgO/g	CaO/g	Na_2O/g	K_2O/g	P_2O_5/g
SiO_2/g	0.001									
TiO_2/g	-0.006	0.035								
Al_2O_3/g	-0.002	0.007	0.002							
$Fe_2O_3^T$/g	-0.011	0.053	0.014	0.099						
MnO/g	-0.008	0.040	0.010	**0.084**	0.102					
MgO/g	-0.011	0.058	0.012	**0.102**	**0.072**	0.130				
CaO/g	-0.008	0.043	0.010	**0.068**	0.042	**0.082**	0.068			
Na_2O/g	-0.003	0.012	0.005	0.027	0.029	0.017	0.017	0.015		
K_2O/g	0.007	-0.038	-0.012	**-0.070**	**-0.063**	**-0.063**	**-0.065**	-0.035	0.110	
P_2O_5/g	-0.008	0.043	0.009	**0.076**	**0.066**	**0.084**	0.055	0.017	**-0.049**	0.064

b. Centered log-ratio covariance matrix of the Brandewynsbank Gneiss.

	SiO_2/g	TiO_2/g	Al_2O_3/g	$Fe_2O_3^T$/g	MnO/g	MgO/g	CaO/g	Na_2O/g	K_2O/g	P_2O_5/g
SiO_2/g	0.003									
TiO_2/g	-0.018	0.147								
Al_2O_3/g	-0.004	0.026	0.007							
$Fe_2O_3^T$/g	-0.020	**0.138**	0.029	0.150						
MnO/g	-0.013	0.095	0.020	0.092	0.093					
MgO/g	-0.025	**0.175**	0.039	**0.185**	0.116	0.254				
CaO/g	-0.019	**0.141**	0.030	**0.140**	0.102	**0.182**	0.159			
Na_2O/g	-0.005	0.038	0.009	0.037	0.027	0.047	0.045	0.018		
K_2O/g	0.011	**-0.079**	-0.017	**-0.084**	**-0.055**	**-0.106**	**-0.100**	-0.032	0.091	
P_2O_5/g	-0.021	**0.176**	0.029	**0.166**	0.115	**0.203**	**0.170**	0.044	**-0.099**	0.220

c. Centered log-ratio covariance matrix of the Noenoemaasberg Gneiss.

	SiO_2/g	TiO_2/g	Al_2O_3/g	$Fe_2O_3^T$/g	MnO/g	MgO/g	CaO/g	Na_2O/g	K_2O/g	P_2O_5/g
SiO_2/g	0.001									
TiO_2/g	-0.004	0.085								
Al_2O_3/g	-0.003	0.009	0.008							
$Fe_2O_3^T$/g	-0.009	0.068	0.022	0.104						
MnO/g	-0.021	0.167	0.050	0.190	0.594					
MgO/g	-0.026	0.158	0.064	0.243	**0.543**	0.681				
CaO/g	-0.021	0.177	0.048	0.227	**0.513**	**0.578**	0.558			
Na_2O/g	-0.003	0.040	0.008	0.042	0.101	0.119	0.108	0.028		
K_2O/g	0.003	-0.064	-0.006	-0.060	**-0.157**	**-0.154**	**-0.170**	-0.041	0.080	
P_2O_5/g	-0.021	0.050	0.052	0.146	0.288	**0.426**	0.282	0.058	-0.023	0.429

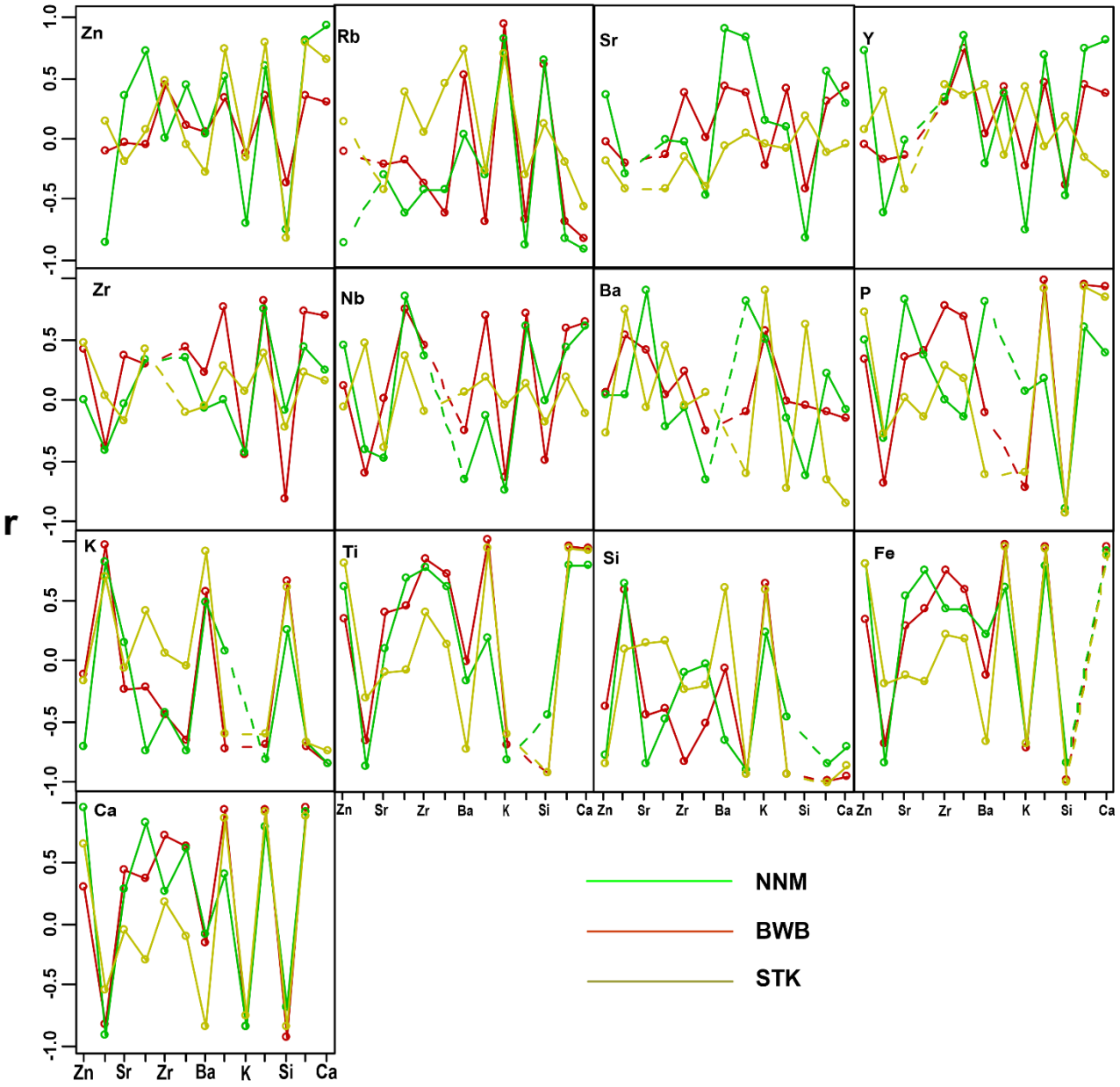

Fig. 5.2. *Correlation coefficient patterns for the BWB, NNM and STK gneisses produced by plotting correlation coefficient values (r) of a selected element against a series of other elements. Solid lines join points in the* observed *pattern, whereas the dashed portions indicate where the correlation coefficient between each element and itself has been omitted. From left to right, the elements (incompatible and semi-incompatible) on the x-axis are: Zn, Rb, Sr, Y, Zr, Nb, Ba, P, K, Ti, Si, Fe and Ca. Taking into account the number of samples for each GS lithology when considering the strength of correlation, each element pair is allowed a standard error of* $[(1-r^2)/n]$*, where r = correlation coefficient and n = number of samples.*

Fig. 5.2 shows bivariate variation diagrams of correlation data (correlation coefficient patterns) for the GS gneisses, after Cox and Clifford (1982). The patterns produced were mostly similar when both the original (measured) element concentrations and the log-ratio compositions were used. These bivariate plots are used to analyze any characteristic trends/relationships that might exist in the dataset. Basically, similarity in correlation patterns between two or more elements means their analogous geochemical behavior, potentially controlled by the same geochemical process (such as fractional crystallization, partial melting, weathering, hydrothermal alteration, etc.). A near-ideal single stage magmatic process will produce a magmatic suite whose elements form generally high (significant) correlations, and form only slightly curved correlation patterns (Wood, 1978; Cox and Clifford, 1982). The zig-zag correlation patterns produced by the GS gneisses (Fig. 5.2) suggest that the magmas were subjected to multiple magmatic processes during their evolution.

Pairs of elements from the series Ti-P-Fe-Ca show consistently high positive correlations, but form consistently high negative correlations with K (and Si) (Fig. 5.2). This observation is generally in line with the importance of minerals such as apatite, a ferromagnesian mineral(s) and/or iron-titanium oxides as variables contributing to the observed rock chemistry. Strong positive correlations occur between Rb, Ba, K and Si, suggesting the importance of a potassic phase (notably K-feldspar). The NNM Gneiss, however, shows a negative correlation between Ba and Si (Fig. 5.2). Sr and Ba show a positive correlation (highest in the NNM Gneiss and lowest in the STK Gneiss), suggesting a greater influence of plagioclase as fractionation increases. Rb, Ba and Sr (LFS elements) show significantly different correlation patterns to each other in each of the GS gneisses, suggesting these elements in each of these different precursor magma(s) were affected by different processes (possibly different amounts of fractional crystallization, magma mixing, peritectic assemblage entrainment and/or element mobility). Zr, Y and Nb (HFS elements) show the same patterns in the BWB and NNM gneisses, but different patterns in the STK Gneiss. Nb shows positive correlations (mostly) with Ba and K. For the Fe plot there is a strong positive peak for all three gneisses between Fe and Ti, and likewise between Fe and P and a low negative peak between Fe and Rb (suggests the role of biotite in all cases with associated apatite). The same applies for the Ca plot. The strong correlation between Ca and P indicates the activity of apatite, more so in the BWB and STK gneisses. The strong positive correlation between Ti and Ba suggests the influence of biotite (also with Zr, where zircons could occur as inclusions in biotite). Generally, the NNM and BWB gneisses tend to show similar patterns (except for a few element pairs involving very mobile elements), which are slightly different from the patterns observed in the STK Gneiss. This could suggest that the latter was generated by a relatively different process to that which generated the NNM and BWB gneisses. Since all three gneisses are intimately interbanded, the differences observed in the correlation patterns may simply reflect their differences in mineralogical composition.

5.3. Element mobility

Element mobility (and chemical changes) in rocks is often caused by processes such as weathering, diagenesis and metamorphism, including hydrothermal fluid interactions (Pearce, 1976, 1983; Winchester and Floyd, 1977; Middelburg et al., 1988; Seewald and Seyfried, 1990; Rollinson, 1993). The HFS incompatible elements (Sc, Y, Th, Zr, Hf, Ti, Nb, Ta and the REE), Co, Ni, V and Cr are relatively immobile, although they can be mobilized under certain conditions;

while the major elements Ca, Na, P, K, Mg and Si, as well as the LFS incompatible elements (Sr, Ba, Cs and Rb) are generally mobile (Rollinson, 1993).

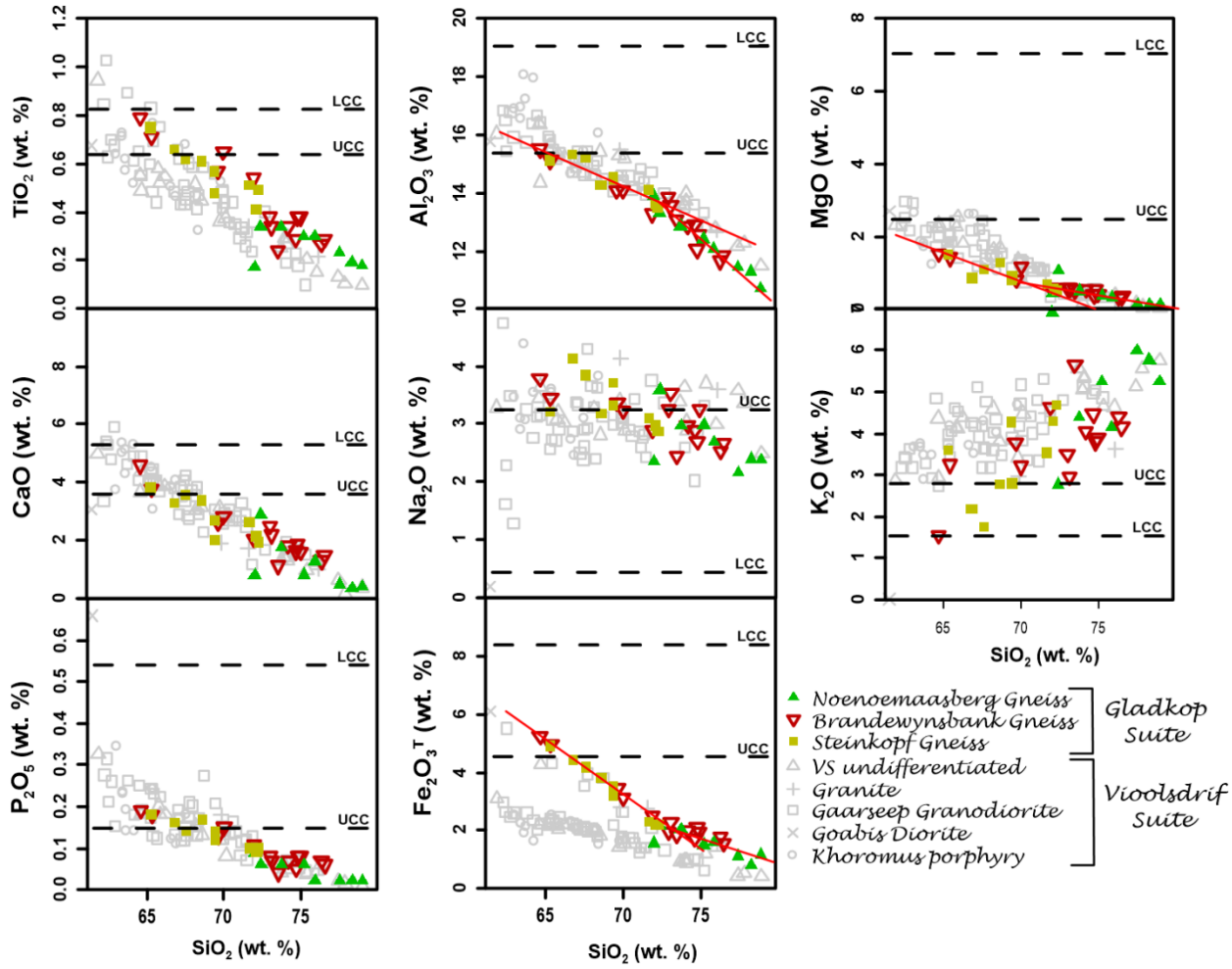

Fig. 5.3. *Major element bivariate (Harker) plots of the Gladkop and Vioolsdrif Suite rocks. Average UCC and LCC compositions sourced from Rudnick and Gao (2003). Negative and positive correlations between SiO_2 and the other major elements are evident, as also shown in Tables 5.4a-c.*

Trace element mobility is generally affected by the mineralogical changes which take place during alteration, metamorphism and/or metasomatism (Rollinson, 1993). Since the GS rocks experienced medium- to high-grade metamorphism (Fig. 1.1; Waters, 1986) and considerable secondary alteration processes, it is possible that most mobile elements have been mobilized, thus making it necessary to investigate whether element concentrations are undisturbed and original before they can be used to make inferences about the petrogenesis of the GS rocks.

The relative mobility of the major elements and selected trace elements was tested by plotting their concentrations against SiO_2 (wt. %) values (Figs. 5.3, 5.4). Binary variation diagrams of Na_2O and K_2O vs. SiO_2 show considerable data scatter, with negative and positive correlations respectively, in both the GS and VS rocks (Fig. 5.3). The rest of the major elements show limited data scatter and good negative correlations with SiO_2 (Fig. 5.3). This indicates that all these major elements probably behaved in a less mobile way during metamorphism, with the scatter observed

in Na_2O and K_2O plots possibly due to variation in feldspar (plagioclase/K-feldspar) fractionation (McCarthy and Robb, 1978). For the trace elements, Co shows very limited data scatter and a good negative correlation with SiO_2 for the GS gneisses (Fig. 5.4), which could suggest typical limited mobilization. Sr is negatively correlated with SiO_2, and shows considerable scatter in both the GS and VS rocks (Fig. 5.4). Zr and Ni show negative correlations with SiO_2, and while plots of these elements vs. SiO_2 produce limited scatter the GS data (Fig. 5.4), the VS samples shown produce considerable scatter. The trends for Hf (not shown) and Zr are exactly the same. Rb shows a positive correlation with SiO_2 and considerable data scatter in the GS gneisses and the VS Gaarseep Granodiorite (Fig. 5.4), suggesting considerable element mobilization. Sm shows limited data scatter against SiO_2 in the NNM Gneiss, but considerable scatter in the BWB and STK gneisses (Fig. 5.4). While the GS gneisses define a negative slope on the Sm vs. SiO_2 plot (Fig. 5.4), the VS rocks define a positive slope. Ba and Y show considerable data scatter and are negatively correlated with SiO_2. The scatter observed on the plots of SiO_2 vs. Sr, Ba and Rb (Fig. 5.4) could be due to either feldspar fractionation or element mobilization, so any inferences made using these elements is done with caution. It is notable from Fig. 5.3 that the VS trend defines a completely different liquid-line-of-descent to the GS.

The Harker plots of molar concentrations of major elements vs. molar Si in the GS (Appendix D) show good strong correlations for Al, Mg, Fe, Ti and less so for Na and K. For the Harker plots of trace element concentrations vs. molar Si, there are reasonably good correlations in the GS generally (Appendix D). Zr and Hf (not shown) show exactly the same trends.

5.4. Major element chemistry

Plutonic rocks have been noted as problematic with respect to classification based on major element geochemical data. However, Rollinson (1993) suggested that, although the normative Ab-An-Or plot of O'Connor (1965) provides an adequate classification scheme, the R_1-R_2 cation plot of De La Roche et al. (1980) is more comprehensive. However, all these classification schemes are applied in this study and similarly show that the GS gneisses span a range of granitic to granodioritic compositions (Fig. 5.5).

The GS orthogneisses invariably have more Fe than Mg content ($Fe_2O_3^T$ = 0.82-5.26 wt. %, MgO = 0.11-1.53 wt. %, mean Mg# = 26-31). These metagranitoids are characterized by low TiO_2, Al_2O_3, CaO, and P_2O_5 concentrations relative to those of both the UCC and the LCC (Fig. 5.3). The Harker variation diagrams (Fig. 5.3) show strong negative correlations of SiO_2 with TiO_2, CaO, P_2O_5, $Fe_2O_3^T$, Al_2O_3 and MgO. In contrast, the alkalis relative to SiO_2 have scattered plots, potentially implying some metamorphic mobility and/or variations in feldspar fractionation. For most elements, the STK and NNM samples plot along the same trends. However, for Al_2O_3 and Fe_2O_3 (MgO to a lesser extent), an inflexion occurs between the trend formed by the STK samples and those of the BWB and NNM samples. This occurs at 72 wt. % silica (Fig. 5.3). The differentiation mechanism responsible for such a pattern were either partial melting or fractional crystallization (with changing cumulate composition) (McCarthy and Robb, 1978; Janoušek et a., 2016).

The VS rocks are K-rich (mean K_2O/Na_2O = 1.10-1.42; max = 3.79), and with relatively high Mg (0.04-7.60 wt. %, mean Mg# = 29.74-58.41) and Al_2O_3 (11.50-18.83 wt. %, mean ~15.20 wt. %) contents but relatively low TiO_2 (0.10-1.03) and total Fe (0.46-9.73) contents (Fig. 5.3). The GS and VS rocks are significantly different in terms of their chemical signatures. This is

clearly evident on the $Fe_2O_3^T$ and MgO vs. SiO_2 plots (Fig. 5.3), as well as in Figs. 5.4 and 5.6a, c, where both suites clearly show two distinct liquid-lines-of-descent.

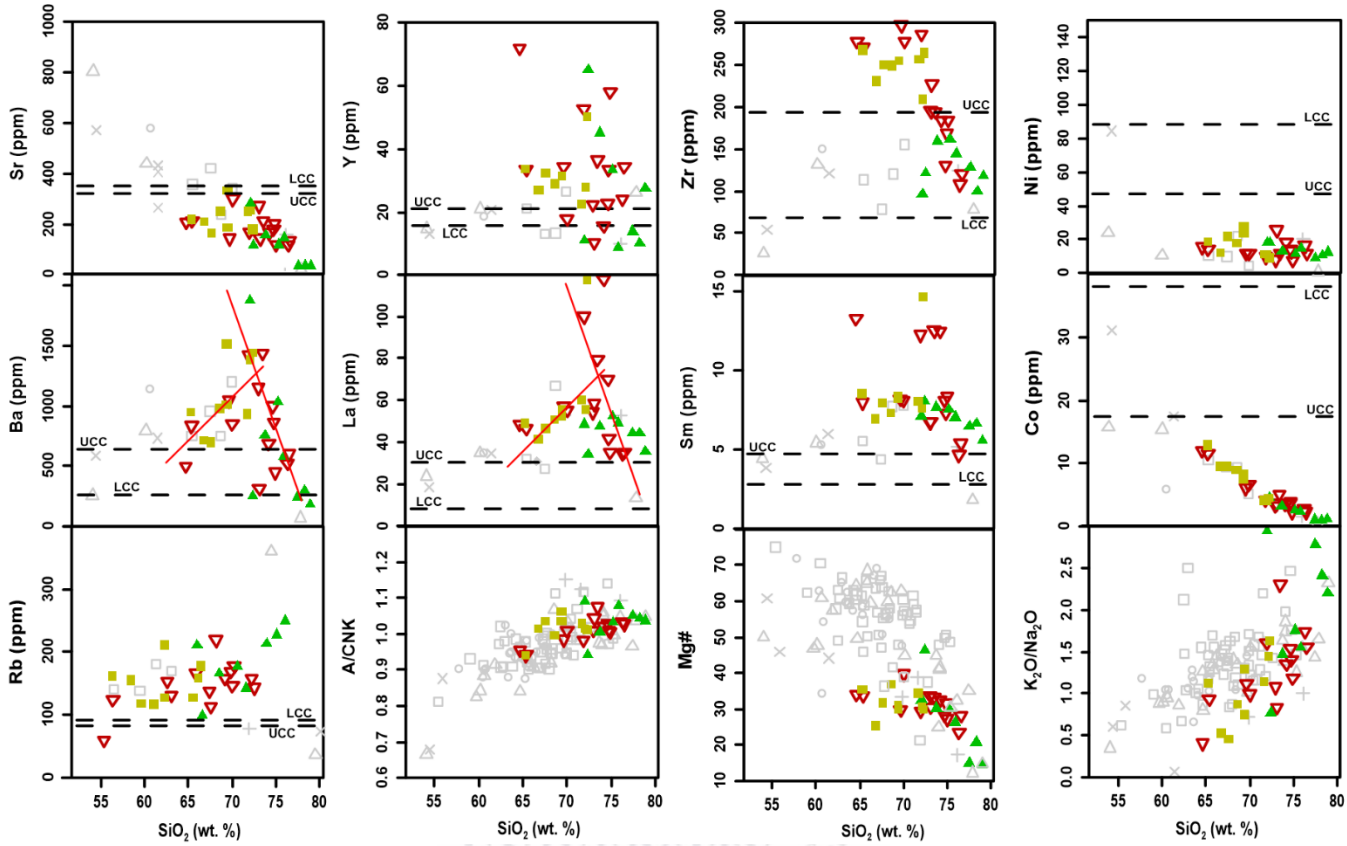

Fig. 5.4. *Bivariate SiO_2 vs. selected trace element plots of the Gladkop Suite and Vioolsdrif Suite rocks. The set of elements plotted include: 1- Incompatible elements [LFS (Sr, Ba, Rb) and HFS (Y, La, Zr, Sm)]; 2- Compatible elements (Ni, Co). Average UCC and LCC concentrations sourced from Rudnick and Gao (2003). Symbols as for Fig. 5.3.*

The GS gneisses are granites to granodiorites, the NNM Gneiss more granitic and the STK Gneiss more granodioritic (Fig. 5.5a-e). The geochemical classification of granitic rocks adapted by Frost et al. (2001) has been used to further characterize the GS gneisses. The binary diagram of Fe* [= $Fe_2O_3^T$ / ($Fe_2O_3^T$ + MgO)] vs. SiO_2 plots 90 % of all samples in the magnesian field (Fig. 5.6a). On the (Na_2O + K_2O - CaO) vs. SiO_2 plot (MALI plot), 90 % of the samples plot across the calcic and calc-alkalic fields (Fig. 5.6d). The aluminium saturation index (ASI), defined as molecular Al_2O_3 / (Na_2O + K_2O + CaO - 1.67P_2O_5), was used to discriminate peraluminous, metaluminous and peralkaline magma series (Fig. 5.6b). This plot reveals that the GS gneisses are largely metaluminous to weakly peraluminous ($0.9 \leq ASI \leq 1.1$). These gneisses are weakly corundum normative ($C \leq 1.0$ wt. %; Table 5.1; Fig. 5.6f) and on the Al_2O_3 / (CaO + Na_2O + K_2O) molecular vs. C variation diagram to distinguish between I- and S-type granitic rocks (Fig. 5.6f; Chappell and White; 1974), the samples from this study plot mainly in the I-type granites field. On the AFM ternary plot, with the dividing line of Irvine and Baragar (1971) to discriminate between tholeiitic and calc-alkaline suites, the GS gneisses generally plot within the calc-alkaline field (Fig. 5.6c), suggesting that the GS magmas are subduction related. Except for the NNM

samples from Reid and Barton (1983) which plot very close to the alkali vertex, and a few STK samples which plot in the tholeiitic series field, the rest of the samples plot along the same calc-alkaline suite trend. On the K_2O vs. SiO_2 plot of Peccerillo and Taylor (1976), most of the samples from Van Aswegen (1983) and Reid and Barton (1983) plot in the high-K calc-alkaline series. While most samples from this study plot in the same series, a few samples plot in the calc-alkaline series. Similarly, the VS rocks are magnesian with a metaluminous to peraluminous character, were generated in a high-K calc-alkaline series and show a calcic to calc-alkalic characteristic (Fig. 5.6a-f). In summary, the GS granitoids show typical I-type characteristics.

5.5. Trace element chemistry

Trace element data are very important in identifying petrogenetic processes based on the assertion that the elements in the various identified groups (REE, transition metals, HFS and LFS) have similar chemical characteristics (Rollinson, 1993). Petrogenetic processes, however, may take advantage of the small changes in chemical characteristics of some elements, causing them to behave differently from the rest of the group. It is a deviation from the group behavior which is exploited to identify any petrogenetic processes which might have occurred. The REE series, which is the most important group of trace elements, will become fractionated relative to each other due to very slight differences in their ionic sizes and chemical behavior which are exploited by petrological processes (Rollinson, 1993). Also, elements which prefer the melt phase (during fractionation or melting) are termed incompatible, whereas those that prefer the mineral phase are termed compatible. It should be noted, however, that the degree of element compatibility depends on the melt composition (Rollinson, 1993). The HFS elements (Sc, Y, Th, U, Pb, Zr, Hf, Ti, Nb and Ta) are generally considered to be immobile during metamorphism (Winchester and Floyd, 1977; Pearce, 1983). Given the metamorphic history of the GS gneisses, immobile (HFS) element plots were also used to classify them, producing similar results obtained using major elements (Fig. 5.5).

On SiO_2 vs. trace element diagrams, data from the NNM and STK gneisses do not fall on the same trend (e.g. Ba, Co, La and Sm). Rather, they tend to form inflexed lines. This rules out binary mixing as a petrogenetic process influencing the rock chemistry (Janoušek et al., 2016). The GS gneisses have elevated Rb, La and Sm (incompatible elements) concentrations relative to both the UCC and LCC (Fig. 5.4), suggesting that they are products of magma fractionation. The STK Gneiss has elevated Ba and Y concentrations relative to the UCC and LCC, while the BWB and NNM gneisses both have average UCC concentrations (Fig. 5.4), implying the former is the least fractionated.

Zr concentrations are significantly higher in the STK Gneiss relative to the NNM Gneiss (Fig. 5.4), concentrations decreasing with increasing SiO_2 (to about 100 ppm), which is consistent with zircon fractionation (Rollinson, 1993). These concentrations could suggest that zircon fractionation was more significant in the evolution of the NNM Gneiss. The GS rocks show elevated Th concentrations relative to the UCC and LCC, and Nb concentrations typical of the UCC (Fig. 5.7a and d). The U concentrations of the GS rocks (mean = 1.37-1.56 ppm; Table 5.2) are lower than those of the UCC (Fig. 5.7b). However, the Th/U ratios for thees rocks (3.3-41) are slightly higher than those normal igneous rocks (Fig. 5.7c). This is consistent with U depletion relative to Th (Fig. 5.7c).

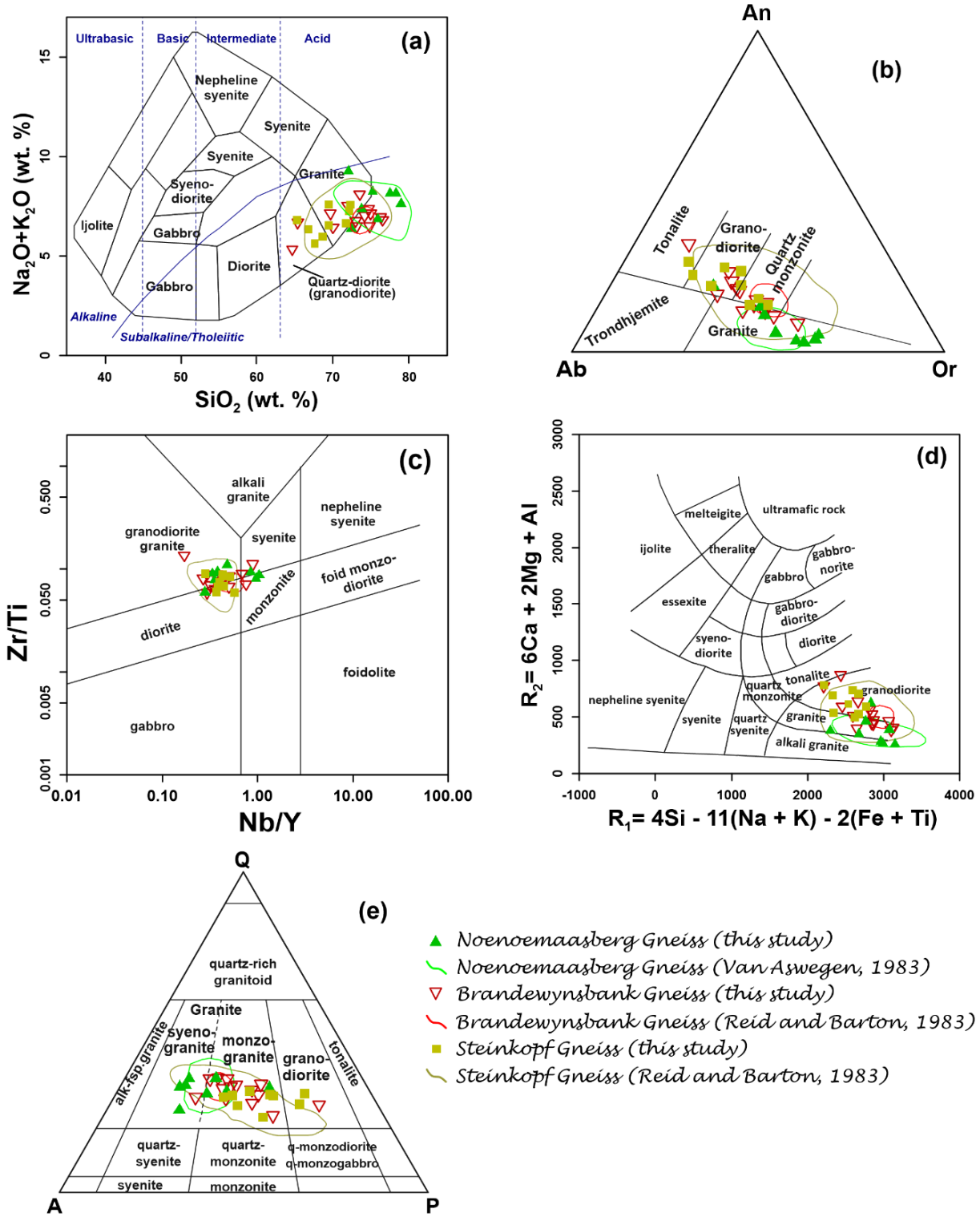

Fig. 5.5. *Classification plots of the Gladkop Suite igneous rocks.* ***(a)*** *The total alkali vs. SiO_2 plot of Cox et al. (1979) modified by Wilson (1989).* ***(b)*** *The normative Ab-An-Or classification plot of O'Connor (1965) modified by Barker (1979).* ***(c)*** *The incompatible element ratios classification diagram of Winchester and Floyd (1977) modified by Pearce (1996), and adapted for plutonic rocks in this study.* ***(d)*** *The R_1 vs R_2 classification plot (after De La Roche et al., 1980), calculated from millication proportions.* ***(e)*** *The Quartz-Alkali Feldspar-Plagioclase (QAP) classification plot (after Streckeisen, 1974).*

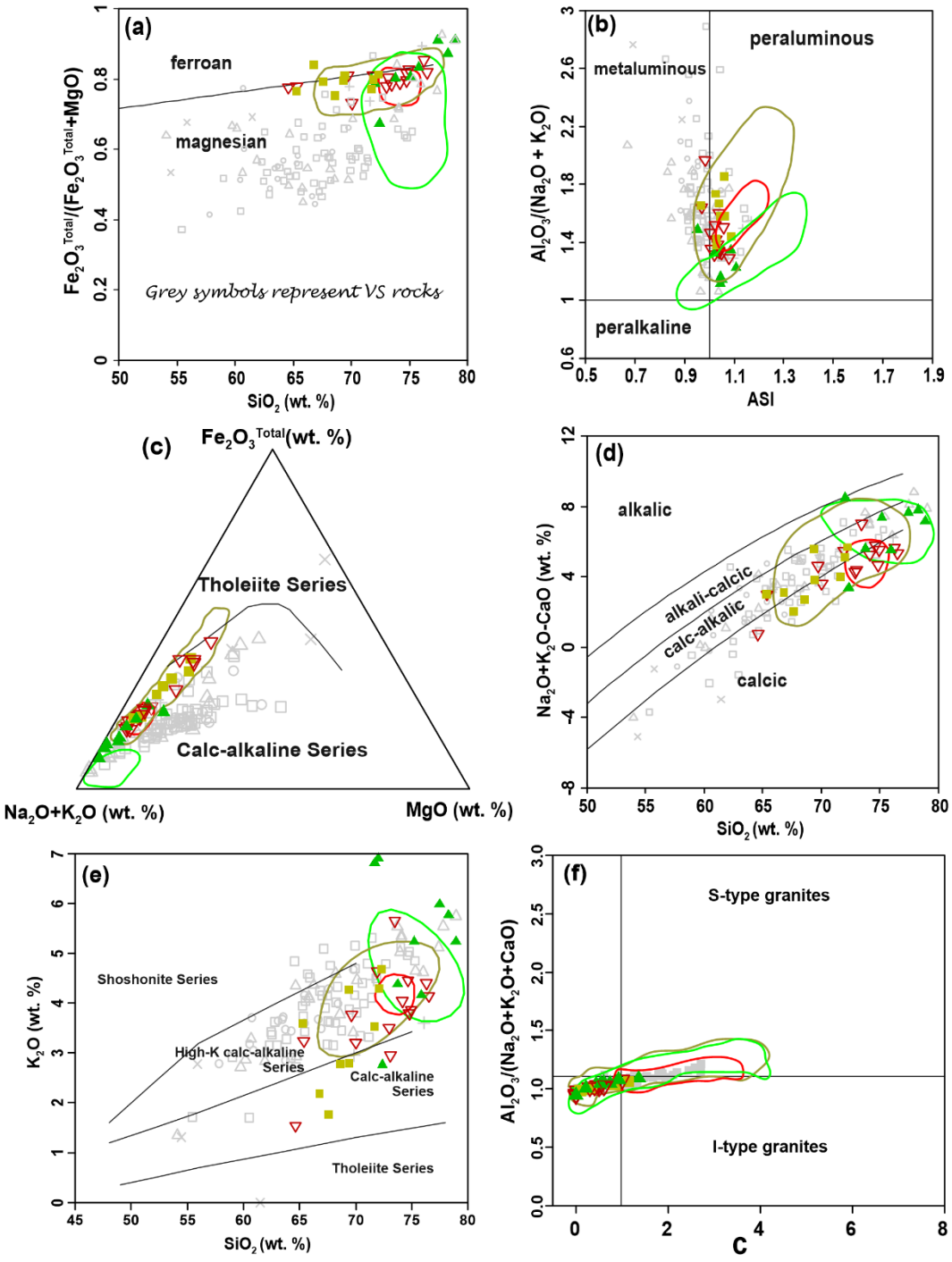

Fig. 5.6. *Characterization plots of the Gladkop and Vioolsdrif Suite igneous rocks.* ***(a)*** *$Fe_2O_3^T$ / ($Fe_2O_3^T$ + MgO) vs. SiO_2 (wt. %) plot differentiating between ferroan and magnesian plutons (after Frost et al., 2001).* ***(b)*** *molecular Al_2O_3 / (Na_2O + K_2O) vs. ASI plot differentiating between metaluminous, peraluminous and peralkaline rocks (after Frost et al., 2001).* ***(c)*** *The AFM classification (after Irvine and Barager, 1971).* ***(d)*** *Plot of MALI (Na_2O + K_2O - CaO) vs. SiO_2 differentiating between alkalic, alkali-calcic, calc-alkalic and calcic rocks (after Frost et al., 2001).* ***(e)*** *The K_2O vs. SiO_2 classification (after Peccerillo and Taylor, 1976).* ***(f)*** *The Al_2O_3 / (CaO + Na_2O + K_2O) vs. normative corundum (C) variation diagram distinguishing between I- and S-type granitic rocks (after Chappell and White, 1974). Symbols are the same as in Figs. 5.3 and 5.5.*

Sr, Rb, and particularly Ba, vary over a wide range in the GS rocks, with Sr and Rb showing good covariations and decrease with increasing silica (Fig. 5.4). The GS gneisses show a range in Rb concentrations between 100 and 2500 ppm, but different ranges of Rb/Sr ratios (Table 5.2), least in the STK Gneiss (mean = 0.70) and highest in the NNM Gneiss (mean = 3.19). While the NNM Gneiss shows ratios between 0.74 and 7.45, the Rb/Sr ratios for the STK and BWB gneisses range between 0.28 and 1.49 (Table 5.2). Except for the undifferentiated VS rocks, the Rb/Sr ratios for the VS rocks (mean = 0.16-0.50) are lower than those of the GS rocks, suggesting that both suites are petrogenetically unrelated. The STK Gneiss shows the largest range in K/Rb values, ranging from 117 to 230 (mean = 183; Table 5.2; Fig. 5.7f), while the BWB Gneiss shows values ranging from 181 to 240 (mean = 215; Table 5.2; Fig. 5.7f) and the NNM Gneiss values ranging from 174 to 274 (mean = 229; Table 5.2; Fig. 5.7f). According to Shaw (1968), these ratios are typical in unmetamorphosed granitic rocks (mean = 200), but because most of the GS samples fall above the 200 slope (Fig. 5.7f) it would suggest some deletion of Rb has occurred in these rocks. The VS rocks have K/Rb values ranging from as low as 0.97 to 387.54 (mean = 147.88 - 387.40; Fig. 5.7f). Most VS samples plot on slopes higher than K/Rb = 200, suggesting considerable depletion. The SiO_2-Rb plot is characterized by a scattered positive trend in both the VS and GS rocks (Fig. 5.4). The Rb/Cs ratios for the GS gneisses are higher than the UCC ratios (Rb/Cs=17; Rudnick and Gao, 2003; or 23; Wedepohl, 1995; or even 30; Taylor and McLennan, 1985). The Rb/Cs ratios for the NNM Gneiss vary between 129 and 600, while the STK and BWB gneisses both range between 35 and 200, suggesting some crustal (and likely upper crustal) influence. The LIL element ratios, together with low Cs values (0.5-3.5 ppm) support element mobility, and possibly fluid loss (Janoušek et al., 2004 and references therein).

On the multi-element diagrams (Fig. 5.8a, c), the NNM Gneiss shows the highest enrichment in Rb and K relative to the STK and BWB gneisses, but the highest depletion in Ba, Sr and P, with respect to both the primitive mantle and the average continental crust. In the GS gneisses, HREE enrichment, with respect to the average crust, is greater relative to LFS enrichment (Fig. 5.8c). The trends shown by the LFS elements in the GS metagranitoids on the multi-element diagrams are variable. The depletions in Ba and Sr (Fig. 5.8a, c) could suggest fractionation of feldspars (notably plagioclase) or magma generated by melting of a plagioclase-poor source rock, while P depletion could be linked to fractionation of apatite (Rollinson, 1993). There are negative Nb and Ti anomalies observed in the GS rocks, geochemical indicators of subduction-related environments (Pearce, 2008). Negative Nb anomalies are also characteristic of the continental crust and may be an indicator of crustal involvement in the magma process (Rollinson, 1993). McCulloch and Gamble (1991) attributed Nb and Ti anomalies in rocks to the presence of rutile at the site of melting. The Ti anomaly could also be related to the fractionation of Fe oxides. The HFS elements also show variable trends in the GS rocks, with depleted U concentrations and elevated Th, Pb, and Y concentrations relative to the UCC (Fig. 5.8a, c).

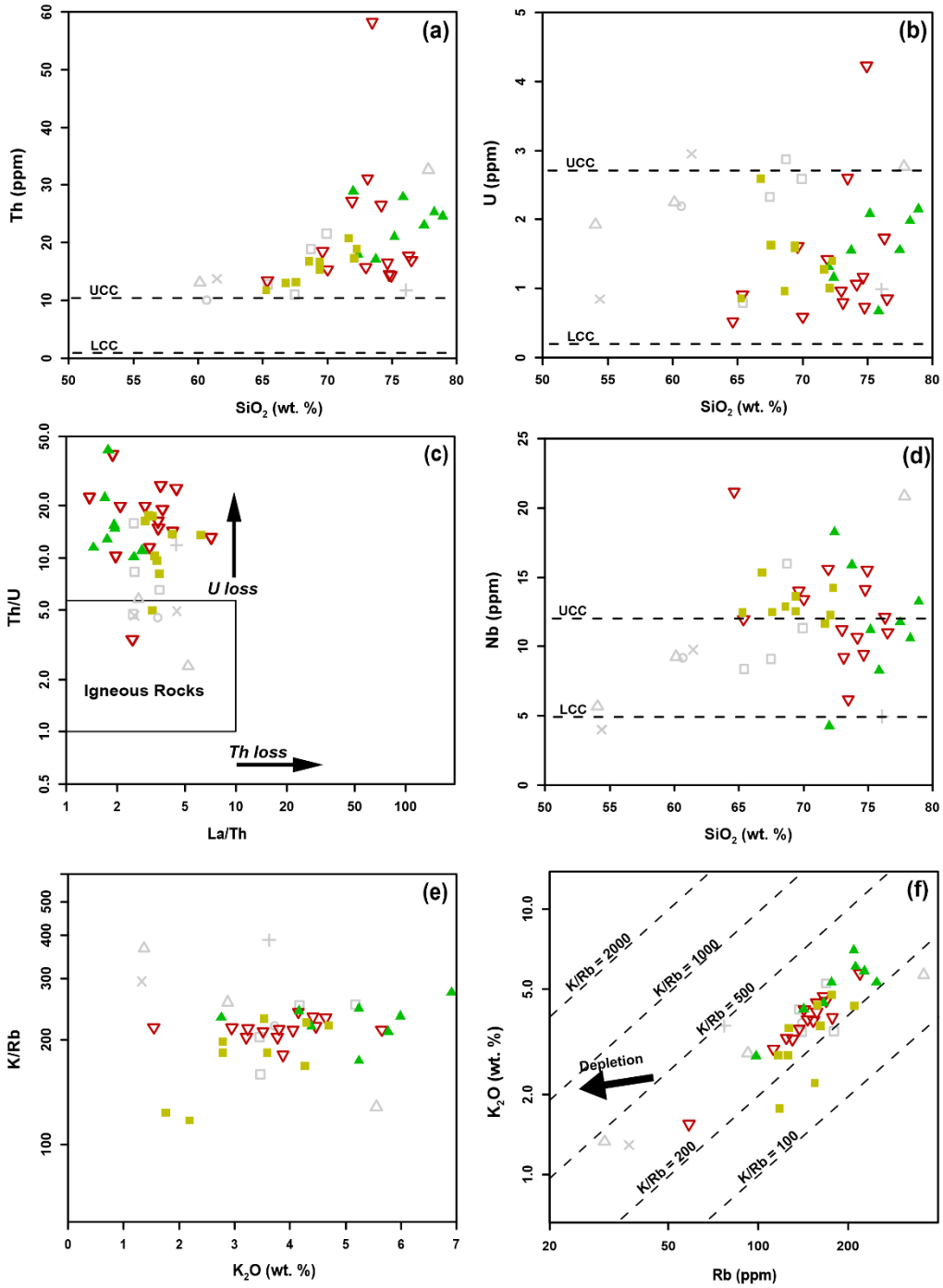

Fig. 5.7. *Trace element plots of the Gladkop Suite and Vioolsdrif Suite rocks.* ***(a)*** *SiO_2 (wt. %) vs. Th (ppm).* ***(b)*** *SiO_2 (wt. %) vs. U (ppm).* ***(c)*** *La/Th vs. Th/U; The box on the left represents field of common igneous rocks (after Rudnick et al., 1985). The negative correlation is simply a function of Th being plotted on both axes. Samples plotting above the box have lost U relative to Th. Samples plotting to the right have lost both U and Th.* ***(d)*** *SiO_2 (wt. %) vs. Nb (ppm).* ***(e)*** *K_2O (wt. %) vs. Log [K/Rb]. In general, K/Rb ratios for the Vioolsdrif Suite gneisses decrease with increasing K_2O content, but increases in the Gladkop Suite gneisses.* ***(f)*** *Log [K_2O (wt. %)] vs. Log [Rb (ppm)]; K represents the concentration of K in ppm, calculated from the oxide. Depletion trends with K/Rb > 500 is taken from Janoušek et al. (2004). UCC and LCC concentrations sourced from Rudnick and Gao (2003). Symbols are the same as in Fig. 5.3.*

The VS rocks show similar primitive mantle-normalized trace-element patterns to the GS rocks, except for Ba concentrations which are higher in the VS rocks (Fig. 5.8a, c). The GS rocks are also more enriched in the HREE relative to the VS rocks (Fig. 5.8a, c). The VS rocks show the negative Nb, Ti and P anomalies typical of volcanic arc magmas (Pearce, 2008). The AFM plot (Fig. 5.6c), however, highlights a more continental magmatic arc signature for the GS rocks. The average continental crust-normalized trace element patterns (Fig. 5.8c) are similar to the those of the primitive mantle-normalized spider (trace element) diagram (Fig. 5.8a, c).

The primitive mantle-normalized REE patterns are similar to those of fractionated granitic rocks, showing a moderate to weak enrichment in the LREE [$(La/Yb)_N$ = 2.72-82.3; Figs. 5.8b; 5.9d] and a negative Eu anomaly ($Eu/Eu^* = Eu_N/[(Sm_N)(Gd_N)]^{1/2}$ = 0.25-0.83; Table 5.3; Figs. 5.8b; 5.9a). This negative anomaly in felsic magmas is commonly attributed to the crystal fractionation of feldspars (plagioclase and K-feldspar) from a felsic melt, or in magma produced by partial melting of sources which retain feldspars (Rollinson, 1993). The NNM Gneiss shows a lower Eu anomaly (mean Eu/Eu* = 0.48; Table 5.3; Fig. 5.8a, b). The STK Gneiss is more enriched in the MREE relative to the LREE and HREE, and is attributed to the presence of significant concentrations of hornblende (Rollinson, 1993) in the STK Gneiss (also evident in the lithology and petrographic descriptions; Section 4.2). The STK Gneiss shows the highest fractionation in the HREE [mean $(Gd/Yb)_N$ = 1.89; Table 5.3], while the NNM Gneiss shows the least [mean $(Gd/Yb)_N$ = 3.55; Table 5.3; Figs. 5.8b; 5.9c]. The NNM Gneiss shows the least enrichment in the LREE [mean $(La/Sm)_N$ = 3.99; Table 5.3; Fig. 5.9b] compared to the BWB and STK gneisses (mean = 4.31 and 4.18 respectively; Table 5.3). Generally, in the GS gneisses, the HREE are more fractionated relative to the LREE [$(La/Yb)_N$ = 2.72 - 82.3; Table 5.3]; with the STK Gneiss showing the least fractionation [mean $(La/Yb)_N^{STK}$ = 12.91; Table 5.3], and the NNM Gneiss showing the most fractionation [mean $(La/Yb)_N^{NNM}$ = 27.41; Table 5.3] (Fig. 5.9d). The REE compositions of the VS and the GS define similar, coherent patterns on the primitive mantle-normalized REE plot (Fig. 5.8b). The patterns agree well with that of typical UCC, with moderate LREE enrichment and moderate Eu anomalies with increasing LREE/HREE.

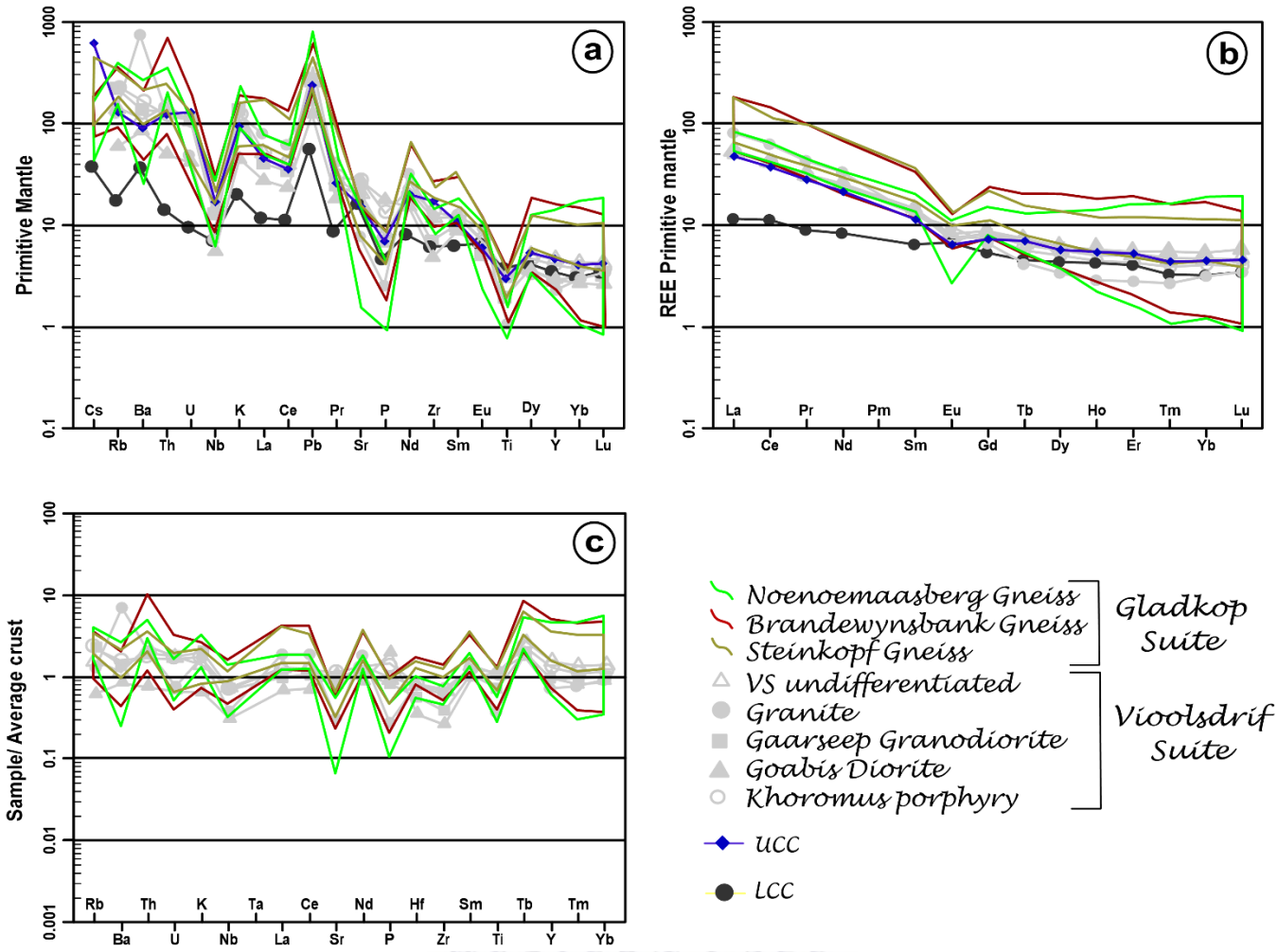

Fig. 5.8. *Representative REE and multi-element plots comparing the Gladkop Suite orthogneisses to the Vioolsdrif Suite rocks, and to UCC and LCC values.* ***(a)*** *Primitive mantle-normalized multi-element plot (normalized after Sun and McDonough, 1989).* ***(b)*** *Primitive mantle-normalized REE plot (normalized after McDonough and Sun, 1995).* ***(c)*** *Average continental crust - normalised multi-element plot (after Weaver and Tarney, 1984). Average UCC and LCC compositions shown for comparison (sourced from Rudnick and Gao, 2003).*

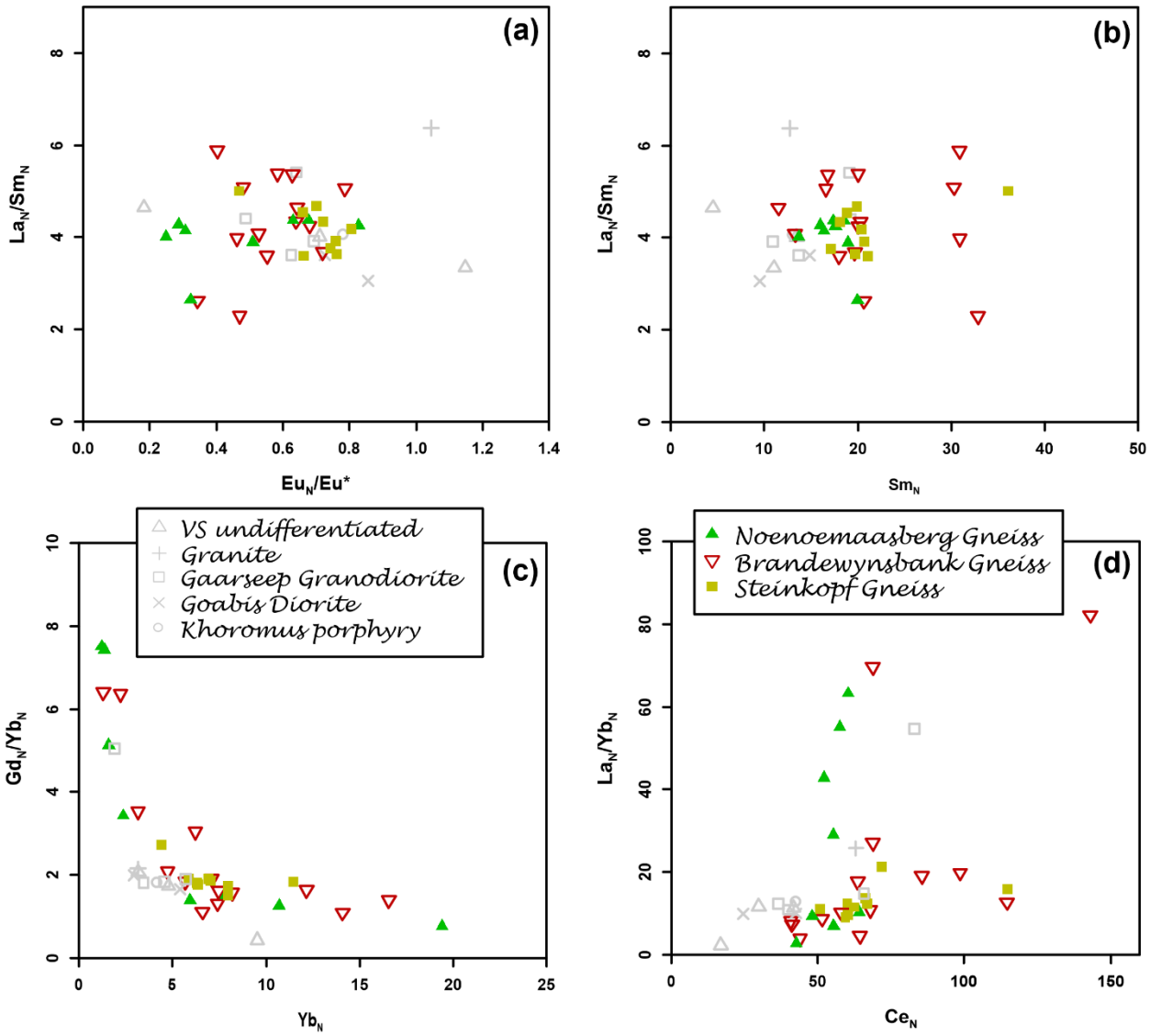

Fig. 5.9. *Primitive mantle-normalized REE fractionation diagrams of the Gladkop and Vioolsdrif Suite rocks.* ***(a)*** *Light REE fractionation with changing Europium anomaly.* ***(b)*** *Light REE,* ***(c)*** *Heavy REE, and,* ***(d)*** *Total REE fractionations with changing REE contents.*

5.6. Tectonic settings

In an attempt to predict the tectonic settings of the highly deformed Palaeoproterozoic GS gneisses from geochemical criteria, multidimensional discrimination diagrams (Verma et al., 2012; 2013) were used. Twenty (20) multidimensional diagrams applicable to the GS gneisses were generated (Fig. 5.10) using the Tectonic Discrimination for Intermediate and Acid magmas (TecDIA) computer program (Verma et al. 2012, 2013; Verma and Verma 2013; Verma 2015). This computer program attempts to eliminate the 'constant sum problem of compositional data' by making use of log-ratio transformations, as proposed by Aitchison (1981, 1984, 1986), before calculating discriminant functions DF_1 and DF_2 from three categories of complex equations (Verma et al., 2006; Agrawal et al., 2008 and Verma and Agrawal, 2011; Verma, 2015). The three categories include: (1) major element data; (2) combined immobile major and trace element data; and (3) selected immobile trace element data. TecDIA then plots the computed values of DF_1 and DF_2 functions for each sample in 35 multidimensional diagrams (for both acid and intermediate rocks) with known tectonic field boundaries (Verma, 2015).

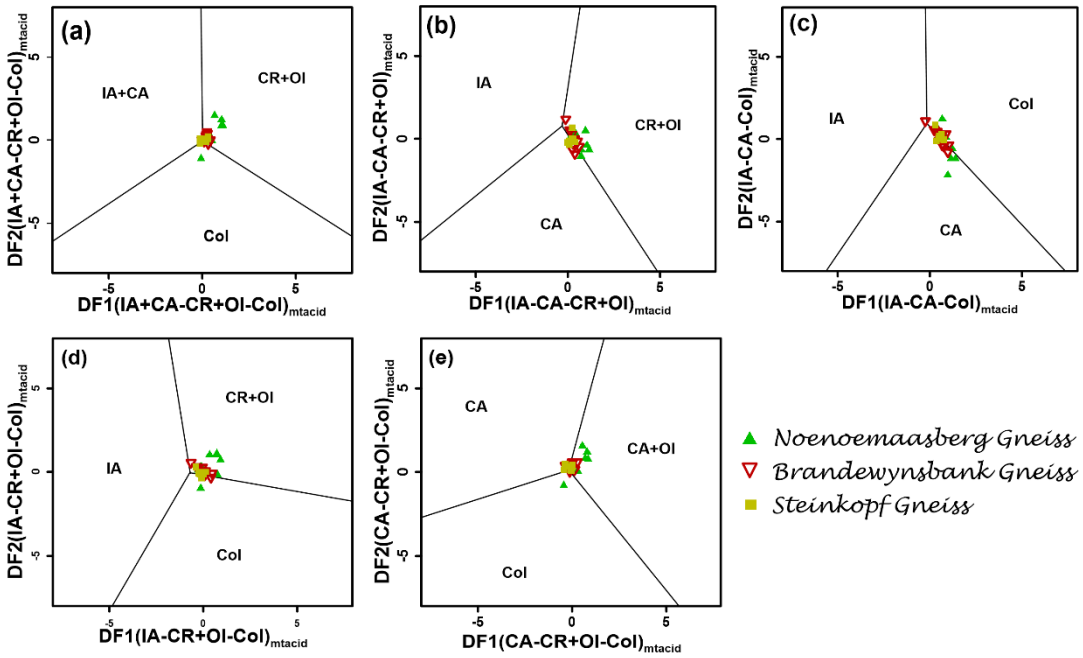

Fig. 5.10. *Felsic (acid) rock samples of the Gladkop Suite plotted in the set of combined immobile major and trace element-based (hence subscript mtacid) multidimensional diagrams of Verma and Verma (2013) for the discrimination of island-arc (IA), continental-arc (CA), within-plate (CR + OI), and collisional (Col) tectonic settings. CR-continental rift; OI-ocean island. Tectonic field boundaries which separate three tectonic settings are shown.* ***(a)*** *IA + CA – CR + OI – Col that separates three fields of combined arc, within-plate, and collision;* ***(b)*** *IA – CA – CR + OI that separates three fields of island arc, continental arc, and within-plate;* ***(c)*** *IA – CA – Col that separates three fields of island arc, continental arc, and collision;* ***(d)*** *IA – CR + OI – Col that separates three fields of island arc, within-plate, and collision, and* ***(e)*** *CA – CR + OI – Col that separates three fields of continental arc, within-plate, and collision.*

After estimating the number of samples plotting in the individual tectonic fields in all thirty-five (35) diagrams, TecDIA calculates the probability values for the tectonic environment of each sample (Verma and Agrawal, 2011; Verma, 2015) and the total percentage probability values synthesized are then interpreted. The calculated probabilities cannot be seen on the resulting diagrams (e.g. Fig. 5.10), however, they represent a graphical output of where the samples plot. A table of results is generated and displays calculated probability values for each tectonic setting, based on both Verma et al. (2012) (major elements only) and Verma et al. (2013) (all three sets of elements, namely: major elements, immobile major and trace elements combined and immobile trace elements). The complete tables generated for each of the GS gneisses can be found in Appendix E (Tables E1, 2 and 3).

According to the criteria given by both Verma et al. (2012) and Verma et al. (2013) for the various TecDIA plots, the major element compositions of the NNM Gneiss are more consistent with a transitional collision to within-plate tectonic setting, with roughly similar percentage probability values for each setting. The combined major and trace element set is more consistent with a within plate tectonic setting (Table 5.5), while the trace element diagram set are more consistent with a collisional tectonic setting (Table 5.5).

According to the Verma et al. (2013) TecDIA plots, major element compositions of the BWB Gneiss samples are more consistent with a transitional collision to within-plate tectonic setting with roughly equal percentage probability values for each setting (Table 5.5). Two samples were not used in these diagrams because their silica weight percentages are 64 % and 65 % (basic) and diagrams generated are applicable to acid (felsic) rocks. However, the major element diagram set of Verma et al. (2012) is consistent with a within-plate tectonic setting (Table 5.5). The combined major and trace element diagram set are more consistent with a within-plate tectonic setting (Table 5.5), while the trace element diagram set are more consistent with a collisional tectonic setting (Table 5.5).

The STK Gneiss shows a different tectonic setting to the BWB and NNM gneisses. The major element diagram set of Verma et al. (2012) are consistent with a within-plate tectonic setting, while the same diagram set of Verma et al. (2013) do not show any meaningful results because the samples were roughly equally distributed in the collision, within-plate and island arc settings (Table 5.5). The combined major and trace element diagram set are consistent with a transitional continental arc to within-plate setting (Table 5.5). The trace element diagram set are more consistent with a transitional continental arc to collision tectonic setting (Table 5.5). If it is believed that the GS gneisses intruded during the Orange River Orogeny, then the transitional tectonic setting could be plausible.

Table 5.5.*Application of multidimensional diagrams to the Palaeoproterozoic (~1.8 Ga) felsic rocks of the Gladkop Suite.*

Lithology	Tectonic diagram	{Number of discriminated samples} {Sum of probability values} [Total percentage probability values for samples]					(Set of elements whose log-ratios are calculated) (Plots used)
		Arc			CR	Col	
		IA+CA	IA	CA			
BWB Gneiss	{Σn} {Σprob} [%prob]	{0} {0} [0%]	{0} {0} [0%]	{3} {1.5149} [4%]	{38} {29.6189} [64%]	{19} {14.8579} [32%]	(Major elements) (Verma et al., 2012)
	{Σn} {Σprob} [%prob]	{0} {0} [0%]	{0} {0} [0%]	{0} {0} [0%]	{30} {23.4316} [52%]	{30} {21.4696} [48%]	(Major elements) (Verma et al., 2013)
	{Σn} {Σprob} [%prob]	{0} {0} [0%]	{1} {0.3946} [1%]	{5} {2.5411} [8%]	{43} {22.3298} [72%]	{11} {5.6527} [19%]	(Major and Trace elements) (Verma et al., 2013)
	{Σn} {Σprob} [%prob]	{0} {0} [0%]	{0} {0} [0%]	{15} {11.9435} [27%]	{3} {1.8288} [5%]	{42} {29.7920} [68%]	(Trace elements) (Verma et al., 2013)
NNM Gneiss	{Σn} {Σprob} [%prob]	{0} {0} [0%]	{0} {0} [0%]	{2} {1.3363} [4%]	{19} {15.2418} [48%]	{19} {14.8737} [48%]	(Major elements) (Verma et al., 2012)
	{Σn} {Σprob} [%prob]	{0} {0} [0%]	{2} {1.4328} [4%]	{0} {0} [0%]	{21} {17.1320} [52%]	{17} {14.4047} [44%]	(Major elements) (Verma et al., 2013)
	{Σn} {Σprob} [%prob]	{0} {0} [0%]	{0} {0} [0%]	{5} {2.9712} [11%]	{27} {19.3161} [70%]	{8} {5.1996} [19%]	(Major and Trace elements) (Verma et al., 2013)
	{Σn} {Σprob} [%prob]	{0} {0} [0%]	{0} {0} [0%]	{6} {5.4198} [16%]	{6} {4.2724} [13%]	{28} {23.1768} [71%]	(Trace elements) (Verma et al., 2013)
STK Gneiss	{Σn} {Σprob} [%prob]	{0} {0} [0%]	{3} {1.8910} [6%]	{5} {3.5817} [11%]	{26} {22.3591} [68%]	{6} {4.7942} [15%]	(Major elements) (Verma et al., 2012)
	{Σn} {Σprob} [%prob]	{0} {0} [0%]	{10} {7.8866} [27%]	{1} {0.3967} [1%]	{14} {10.1474} [35%]	{15} {10.6866} [37%]	(Major elements) (Verma et al., 2013)
	{Σn} {Σprob} [%prob]	{3} {1.1482} [---]	{0} {0} [0%]	{14} {7.3094} [42%]	{18} {8.8233} [45%]	{5} {2.5230} [13%]	(Major and Trace elements) (Verma et al., 2013)
	{Σn} {Σprob} [%prob]	{0} {0} [0%]	{0} {0} [0%]	{20} {14.2919} [53%]	{1} {0.5029} [2%]	{19} {12.3379} [45%]	(Trace elements) (Verma et al., 2013)

IA−island arc; **CA**−continental arc; **IA+CA**–combined island and continental arcs, i.e., arc setting; **CR**−continental rift; **OI**−ocean island; **CR+OI**–combined continental rift and ocean island, i.e., within-plate (WP) setting; **Col**−collision; the probability estimates for all samples discriminated in a given tectonic setting are reported in [ ], the values are rounded mostly following the indications put forth by Verma (2005); the rows give a synthesis of results as {Σn} {Σprob} [%prob], where {Σn} is the total number of samples or data points plotting in all five diagrams is reported in the column of total number of samples, whereas the sum of samples plotting in a given tectonic field is reported in the respective tectonic field column; {Σprob} is the sum of probability values for all samples plotting in a given tectonic field is reported in the respective tectonic field column; and [%prob] is the total probability of a given tectonic setting expressed in percent after assigning the probability of IA + CA to IA and CA (using weighing factors explained in Verma and Verma, 2013).

5.7. Summary

- The association (covariance) between major elements is strongest in the BWB Gneiss and weakest in the STK Gneiss. In the GS gneisses, positive covariances support the association/coexistence of the elements Fe-Mg-Mn-P-Ca, suggesting a mineral assemblage of major ferromagnesian minerals and accessory phases (such as apatite) is controlling the composition of the GS gneisses. This positive association, together with the negative covariances with K, indicate an inverse relationship between a potassic phase (such as K-feldspars) and Fe, Mg, Mn, P and Ca. The significant positive covariance between the pairs Ca-P, Ni-Fe, Ni-Mg, Ni-Mn, together with the negative covariance between P and Ce, La and Th (Appendix C) suggests the importance of apatite and magnetite as the main accessory phases controlling the chemistry of the GS gneisses, and rules out monazite as a possibility. The association between Ba and Sr is stronger in the NNM Gneiss relative to the BWB and STK gneisses, least in the latter, suggesting a greater influence of plagioclase in the NNM Gneiss chemistry. The consistent significant positive covariance between Ca and Mg in all of the GS lithologies suggests the importance of pyroxenes, specifically more clinopyroxene, in the source region.
- The GS experienced several different magmatic processes, based on correlation coefficient patterns (Fig. 5.1), possibly fractional crystallization and PAE.
- Based on the amount of scatter on plots of major elements vs. SiO_2, the major elements (except Na and K) probably behaved in a less mobile way during metamorphism.
- The STK Gneiss is granitic to granodioritic, while both the BWB and NNM gneisses are granitic (Fig. 5.5).
- Relative to the GS gneisses, the VS rocks have higher K, Mg and Al, but lower total Fe and Ti contents. Although both the GS and VS rocks show similar trends on $Fe_2O_3^T$ and MgO vs. SiO_2 plots, the VS rocks show a steeper slope in the former and a shallower slope in the latter. For MgO and Fe_2O_3 (Al_2O_3 to a lesser extent) vs. SiO_2 plots (Fig. 5.3), an inflexion occurs between the trends formed by the STK and NNM samples.
- Both the GS and VS rocks are magnesian, metaluminous to slightly peraluminous, calcic to calc-alkalic, generated in a high-K calc-alkaline magma series and show I-type granite characteristics (Fig. 5.6a-f).
- A few differences occur between the data for this study and the literature data evident from the differences in the spread between the two sets of data. Note should be taken that some of the differences observed could be as a result of using data sets obtained from different laboratories and measured using different analytical equipment.
- The GS rocks exhibit a general fractional crystallization trend as indicated by decreasing Al_2O_3, CaO, $Fe_2O_3^T$, MgO, TiO_2, Na_2O, P_2O_5, Ba and Sr with increasing SiO_2 (Figs. 5.3, 5.4). The moderate to strong covariance of CaO, Al_2O_3, K_2O, Rb and Sr relative to SiO_2 is compatible with biotite, plagioclase and K-feldspar crystallization. The strong linear relationship between Ba and Sr (Fig. 6.7) does, however, suggest simultaneous plagioclase and K-feldspar crystallization. Constant Nb and a slight increase in Th contents (Fig. 5.7) is consistent with the absence of titanite fractionation, whereas a decrease in Zr with increasing SiO_2 indicates zircon fractionation. Low CaO and Sr values suggest that plagioclase was partly residual during melting, or that the source was depleted in plagioclase, possibly during previous melting episodes. The generally large data scatter in mobile elements such as Rb, Sr and Ba (Fig. 5.4) indicate considerable alteration during metamorphism or weathering.

- The GS gneisses have elevated K_2O compositions relative to the UCC, as well as high Ba, Rb, La, Sm and Y compositions (Figs. 5.3, 5.4), possibly highlighting the effects of fractional crystallization during magma evolution. However, these metagranitoids have lower MgO, TiO_2, Al_2O_3, CaO, Na_2O, P_2O_5, Co and Sr compositions relative to the UCC (Figs. 5.3, 5.4). The GS gneisses have higher concentrations of incompatible elements relative to the VS rocks, suggesting the latter represents less fractionated rocks in comparison to the GS.
- The GS gneisses are generally enriched in the light REE. The STK Gneiss is enriched in the heavy REE (Fig. 5.8), suggesting it is slightly less fractionated, while the NNM and BWB gneisses have average UCC compositions. The REE compositions of the VS and the GS define similar, coherent patterns on the primitive mantle-normalized plot (Fig. 5.8b). The patterns agree well with that of typical UCC, with moderate LREE enrichment and moderate Eu anomalies with increasing LREE/HREE.
- The BWB and NNM gneisses are consistent with a transitional tectonic setting, from collisional to within plate, while the STK Gneiss is consistent with a transitional tectonic setting, from continental arc to collisional to within plate.

CHAPTER 6

RADIOGENIC ISOTOPE GEOCHEMISTRY

6.1. Introduction

This chapter presents radiogenic isotope data for the GS gneisses. The isotope systems analysed include Rb-Sr, Sm-Nd, U-(Th)-Pb and Lu-Hf systems. Previous data on the GS (Barton, 1983) and VS (Macey et al., 2017) rocks are provided for the sake of comparison, and additional U-Pb and Lu-Hf data (P. Macey, pers. comm., 2018) on the GS is also presented. The locations of the samples analysed are shown in Fig. 6.1.

6.2. Rb (-Sr) and Sm (-Nd) systems

The main aim of this section is to use radiogenic isotopes (Nd and Sr) to determine the source region(s) of the GS granitic gneisses (petrogenesis). The source(s) of these gneisses are also compared to the sources of the VS magmas. The radiogenic isotopic signatures are used to determine magma sources because magmas (and the subsequent rock they produce) inherit isotope ratios characteristic of the sources from which they were produced, which remain unchanged during differentiation (e.g. fractionation) and metamorphic processes (Rollinson, 1993). The isotope ratios remain unchanged because the mass difference between the isotope pair is too small for them to be fractionated by processes controlled by crystal-liquid equilibria.

In determining the parent magma source characteristics, using Nd and Sr ratios, the significance of any role played by mixing of components from different sources (such as through contamination), in the formation of the gneisses of the GS, was considered. The application of Sr data is, however, limited, due to the relative mobility of Sr in the GS gneisses (Section 5.3). Radiogenic isotope data were acquired using an HR mass spectrometer, as described in Chapter 3. Data management, recalculation, plotting, and statistical evaluation were performed using the GeoChemical Data ToolKIT (GCDkit) computer program (Janoušek et al., 2006).

Sm and Nd have similar incompatible characteristics (Nd is, however, slightly less compatible) and are not significantly fractionated within the continental crust by metamorphic processes and thus preserve the parent/daughter ratio of their source region (Rollinson, 1993). This makes them more useful in predicting petrogenetic processes than Rb and Sr which show very different characteristics (Rb is significantly more incompatible compared to Sr) between the pair and are thus strongly fractionated from one another. Rb and Sr are easily separated so that there is extreme fractionation between the crust and mantle leading to the accelerated Sr isotope evolution in the crust relative to the mantle. Within the continental crust, Rb and Sr are further separated by remelting, metamorphism and sedimentation, for Sr is partitioned into, and retained by plagioclase, whereas Rb is preferentially partitioned into the melt or fluid phase (Rollinson, 1993).

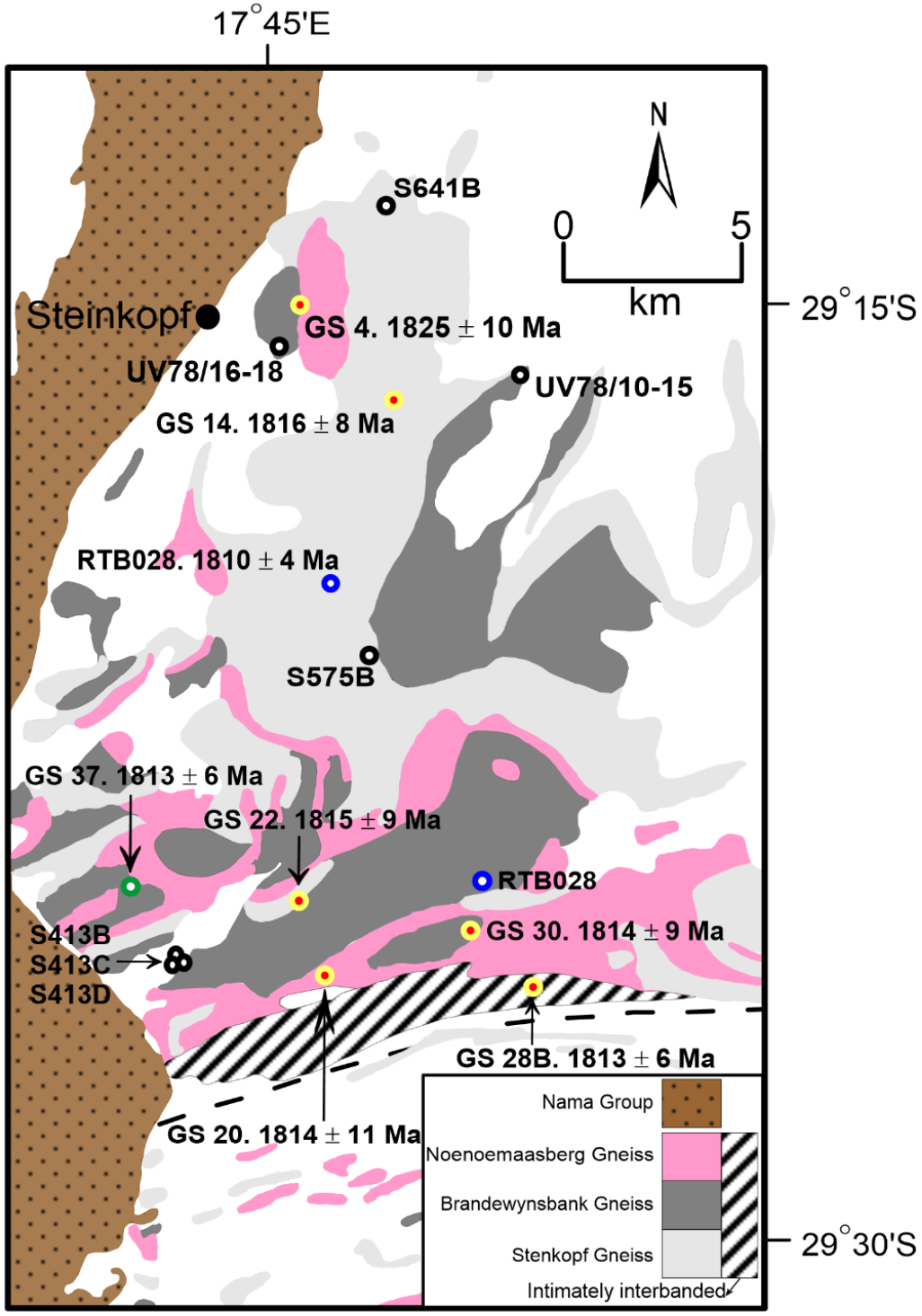

Fig. 6.1. *Locations of samples analysed for isotopic signatures across the Gladkop Suite. Sample numbers and U-Pb zircon ages are shown.* ***Yellow circles****: samples with Rb (-Sr), Sm (-Nd) and U-Pb isotopic data (this study).* ***Blue circles****: samples with U-Pb and Lu-Hf isotopic data (P. Macey, pers. comm., 2018).* ***Green circle****: samples with only U-Pb isotopic data (this study).* ***Black circles****: samples with only Rb (-Sr) isotopic data (Barton, 1983).*

6.2.1. Rb-Sr isotopic signature

The newly measured Sr-isotopic ratios for the GS samples (this study) show relatively high values ($^{87}Sr/^{86}Sr$: 0.738 - 0.811; Table 6.1), with the NNM samples showing the highest ratios ($^{87}Sr/^{86}Sr$: 0.771 - 0.811; Table 6.1). The isotopic ratios measured by Barton (1983) are similarly high, with $^{87}Sr/^{86}Sr$ values of 0.735 - 0.782 (Table 6.1). The STK samples generally have the lowest measured Sr-isotopic ratios both for this study ($^{87}Sr/^{86}Sr$: 0.738 - 0.744; Table 6.1) and those measured by Barton (1983) ($^{87}Sr/^{86}Sr$: 0.735 - 0.782; Table 6.1). The BWB samples for this study have measured Sr-isotopic ratios of 0.739 - 0.782 (Table 6.1), while the samples from Barton (1983) have Sr-isotopic values ranging from 0.775 to 0.779 (Table 6.1). These ratios demonstrate isotopic disequilibrium between the STK, BWB and NNM gneisses. Generally, the initial $^{87}Sr/^{86}Sr$ ratios for the GS gneisses are positively correlated with SiO_2 (Fig. 6.2c). This is interpreted as a significant crustal contribution to the GS magmas.

The significance of the individual Sr-isotopic ratios should not be overestimated since the system is known to be prone to resetting by metamorphism. Nonetheless, the measured Sr-isotopic ratios of the GS rocks yield relatively high calculated initial ratios ($^{87}Sr/^{86}Sr_i$), between 0.7055 and 0.7192 (Table 6.1). These ratios are comparable to crustally derived granites typically characterized by high initial ratios ($^{87}Sr/^{86}Sr_i > 0.7040$), or magmas contaminated by crustal material (Rollinson, 1993; Dickinson, 2018).

6.2.2. Sm-Nd isotopic signature

The GS and VS samples generally show low Sm/Nd ratios (GS: 0.17-0.19; VS: 0.16-0.27) which in turn yield low present-day $^{143}Nd/^{144}Nd$ ratios (GS: 0.511400 - 0.511553; VS: 0.511332 - 0.512264; Table 6.2). The $\varepsilon_{Nd(t)}$ value represents a measure of the deviation of the $^{143}Nd/^{144}Nd$ ratio of a sample from that of CHUR (chondritic uniform reservoir) at the time of crystallization (Rollinson, 1993). The age of crystallization of the GS rocks was taken as 1820 Ga, from literature, for the purpose of $\varepsilon_{Nd(t)}$ calculations, hence $\varepsilon_{Nd(1820)}$.

On the $\varepsilon_{Nd(t)}$ vs. $^{87}Sr/^{86}Sr_i$ plot (Fig. 6.2a), the STK and BWB gneisses form generally subparallel trends. They run along a steep negatively sloping diagonal with $^{87}Sr/^{86}Sr_i$ values for both the BWB and STK samples being similar (0.7061 - 0.7062 and 0.7086 - 0.7094 respectively, Fig. 6.2a). The NNM samples form a diagonal trend running from higher $^{143}Nd/^{144}Nd$ and lower $^{87}Sr/^{86}Sr$ ratios, to lower $^{143}Nd/^{144}Nd$ ratios and more radiogenic Sr isotopic compositions (Fig. 6.2a). Except for one NNM Gneiss sample (GS 20), these initial radiogenic Sr compositions are typical of common granitic rocks and the fields they form on the $\varepsilon_{Nd(1820)}$ vs. $^{87}Sr/^{86}Sr_i$ plot suggest the parent magmas originated from the upper continental crust. Furthermore, the GS samples generally plot below the "mantle array"/CHUR curve, at the enriched end (Fig. 6.2a), suggesting a slightly enriched source.

On the $\varepsilon_{Nd(1820)}$ vs. age (also known as the epsilon-time or the mantle evolution) plot (Fig. 6.2b), the GS samples generally plot below the CHUR line (negative ε_{Nd} values), and, the bulk of the VS samples have predominantly negative ε_{Nd} values (Fig. 6.2b). This suggests that both the VS and GS rocks are largely lower crustal to crustally derived (a mildly to relatively enriched source). The negative $\varepsilon_{Nd(t)}$ values imply a lower $^{143}Nd/^{144}Nd$ composition of the magma source(s), relative to that of CHUR at the time of crystallization.

Although the GS gneisses show a limited range in ε_{Nd} values close to the bulk Earth, the NNM Gneiss samples show the most negative values (-4.69 and -3.14; Table 6.2; Fig. 6.2). The STK and BWB gneisses show values which are similar and less negative (-2.02 and -0.53; -2.09 and -1.39; Table 6.2; Fig. 6.2). The VS rocks similarly show a limited range in ε_{Nd} values close to CHUR (-3.19 to 0.53; Table 6.2; Fig. 6.2b, d). The negative ε_{Nd} values observed for the VS rocks are reflected by high mean crustal residence ages (T_{DM}: two-stage depleted-mantle Nd model ages; Liew and Hofmann, 1988). The model ages for the GS gneisses are similarly high, with T_{DM} values ranging from 2.3 to 2.7 Ga and T_{CHUR} values ranging between 1.9 and 2.3 Ga (Table 6.2; Fig. 6.2b). Model ages for the VS rocks fall in a narrow range with the majority of T_{DM} ages ranging between 2.2 and 2.4 Ga (Table 6.2; Fig. 6.2b). The colinear trend from the VS rocks through the GS gneisses, together with their 2.3-2.7 Ga T_{DM} values, suggest that the GS granitoid gneisses represent a reworking of Palaeoproterozoic-aged crust, possibly reworking of the VS material.

Table 6.1. *Rb-Sr concentrations and isotope ratios for the GS rocks. Methods used to calculate ratios were taken from Rollinson (1993).*

Sample No.	Latitude	Longitude	Domain	Rock type/ Lithology	Suite	Rb (ppm)	Sr (ppm)	$^{87}Sr/^{86}Sr$ (Meas.)	$^{87}Sr/^{86}Sr$ Initial (Calc.)	$^{87}Rb/^{86}Sr$ (Calc.)	±2s int. (Sr)	Age (Ga)	Reference
GS 4	-29.2521	17.7523	NBD	NNM	GS	209.65	283.60	0.770585	0.7192	1.9636	19	1.820	This study
GS 14	-29.2737	17.7891	NBD	STK	GS	126.15	332.00	0.738257	0.7118	1.0093	13	1.820	This study
GS 20	-29.4337	17.7702	NBD	NNM	GS	176.65	118.65	0.810541	0.7070	3.9547	19	1.820	This study
GS 22	-29.4523	17.7407	NBD	STK	GS	116.75	251.20	0.743930	0.7116	1.2345	13	1.820	This study
GS 28B	-29.4307	17.8325	NBD	BWB	GS	125.50	291.55	0.738802	0.7089	1.1434	14	1.820	This study
GS 30	-29.4200	17.8133	NBD	BWB	GS	177.25	177.90	0.782257	0.7130	2.6465	21	1.820	This study
S413B	-29.4233	17.7233	NBD	STK	GS	138.00	294.00	0.741000	0.7084	1.9683		1.820	Barton (1983)
S413C	-29.4233	17.7233	NBD	STK	GS	152.00	244.00	0.752000	0.7087	1.9975		1.820	Barton (1983)
S413D	-29.4233	17.7233	NBD	STK	GS	152.00	228.00	0.756000	0.7096	2.0081		1.820	Barton (1983)
S765J	-29.2133	17.7850	NBD	STK	GS	140.00	282.00	0.740000	0.7055	1.9656		1.820	Barton (1983)
S765K	-29.2083	17.7933	NBD	STK	GS	169.00	428.00	0.735000	0.7075	1.9523		1.820	Barton (1983)
S641B	-29.2217	17.8033	NBD	STK	GS	165.00	180.00	0.774000	0.7103	2.0559		1.820	Barton (1983)
S768E	-29.1917	17.8283	NBD	STK	GS	167.00	168.00	0.782000	0.7129	2.0772		1.820	Barton (1983)
S575B	-29.3417	17.7850	NBD	STK	GS	153.00	263.00	0.750000	0.7095	1.9922		1.820	Barton (1983)
UV78/10	-29.2667	17.8317	NBD	BWB	GS	168.00	174.00	0.779000	0.7119	2.0692		1.820	Barton (1983)
UV78/11	-29.2667	17.8317	NBD	BWB	GS	174.00	180.00	0.779000	0.7118	2.0692		1.820	Barton (1983)
UV78/12	-29.2667	17.8317	NBD	BWB	GS	168.00	186.00	0.775000	0.7122	2.0586		1.820	Barton (1983)
UV78/13	-29.2667	17.8317	NBD	BWB	GS	176.00	180.00	0.776000	0.7080	2.0613		1.820	Barton (1983)
UV78/14	-29.2667	17.8317	NBD	BWB	GS	218.00	244.00	0.775000	0.7129	2.0586		1.820	Barton (1983)
UV78/15	-29.2667	17.8317	NBD	BWB	GS	168.00	173.00	0.776000	0.7085	2.0613		1.820	Barton (1983)
UV78/16	-29.2617	17.7500	NBD	BWB	GS	159.00	174.00	0.776000	0.7125	2.0613		1.820	Barton (1983)
UV78/17	-29.2617	17.7500	NBD	BWB	GS	168.00	179.00	0.776000	0.7107	2.0613		1.820	Barton (1983)
UV78/18	-29.2617	17.7500	NBD	BWB	GS	160.00	175.00	0.775000	0.7114	2.0586		1.820	Barton (1983)

$^{87}Sr/^{86}Sr$ of the BHVO-2 standard is 0.703483 ± 11;
(0.703479 ± 20, Weis et al., 2006);
(0.703489 ± 44, long-term UCT average, n=124/exclude 6);
(0.703469 ±17, GEOREM).

$^{87}Sr/^{86}Sr$ of the ref NIST987 standard is 0.710255 ± 20 (P. le Roux, pers. comm., 2018; n=56).

Table 6.2. *Sm-Nd concentrations and isotope ratios for the GS and the VS rocks and calculated $\varepsilon_{Nd(t)}$ and model ages (at 1820 Ma and 1885 Ma respectively).*

Sample No.	Latitude	Longitude	Domain	Rock type/ Lithology	Suite	Sm (ppm)	Nd (ppm)	$^{143}Nd/^{144}Nd$ (Meas.)	$^{143}Nd/^{144}Nd$ Initial (Calc.)	$^{147}Sm/^{144}Nd$ (Calc.)	±2s int. (Nd)	$\varepsilon_{Nd(t)}$	Age (Ga)	$f^{Sm/Nd\ (DM)}$	T_{DM} (Ga)	T_{CHUR} (Ga)	Reference
GS 4	-29.2521	17.7523	NBD	NNM	GS	7.15	36.78	0.511450	0.510043	0.1175	11	**-4.69**	1.820	-0.470670	2.681	2.276	This study
GS 14	-29.2737	17.7891	NBD	STK	GS	8.40	45.50	0.511515	0.510180	0.1115	11	**-2.02**	1.820	-0.497670	2.429	2.003	This study
GS 20	-29.4337	17.7702	NBD	NNM	GS	7.54	42.40	0.511409	0.510122	0.1074	8	**-3.14**	1.820	-0.516178	2.487	2.091	This study
GS 22	-29.4523	17.7407	NBD	STK	GS	7.34	41.86	0.511525	0.510256	0.1060	12	**-0.53**	1.820	-0.522549	2.292	1.865	This study
GS 28B	-29.4307	17.8325	NBD	BWB	GS	8.05	43.43	0.511553	0.510212	0.1120	12	**-1.39**	1.820	-0.495351	2.385	1.946	This study
GS 30	-29.4200	17.8133	NBD	BWB	GS	14.66	86.65	0.511400	0.510176	0.1022	9	**-2.09**	1.820	-0.539547	2.383	1.990	This study
PM13052	-28.8903	19.2265	PD (RMA)	Bt granite augen gneiss	VS	5.48	34.17	0.511334	0.510132	0.0970	12	**-1.32**	1.885	-0.563063	2.259	1.987	Macey et al. (2017)
PM13025	-28.8235	19.1197	PD (RMA)	Hbl-Bt orthogneiss	VS	4.01	20.54	0.511552	0.510088	0.1180	10	**-2.14**	1.885	-0.468468	2.402	2.094	Macey et al. (2017)
PM13151	-28.7482	18.6054	PD (RMA)	Augen gneiss	VS	9.15	57.02	0.511332	0.510129	0.0970		**-1.35**	1.885	-0.563063	2.263	1.989	Macey et al. (2017)
PM13235	-28.8089	18.5059	PD (RMA)	Hbl-bt orthogneiss	VS	4.06	25.77	0.511332	0.510151	0.0952		**-0.92**	1.885	-0.571171	2.231	1.955	Macey et al. (2017)
CHM280	-28.7649	16.1469	VD (RMA)	Qtz monzonite gneiss	VS	5.31	30.94	0.511412	0.510125	0.1037		**-1.42**	1.885	-0.532883	2.290	2.003	Macey et al. (2017)
PM15195	-27.8981	16.8546	VD (RMA)	Granodiorite	VS	4.42	25.45	0.511416	0.510114	0.1049	10	**-1.70**	1.885	-0.527477	2.309	2.022	Macey et al. (2017)
PM13228	-28.8251	18.8496	PD (RMA)	Eq. granite gneiss	VS	7.66	45.08	0.511365	0.510091	0.1027		**-2.09**	1.885	-0.537387	2.330	2.056	Macey et al. (2017)
PM13152	-28.7482	18.6054	PD (RMA)	Eq. granite gneiss	VS	6.89	26.11	0.512028	0.510049	0.1595		**-2.91**	1.885	-0.281532	2.860	2.486	Macey et al. (2017)
RPGV18	-27.6827	16.7189	PD (RMA)	Alkali granite gneiss	VS	2.96	14.5	0.511562	0.510032	0.1233	9	**-3.19**	1.885	-0.444594	2.520	2.226	Macey et al. (2017)
CHM288	-28.7887	18.2677	VD (RMA)	C.g alkali granite	VS	4.36	23.18	0.511471	0.510061	0.1137		**-2.68**	1.885	-0.487837	2.420	2.134	Macey et al. (2017)
DRV-90	-28.875	17.8944	VD (RMA)	Tonalite	VS	7.3	38.8	0.511541	0.51013	0.1140	22	**-1.33**	1.885	-0.486486	2.321	2.008	Reid (1997)
DRV-02	-28.7758	17.6583	VD (RMA)	Granite	VS	7.49	42.7	0.511504	0.510189	0.1060	30	**-0.18**	1.885	-0.522523	2.213	1.900	Reid (1997)
DRS-83	-28.8839	17.745	VD (RMA)	Gabbro	VS	4.65	17.1	0.512264	0.510225	0.1650	26	**0.53**	1.885	-0.256757	2.463	1.759	Reid (1997)

Abbreviations: Bt - Biotite; Calc. - Calculated; C.g - Coarse-grained; Eq - Equigranular; GS - Gladkop Suite; Hbl - Hornblende; Meas. - Measured; Qtz - Quartz; VS - Vioolsdrif Suite.

$^{143}Nd/^{144}Nd$ value for the JG2 standard is 0.512226 ± 10;
(0.512232 ±24, long-term UCT average n=17/exclude 0);
(0.51221-51224, GEOREM).

$^{143}Nd/^{144}Nd$ value for the ref JNdi-1 standard is 0.512115 ± 7 (Tanaka et al., 2000).

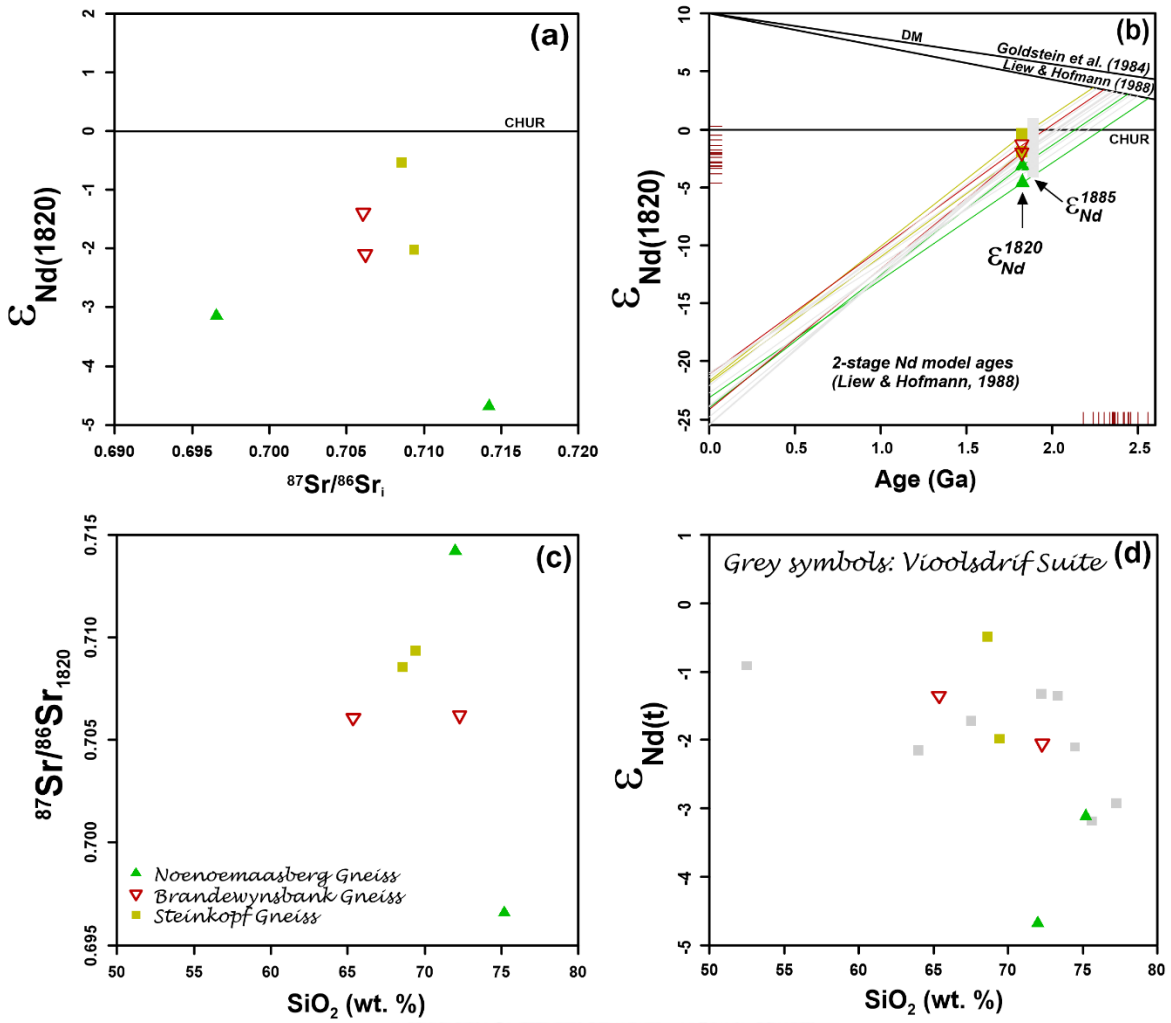

Fig. 6.2. (a) *$\varepsilon_{Nd(1820)}$ vs. $^{87}Sr/^{86}Sr_{1820}$ plot of the Gladkop Suite gneisses. CHUR line is represented.* ***(b)*** *Two-stage Nd development diagram of the Gladkop Suite and Vioolsdrif Suite rocks.* ***DM:*** *Depleted Mantle evolution lines after Goldstein et al. (1984) and Liew and Hofmann (1988).* ***(c)*** *$^{87}Sr/^{86}Sr_{1820}$ vs. SiO_2 plot for the Gladkop Suite gneisses, showing a general positive correlation.* ***(d)*** *$\varepsilon_{Nd(t)}$ vs. SiO_2 plot for both the Gladkop Suite and Vioolsdrif Suite rocks, showing a negative correlation for the BWB, STK and VS gneisses with SiO_2 and a positive correlation with SiO_2 for the NNM Gneiss.*

Both the GS and VS samples represent granites derived from fractionated sources, with respect to the depleted mantle (DM), as they have negative $f^{Sm/Nd}$ and negative $\varepsilon_{Nd(t)}$ values (Table 6.2). The magma source reservoir is compared to the DM in this case because every magma reservoir is undoubtedly fractionated with respect to CHUR. The parameter f, commonly written as $f^{Sm/Nd}$, is a fractionation factor and is the $^{147}Sm/^{144}Nd$ analogue of the $\varepsilon_{Nd(t)}$ ratio as it is a measure of Sm/Nd enrichment in a given reservoir relative to the depleted mantle, with negative $f^{Sm/Nd}$ values suggesting a highly fractionated source relative to DM. It is calculated from the expression $f = [(^{147}Sm/^{144}Nd)_{today}/(^{147}Sm/^{144}Nd)_{CHUR}] - 1$. Thus the negative $f^{Sm/Nd}$ values of the GS and VS rocks (Table 6.2) suggest derivation from a relatively fractionated source, further supported by the high LREE, Hf, Zr, Nb, Ta, Y and Pb contents (Section 5.5).

Both the GS and VS samples generally show a negative correlation between $\varepsilon_{Nd(t)}$ and SiO_2 (Fig. 6.2d). The negative correlation trend suggests that the highly fractionated granitic gneisses (higher SiO_2) were derived from enriched sources (negative ε_{Nd} values).

6.3. Zircon U-Pb dating and Lu-Hf isotopes

Emplacement age data for the GS rocks has been provided by Barton (1983) and Robb et al. (1999), with the former obtaining average errorchron Rb-Sr ages (comprising both the BWB and the STK gneisses) of 1.82 Ga and the latter obtaining similar SHRIMP zircon U-Pb ages of 1.83 Ga. This age (1.83-1.82 Ga) has been considered the crystallization age of the GS magmatic rocks. This chapter presents new LA-(SF)-ICP-MS U-Pb zircon data for the GS zircons from this study including new data for the NNM Gneiss (Table 6.3), as well as data provided by P. Macey (pers. comm., 2018) (Appendix F, Tables F1, F2). The main objectives of the U-Pb zircon geochronology were to: (1) obtain the age of crystallization of, and any other tectonomagmatic events recorded by the GS rocks; (2) test the relative age relationships, if any, between the STK, BWB and NNM gneisses, as postulated by Van Aswegen (1983); (3) provide updated U-Pb LA-(SF)-ICP-MS ages for the STK and BWB gneisses, and a crystallization age for the NNM Gneiss.

U-Pb and Lu-Hf isotope systems in zircon are used as geochronometer and geochemical tracer respectively (Bhattacharya and Janwari, 2015). Authors such as Patchett et al. (1981) and Vervoort and Patchett (1996) have highlighted the importance of Lu-Hf data in understanding mantle-crust differentiation. Hf is more incompatible with respect to Lu, hence, mantle melting results in Hf becoming more concentrated in the continental crust relative to Lu. The effect of this is non-radiogenic $^{176}Hf/^{177}Hf$ isotopic ratios in the continental crust and radiogenic ratios in the depleted mantel reservoirs (Patchett et al., 1981). Documented Lu/Hf ratios are usually low (<0.002) and as a result $^{176}Hf/^{177}Hf$ ratios preserved in zircons are usually close to the initial ratios (Patchett et al., 1981). The intra-crystalline diffusion rate of Hf in zircons is very low (Cherniak et al., 1999), allowing the preservation of isotopic variations induced by interaction between various magmas (Griffin et al., 2002) or the presence of components from different ages during zircon crystallization. Thus, by combining Lu-Hf and U-Pb isotope analyses of zircon grains, in particular, by doing spot analyses on the same growth zone, as has been done here, the isotopic heterogeneity of the source area at a certain time, e.g. whether the whole provenance was juvenile, evolved or mixed can be determined (Patchett et al., 1981; Vervoort and Patchett, 1996; Griffin et al., 2000). This makes Hf isotope in zircons very important in understanding the evolution of silicic magma generation and differentiation processes (Bhattacharya and Janwari, 2015).

For this study, seven samples (two STK, three BWB and two NNM gneisses; Table 6.3) were selected to be representative of the orthogneisses of the GS. Samples were prepared as described in Chapter 3. The CL imaging technique was used to observe zircon grain characteristics such as inherited cores, magmatic zoning and overgrowths. CL mages were obtained using a LEO 1450VP SEM, and individual zircon grains were subjected to U-Pb isotope analyses using the LA-SF-ICP-MS at the Central Analytical Facilities (CAF), Stellenbosch University. The calculation of weighted mean and concordia ages, as well as plotting of concordia diagrams were performed using Isoplot/Ex. 3.0 (Ludwig, 2003). $^{207}Pb/^{206}Pb$ ages are reported as the best ages for all spots older than ~1.0 Ga, while the $^{206}Pb/^{238}U$ ages are reported for all zircon analyses with younger ages. This is because the $^{207}Pb/^{206}Pb$ ages become increasingly imprecise below ~1.0 Ga, due to the change of the concordia slope as a result of the greater imprecision and significantly lower

count rate of the ^{207}Pb relative to ^{206}Pb at zircon ages younger than ~1.0 Ga (Gerdes and Zeh, 2006; Gehrels et al., 2008). All uncertainties are at the 2-sigma (2σ) level. U-Pb and Lu-Hf zircon data of the two samples (RTB027 and RTB028) from P. Macey (pers. comm. 2018) were obtained at the GeoHistory Facility, Curtin University, acquired by Laser ablation ICP-MS. The near concordant (>95 % concordance) zircon spots from U-Pb analyses were further analysed for their respective Lu-Hf isotopic compositions. The analyses were performed using a Thermos Scientific Neptune Plus MC-ICP-MS coupled to a New Wave Research UP193UC excimer laser ablation system and a TwoVol2 ablation cell. The methods employed for the Lu-Hf isotope analysis are described by Spencer et al. (2015).

Table 6.3. *U-Pb zircon laser ablation SF-ICP-MS data of the NNM (GS 04 and GS 20), STK (GS 14 and GS 22) and BWB (GS 28B, GS 30 and GS 37) gneisses.*

Analysis	U [ppm][a]	Pb [ppm][a]	Th/U meas.	RATIOS							AGES [Ma]						Concordance
				$^{207}Pb/^{235}U$[b]	2 □[d]	$^{206}Pb/^{238}U$[b]	2 □[d]	rho[c]	$^{207}Pb/^{206}Pb$[e]	2 □[d]	$^{207}Pb/^{235}U$	2 □	$^{206}Pb/^{238}U$	2 □	$^{207}Pb/^{206}Pb$	2 □	%
Noenoemaasberg Gneiss (GS 04)																	
04-01	229	66	1.65	4.503	0.149	0.2888	0.0066	0.69	0.1131	0.0027	1731	57	1635	37	1850	43	88
04-02	160	52	1.28	4.903	0.156	0.3220	0.0073	0.71	0.1105	0.0025	1803	57	1799	41	1807	41	100
04-03	50	10	3.22	2.345	0.090	0.2083	0.0049	0.61	0.0817	0.0025	1226	47	1220	29	1237	60	99
04-05	69	23	1.40	5.107	0.178	0.3275	0.0076	0.67	0.1131	0.0029	1837	64	1826	42	1849	47	99
04-06	105	32	1.84	4.617	0.224	0.3009	0.0079	0.54	0.1113	0.0045	1752	85	1696	45	1821	74	93
04-07	606	108	0.09	1.825	0.067	0.1787	0.0040	0.61	0.0741	0.0021	1054	39	1060	24	1044	58	102
04-08	2287	233	0.24	1.049	0.033	0.1021	0.0023	0.72	0.0745	0.0016	728	23	626	14	1055	44	59
04-09	274	59	0.69	3.305	0.132	0.2144	0.0052	0.60	0.1118	0.0036	1482	59	1252	30	1829	58	68
04-10	126	41	1.23	4.973	0.162	0.3253	0.0074	0.70	0.1109	0.0026	1815	59	1816	41	1814	42	100
04-11	203	55	0.94	3.634	0.120	0.2732	0.0062	0.69	0.0965	0.0023	1557	51	1557	35	1557	45	100
04-12	66	20	1.09	4.567	0.169	0.3092	0.0073	0.64	0.1071	0.0030	1743	64	1737	41	1751	52	99
04-13	195	36	0.18	1.872	0.063	0.1842	0.0042	0.68	0.0737	0.0018	1071	36	1090	25	1033	49	106
04-14	126	21	0.17	1.743	0.084	0.1704	0.0043	0.52	0.0742	0.0030	1025	49	1014	25	1047	83	97
04-15	184	53	1.69	4.408	0.154	0.2876	0.0067	0.67	0.1112	0.0029	1714	60	1629	38	1819	47	90
04-16	170	49	0.36	4.064	0.133	0.2900	0.0066	0.70	0.1017	0.0024	1647	54	1641	37	1654	44	99
04-17	264	76	0.49	4.042	0.131	0.2885	0.0066	0.70	0.1016	0.0024	1643	53	1634	37	1654	43	99
04-18	86	27	1.15	4.622	0.161	0.3121	0.0072	0.66	0.1074	0.0028	1753	61	1751	40	1756	48	100
04-19	169	55	1.07	5.007	0.166	0.3276	0.0075	0.69	0.1109	0.0027	1820	60	1827	42	1813	44	101
04-20	152	50	0.90	5.073	0.168	0.3275	0.0075	0.69	0.1123	0.0027	1832	61	1826	42	1837	43	99
04-21	108	36	1.27	5.035	0.210	0.3296	0.0082	0.59	0.1108	0.0037	1825	76	1836	45	1813	61	101
04-22	446	81	0.06	1.853	0.065	0.1807	0.0042	0.66	0.0744	0.0020	1064	37	1071	25	1052	53	102
04-23	107	32	1.17	4.520	0.166	0.2979	0.0070	0.65	0.1101	0.0031	1735	64	1681	40	1800	51	93
04-24	1760	214	0.30	1.246	0.041	0.1218	0.0028	0.70	0.0742	0.0017	822	27	741	17	1047	47	71
04-25	276	91	1.02	5.050	0.167	0.3283	0.0075	0.69	0.1116	0.0027	1828	61	1830	42	1825	43	100
04-26	69	23	1.13	5.058	0.225	0.3291	0.0084	0.57	0.1115	0.0041	1829	81	1834	47	1824	66	101
04-27	142	47	0.82	5.128	0.234	0.3323	0.0086	0.56	0.1119	0.0042	1841	84	1850	48	1831	68	101
Noenoemaasberg Gneiss (GS 20)																	
20-01	279	78	1.31	4.308	0.137	0.2793	0.0064	0.72	0.1119	0.0025	1695	54	1588	36	1830	40	87
20-02	221	64	1.20	4.524	0.145	0.2918	0.0067	0.72	0.1124	0.0025	1735	55	1651	38	1839	40	90
20-03	280	57	0.57	2.832	0.096	0.2033	0.0047	0.68	0.1010	0.0025	1364	46	1193	28	1643	46	73
20-04	612	81	0.81	2.005	0.066	0.1318	0.0030	0.70	0.1104	0.0026	1117	37	798	18	1805	43	44
20-05	161	27	0.78	2.610	0.087	0.1688	0.0039	0.70	0.1121	0.0027	1303	43	1005	23	1834	43	55
20-06	189	16	0.32	1.295	0.045	0.0848	0.0020	0.67	0.1108	0.0029	844	29	525	12	1813	47	29
20-07	115	37	0.91	4.964	0.165	0.3259	0.0076	0.70	0.1105	0.0026	1813	60	1819	42	1807	43	101
20-08	109	35	0.83	4.939	0.163	0.3229	0.0075	0.70	0.1110	0.0026	1809	60	1804	42	1815	43	99
20-09	250	51	1.22	3.119	0.102	0.2049	0.0047	0.71	0.1104	0.0025	1437	47	1202	28	1806	42	67
20-10	513	65	1.05	1.962	0.065	0.1270	0.0029	0.70	0.1120	0.0027	1103	37	771	18	1833	43	42
20-11	148	48	0.96	4.916	0.160	0.3237	0.0075	0.71	0.1102	0.0025	1805	59	1808	42	1802	42	100
20-12	131	43	0.96	5.000	0.166	0.3261	0.0076	0.70	0.1112	0.0026	1819	60	1819	42	1819	43	100
20-14	80	26	0.88	5.027	0.173	0.3266	0.0077	0.68	0.1117	0.0028	1824	63	1822	43	1826	46	100
20-15	461	87	0.66	2.890	0.094	0.1879	0.0043	0.71	0.1116	0.0026	1379	45	1110	26	1825	42	61
20-16	219	29	0.33	2.018	0.099	0.1320	0.0035	0.53	0.1109	0.0046	1122	55	799	21	1814	76	44
20-17	130	42	1.42	4.982	0.247	0.3271	0.0088	0.54	0.1105	0.0046	1816	90	1824	49	1807	76	101
20-18	858	178	0.32	3.143	0.123	0.2069	0.0050	0.62	0.1102	0.0034	1443	57	1212	30	1802	56	67
20-19	288	47	0.42	2.238	0.075	0.1622	0.0038	0.69	0.1001	0.0024	1193	40	969	22	1626	45	60
20-20	325	72	1.08	3.400	0.117	0.2220	0.0052	0.68	0.1111	0.0028	1504	52	1292	30	1817	45	71
20-21	185	60	0.94	4.933	0.167	0.3242	0.0076	0.69	0.1104	0.0027	1808	61	1810	42	1805	44	100
20-22	145	40	0.90	4.207	0.143	0.2735	0.0064	0.69	0.1116	0.0028	1675	57	1559	36	1825	45	85
20-23	302	80	0.87	4.022	0.136	0.2634	0.0061	0.69	0.1107	0.0027	1639	55	1507	35	1812	44	83
Steinkopf Gneiss (GS 14)																	
14-01	137	45	0.90	5.037	0.160	0.3276	0.0073	0.70	0.1115	0.0025	1826	58	1827	41	1824	41	100
14-02	294	96	1.40	4.995	0.155	0.3260	0.0072	0.71	0.1111	0.0024	1819	56	1819	40	1818	40	100
14-03	122	35	1.22	4.427	0.151	0.2885	0.0066	0.67	0.1113	0.0028	1717	59	1634	37	1820	46	90
14-04	197	64	1.10	4.989	0.157	0.3259	0.0072	0.71	0.1110	0.0025	1817	57	1818	40	1817	40	100
14-05	231	73	1.28	4.856	0.156	0.3165	0.0071	0.70	0.1113	0.0026	1795	58	1773	40	1820	42	97
14-07	141	44	1.29	4.598	0.150	0.3104	0.0070	0.69	0.1074	0.0025	1749	57	1743	39	1756	43	99
14-08	96	31	1.23	5.013	0.163	0.3275	0.0073	0.69	0.1110	0.0026	1822	59	1826	41	1816	43	101
14-09	138	45	0.93	5.020	0.162	0.3269	0.0073	0.69	0.1114	0.0026	1823	59	1823	41	1822	42	100
14-11	1315	433	0.11	5.002	0.157	0.3289	0.0073	0.71	0.1103	0.0024	1820	57	1833	41	1805	40	102
14-12	277	90	1.65	4.929	0.160	0.3244	0.0073	0.69	0.1102	0.0026	1807	59	1811	41	1803	43	100
14-13	150	47	1.30	4.620	0.151	0.3115	0.0070	0.69	0.1076	0.0025	1753	57	1748	39	1758	43	99
14-14	152	50	0.99	5.045	0.180	0.3281	0.0076	0.65	0.1115	0.0030	1827	65	1829	42	1824	49	100

Continued on next page

Table 6.3. (continued)

U-Pb zircon laser ablation SF-ICP-MS data of the NNM (GS04 and GS 20), STK (GS 14 and GS 22) and BWB (GS 28B, GS 30 and GS 37) gneisses.

Analysis	U [ppm][a]	Pb [ppm][a]	Th/U meas.	RATIOS							AGES [Ma]						Concordance
				$^{207}Pb/^{235}U$[b]	2 □[d]	$^{206}Pb/^{238}U$[b]	2 □[d]	rho[c]	$^{207}Pb/^{206}Pb$[e]	2 □[d]	$^{207}Pb/^{235}U$	2 □	$^{206}Pb/^{238}U$	2 □	$^{207}Pb/^{206}Pb$	2 □	%
14-15	136	42	1.02	4.601	0.165	0.3103	0.0072	0.64	0.1075	0.0030	1749	63	1742	40	1758	50	99
14-16	215	66	1.35	4.733	0.152	0.3086	0.0069	0.69	0.1112	0.0026	1773	57	1734	39	1820	42	95
14-17	229	54	0.78	3.602	0.118	0.2351	0.0053	0.69	0.1111	0.0026	1550	51	1361	31	1817	43	75
14-18	499	96	0.17	2.362	0.076	0.1920	0.0043	0.69	0.0892	0.0021	1231	40	1132	25	1408	45	80
14-19	302	79	0.69	4.007	0.130	0.2613	0.0058	0.69	0.1112	0.0026	1636	53	1496	33	1819	42	82
14-20	121	39	1.46	4.916	0.194	0.3207	0.0077	0.60	0.1112	0.0035	1805	71	1793	43	1819	57	99
14-21	95	27	1.02	4.350	0.171	0.2833	0.0067	0.60	0.1114	0.0035	1703	67	1608	38	1822	57	88
14-22	370	121	1.39	4.987	0.163	0.3276	0.0074	0.69	0.1104	0.0026	1817	59	1827	41	1806	43	101
14-23	212	66	1.51	4.603	0.151	0.3105	0.0070	0.68	0.1075	0.0026	1750	58	1743	39	1758	44	99
14-25	262	69	1.28	3.903	0.149	0.2648	0.0062	0.62	0.1069	0.0032	1614	61	1515	36	1747	55	87
Steinkopf Gneiss (GS 22)																	
22-01	61	19	1.00	4.581	0.184	0.3112	0.0075	0.60	0.1068	0.0034	1746	70	1747	42	1745	59	100
22-02	94	29	1.39	4.555	0.152	0.3096	0.0070	0.68	0.1067	0.0026	1741	58	1739	39	1744	45	100
22-03	170	38	0.49	3.078	0.100	0.2232	0.0050	0.69	0.1000	0.0023	1427	46	1299	29	1624	44	80
22-04	117	38	1.18	4.964	0.160	0.3259	0.0073	0.69	0.1105	0.0026	1813	59	1819	41	1807	42	101
22-05	95	31	0.91	5.034	0.174	0.3282	0.0075	0.66	0.1112	0.0029	1825	63	1830	42	1820	47	101
22-06	74	23	1.20	4.608	0.167	0.3096	0.0072	0.64	0.1080	0.0030	1751	63	1738	40	1765	51	98
22-07	97	31	1.44	4.874	0.159	0.3220	0.0072	0.69	0.1098	0.0026	1798	59	1800	40	1796	43	100
22-08	136	43	1.06	4.558	0.170	0.3127	0.0073	0.63	0.1057	0.0031	1742	65	1754	41	1727	53	102
22-09	87	28	1.04	5.013	0.165	0.3257	0.0073	0.68	0.1116	0.0027	1821	60	1818	41	1826	44	100
22-10	167	47	1.38	4.227	0.150	0.2793	0.0064	0.65	0.1098	0.0030	1679	60	1588	36	1795	49	88
22-11	200	61	0.91	4.677	0.154	0.3060	0.0069	0.68	0.1109	0.0027	1763	58	1721	39	1813	44	95
22-12	109	36	1.12	5.033	0.168	0.3265	0.0074	0.68	0.1118	0.0027	1825	61	1821	41	1829	44	100
22-13	242	48	0.68	2.472	0.081	0.1984	0.0044	0.69	0.0904	0.0021	1264	41	1167	26	1433	45	81
22-14	74	21	0.93	4.154	0.153	0.2840	0.0066	0.63	0.1061	0.0030	1665	61	1611	37	1733	53	93
22-15	117	38	1.42	4.909	0.160	0.3204	0.0072	0.69	0.1111	0.0026	1804	59	1792	40	1818	43	99
22-16	105	34	0.94	5.005	0.165	0.3274	0.0074	0.68	0.1109	0.0027	1820	60	1826	41	1814	44	101
22-17	179	51	1.28	4.221	0.138	0.2871	0.0064	0.69	0.1066	0.0025	1678	55	1627	36	1742	43	93
22-18	105	34	0.96	4.915	0.163	0.3233	0.0073	0.68	0.1103	0.0027	1805	60	1806	41	1804	44	100
22-19	109	35	2.26	4.843	0.161	0.3161	0.0071	0.68	0.1111	0.0027	1792	60	1771	40	1818	44	97
22-20	127	39	1.46	4.523	0.153	0.3097	0.0070	0.67	0.1059	0.0027	1735	59	1739	39	1731	46	101
22-22	73	20	1.02	4.260	0.207	0.2777	0.0072	0.54	0.1113	0.0046	1686	82	1580	41	1820	74	87
22-23	73	24	1.17	5.084	0.191	0.3294	0.0077	0.63	0.1120	0.0033	1833	69	1835	43	1831	53	100
22-24	71	23	1.08	5.021	0.176	0.3271	0.0075	0.66	0.1113	0.0029	1823	64	1824	42	1821	48	100
22-25	117	32	0.76	3.849	0.131	0.2710	0.0061	0.67	0.1030	0.0026	1603	54	1546	35	1679	47	92
Brandewynsbank Gneiss (GS 28B)																	
28b-02	88	27	0.87	4.644	0.159	0.3131	0.0076	0.71	0.1076	0.0026	1757	60	1756	43	1758	44	100
28b-03	103	33	1.08	4.996	0.171	0.3246	0.0079	0.71	0.1116	0.0027	1819	62	1812	44	1826	44	99
28b-04	171	55	1.10	4.984	0.177	0.3243	0.0080	0.69	0.1115	0.0029	1817	65	1811	45	1824	47	99
28b-05	114	37	1.54	4.988	0.170	0.3252	0.0079	0.72	0.1112	0.0026	1817	62	1815	44	1820	43	100
28b-06	317	70	0.36	2.945	0.101	0.2216	0.0054	0.71	0.0964	0.0023	1393	48	1290	31	1555	45	83
28b-07	69	21	0.84	4.604	0.164	0.3129	0.0077	0.70	0.1067	0.0027	1750	62	1755	43	1744	47	101
28b-08	195	56	1.08	4.367	0.151	0.2859	0.0070	0.71	0.1108	0.0027	1706	59	1621	40	1812	44	89
28b-09	146	48	1.30	5.016	0.171	0.3256	0.0080	0.72	0.1118	0.0026	1822	62	1817	45	1828	43	99
28b-10	145	47	0.72	4.949	0.173	0.3236	0.0080	0.71	0.1109	0.0027	1811	63	1807	45	1815	45	100
28b-11	122	37	1.07	4.597	0.225	0.3014	0.0084	0.57	0.1106	0.0044	1749	85	1698	47	1810	73	94
28b-12	106	27	0.84	3.286	0.117	0.2521	0.0063	0.70	0.0945	0.0024	1478	53	1449	36	1519	48	95
28b-13	290	94	1.43	4.944	0.170	0.3253	0.0081	0.73	0.1103	0.0026	1810	62	1815	45	1804	43	101
28b-14	192	63	1.68	4.952	0.173	0.3256	0.0082	0.72	0.1103	0.0027	1811	63	1817	46	1804	44	101
28b-15	199	45	0.71	3.013	0.106	0.2254	0.0057	0.72	0.0969	0.0024	1411	49	1310	33	1566	46	84
28b-16	233	58	0.56	3.342	0.117	0.2498	0.0063	0.72	0.0970	0.0023	1491	52	1437	36	1568	45	92
28b-17	151	41	1.01	3.593	0.135	0.2680	0.0069	0.69	0.0972	0.0027	1548	58	1531	39	1571	51	97
28b-18	177	42	1.31	3.294	0.147	0.2396	0.0065	0.61	0.0997	0.0035	1480	66	1385	37	1619	66	86
28b-19	131	34	0.88	3.424	0.124	0.2592	0.0066	0.71	0.0958	0.0024	1510	55	1486	38	1544	48	96
28b-20	147	44	1.48	4.601	0.220	0.3019	0.0085	0.59	0.1106	0.0043	1749	84	1701	48	1808	70	94
28b-21	112	36	1.10	4.968	0.186	0.3251	0.0085	0.70	0.1108	0.0030	1814	68	1814	47	1813	49	100
28b-22	128	42	1.33	4.995	0.189	0.3255	0.0085	0.69	0.1113	0.0030	1819	69	1816	48	1821	50	100
28b-23	107	35	1.15	4.908	0.193	0.3227	0.0086	0.67	0.1103	0.0032	1804	71	1803	48	1805	53	100
28b-24	111	36	1.46	4.954	0.189	0.3248	0.0086	0.69	0.1106	0.0031	1812	69	1813	48	1809	50	100
28b-25	310	63	0.09	2.242	0.086	0.2036	0.0054	0.69	0.0799	0.0022	1194	46	1195	31	1194	55	100
Brandewynsbank Gneiss (GS 30)																	
30-01	161	42	0.85	3.800	0.137	0.2628	0.0063	0.67	0.1049	0.0028	1593	57	1504	36	1712	49	88

Continued on next page

Table 6.3. (continued)
U-Pb zircon laser ablation SF-ICP-MS data of the NNM (GS04 and GS 20), STK (GS 14 and GS 22) and BWB (GS 28B, GS 30 and GS 37) gneisses.

Analysis	U [ppm][a]	Pb [ppm][a]	Th/U meas.	RATIOS							AGES [Ma]						Concordance
				$^{207}Pb/^{235}U$[b]	2 □[d]	$^{206}Pb/^{238}U$[b]	2 □[d]	rho[c]	$^{207}Pb/^{206}Pb$[e]	2 □[d]	$^{207}Pb/^{235}U$	2 □	$^{206}Pb/^{238}U$	2 □	$^{207}Pb/^{206}Pb$	2 □	%
30-02	67	21	0.98	4.654	0.173	0.3054	0.0074	0.66	0.1105	0.0031	1759	65	1718	42	1808	51	95
30-03	710	130	0.10	2.022	0.066	0.1831	0.0043	0.72	0.0801	0.0018	1123	37	1084	25	1200	45	90
30-04	219	71	0.87	4.970	0.161	0.3260	0.0077	0.72	0.1106	0.0025	1814	59	1819	43	1809	41	101
30-05	96	31	0.95	4.966	0.178	0.3274	0.0079	0.67	0.1100	0.0029	1814	65	1826	44	1800	48	101
30-06	154	50	1.24	4.907	0.162	0.3231	0.0076	0.71	0.1102	0.0026	1803	60	1805	43	1802	42	100
30-07	256	84	1.23	5.060	0.171	0.3273	0.0078	0.70	0.1121	0.0027	1829	62	1825	43	1834	44	100
30-08	341	111	1.00	4.994	0.191	0.3269	0.0081	0.64	0.1108	0.0032	1818	70	1823	45	1813	53	101
30-09	163	54	0.87	5.032	0.203	0.3302	0.0083	0.62	0.1105	0.0035	1825	74	1839	46	1808	58	102
30-10	148	44	0.95	4.587	0.153	0.2997	0.0071	0.71	0.1110	0.0026	1747	58	1690	40	1816	43	93
30-11	103	33	0.84	4.936	0.168	0.3231	0.0077	0.70	0.1108	0.0027	1808	61	1805	43	1813	44	100
30-12	154	50	0.69	4.975	0.166	0.3270	0.0077	0.71	0.1104	0.0026	1815	61	1824	43	1806	43	101
30-13	181	49	0.62	4.066	0.150	0.2700	0.0066	0.66	0.1092	0.0030	1648	61	1541	38	1787	51	86
30-14	532	160	0.61	4.534	0.164	0.3002	0.0073	0.67	0.1095	0.0029	1737	63	1692	41	1792	49	94
30-15	458	99	0.48	3.304	0.115	0.2158	0.0052	0.69	0.1111	0.0028	1482	51	1259	30	1817	46	69
30-16	182	59	0.87	5.009	0.171	0.3259	0.0078	0.70	0.1115	0.0027	1821	62	1818	43	1824	44	100
30-17	87	28	0.96	4.839	0.171	0.3220	0.0078	0.68	0.1090	0.0028	1792	63	1799	43	1783	47	101
30-18	327	75	0.48	3.501	0.125	0.2282	0.0055	0.68	0.1113	0.0029	1527	54	1325	32	1820	48	73
30-19	208	40	0.73	2.951	0.111	0.1929	0.0047	0.65	0.1110	0.0032	1395	53	1137	28	1815	52	63
Brandewynsbank Gneiss (GS 37)																	
37-01	129	42	0.72	5.013	0.164	0.3267	0.0076	0.71	0.1113	0.0026	1822	60	1822	43	1821	42	100
37-02	135	44	1.31	4.957	0.164	0.3256	0.0076	0.71	0.1104	0.0026	1812	60	1817	43	1806	42	101
37-03	135	44	1.05	5.014	0.164	0.3272	0.0077	0.72	0.1112	0.0025	1822	60	1825	43	1818	41	100
37-04	273	85	1.04	4.564	0.148	0.3112	0.0073	0.72	0.1064	0.0024	1743	56	1747	41	1738	41	100
37-05	99	32	1.30	4.959	0.165	0.3243	0.0076	0.71	0.1109	0.0026	1812	60	1811	43	1814	43	100
37-06	91	28	1.00	4.577	0.158	0.3077	0.0073	0.69	0.1079	0.0027	1745	60	1729	41	1764	46	98
37-07	157	50	1.12	4.834	0.158	0.3164	0.0074	0.72	0.1108	0.0025	1791	58	1772	41	1812	41	98
37-08	168	54	1.24	4.804	0.167	0.3183	0.0076	0.68	0.1095	0.0028	1786	62	1781	42	1791	46	99
37-09	132	43	1.59	5.048	0.168	0.3281	0.0077	0.71	0.1116	0.0026	1827	61	1829	43	1825	43	100
37-10	112	32	1.31	4.400	0.197	0.2869	0.0074	0.58	0.1112	0.0041	1712	77	1626	42	1819	66	89
37-11	106	34	1.24	4.941	0.165	0.3241	0.0076	0.71	0.1106	0.0026	1809	60	1810	43	1809	43	100
37-12	206	68	1.72	5.033	0.182	0.3284	0.0079	0.67	0.1112	0.0030	1825	66	1831	44	1818	49	101
37-13	65	21	1.15	4.925	0.176	0.3229	0.0078	0.67	0.1106	0.0029	1807	64	1804	43	1810	48	100
37-14	246	72	1.01	4.432	0.148	0.2910	0.0069	0.71	0.1105	0.0026	1718	57	1646	39	1807	43	91
37-15	162	53	1.57	5.003	0.167	0.3265	0.0077	0.71	0.1111	0.0026	1820	61	1821	43	1818	43	100
37-16	147	48	0.91	4.957	0.168	0.3267	0.0077	0.70	0.1100	0.0027	1812	61	1823	43	1800	44	101
37-17	80	26	1.10	4.882	0.168	0.3234	0.0077	0.69	0.1095	0.0027	1799	62	1806	43	1791	45	101
37-18	138	45	1.46	4.949	0.170	0.3279	0.0078	0.69	0.1095	0.0027	1811	62	1828	44	1790	45	102
37-19	214	70	1.24	5.036	0.168	0.3273	0.0077	0.71	0.1116	0.0026	1825	61	1825	43	1825	43	100
37-20	61	19	0.99	4.828	0.169	0.3181	0.0076	0.68	0.1101	0.0028	1790	63	1781	43	1801	47	99
37-21	158	52	1.25	5.015	0.236	0.3275	0.0087	0.56	0.1111	0.0043	1822	86	1826	49	1817	71	101
37-22	97	32	0.92	5.081	0.179	0.3288	0.0079	0.68	0.1121	0.0029	1833	64	1833	44	1833	47	100
37-23	254	45	0.05	1.871	0.080	0.1785	0.0044	0.58	0.0760	0.0026	1071	46	1059	26	1096	70	97
37-24	75	23	1.34	4.581	0.161	0.3008	0.0072	0.68	0.1105	0.0028	1746	61	1695	41	1807	47	94
37-25	61	20	1.06	4.984	0.206	0.3239	0.0078	0.58	0.1116	0.0038	1817	75	1809	43	1825	61	99
37-26	67	22	0.99	5.003	0.195	0.3248	0.0081	0.64	0.1117	0.0034	1820	71	1813	45	1828	55	99
37-27	94	29	1.44	4.562	0.167	0.3105	0.0075	0.66	0.1066	0.0029	1742	64	1743	42	1742	50	100
37-28	84	27	0.96	4.986	0.235	0.3247	0.0087	0.57	0.1114	0.0043	1817	86	1813	48	1822	70	99
37-29	83	26	0.90	4.647	0.203	0.3146	0.0081	0.59	0.1071	0.0038	1758	77	1763	45	1751	65	101
37-30	240	58	0.85	3.413	0.117	0.2434	0.0058	0.70	0.1017	0.0025	1507	52	1404	33	1655	46	85
37-31	615	110	0.29	1.864	0.071	0.1790	0.0043	0.64	0.0755	0.0022	1068	40	1062	26	1082	58	98

[a]: U and Pb concentrations and Th/U ratios are calculated relative to GJ-1 reference zircon.

[b]: Corrected for background and within-run Pb/U fractionation and normalised to reference zircon GJ-1 (ID-TIMS values/measured value); $^{207}Pb/^{235}U$ calculated using $(^{207}Pb/^{206}Pb)/(^{238}U/^{206}Pb \times 1/137.88)$.

[c]: Rho is the error correlation defined as the quotient of the propagated errors of the $^{206}Pb/^{238}U$ and the $^{207}Pb/^{235}U$ ratio.

[d]: Quadratic addition of within-run errors (2 SD) and daily reproducibility of GJ-1 (2 SD).

[e]: Corrected for mass-bias by normalising to GJ-1 reference zircon (~0.6 per atomic mass unit) and common Pb using the model Pb composition of Stacey and Kramers (1975).

6.3.1. NNM Gneiss

The NNM Gneiss samples (GS 04 and GS 20) host zircons between 60 and 200 µm in length (Fig. 6.3a, b). The zircon populations show a slight variation in both size and shape (but similar age groups), including acicular and stubby types, as well as double- and single-sided prismatic varieties (Fig. 6.3a, b). These grains tend to be euhedral to subhedral. Some grains appear completely dark in CL images (Fig. 6.3a, b). Resorption is limited and cores are weakly zoned. CL images reveal both thin and thick unzoned dark rims, up to 25 µm thick (Fig. 6.3a, b).

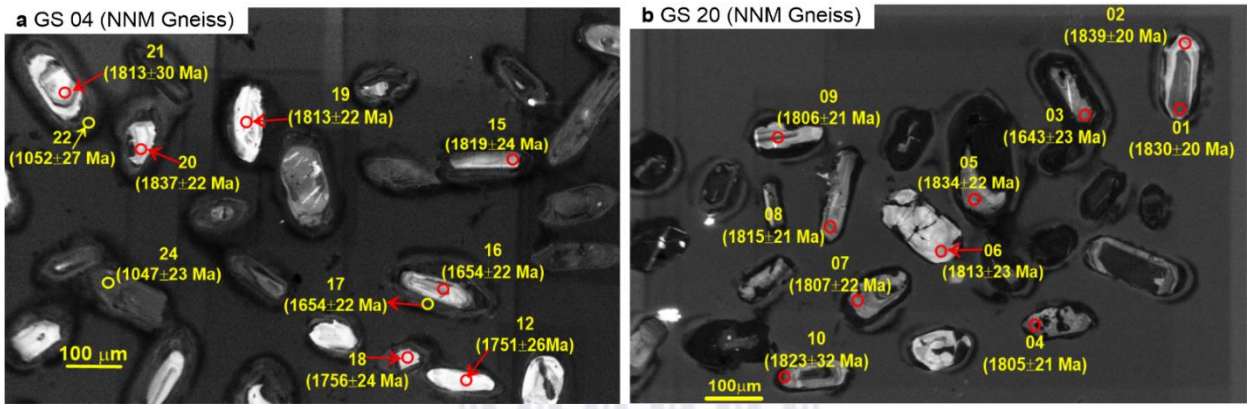

Fig. 6.3. *Zircon CL images of the Noenoemaasberg Gneiss. Ages reported next to analysed spots (yellow and red circles) are $^{207}Pb/^{206}Pb$ ages with 2σ error from Table 6.3.*

Zircon Th/U ratios for sample GS 04 are slightly variable, but most spots (n = 25) show ratios ranging from 0.24 to 1.84 (Table 6.3), while the remaining two spots (GS 04-22 and GS 04-07) have Th/U values <0.1 (Table 6.3). These two spots are found on the dark, unzoned rims (e.g. spot 22 on Fig. 6.3a) which are interpreted as metamorphic rims. They provided concordant ages of 1044 ± 58 and 1052 ± 53 Ma (Table 6.3) which coincide with the Namaqua Orogeny (Macey et al., 2018). Most spots have U concentrations between 69 and 606 ppm, but two spots (GS 04-24 and GS 04-08) have U concentrations of 1760 ppm and 2287 ppm with Th/U ratios of 0.30 and 0.24 respectively, and provided discordant age data (Table 6.3). Out of the twenty-seven (27) spots analyzed, twenty-two (22) provided concordant data (Fig. 6.4b); the remaining five more discordant spots (GS 04-01, -08, -09, -15 and -24) include spots with ages in two main groups, 1050 and 1820 Ma as shown by the light-grey probability curves on Fig. 6.4b. The age spectrum indicates that sample GS 04 contains zircon grains predominantly formed between 1780 - 1840 Ma (n = 12) and between 1020 - 1040 Ma (n = 4), with minor age populations at 1220, 1540, 1640 and 1740 Ma (Fig. 6.4b). The ICP-MS data, however, reveals that the zircons formed (or were affected) at five statistically distinct events (occurring at 1042, 1237, 1557, 1654 and 1816 Ma), as shown by the peaks of the dark-grey probability density distribution curves (Fig. 6.4b). The concordant data spots provided an average concordia age of 1825 ± 10 Ma (MSWD = 0.44) for sample GS 04 (Fig. 6.4a) and is interpreted as the age of crystallization of the zircon grains.

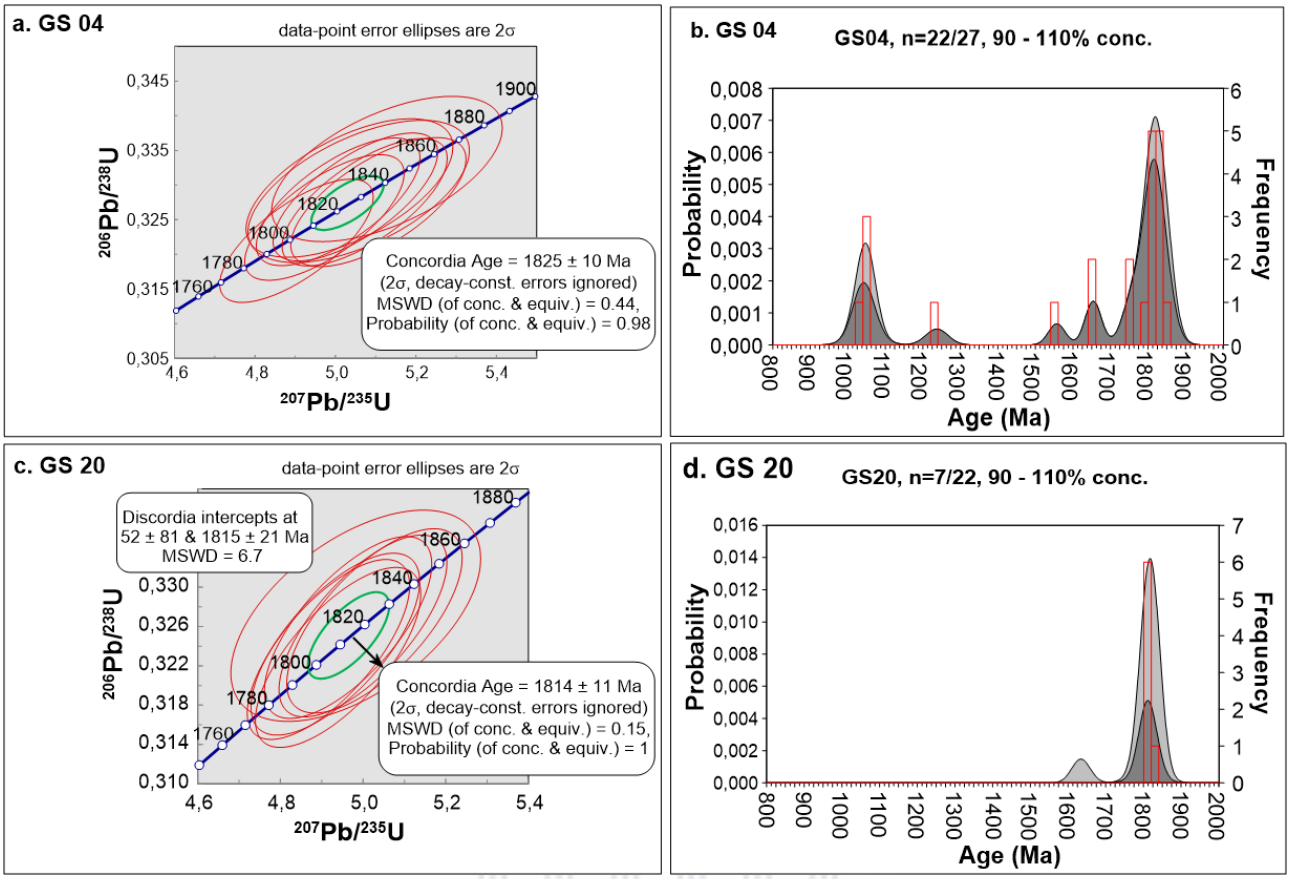

Fig. 6.4. *U-Pb isochron diagrams (**a** and **c**) and probability distribution vs. U-Pb zircon age data (**b** and **d**) of the Noenoemaasberg Gneiss. **Dark grey** distribution curve - zircon grains with 90-110 % concordance, **light grey** distribution curve - more discordant zircon analyses, **red bars** - the frequency (n) of individual zircon populations.*

Sample GS 20 shows a Th/U ratio range of 0.32-1.42, and with U concentrations for the various spots generally ranging from 80 to 858 ppm, while Pb concentrations range from 16 to 148 ppm (Table 6.3). 22 spots were analysed on sample GS 20, with seven providing concordant data and the remaining 15 spots providing discordant data belonging to two main age groups, 1620 and 1820 Ma (Fig. 6.4d). The age spectrum indicates that sample GS 20 contains zircon grains predominantly formed between 1800-1820 Ma (n = 7) (Fig. 6.4d). The probability distribution curve of sample GS 20 reveals a statistically distinct tectono-thermal event at 1812 Ma (Fig. 6.4d), most probably corresponding to zircon crystallization in the GS. The concordant data provide a concordia age of 1814 ± 11 Ma (MSWD = 0.15) (Fig. 6.4c), interpreted as the age of emplacement of sample GS 20. Based on the U-Pb geochronology data obtained from both samples GS 04 and GS 20, the emplacement age of the NNM Gneiss is taken as being between 1825 and 1814 Ma. The ICP-MS results further indicate that the NNM Gneiss experienced at least two thermal events, with the probability distribution on the age spectrum revealing two main events at ~1800 Ma and between 1000-1100 Ma, and with a minor event between 1600-1700 Ma, 1500-1600 Ma and 1200-1300 Ma (Fig. 6.4b, d).

6.3.2. STK Gneiss

a. Zircon U-Pb results

Zircon crystals of the STK Gneiss samples (GS 14, GS 22 and RTB 028) are between 60 and 200 µm in length (Fig. 6.5a-d). The crystals are mostly euhedral to subhedral with largely short prisms, and are typically characterized by rounded to sub-rounded cores of highly varying sizes (Fig. 6.5a-d). Acicular zircons (length to width ratio of 3:1 or 4:1) are rarely present, but where present are poorly zoned and cores are poorly visible, whereas the more abundant stubby grains (aspect ratios of 2:1 or 1:1) show pronounced oscillatory zoning (Fig. 6.5a-d) typical of magmatic zircons crystallised directly from the granitic magma (Corfu et al., 2003; Belousova et al., 2006). Many zircon grains are characterized by dark outer rims of varying thicknesses, with rims of up to 25 µm identified. Resorption of zircon crystals is pronounced, and while some resorption surfaces are regular, most are irregular (Fig. 6.5a, b). The zircon population of the STK samples is generally simple in terms of zircon morphology, suggesting the protoliths of the granodioritic gneiss are likely granitoids with mostly I-type components or I-type rock (Poller, 1999).

Zircon Th/U ratios for sample GS 14 generally range from 0.78-1.51, with variable U concentrations (95-1315 ppm) (Table 6.3). However, spot GS 14-11 yielded a Th/U ratio of 0.11, but with a concordant age of 1805 Ma, and spot GS 14-18 yielded a ratio of 0.17 with a discordant age of 1408 Ma (Table 6.3). Out of the 22 spots analyzed, 16 provided concordant data, with the majority (n = 12) providing $^{207}Pb/^{206}Pb$ ages between 1800 and 1825 Ma, with a minor age population (n = 4) around 1740 Ma (Fig. 6.6b). The remaining six more discordant analyses (GS 14-03, -17, -18, -19, -21 and -25) include spots with ages belonging to three main groups: 1400, 1750 and 1820 Ma (Fig. 6.6b; Table 6.3). The more concordant data provided a mean concordia age of 1816 ± 8 Ma (MSWD = 0.57) (Fig. 6.6a). The entire data, including the more discordant analyses, is well constrained and provides an upper intercept of 1816 ± 12 Ma (MSWD = 0.102), which is very similar to the mean concordia age. This age is interpreted as the emplacement age of this STK Gneiss sample.

Zircon Th/U ratios for sample GS 22 are high, generally ranging from 0.76-2.26, with variable U concentrations (61-242 ppm) (Table 6.3). Of the 24 spots analyzed for this sample, 20 provided concordant data (Fig. 6.6d), with the four remaining spots (GS 22-03, -10, -13 and -22) providing more discordant data, belonging to three age groups: 1430, 1620 and 1800 Ma (Fig. 6.6d; Table 6.3). The concordant data provided a mean age of 1815 ± 9 Ma (MSWD = 0.67) (Fig. 6.6c), interpreted as the emplacement age of this sample. The entire dataset, including the more discordant data defines a well constraint discordia with an upper intercept age of 1826 ± 19 Ma (MSWD = 0.61).

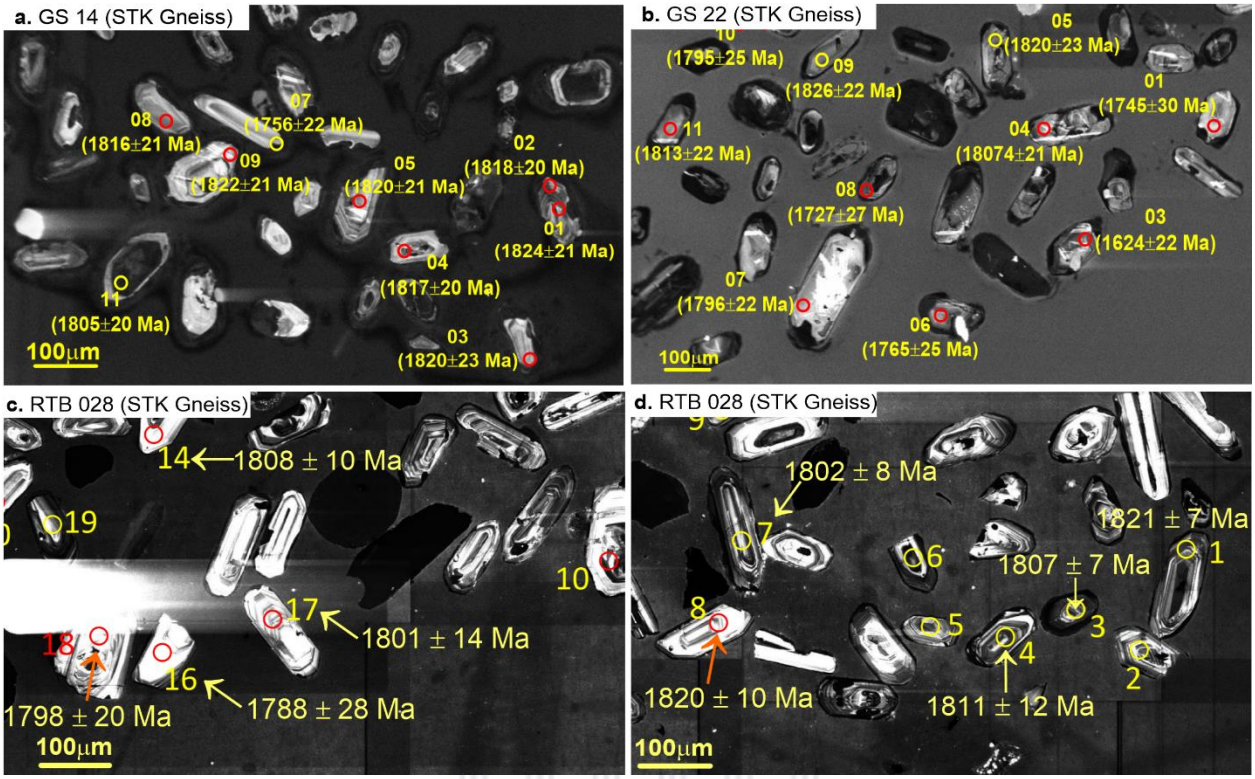

Fig. 6.5. *Zircon CL images of the Steinkopf Gneiss. Ages reported next to analysed spots (yellow and red circles) are $^{207}Pb/^{206}Pb$ ages with 2σ error from Tables 6.3 (GS 14 and GS 22) and 6.4 (RTB028).*

Sample RTB028 is a medium-grained, grey biotite migmatitic gneiss with a granitic to granodioritic composition, collected from a location 7.0 km south of Steinkopf (-29.3222S, 017.7699E; Fig. 6.1). The sample is compositional heterogeneous, imparted by a well-developed penetrative secondary E-W oriented banding. It contains a mineral assemblage of quartz (30-40 %), plagioclase (20-40 %), K-feldspars (15-30 %), biotite (10 %) ± hornblende (0-5 %) (P. Macey, pers. comm., 2018). Zircons separated from this sample are mainly euhedral to subhedral in shape, with most zircons varying in length between 50 and 200 µm (Fig. 6.5c, d). Most grains have obvious oscillatory zoning and dark outer rims are rare (very thin where present; Fig. 6.5c, d). Zircon Th/U ratios for sample RTB028 generally range from 0.48 to 2.09 (Table 6.4). Twenty spots were analysed, all representing cores, and produced eleven concordant ages. The eleven concordant analyses of cores yielded $^{207}Pb/^{206}Pb$ ages between 1762 ± 26 and 1808 ± 14 Ma (Appendix F, Table F1). The concordant analyses for cores produced a weighted robust mean age of 1798 ± 8 Ma (MSWD = 0.0051), calculated after Hoaglin et al. (1983) for more meaningful results (Fig. 6.7b), and is interpreted as the age of emplacement of this sample.

Based on the data obtained from analyzing the STK Gneiss samples, a weighted robust mean age from the three samples produced a value of 1812 ± 1.2 Ma and is taken as the emplacement age of the STK Gneiss. LA-ICP-MS data reveals, statistically, that the STK Gneiss experienced at least two distinct thermal events, as shown by peak probabilities at 1741 and 1815 Ma on the dark-grey probability distribution curves, and possibly another minor event between

1400 and 1500 Ma (Fig. 6.6b, d). The 1815 Ma has the highest probability and is interpreted as the main event.

b. Zircon Lu-Hf isotopic composition

Twenty Lu-Hf analyses (Table 6.4) were performed on zircon grains from sample RTB028, which were also analysed for U-Pb isotopes, using LA-ICP-MS at Curtin University. All of the $^{176}Lu/^{177}Hf$ ratios from the twenty analyses are less than 0.002 (0.000455 - 0.001656), consistent with a low level of radiogenic ^{176}Lu accumulation. They have coherent $^{176}Hf/^{177}Hf$ ratios of 0.281469 - 0.281725. Calculated $\varepsilon_{Hf(t)}$ values for concordant zircons, with a mean weighted age of 1798 Ma, are mostly negative, ranging from -7.1 to +1.96 (Table 6.4), suggesting that these zircons largely crystallised from magma derived from old continental crust (Patchett et al., 1981).

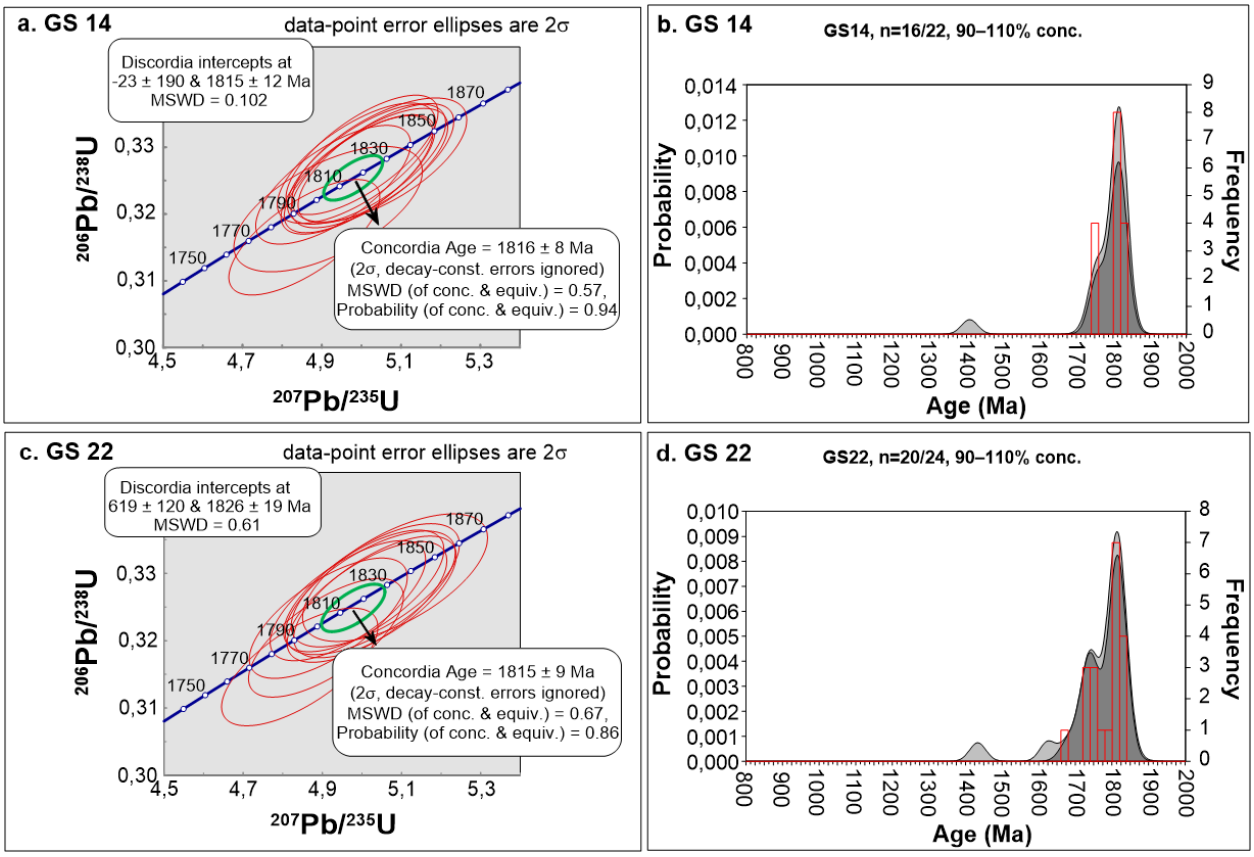

Fig. 6.6. *U-Pb isochron diagrams (**a** and **c**) and probability distribution vs. U-Pb zircon age data (**b** and **d**) of the Steinkopf Gneiss. **Dark grey** - zircon grains with 90-110 % concordance, **light grey** - more discordant zircon analyses, **red bars** - the frequency (n) of individual zircon populations.*

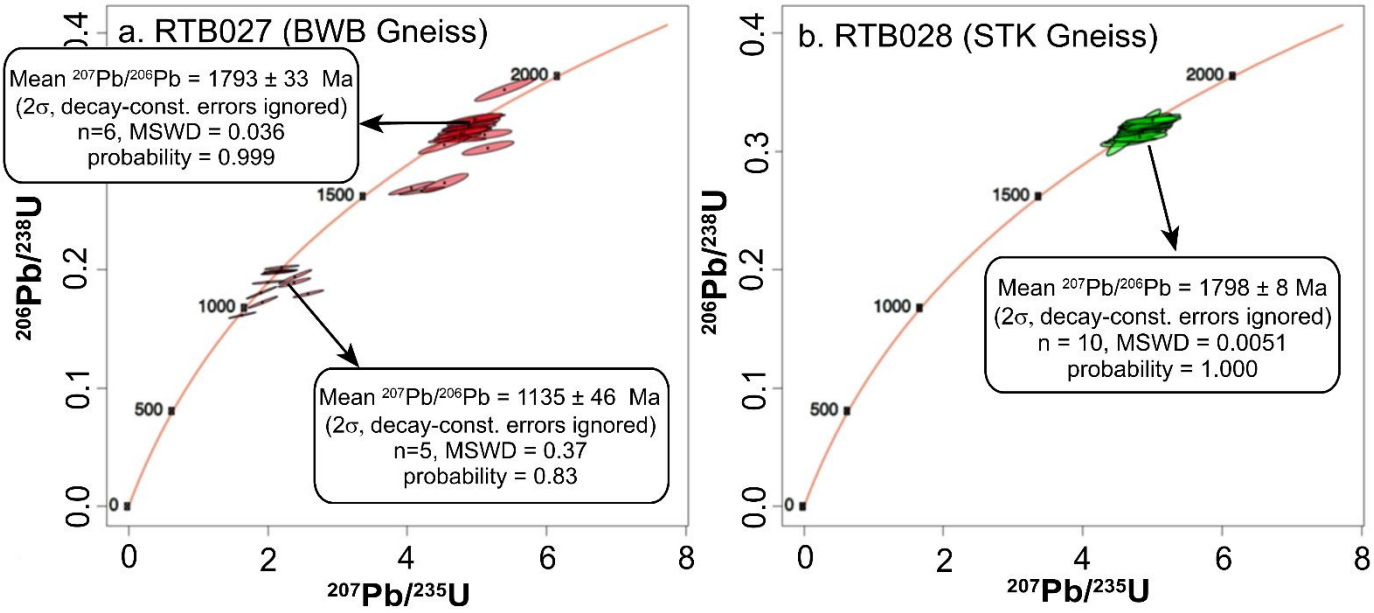

Fig. 6.7. *U-Pb isochron diagrams of the Brandewynsbank Gneiss* ***(a)*** *and the Steinkopf Gneiss* ***(b)*** *samples from P. Macey (pers. comm., 2018).*

Table 6.4. *U-Pb and Lu-Hf zircon ICP-MS data of the STK (RTB028) and BWB (RTB027) gneisses (for the complete dataset, refer to Appendix F, Tables F1 and F2).*

Analysis	U [ppm]	Pb [ppm]	Th/U meas.	$^{207}Pb/^{206}Pb$ Age [Ma]	2 □	$^{176}Yb/^{177}Hf$	2 □	$^{176}Lu/^{177}Hf$	2 □	Hf_{Total}	2 □	$^{176}Hf/^{177}Hf$	2 □	εHf(t)	2 □	LOCATION	Concordance vs. Discordance
Brandewynsbank Gneiss (RTB027)																	
RTB027 - 1	254	236	1.11	1814	11	0.031400	0.002300	0.001038	0.000071	2.050000	0.100000	0.281557	0.000067	-5.49	0.67	Core	discordant
RTB027 - 2	62	60	1.14	1800	23	0.020600	0.001500	0.000670	0.000032	1.854000	0.079000	0.281573	0.000067	-2.78	0.67	Core	CONCORDANT
RTB027 - 3	167	169	1.23	1796	15	0.034390	0.000590	0.001099	0.000033	1.871000	0.047000	0.281580	0.000140	-4.00	1.4	Core	discordant
RTB027 - 4	896	108	0.17	1174	17	No Lu-Hf data											
RTB027 - 5	2060	82	0.08	1008	8	0.033650	0.000130	0.001183	0.000010	2.326000	0.088000	0.282006	0.000091	-6.17	0.91	Rim	discordant
RTB027 - 6	125	167	1.44	1994	59	No Lu-Hf data											
RTB027 - 7	115	172	1.82	1789	22	0.047270	0.000580	0.001442	0.000024	1.805000	0.048000	0.281615	0.000092	-3.35	0.92	Core - ign conc zoned	CONCORDANT
RTB027 - 8	1327	63	0.09	1103	8	No Lu-Hf data											
RTB027 - 9	103	107	1.20	1792	17	0.027810	0.000220	0.000839	0.000004	1.823000	0.068000	0.281580	0.000120	-2.59	1.2	Core - ign conc zoned	discordant
RTB027 - 10	1590	78	0.08	1097	14	0.025200	0.001300	0.000970	0.000026	2.740000	0.120000	0.282014	0.000091	-3.56	0.91	Rim	CONCORDANT
RTB027 - 11	319	442	1.67	1801	10	0.039200	0.001800	0.001182	0.000039	1.880000	0.120000	0.281470	0.000100	-8.10	1		discordant
RTB027 - 12	119	154	1.45	1808	17	0.032330	0.000580	0.001043	0.000017	1.238000	0.016000	0.281670	0.000140	3.03	1.4		discordant
RTB027 - 13	192	182	1.11	1795	11	0.048700	0.001200	0.001630	0.000100	1.770000	0.200000	0.281566	0.000080	-4.62	0.8	Core	CONCORDANT
RTB027 - 14	1260	65	0.10	1149	9	No Lu-Hf data											
RTB027 - 15	133	139	1.22	1780	19	0.038700	0.000930	0.001171	0.000022	1.700000	0.088000	0.281520	0.000100	-11.42	1	Core - ign conc zoned	discordant
RTB027 - 16	1779	711	0.34	1685	39	No Lu-Hf data											
RTB027 - 17	1255	107	0.19	1211	14												
RTB027 - 18	105	121	1.38	1749	13	0.049800	0.001200	0.001568	0.000049	1.640000	0.063000	0.281570	0.000110	-6.11	1.1	Core - ign conc zoned	CONCORDANT
RTB027 - 19	84	117	1.62	1813	16	0.034940	0.000190	0.001060	0.000014	1.832000	0.065000	0.281510	0.000120	-5.98	1.2	Core	CONCORDANT
RTB027 - 20	1130	144	0.18	1426	76	No Lu-Hf data											
RTB027 - 21	110	166	7.64	1953	21	0.050500	0.001300	0.001473	0.000054	1.775000	0.058000	0.281653	0.000076	-6.54	0.76	Core - ign conc zoned	discordant
RTB027 - 22	501	298	0.53	1851	74	0.022090	0.000220	0.000738	0.000008	2.366000	0.097000	0.281851	0.000055	0.51	0.55	Core	discordant
RTB027 - 23	147	231	1.88	1772	22	0.051400	0.001200	0.001514	0.000033	1.716000	0.085000	0.281614	0.000080	-3.86	0.8	Rim	discordant
RTB027 - 24	1566	108	0.12	1160	6	0.015410	0.000250	0.000656	0.000006	2.530000	0.140000	0.281888	0.000077	-5.65	0.77	Core - ign conc zoned	CONCORDANT
RTB027 - 25	207	253	1.41	1801	9	0.038350	0.000600	0.001159	0.000010	1.861000	0.091000	0.281538	0.000086	-5.22	0.86	Core - ign conc zoned	CONCORDANT
RTB027 - 26	1280	235	0.29	1400	10	0.037270	0.000490	0.001258	0.000012	2.170000	0.120000	0.281697	0.000079	-11.64	0.79	Rim	discordant
RTB027 - 27	975	1100	1.27	1803	6	0.068400	0.002100	0.002180	0.000042	2.311000	0.059000	0.281569	0.000058	-4.56	0.58	Core	discordant
RTB027 - 28	1467	81	0.10	1162	7	No Lu-Hf data											
RTB027 - 29	3570	2540	0.05	3728	43	0.016520	0.000650	0.000868	0.000012	2.890000	0.110000	0.281804	0.000052	-24.34	0.52	Rim	discordant
RTB027 - 30	163	246	1.66	1919	13	0.046300	0.001400	0.001453	0.000029	1.564000	0.041000	0.281630	0.000120	-2.93	1.2	Core - ign conc zoned	discordant
Steinkopf Gneiss (RTB028)																	
RTB028 - 1	138	147	1.19	1808	14	0.035350	0.000990	0.001089	0.000020	1.841000	0.049000	0.281690	0.000091	0.97	0.91	Core - ign conc zoned	CONCORDANT
RTB028 - 2	129	167	1.51	1807	13	0.041700	0.001400	0.001295	0.000061	1.766000	0.069000	0.281628	0.000096	-2.23	0.96	Core - ign conc zoned	discordant
RTB028 - 3	180	323	2.05	1800	9	0.054900	0.003200	0.001623	0.000072	1.714000	0.048000	0.281550	0.000110	-5.05	1.1	Core - ign conc zoned	CONCORDANT
RTB028 - 4	188	215	1.29	1807	15	0.036590	0.000920	0.001097	0.000039	1.973000	0.075000	0.281501	0.000089	-6.10	0.89	Core - ign conc zoned	CONCORDANT
RTB028 - 5	161	237	1.76	1793	14	0.041100	0.001000	0.001229	0.000018	1.652000	0.048000	0.281630	0.000100	-2.80	1	Core - ign conc zoned	discordant
RTB028 - 6	258	322	1.46	1791	9	0.049200	0.001500	0.001518	0.000043	1.950000	0.035000	0.281538	0.000092	-6.81	0.92	Core - ign conc zoned	discordant
RTB028 - 7	126	180	1.60	1794	17	0.050100	0.001900	0.001451	0.000063	1.796000	0.062000	0.281540	0.000110	-5.26	1.1	Core - ign conc zoned	CONCORDANT
RTB028 - 8	99	101	1.12	1806	16	0.046000	0.002300	0.001399	0.000055	1.634000	0.055000	0.281680	0.000120	-0.01	1.2	Core - ign conc zoned	CONCORDANT
RTB028 - 9	148	211	1.66	1807	11	0.049110	0.000790	0.001445	0.000033	1.794000	0.079000	0.281570	0.000110	-4.97	1.1	Core - ign conc zoned	discordant
RTB028 - 10	144	49	0.46	1552	59	0.037050	0.000970	0.001153	0.000010	2.047000	0.092000	0.281624	0.000093	-8.78	0.93	core - inherited? !	CONCORDANT
RTB028 - 11	173	278	1.83	1823	21	0.057600	0.001700	0.001656	0.000036	1.838000	0.053000	0.281610	0.000110	-4.08	1.1	Core	discordant
RTB028 - 12	212	226	1.32	1631	17	0.034700	0.001000	0.001080	0.000017	2.121000	0.033000	0.281474	0.000049	-13.53	0.49	Core	discordant
RTB028 - 13	116	193	1.86	1794	18	0.041800	0.002200	0.001232	0.000044	1.710000	0.062000	0.281540	0.000130	-4.73	1.3	Core - ign conc zoned	CONCORDANT
RTB028 - 14	85	84	1.07	1801	14	0.035080	0.000700	0.001077	0.000012	1.549000	0.056000	0.281600	0.000130	-2.56	1.3	Core - ign conc zoned	CONCORDANT
RTB028 - 15	289	296	1.21	1813	11	0.033210	0.000300	0.001000	0.000004	2.032000	0.076000	0.281567	0.000061	-4.35	0.61	Core - ign conc zoned	discordant
RTB028 - 16	31	29	1.03	1762	26	0.014940	0.000300	0.000455	0.000004	1.704000	0.044000	0.281610	0.000120	-1.56	1.2	Core - ign conc zoned	CONCORDANT
RTB028 - 17	124	148	1.33	1804	11	0.030270	0.000820	0.000900	0.000017	1.801000	0.075000	0.281469	0.000084	-7.31	0.84	Core - ign conc zoned	CONCORDANT
RTB028 - 18	61	64	1.17	1785	23	0.028800	0.001800	0.000877	0.000061	1.726000	0.084000	0.281725	0.000089	2.03	0.89	Core - ign conc zoned	CONCORDANT
RTB028 - 19	119	140	1.32	1796	14	0.052250	0.000890	0.001523	0.000017	1.831000	0.034000	0.281588	0.000086	-3.27	0.86	Core	discordant
RTB028 - 20	86	113	1.51	1770	21	0.036600	0.001400	0.001104	0.000023	1.446000	0.095000	0.281600	0.000130	-4.18	1.3	Core	discordant

Ign-Igneous

6.3.3. BWB Gneiss

a. Zircon U-Pb results

The BWB samples (GS 28B, GS 30, GS 37 and RTB027) generally host the largest zircon crystals, with 80% of the crystal population made up of 150 to 250 µm long crystals (Fig. 6.8a-d). Most of the zircon crystals are euhedral to subhedral, but stubby types are also present which display more pronounced zonation relative to the former. CL images reveal magmatic zonation, cores of varying sizes and new dark overgrowths (Fig. 6.8a-d). Where present, dark rims are thin and vary in size up to 15 µm (Fig. 6.8a-d). Zircons of the BWB Gneiss generally have concentrically-zoned cores with low to medium U contents (60-200 ppm) and rims with high U contents (300-3500 ppm) (Table 6.3; Appendix F, Table F1).

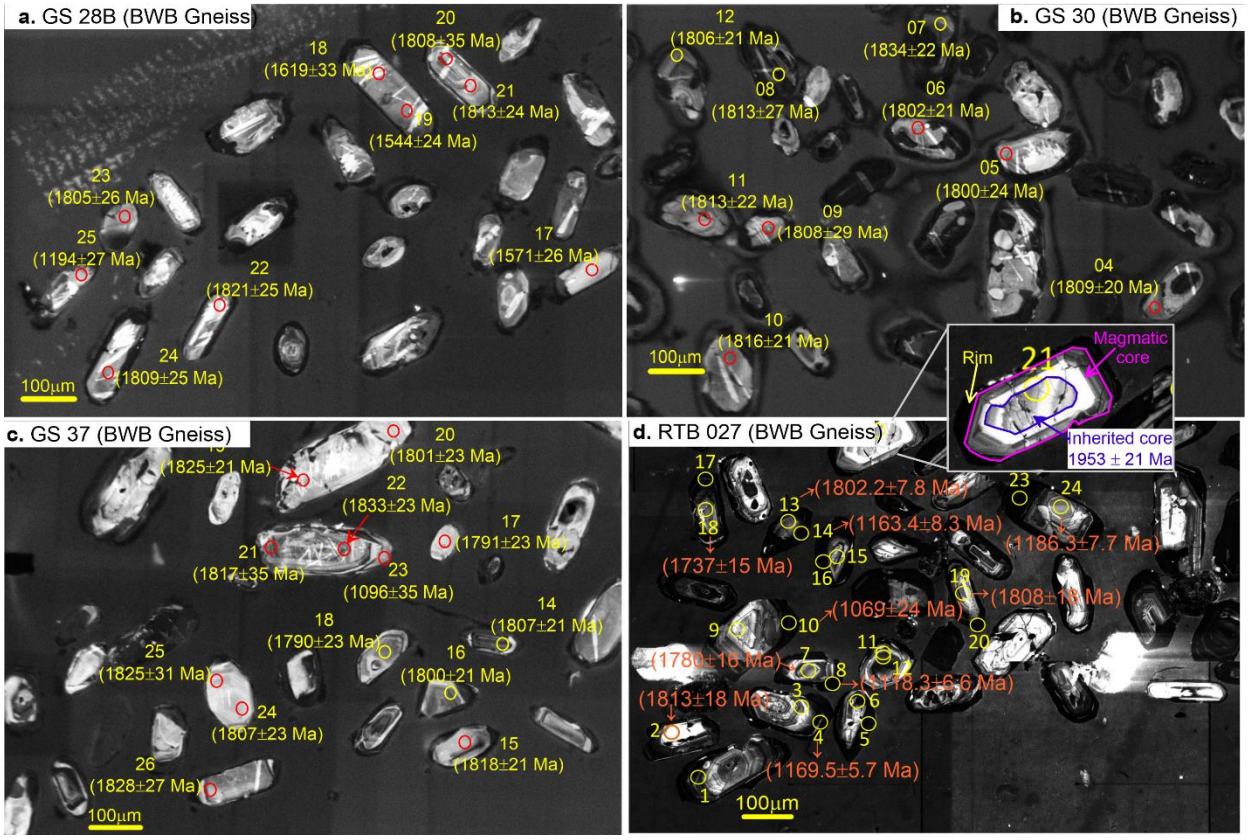

Fig. 6.8. *Zircon CL images of the dated Brandewynsbank Gneiss samples. Ages reported next to representations of analysed spots (circles) are $^{207}Pb/^{206}Pb$ ages with 2σ error from Table 6.3 (GS 28B, GS 30 and GS 37) and Tables 6.4, F1 (RTB027).*

Zircon Th/U ratios for sample GS 28B generally range from 0.87-1.48 and U concentrations vary from 69-317 ppm (Table 6.3). However, spot GS 28B-25 has a Th/U ratio of 0.09, with a U concentration of 310 ppm and a $^{207}Pb/^{206}Pb$ age of 1194 Ma (Table 6.3). Out of the twenty-five (25) spots analyzed, twenty-one (21) provided concordant data (Fig. 6.9b), with majority of the of the spots (n = 14) providing ages between 1800 and 1820 Ma, and minor distributions at 1740 Ma (n = 2), 1500-1560 Ma (n = 4) and 1180 Ma (n = 1) (Fig. 6.9b). Peak

probabilities suggest that zircons formed (or were affected) at three separate events: 1194 Ma (probably related to emplacement of the LNS), 1557 Ma and 1815 Ma (Fig. 6.9b). The four remaining spots (GS 28B-06, -08, -15 and -18) provided discordant ages belonging to three main groups: 1550 - 1560 Ma, 1619 Ma and 1812 Ma (Fig. 6.9b; Table 6.3). The twenty-one (21) spots with 99-102% concordance provided a concordia age of 1814 ± 9 Ma (MSWD = 0.1) (Fig. 6.9a).

Zircon Th/U ratios for the analyzed spots on sample GS 30 generally range from 0.48-1.24 and with U concentrations varying from 67-710 ppm (Table 6.3). One analyzed spot (GS 30-03), however, has a Th/U ratio of 0.1, and a discordant $^{207}Pb/^{206}Pb$ age of 1200 Ma (Table 6.3). Out of the nineteen (19) spots analyzed, ten (10) provided data with 100-102 % concordance, with the remaining nine providing discordant ages in two main groups, namely 1200 Ma and 1700-1800 Ma (Fig. 6.9d). Fourteen spots yielded 90-110 % concordance, and most (n = 13) provided ages between 1780 and 1820 Ma, with only a minor population (n = 1) at 1200 Ma (Fig. 6.9d). There are two peak probabilities in the age spectrum, as shown by the probability density distribution curves, with the highest probability at ~1809 Ma interpreted as the main zircon formation age, which were later affected an ~1200 Ma thermal event (Fig. 6.9d). The concordant data spots provided a concordia age of 1814 ± 9 Ma (MSWD = 0.41) (Fig. 6.9c), which is within error of the upper intercept age of 1804 ± 14 Ma (MSWD = 1.3) provided by the entire dataset, including the more discordant data.

Zircon Th/U ratios for sample GS 37 generally range from 0.85-1.72 and U concentrations vary from 61-615 ppm (Table 6.3). Spot GS 37-23 has a Th/U ratio of 0.05, and has a discordant $^{207}Pb/^{206}Pb$ age of 1096 Ma suggesting the rim is of metamorphic origin. However, it lies on a fairly bright rim, as opposed to a typical dark unzoned metamorphic rim (Fig. 6.8c). Spot GS 37-31 has a ratio of 0.29 with a discordant age of 1082 Ma (Table 6.3). Out of the thirty-one (31) spots analyzed, twenty-nine (29) provided 90-110 % concordant data, with the age spectrum indicating that zircons predominantly formed between 1720 - 1820 Ma (n = 27), with a minor age population at 1080 Ma (n = 2) (Fig. 6.9f). There are two statistically distinct thermal events, with peak probabilities at 1087 Ma and 1812 Ma (Fig. 6.9f). Only seventeen (17) spots provided 99-102 % concordance, and yielded an average concordia age of 1813 ± 6 Ma (MSWD = 0.56) (Fig. 6.9e). All the spots, including the more discordant data, provided an upper intercept age of 1815 ± 15 Ma (MSWD = 0.59).

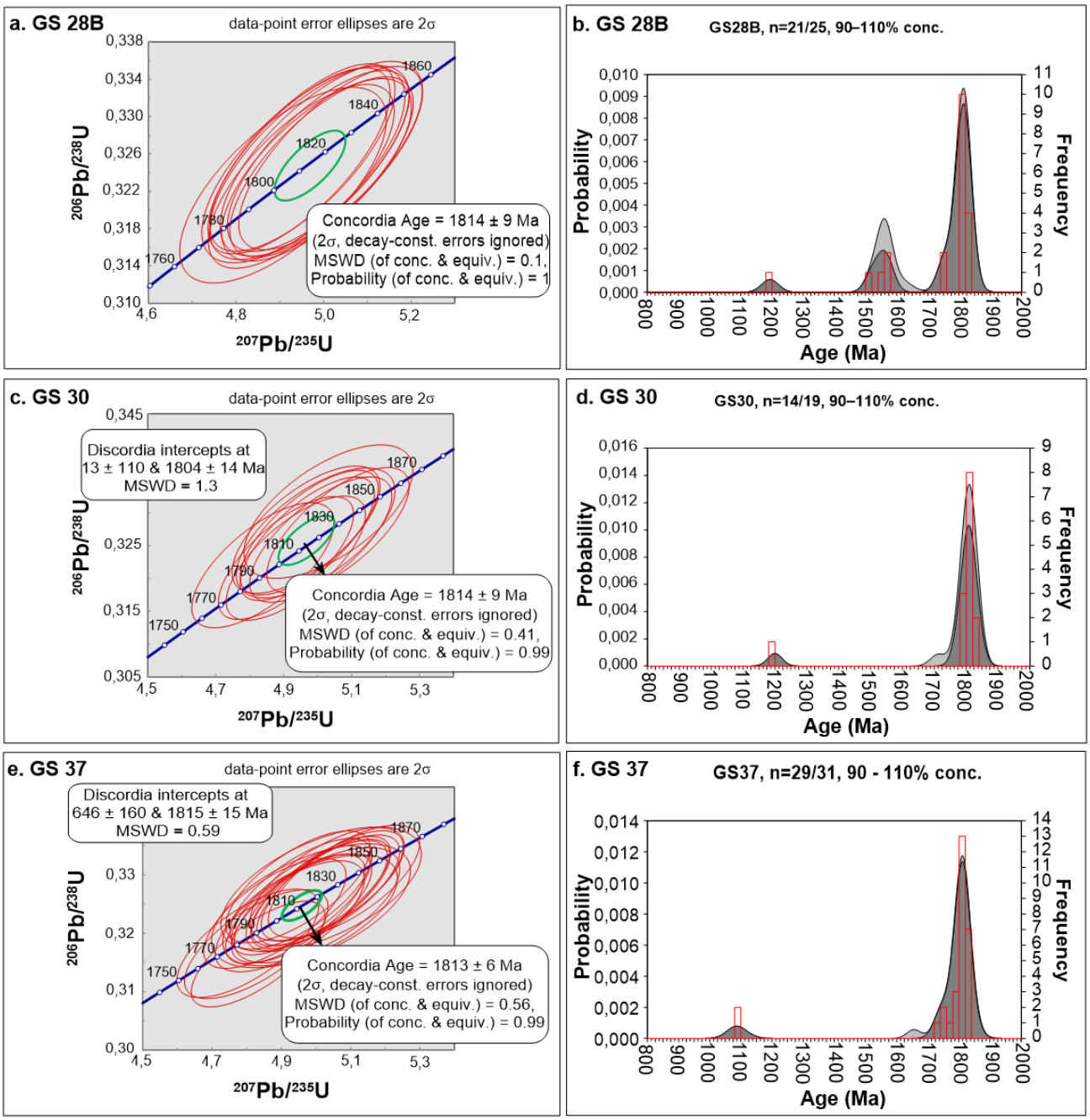

Fig. 6.9. *Probability distribution and histogram (red blocks, $^{207}Pb/^{206}Pb$ ages) plots of U-Pb zircon age data for the Brandewynsbank Gneiss. The number (n) of zircons analysed that are between 90 and 110 % concordant are also shown.*

Sample RTB027 is a compositionally homogeneous medium-grained, grey biotite gneiss collected from the south of Steinkopf about 10 km north of the Ratelpoort Synform (-29.4077S, 17.8136E; Fig. 6.1). The sample has an equigranular texture and contains a mineral assemblage of quartz (30-45 %), K-feldspar (30-45 %), plagioclase (10-20 %) and biotite (5 %) (P. Macey, pers. comm., 2018). Zircons separated from this sample are mainly euhedral in shape with most zircons varying in length between 80 and 150 µm (Fig. 6.8d). Most grains have obvious oscillatory zoning.

Zircon Th/U ratios for this sample generally range from 0.12 to 1.74 for the core, and from 0.04 to 0.32 for rims (Table 6.4). However, spot RTB027-21 (core) has a ratio of 7.5 with a U content of 109.9 ppm and a discordant age of 1738 Ma, while spot RTB027-23 (rim) has a ratio of 1.8 with a U content of 147 ppm and a discordant age of 1772 Ma (Table 6.4). Out of the thirty spots analyzed, twelve (seven cores and five rims) produced concordant ages. The seven analyses of cores yielded $^{207}Pb/^{206}Pb$ ages between 1749 ± 13 and 1813 ± 16 Ma (Appendix F, Table F1), with a weighted Tukey's Biweight mean age (Hoaglin et al., 1983) of 1793 ± 23 Ma, and is interpreted as the period of emplacement of this BWB sample (Fig. 6.7a). One core analysis (RTB027-024), however, yields a $^{207}Pb/^{206}Pb$ age of 1160 ± 6 Ma (Appendix F, Table F1). The five analyses of rims yielded $^{207}Pb/^{206}Pb$ ages between 1097 ± 14 Ma and 1174 ± 17 Ma (Table F1), with a robust weighted mean age of 1135 ± 47 Ma interpreted as the period of metamorphism of this sample (Fig. 6.7a). Based on the emplacement ages for all the above GS samples, the weighted mean emplacement age of the GS rocks is 1813 ± 48 Ma (Fig. 6.10).

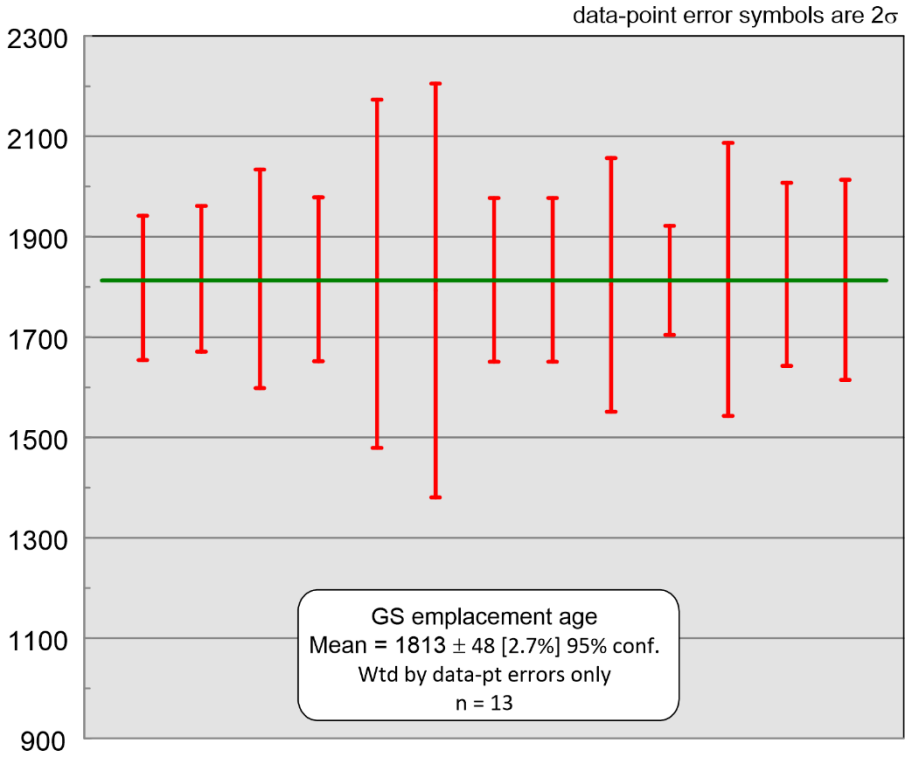

Fig. 6.10. *Weighted mean emplacement age of the Gladkop Suite gneisses.*

Based on the weighted ages obtained from the U-Pb data of the four BWB Gneiss samples, the age of emplacement of this gneiss is taken as 1814 Ma. The BWB Gneiss samples consistently illustrate a minor thermal event at ~1200 Ma, and the typical ~1800 Ma event in the NNM and STK gneisses, based on statistical probabilities as shown by the peaks on probability distribution curves for all the BWB Gneiss samples (Fig. 6.9). The ~1200 Ma event is poorly illustrated in the NNM and STK gneisses. The BWB Gneiss also illustrates an event which took place between ~1500 and 1600 Ma, which is consistently evident in both the STK and NNM gneisses, and could just represent a false signature brought about as a result of Pb loss, or could

represent an undocumented event. The three gneisses which make up the GS have consistent crystallization ages suggesting that these gneisses might be the product of the same magmatic event.

b. Zircon Lu-Hf isotopic composition

Twenty-two (22) Lu-Hf analyses (Table 6.4) were performed on zircon grains from sample RTB027. They have $^{176}Lu/^{177}Hf$ ratios ranging from 0.000656 to 0.002180, and similar $^{176}Hf/^{177}Hf$ ratios to the STK Gneiss sample, of 0.281470-0.282014. Calculated ε_{Hf} values of concordant zircons range from -5.7 to -2.9 (Table 6.4), suggesting that the parent magmas were derived from old continental crust (Patchett et al., 1981).

CHAPTER 7

DISCUSSION

This discussion focusses on a number of key points on the formation and evolution of the GS rocks, based on the questions of the lithostratigraphic and temporal equivalence of the migmatitic Steinkopf Gneiss, the K-feldspar megacrystic Brandewynsbank Gneiss, and the pink leucocratic Noenoemaasberg Gneiss; the origin and nature of the protolith rocks to the GS orthogneisses, the geochemical characteristics of the GS gneisses, the petrogenetic model for the granites and their relationship to the Richtersveld Magmatic Arc (RMA), as well as their role in the formation of the western Namaqua Sector. This discussion begins with the geochemical characterization of the GS rocks, and comparing their major and trace element concentrations to well documented rock suites. Following this is a discussion on the nature and origin of the protolith to the GS rocks, and includes the type, the source and the possible processes which affected the rising magma(s) generated from partial melting of these source rocks. The next section discusses the geotectonic settings in which the GS rocks were emplaced, followed by the age distribution in the GS rocks, and their significance. In the final sections, the relationship between the GS and VS rocks is discussed and an overview of the evolution of the GS rocks is summarized.

7.1. Geochemical characterization

The Precambrian continental crust is dominated by grey gneisses made up mostly of sodic granitoids commonly referred to as tonalite-trondhjemite-granodiorite (TTG) suite (Jahn et al., 1981). Unlike true TTG (Martin et al., 2005), the GS gneisses are: (1) potassic in nature with high K_2O and relatively low Na_2O contents (K_2O/Na_2O > 1.0; Table 5.1); (2) have high Y and Yb contents (Table 5.2); (3) have low Sr/Y ratios (Table 5.2); and (4) are characterized by moderately fractionated REE patterns (Fig. 5.8). The GS gneisses are also characterized by high SiO_2 (avg. 70 wt. %; Table 5.1, Fig. 5.3) and moderate to low ferromagnesian contents (mean $Fe_2O_3^T$ + MgO <5 wt. %; Table 5.1) (except for the STK Gneiss), with small to moderate Eu anomalies (Eu/Eu* = 0.25-0.83; Table 5.3, Fig. 5.8). These gneisses have higher SiO_2 contents and lower Mg# values relative to sanukitoids (Shirey and Hanson, 1984). The GS gneisses are granitic to granodioritic, magnesian, with a high-K calc-alkaline affinity and with a metaluminous to weakly peraluminous character (Figs. 5.5, 5.6; Table 5.1). In addition, these rocks have ASI values between 0.9 and 1.1, are weakly corundum normative (< 1 %; Table 5.1) and typically have high incompatible element (except Sr) and low compatible element concentrations (Table 5.2; Fig. 5.4). The GS gneisses also show more enrichment in light REE relative to heavy REE (Table 5.3; Fig. 5.9).

Geochemically, the STK Gneiss is distinct from the BWB and NNM gneisses in that it has lower SiO_2 contents (65-72 wt. %; mean = 69 %) and K_2O/Na_2O values (0.5-1.6; mean ~ 1), with higher Al_2O_3 (13-15 %; mean = 14 %) and ferromagnesian contents ($Fe_2O_3^T$ + MgO = 3-7; mean ~ 5 %) (Table 5.1). The STK Gneiss also shows the highest enrichment in the light REE and the least fractionation of the heavy REE, relative to the BWB and NNM gneisses, while the NNM

Gneiss shows the least enrichment in the light REE and the most fractionation of heavy REE (Table 5.3; Figs. 5.8, 5.9). In addition, the STK Gneiss is more enriched in the medium REE in relation to the light and heavy REE. The NNM Gneiss has the highest concentration of incompatible elements (e.g. Ba, Pb, Th and Rb; Table 5.2; Fig. 5.8), suggesting it is the most fractionated (evolved) of the three GS gneisses, as opposed to the STK Gneiss which has relatively low incompatible element concentrations, indicating it is the least fractionated. This is further supported by REE and multi-element fractionation patterns (Fig. 5.8).

There are slight variations observed in the geochemical dataset between the samples from this study and those from Van Aswegen (1983), Barton (1983) and Reid and Barton (1983), and are taken to represent the difference in laboratories, instruments and methods used to measure the elemental and isotopic concentrations. The reasoning behind this stems from the observation that, although there are slight differences in the datasets, the overall conclusions drawn from them are similar, if not the same.

7.2. Nature and origin of igneous protolith to the Gladkop Suite orthogneisses

7.2.1. Source rock typology

The protolith to the GS orthogneisses corresponds geochemically to Cordilleran-type granitoids (Frost et al., 2001; Frost and Frost, 2008) formed in post-collisional and arc settings. Osbourn (1959) attributed their primarily magnesian character to formation under oxidizing conditions. The zircon population of the STK Gneiss samples generally show a constant/simple morphology (Section 6.3.2) which is in line with I-type protolith rocks (Poller, 1999). Furthermore, ASI values have been used to distinguish I-types from S-types. For S-type granites, the plot of ASI vs. (Fe + Mg) produces a positive slope, while I-type granites produce a negative slope (Clemens et al., 2011). The GS samples produce a negative slope typical of I-type granites on the plot of ASI vs. (Fe + Mg) (Fig. 7.5), providing further evidence that the protoliths to the GS gneisses were I-type granites. It is shown that P_2O_5 concentrations are very low in the GS granites, and decrease with increasing SiO_2 concentrations (Fig. 5.3), whereas Pb increases with increasing SiO_2 (Fig. 7.1a). Y concentrations are generally high in the GS granites, but for samples with more than 70 wt. % SiO_2 increase dramatically, by about four (4) times average crustal concentrations (Fig. 5.4). These are very important characteristics in differentiating between I- and S-type granites (Chappell and White, 1992), suggesting that the protolith rocks to the GS orthogneisses are not S-type, but belong to the I- or A-types. According to Whalen et al. (1987), characteristics of A-type granites include $Fe_2O_3^T/MgO > 10$, $Zr+Nb+Ce+Y > 350$ ppm and $(Na_2O+K_2O)/CaO > 10$. Although the GS samples show high HFSE contents (Zr+Nb+Ce+Y), the $Fe_2O_3^T/MgO$ and $(Na_2O+K_2O)/CaO$ ratios are significantly lower than those of typical A-type granites (Fig. 7.1b, c). In the discrimination diagrams of Whalen et al. (1987) shown in Fig. 7.1b and c, the GS gneisses straddle the fields of A-types and fractionated felsic granites with the NNM Gneiss clearly the most fractionated. In addition, the absence of mafic alkaline minerals such as arfvedsonite, riebeckite, etc. and Al-rich minerals such as cordierite and muscovite in the GS gneisses strongly suggests that they belong to I-types. As opposed to previously published data, the GS gneisses are interpreted as I-type granites in this study, with the NNM being the most fractionated, and the STK Gneiss the least fractionated.

The GS gneisses have similar $\varepsilon_{Nd(t)}$ values, and as such, the subsequent modelling assumes the same type of source for the individual gneisses which make up the GS Suite. The STK Gneiss samples, which seem to be the least differentiated of the GS gneisses, represent the compositions

closest to the source compositions and are thus considered in assessing the possible GS magmatic sources.

7.2.2. Possible sources

Based on Chappell and White (1974), I-type granites are generally accepted to have formed from melting of an igneous source rock, although the precise nature of suitable igneous protoliths remains a challenge. Also, experiments involving partial melting of igneous and meta-igneous rocks of various compositions have provided evidence that it is impossible to produce the high- to medium-K series of I-type granites by melting basaltic rocks, as they are usually too Na-rich (Roberts and Clemens, 1993). These authors further suggested that if partial melts from a single source produce an I-type granite, then the source must be made up of potassic arc andesitic to dacitic and/or tonalitic rocks. Apart from low Rb/Sr ratios, any significant role of muscovite dehydration melting to produce the GS magmas can be discounted based on low Sr/Ba ratios of 0.1 to 0.3 (Harris and Inger, 1992), possibly eliminating the option of a granitic/rhyolitic source rock. In addition to being characterized by metaluminous to slightly peraluminous compositions (Fig. 5.6; Table 5.1), the GS gneisses have high CaO/Na_2O^{STK} ratios (~ 0.6-1.2) and fairly low Al_2O_3/TiO_2^{STK} (~ 20-35), Rb/Ba^{STK} (~ 0.15) and Rb/Sr^{STK} (~ 0.4-1.1) ratios, possibly ruling out a metapelitic parentage source of the GS magmas (Sylvester, 1998). Furthermore, the slightly negative $\varepsilon_{Nd(t)}$ values are consistent with partial melting of crustal material to produce the protolith to the GS orthogneisses. These characteristics are consistent with melts generated from the partial melting of igneous rocks, possibly TTGs and granodiorite, in the shallow continental crust (Moyen, 2011). The GS magmas could also have been derived either from metapsammitic parents or by anatexis of K-rich orthogneisses, but according to Barbarin (1996) and Sylvester (1998), this distinction is difficult using geochemical characteristics.

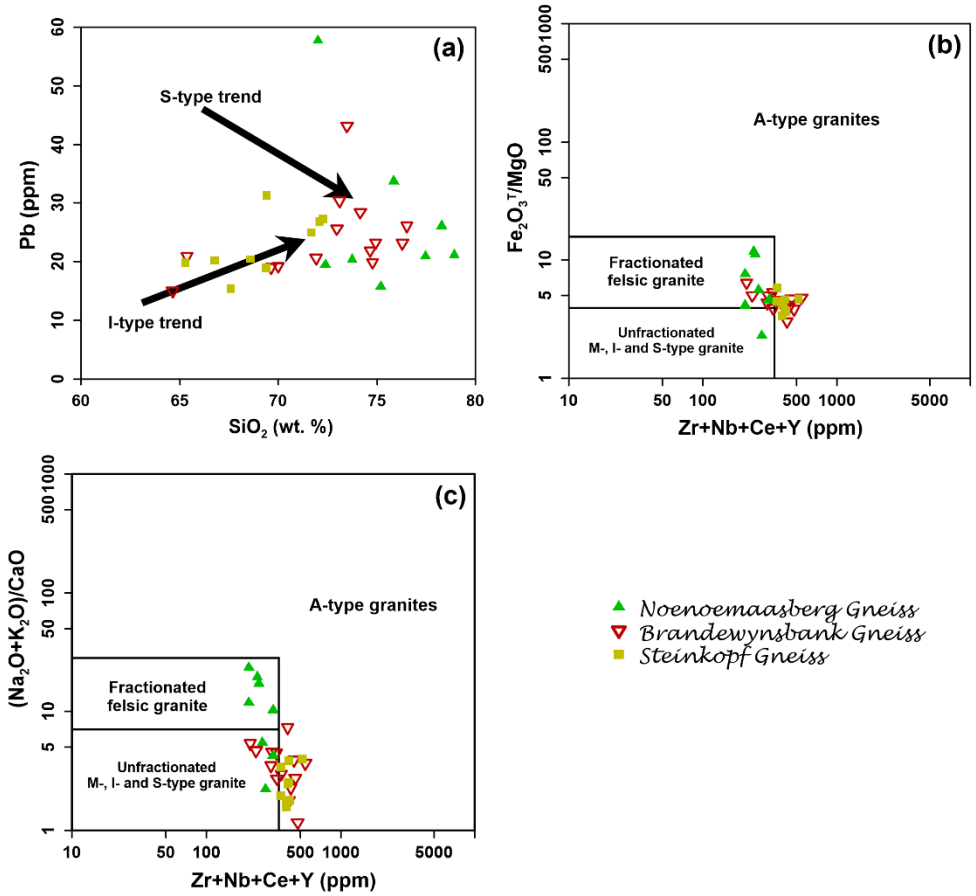

Fig. 7.1. (a) *Pb (ppm) vs. SiO_2 (wt. %) variation diagram showing that the Gladkop Suite orthogneisses follow the I-type trend proposed by Chappell and White (1992).* ***(b)*** *$Fe_2O_3^T$/MgO vs. (Zr+Nb+Ce+Y) and* ***(c)*** *(K_2O+Na_2O)/CaO vs. (Zr+Nb+Ce+Y) indicating that the Gladkop Suite orthogneisses are transitional between the I-, S-, M- and A-types or highly fractionated.*

The range in model ages (T_{DM} = 2.29-2.68 Ga) and slightly negative $\varepsilon_{Nd\ (1820)}$ values (-4.69 to -0.52) (Table 6.2), suggest that the GS magmas were derived from reworking of a slightly enriched Palaeoproterozoic source rock which first separated from the mantle between 2.29 and 2.68 Ga (and was remobilized at around 1815 Ma, the emplacement age of the GS rocks). The VS rocks have similar $\varepsilon_{Nd\ (1885)}$ values (-3.24 to 0.53; Table 6.2) to the GS gneisses, but these suites show distinct liquid-lines-of-descent as well as different geotectonic settings. The GS gneisses and VS rocks also have similar initial $^{143}Nd/^{144}Nd$ values of 0.510043 - 0.510256 and 0.510032 - 0.510225 respectively (Table 6.2). The initial $^{87}Sr/^{86}Sr$ ratios in the GS samples from this study range from 0.7070 to 0.7192, while those from Barton (1983) range from 0.7055 to 0.7129 (Table 6.1). The wide range in Sr isotopic range can be attributed to the effects of amphibolite facies metamorphism (Rollinson, 1993) in the Steinkopf area. The Nd-isotope signatures of the GS gneisses and the range of Sr-isotope concentrations are typical of crustal sources (initial Sr-isotope ratios of ~ 0.7069), indicating derivation from heterogeneous crustal sources (Pandey et al., 2011). The sub-chondritic $\varepsilon_{Hf(t)}$ values (Table 6.4) for the GS point to the generation of the GS magma(s) by reworking of pre-existing crust, and is in line with the negative $\varepsilon_{Nd(t)}$ values.

7.2.3. Magmatic evolution

This section presents a qualitative evaluation and description of the processes and minerals involved in the evolution of the GS magmas. Questions raised here include: (1) What fractional crystallization cumulate produced the GS gneisses? (2) What is the source of the K-feldspar augen in the BWB Gneiss which is clearly absent in the other two gneisses? (3) Could the compositional range (differentiation) observed in this igneous suite be the result of fractionation from a common parent?

From the zig-zag correlation coefficient patterns (Fig. 5.2), it can be seen that the GS magmas were likely affected by more than one magmatic process. Magma mixing is not considered here as one of the magmatic processes affecting the GS magmas due to inflexions created on trace and major element vs. SiO_2 plots (Figs. 5.3, 5.4), an observation which could rather suggest the role of fractional crystallization (Janoušek et al., 2016). Evidence of the latter is also seen from depletions in Ba, Sr, Nb, P, Ti and Eu, shown in the multi-element spider diagram (Figs. 5.8), and the high concentration of incompatible elements in the GS rocks (Section 5.5). Centered log-ratio covariance matrices of Aitchison (1986) (Table 5.4) reveal positive covariances between Fe, Mg, Mn, P and Ca as observed in the GS gneisses and is interpreted to highlight the role of peritectic assemblage and accessory minerals (possibly apatite, a ferro-magnesian mineral and/or Fe-Ti oxides) co-entrainment as variables contributing to the observed rock chemistry. Fractional crystallization and the role of PAE are further investigated.

a. Fractional crystallization

The importance of fractional crystallization in the evolution of the GS granitic gneisses is also evident from the almost vertical trends formed by the GS samples on log(incompatible) vs. log(compatible) plots, after Martin (1987) (Fig. 7.2). Eu anomalies are considered to be related to extensive plagioclase and/or K-feldspar fractionation (Rollinson, 1993).

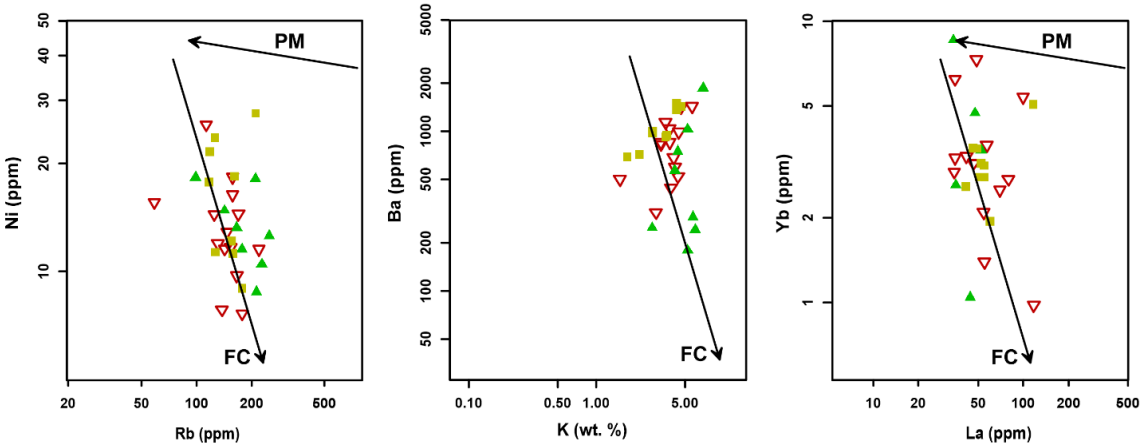

Fig. 7.2. *Log [Rb, K, La] vs. log [Ni, Ba, Yb] diagrams for the GS gneisses. The samples almost always plot along a slightly vertical line, suggesting that fractional crystallization (FC) is the main process controlling differentiation (after Martin, 1987). PM – Partial melting. Element compatibility and incompatibility in the GS gneisses is determined by correlation with SiO_2; positive correlation implying incompatibility and negative correlation implying compatibility (after Janoušek et al., 2016). Symbols are the same as in Fig. 7.1.*

Fractionation of plagioclase causes negative Sr and Eu anomalies, and fractionation of K-feldspar causes negative Eu and Ba anomalies (Rollinson, 1993; Glazner et al., 2006). Also, the moderate to strong negative covariance of CaO, Al_2O_3, K_2O and Sr relative to SiO_2 (Table 5.4), a Rb enrichment and the negative correlation of Eu/Eu* with SiO_2 are consistent with both plagioclase and K-feldspar fractionation from a rather siliceous source (SiO_2 ~70 wt. %) (Rollinson, 1993; Glazner et al., 2006). The negative anomalies observed in Nb and Ti are associated with fractionation of Ti-bearing phases (titanite, etc.) and the negative P anomalies are associated with the removal of apatite. However, Nb concentrations in the GS rocks are fairly constant with increasing SiO_2 (Fig. 5.7d). A decrease in Zr with increasing SiO_2 suggests zircon fractionation (Fig. 5.4). Low CaO and Sr values suggest that plagioclase was partly residual during melting, or that the source was depleted in plagioclase, possibly caused by previous melting episodes. These patterns are inconsistent with a partial melting model as the dominant cause of chemical variation in the GS rocks, as unreasonably large degrees of partial melting (>> 80 %) would be required to produce a broad compositional range (Janoušek et al., 1997), such as those observed in the GS gneisses.

Based on their compatibility with the petrogenetic processes taking place, Ba, Rb and Sr are used in identifying the possible mineral phases involved in fractional crystallization during the evolution of the GS magmas (Fig. 7.3a, b), as suggested by Janoušek et al. (2016). It should be noted that these elements behaved in a mobile way during metamorphism in the GS (Section 5.3), and as a result, are only used here to identify possible fractionating minerals without going into the details of the fractionating masses. Also, McCarthy and Robb (1978) suggested that the variations produced on Harker diagrams of SiO_2 vs. Ba, Sr and Rb rather reflect plagioclase/K-feldspar variation. In the log – log vector diagram of Ba vs. Sr (Fig. 7.3a), the STK and NNM gneisses lie on the same trend defined by a fairly sharp decrease in Ba in the early stages (high Sr) followed by a slower decrease (shallower slope) in the later stages (low Sr), while the BWB Gneiss defines a steeper more consistent trend. In the log – log diagram of Rb vs. Sr (Fig. 7.3b), the change from high Sr to low Sr is accompanied by a steep positive sloped defined by the STK Gneiss to a relatively shallower slope defined by the NNM Gneiss. The trends produced can be accounted for by the fractionation of an assemblage dominated by K-feldspar with minor biotite to produce the BWB magmas, and the fractionation of an assemblage of K-feldspar and plagioclase, with K-feldspar fractionation dominant in the STK magmas and plagioclase fractionation dominant in the NNM magmas.

It appears that there is a continuous trend from the STK Gneiss to the NNM Gneiss on both the log(Ba) and log(Rb) vs. log(Sr) plots (Fig. 7.3a, b). This is explained by fractionation of relatively more K-feldspar than plagioclase to produce the STK magma, and more plagioclase than K-feldspar to produce the NNM magma. This is evident in the petrography where the NNM Gneiss has K-feldspar as the dominant feldspar, as well as the highest covariance between Ba and Sr (Section 5.2), and in proportions significantly higher than in the BWB and STK gneisses. This suggests that the NNM Gneiss could represent extensive fractional crystallization products, with the less fractionated melts represented by the STK and BWB gneisses. The megacrystic BWB Gneiss, which is also intimately associated spatially with both the STK and NNM gneisses could represent evidence of early fractionation. The GS gneisses are characterized by low MgO contents which could suggest the fractionation of mafic minerals, and petrographic evidence suggests possible biotite fractionation. In a diagram of $(La/Yb)_N$ vs. Yb_N (Fig. 7.3c), plagioclase seems to play a significant role in the chemistry of the STK and BWB gneisses, with hornblende and clinopyroxene the dominant fractionating minerals in the NNM magmas.

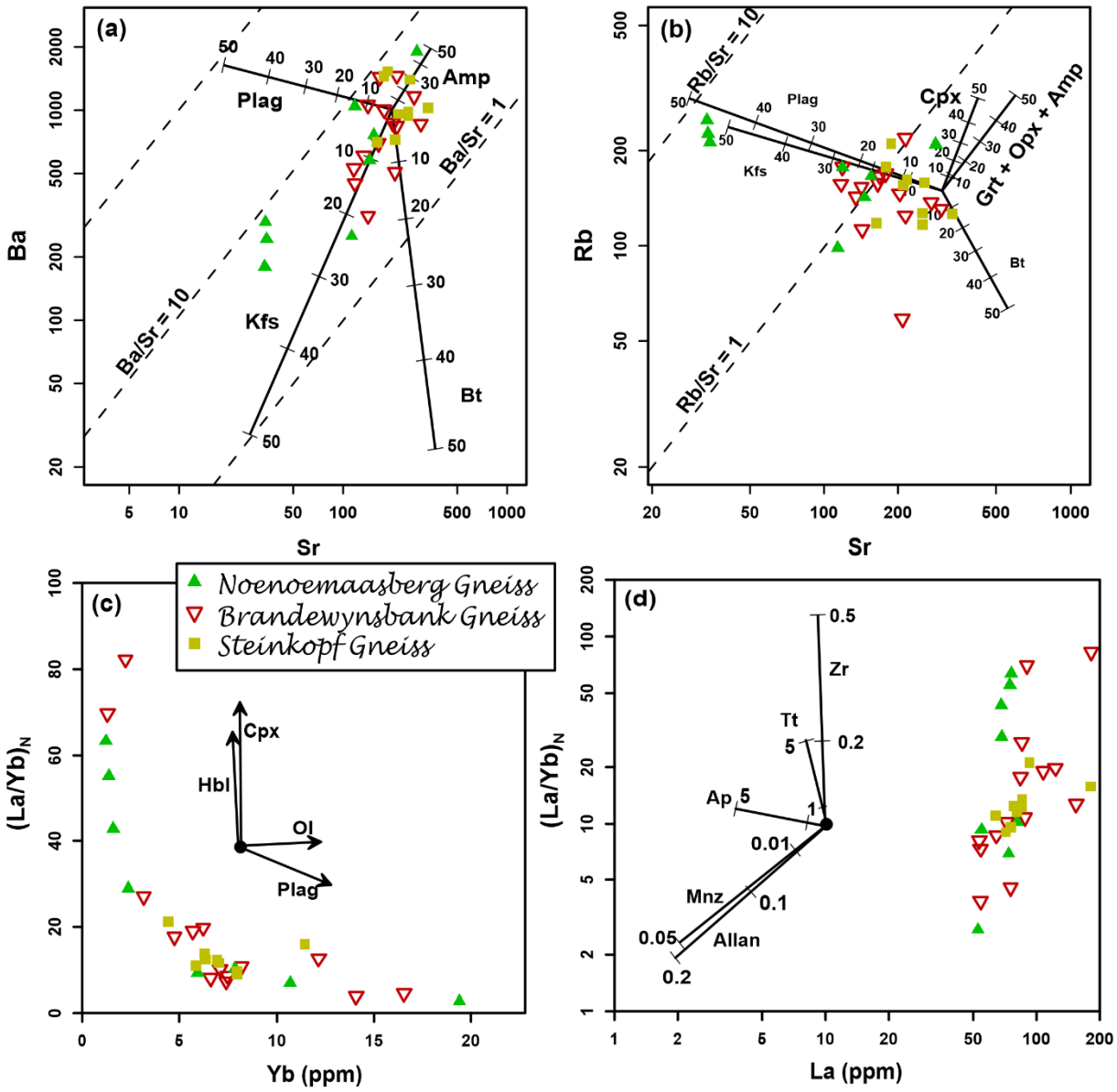

Fig. 7.3. (a) *Log Ba vs. log Sr; and* ***(b)*** *Log Sr vs. log Rb plots of the Gladkop Suite gneisses. The initial concentrations used were obtained by averaging the concentrations in the Steinkopf Gneiss, the least fractionated of all three gneisses.* ***(c)*** *$(La/Yb)_N$ vs. Yb_N,* ***(d)*** *$(La/Yb)_N$ vs. La diagram showing the change of REE patterns. In (a) and (b), labelled vectors correspond to up to 50 % fractional crystallization of the main rock-forming minerals. Partition coefficients are from Green and Pearson (1986) for sphene (titanite), Mahood and Hildreth (1983) for zircon, Green et al. (1989) for allanite and Yurimoto et al. (1990) for monazite. The rest of the partition coefficients are from Arth (1976).*

Taylor (1980) and DePaolo (1981) suggested that fractional crystallization (FC) and assimilation are generally combined and may occur simultaneously (AFC). However, Cribb and Barton (1986) suggested that these two processes may not always be related, in other words decoupled (FCA). As a result, these different scenarios are investigated using the FC-modeling Excel® spreadsheet by Ersoy and Helvacı (2010). The Bulk Continental Crust composition of

Taylor and McLennan (1995) was used as C_a, for the assimilant composition, based on the crustal origin of the GS magmas. A STK sample (GS 16), being the least fractionated, was taken to represent the starting composition (C_0) and has a Mg# of 37. An overall fractionating assemblage consisting of plagioclase and K-feldspar (30 % each), biotite (20 %) and equal proportions of amphibole and clinopyroxene (10 % each) was assumed, applying the partition coefficients for an intermediate melt composition (cf. references in Ersoy and Helvacı, 2010). Fig. 7.4 shows a comparison, between the trace element patterns produced by models of: (1) FC; (2) AFC; and (3) FCA, and those produced by the GS gneisses. An r-factor of 0.3 was assumed for the AFC model, and steps of 10 % were calculated for each model.

It is immediately obvious from Fig. 7.4 that AFC and FCA cannot account for the observed trace element pattern in the GS components given the above assumptions. This is true even with various other combinations of the fractionating assemblage. Moreover, this suggests that there is no continuous progression from the more mafic gneisses (STK and BWB) to the leucocratic NNM Gneiss in terms of their trace element abundances. FC is the only process, out of these three (FC, AFC and FCA) that can potentially account for the trace element systematics observed in the GS gneisses. Mixing was also modelled but similarly fails to account for the observed trace element patterns.

The REE variation in the GS gneisses seems to have been controlled by the accessory minerals (Fig. 7.3c), in combination with the major phases. The negative correlation between the REE and SiO_2 in the NNM and BWB gneisses is consistent with the separation of minerals with high partition coefficients, such as zircon, allanite and apatite; whereas REE concentration increases slightly with increasing SiO_2 in the STK Gneiss. Petrographic evidence suggests that these accessory minerals are important accessory minerals in the GS rocks. In a diagram of $(La/Yb)_N$ vs. La (Fig. 7.3d), zircon, and allanite, and titanite to a lesser extent seem to have been the main accessory minerals fractionated in the evolution of the NNM Gneiss, with allanite being the dominant phase in the evolution of the STK Gneiss. However, negative covariances between P and Ce, La and Th (Appendix C) rules out the fractionation of monazite in the evolution of the GS gneisses. Fractionation of allanite from the NNM and BWB gneisses is supported by positive Th and P covariances (Section 5.2) and the relatively greater LREE fractionation compared to the STK Gneiss. The megacrysts and relatively more mafic nature of the BWB Gneiss relative to the NNM Gneiss suggests that the BWB Gneiss was relatively less fractionated and began crystallizing at slightly deeper levels. The non-megacrystic BWB variety, which is more felsic than the megacrystic variety could represent the later, more fractionated BWB magmas which crystallised at the same level as the NNM and STK gneisses. Geochemical data of the two BWB varieties are required, however, to verify this.

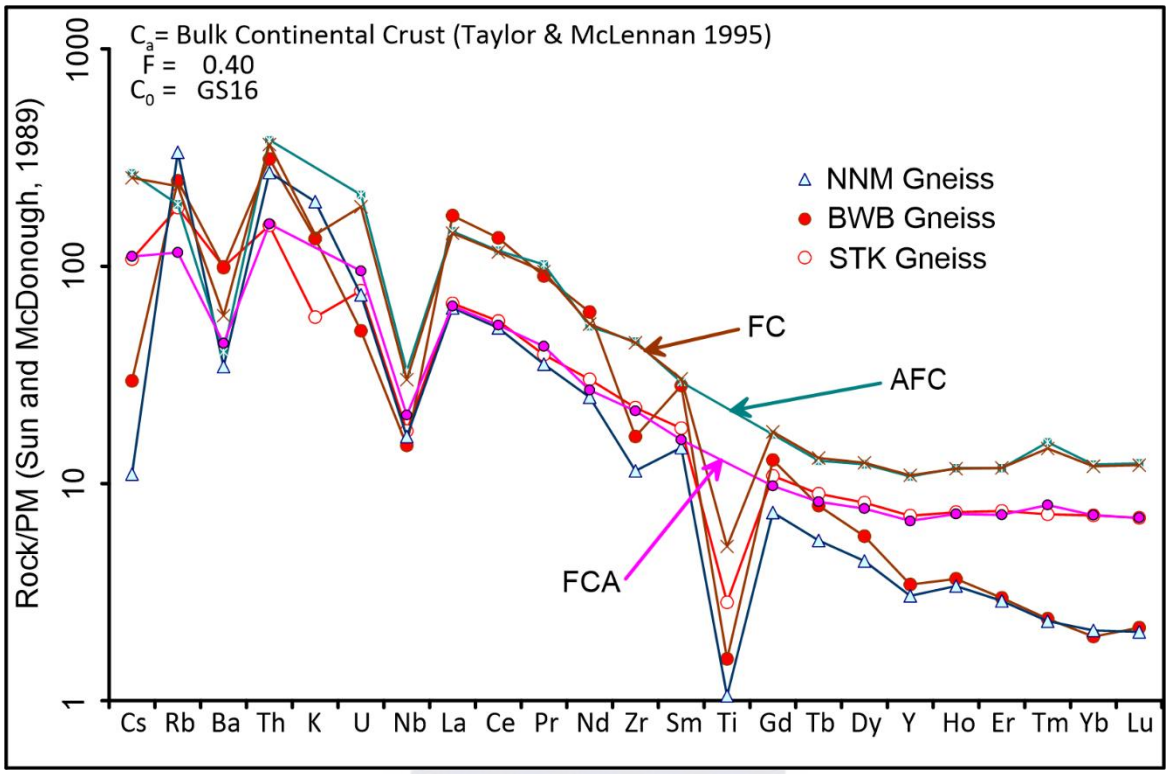

Fig. 7.4. *Fractional crystallization (FC), assimilation and fractionation crystallization (AFC) and decoupled fractional crystallization and assimilation (FCA) modelling of differentiation of the GS gneisses.*

b. Peritectic assemblage entrainment

Stevens et al. (1997) observed that although Ti, Fe and Mg are present in variable concentrations in granitic rocks, they are present in very low concentrations in the liquid melt portions of granitic magmas. Stevens et al. (2007) and Clemens and Stevens (2012) used this principle to differentiate between rocks which crystallized from 'pure' liquid magmas and those that crystallized from liquid melts which carried either crystalline material formed during peritectic melting reactions or inherited undissolved accessory mineral assemblages, commonly pyroxene, ilmenite, plagioclase or garnet (peritectic mineral assemblage). This phenomenon is referred to as peritectic assemblage entrainment (PAE). The association between Fe + Mg (termed maficity after Stevens et al., 2007) and selected elements in the GS gneisses is used here to investigate the role of PAE as a possible source of the observed chemical variations. Fe and Mg have similar electronegativities, and as a result occupy the same sites in ferromagnesian minerals, forming complete solid solutions. However, these elements have different atomic weight values (55.85 and 24.31 respectively). As a result of this difference, molar concentrations are used in binary maficity (Fe + Mg) plots rather than the traditional wt. % oxide plots. Using molecular concentrations eliminates variations in wt. % oxides introduced by the differences in Mg# [=100 x Mg / (Mg + Fe)] between samples, allowing trends observed on maficity plots to be attributed to either the addition or removal of ferromagnesian minerals, or mixing with another magma or mineral assemblage, without the influence of Mg#. The molar concentrations (M) are calculated as explained above Section 5.1).

Fig. 7.5 illustrates the covariations between Si, K, Na, Mg#, Ti, P, Ca, Zr, HREE (Dy + Ho +Er) and ASI with Fe + Mg (maficity) for the GS gneisses and the VS rocks. ASI values for the GS gneisses range from 0.9 to 1.1 but have a wider range in the VS rocks. Both the GS and VS rocks show negative slopes on the ASI vs. maficity plot, typical in I-type granites (Clemens et al., 2011). Na and K, which are derived from major reactant phases involved in the partial melting of source rocks, produce scattered positive and negative correlation patterns, respectively, with maficity (Fig. 7.5). In the VS rocks, there is no meaningful trend between Na and maficity. The negative pattern produced by K in both the VS and GS rocks can be attributed to its occurrence in the melt phase, which influences a decrease in its concentration as an entrained (melt-insoluble) phase increases in concentration (Clemens et al., 2011). The positive correlation between Na and maficity in the GS rocks could be attributed to its inclusion in the entrained mineral assemblage. Si decreases with maficity in both the VS and GS rocks, and can also be attributed to its concentration in the melt phase (Fig. 7.5). Ti, P, and Ca define tight positive correlations with maficity in the GS rocks (Fig. 7.5), and is interpreted as representing their low solubilities in the melt phase, most likely as a result of their inclusion in an entrained peritectic mineral assemblage dominated by a Ca-Fe-Mg-Ti bearing phase (commonly Opx + Cpx + Plag ± Grt ± Mag; Clemens et al., 2011). ASI values for both the GS and VS rocks decrease with increasing maficity (Fig. 7.5). The observed negative correlation in I-type granites can be attributed to the entrainment of a mineral capable of lowering ASI values in a magma, typically clinopyroxene which is a product of hornblende incongruent melting in rocks of intermediate to mafic composition (Clemens et al., 2011). Zr forms a steep positive correlation with maficity in the GS gneisses and a shallow positive correlation in the VS rocks (Fig. 7.5). The positive correlation can be attributed to co-entrained accessory zircon. Clemens et al. (2011) pointed out that at any given temperature and pressure, while the peritectic mineral assemblage concentrations in melts depends on the source composition, the amount of accessory minerals varies from melt to melt and depends solely on the amount of accessory phases transported. As a result, the limited scatter observed in the NNM Gneiss, relative to the STK Gneiss (Fig. 7.5), is taken to indicate higher zircon concentrations co-entrained in the STK Gneiss with respect to the NNM Gneiss. Similarly, the HREE vs. maficity plot shows a positive slope for the GS rocks (Fig. 7.5). Relatively more scatter is observed in the STK Gneiss (and shallower slope) relative to the NNM Gneiss and can be attributed to higher accessory alllanite concentrations in the former. Mg# vs. maficity plot shows a steeper (positive) slope for the NNM Gneiss relative to the STK Gneiss (Fig. 7.5), and is interpreted as a higher mafic (PAE) influence in the NNM Gneiss relative to the STK Gneiss. The STK Gneiss and the VS rocks show identical slopes on the Mg# vs. maficity plot (Fig. 7.5).

The effect of peritectic phase(s) entrainment in the evolution and compositional variation of the GS magma(s) may be shown in the very good, positive correlation between maficity and the components which occur predominantly in peritectic assemblages (such as Ti, P and Ca; Fig. 7.5). Maficity plots (Fig. 7.5) for the GS gneisses are consistent with felsic, peraluminous magma sources (Clemens et al., 2011). The K/Na ratios that characterize the GS rocks (K/Na >1; Table 5.1) are consistent with a melting reaction that has biotite as a major reactant phase (Clemens et al., 2011, and references therein). This, in combination with the suggestion that a PAE dominated by a (Ca-Fe-Mg-Ti)-bearing phase is generated from melting a hornblende-rich source (Clemens et al., 2011), implies that the source of the GS magmas underwent concurrent biotite and amphibole incongruent melting. Fluid-absent incongruent melting of these two phases produces both peritectic clinopyroxene (Cpx) and orthopyroxene (Opx), with the two pyroxenes forming an intergrowth at low pressures (Skjerlie and Johnston, 1996). The incongruent melting of both biotite

and hornblende produces ilmenite as the common Ti-bearing peritectic phase (e.g. Vielzeuf and Montel, 1994), and the positive correlation between Ti and maficity (Fig. 7.5) can be explained by entrainment of 1-2 wt. % ilmenite (Stevens et al., 2007). The significant positive covariance between V and TiO_2 in all of the GS gneisses (Appendix C, Table C2) supports the entrainment of ilmenite. The high partition coefficient of V in ilmenite in granodiorites is demonstrated by Latourrette et al. (1991). The maficity vs. ASI plot suggests the importance of clinopyroxene in the peritectic assemblage which drives the magma toward a metaluminous composition, as opposed to natural high-grade hornblende which would require significantly larger quantities to explain the negative correlation and would produce shallower slopes due to their aluminous and low SiO_2 contents (Clemens et al., 2011). A steeper slope would also be generated if orthopyroxene had a significant role in the peritectic assemblage entrainment. Plagioclase and garnet additions are also incapable of decreasing the ASI value. Petrographic evidence of clinopyroxene in the BWB Gneiss could possibly represent evidence of peritectic entrainment, as well as polycrystalline grains of Hbl, although detailed geochemical studies of these phases is required to gain insights to their origin. However, lack of unambiguous petrographic evidence of the occurrence of peritectic phases in the GS rocks makes the role of peritectic assemblage entrainment questionable.

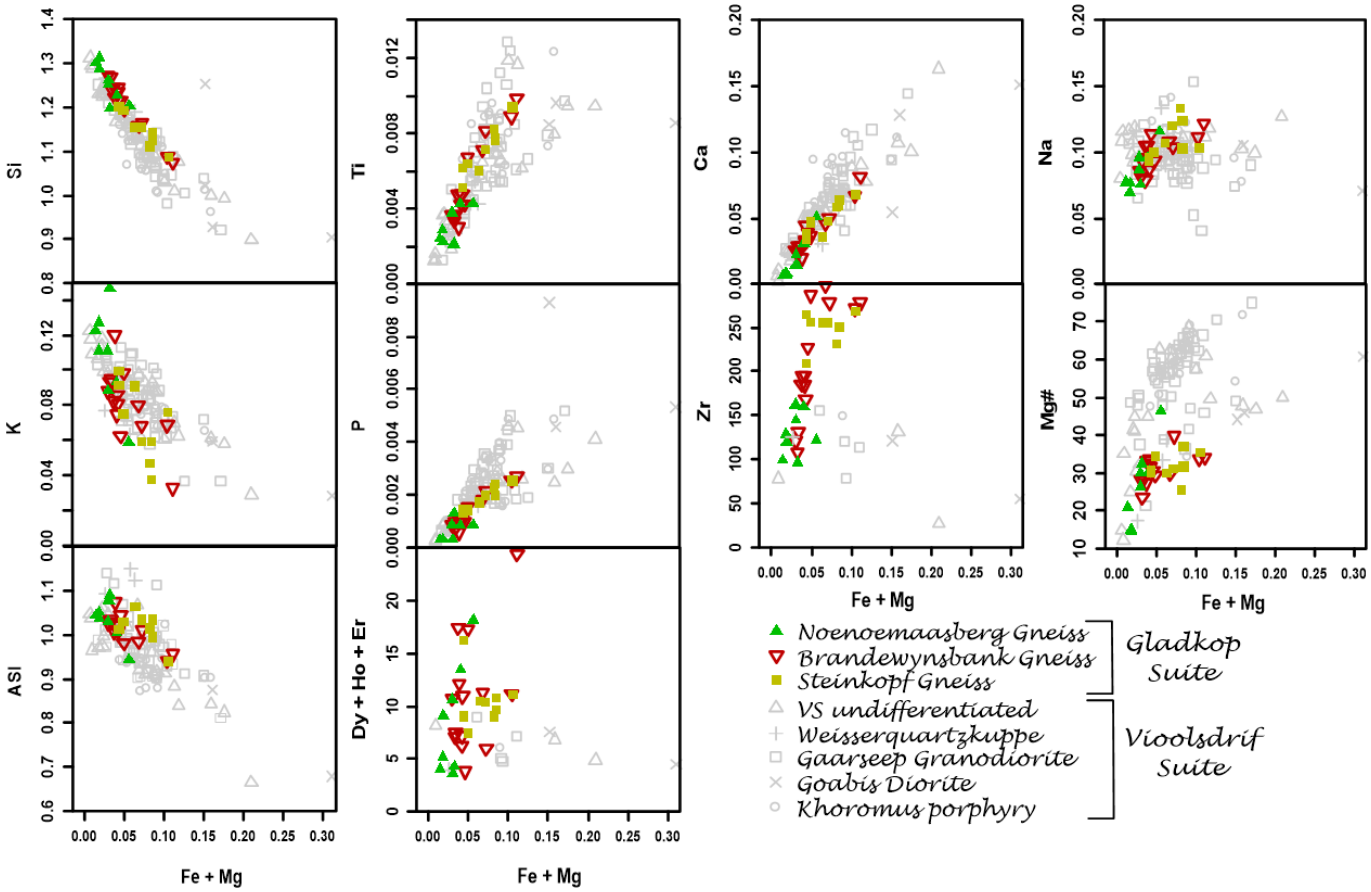

Fig. 7.5. *Plots of selected major and trace elements vs. maficity (Fe + Mg) of the Gladkop Suite and Vioolsdrif Suite rocks. Element concentrations are molar concentrations calculated as (wt. % oxide/molecular wt. oxide) x no. of cations.*

Protolith material that can produce felsic and mildly peraluminous melts which coexist with Cpx are typically metaluminous to weakly peraluminous, and include potassic andesitic and dacitic volcanic rocks (Roberts and Clemens, 1993; Skjerlie and Johnston, 1996). Assuming that the protolith rocks are andesitic to dacitic, this eliminates mixing between the partial melts and mafic magmas (increasing maficity) as it will be insufficient to drive peraluminous compositions toward a metaluminous composition as observed in the GS gneisses (Clemens et al., 2011). Other possible protolith materials could be Bt- and/or Hbl-rich granodioritic to tonalitic rocks which could produce reasonable amounts of melts through fluid-absent reactions (Clemens et al., 2011).

The negative covariance between P and Ce, La and Th rules out monazite from the peritectic phases in the GS gneisses. There is an inverse relationship between elements in feldspars and those which make up peritectic phases as shown by the invariable negative covariances between K and elements such as Ca, Mg, Fe, Mn and P. This relationship is consistent with the removal of feldspars with associated entrainment of mafic and accessory phases.

Other models which have been used to explain the formation of calc-alkaline I-type granites include: mixing between crustal melts and mantle magmas, assimilation of crustal rocks by mantle-derived mafic magmas and fractionation of mafic magmas. However, Gladzner (2007) and Clemens et al. (2011) showed that assimilation plays only a very small role, if any, in the chemical variations observed in I-type granites. The evidence of fractionation of mafic magmas to produce felsic I-type rocks, provided by Sisson et al. (2005), was largely controversial (Clemens et al., 2011). The mixing of crustal and mantle material can be confidently disregarded here due to the fairly constant $\varepsilon_{Nd(t)}$ values which point to a crustal source, its inability to account for the observed Ti-maficity ratios typical in I-type granites (Clemens and Stevens, 2012) and the absence of mafic enclaves.

7.3. Geotectonic settings

Granitoids form predominantly in subduction-related settings, although they can also form as a result of progressive maturation related to lower crust delamination or mantle upwelling (e.g. Moyen and Martin, 2012; Arndt, 2013, Laurent et al., 2014). The GS rocks are characterized by pronounced negative Nb and Ti anomalies, corresponding low Nb/Th ratios (0.1-3.1) and a calc-alkaline character, and, according to Pearce (2008) and Rollinson (1993), these characteristics are consistent with subduction-related (arc) environments.

Van Hunen and Moyen (2012) suggested that subduction in the Archean was short-lived and occurred in spatially limited subduction zones, but a change occurred between the late Archean and the Palaeoproterozoic (~2.0 Ga), from Archean to modern plate tectonics, resulting in long-lived and stable subduction zones. Researchers such as Laurent et al. (2014) attributed the change in subduction rate to either a thickness decrease of the oceanic crust and/or increase in volume/strength of the continental crust. If these theories are accepted as plausible, then the slow subduction rate and/or mantle convection in the Palaeoproterozoic (younger than 1.9 Ga) can account for the transitional tectonic settings of the GS rocks.

The multidimensional tectonic diagrams of Verma et al. (2012, 2013) suggest a transitional collisional to within-plate tectonic setting for the precursor to the GS gneisses (Section 5.6). Also, the emplacement of the GS rocks overlaps with the youngest metamorphic overprinting event in the VS rocks corresponding to the Orange River Orogeny (Fig. 7.6) (Blignault et al., 1983; Macey et al., 2017). This could be explained by emplacement of the GS protolith rocks in a

collisional to continental rift setting relating to the Orange River Orogeny, at a time when collision was waning and collapse was initiated due to crustal thickening (Blignault et al., 1983). If this scenario is the case, then the continental arc could be represented by the RMA, and that GS intruded during a collisional to post-collisional phase (within-plate setting) (Fig. 7.7).

7.4. Age distribution in the Gladkop Suite

The emplacement of the GS rocks occurred in the northern BD (NBD), during the Palaeoproterozoic, adjacent to the slightly older RMA (Macey et al., 2017) in the north. In the present study, new geochronological data reported is used to qualitatively determine the possible time frame of the petrogenesis of the precursors to GS orthogneisses. A summarized overview and comparison of U-Pb ages between the GS and VS rocks is also presented.

The GS rocks yielded discordia ages with upper intercepts varying between 1804 ± 14 and 1826 ± 19 Ma, and concordia ages between 1813 ± 6 and 1825 ± 10 Ma (Figs. 6.4a, c; 6.6a, c; 6.9a, c, e). The concordia ages, representing concentrically zoned cores, correspond to the crystallization of zircon during the emplacement (Corfu et al., 2003; Belousova et al., 2006) of the precursors to the GS orthogneisses in the Steinkopf locality (NBD). These ages provide a mean emplacement age of 1813 Ma. Considering dating errors, these ages are analogous to those reported by Barton (1983) (Rb-Sr whole-rock age of 1824 ± 70 Ma) and Robb et al. (1999) (SHRIMP U-Pb age of 1822 ± 36 Ma). These ages are significantly younger than the mean emplacement age of 1885 ± 12 Ma reported for the VS rocks in the RMA (Macey et al., 2017).

Older inherited cores found in three (3) zircon grains of sample RTB027 provide discordant $^{207}Pb/^{206}Pb$ ages of 1994 ± 59, 1953 ± 21 and 1919 ± 13 Ma (Appendix F, Table F1). Similarly, Robb et al. (1999) reported a xenocrystic core with a discordant $^{207}Pb/^{206}Pb$ age of 2018 ± 8 Ma from a BWB Gneiss sample. The inherited ages (1994, 1953 and 1919 Ma), together with those reported by Robb et al. (1999), are similar to the inherited ages in the VS rocks (Fig. 7.6) (Macey et al., 2017). The VS and GS rocks also have similar T_{DM} ages (2.2-2.8 Ga; Fig. 7.6). The T_{DM} and inherited ages, as well as similar $\varepsilon_{Nd(t)}$ values of -0.53 to -4.69 (GS) and 0.53 to -3.19 (VS) (Table 6.2) strongly suggests a similar origin for both set of rocks.

Metamorphism in the NS, as a result of the Namaqua Orogeny, has been recorded at ~1.2-1.14 Ga and again at ~1.0-1.06 Ga (Fig. 7.6; Robb et al., 1999; Clifford et al., 2004; Eglington, 2006). Also, a distinct magmatic event (extensional) has been recognized in the NS and dated at ~1.38-1.34 Ga, which Cornell et al. (2015) attributed to rifting, and Bial et al. (2015b) to back-arc extension. Furthermore, Reid et al. (1987) provided a sedimentation age of 1649 ± 90 Ma, although relatively new data indicates sedimentation possibly also occurred during two distinct periods in the Mesoproterozoic, 1300-1200 Ma and a younger succession deposited after the LNS (Robb et al., 1999; Raith et al., 2003; Eglington, 2006; McClung 2006; Bailie et al., 2007a, b; Cornell et al, 2009). Although more U-Pb age groups were obtained from the GS zircons, peak probabilities from the age distribution spectrum, corresponding to recorded geological events, occur at ~1815, 1741, 1654, 1557, 1237, 1200, 1194, 1087 and 1042 Ma (Section 6.3, Fig. 7.6). These peak probability ages are interpreted by comparing them to recorded ages of sedimentation, magmatism, metamorphic and tectonic events in the BD (Fig. 7.6). The peaks at 1200, 1194 and 1042 Ma can be explained by the intrusion of the LNS and the KS, and also correspond to recorded ages of metamorphic zircon growth in the BD (Fig. 7.6) (e.g. Eglington, 2006). The peak probability recorded at 1087 Ma corresponds to the intrusion of the KS, while ages recorded between 1100

and 1150 Ma (Section 6.3) correspond to granitic orthogneiss intrusive events (Fig. 7.6) (e.g. Robb et al., 1999; Bial et al., 2015b; Spencer et al., 2015).

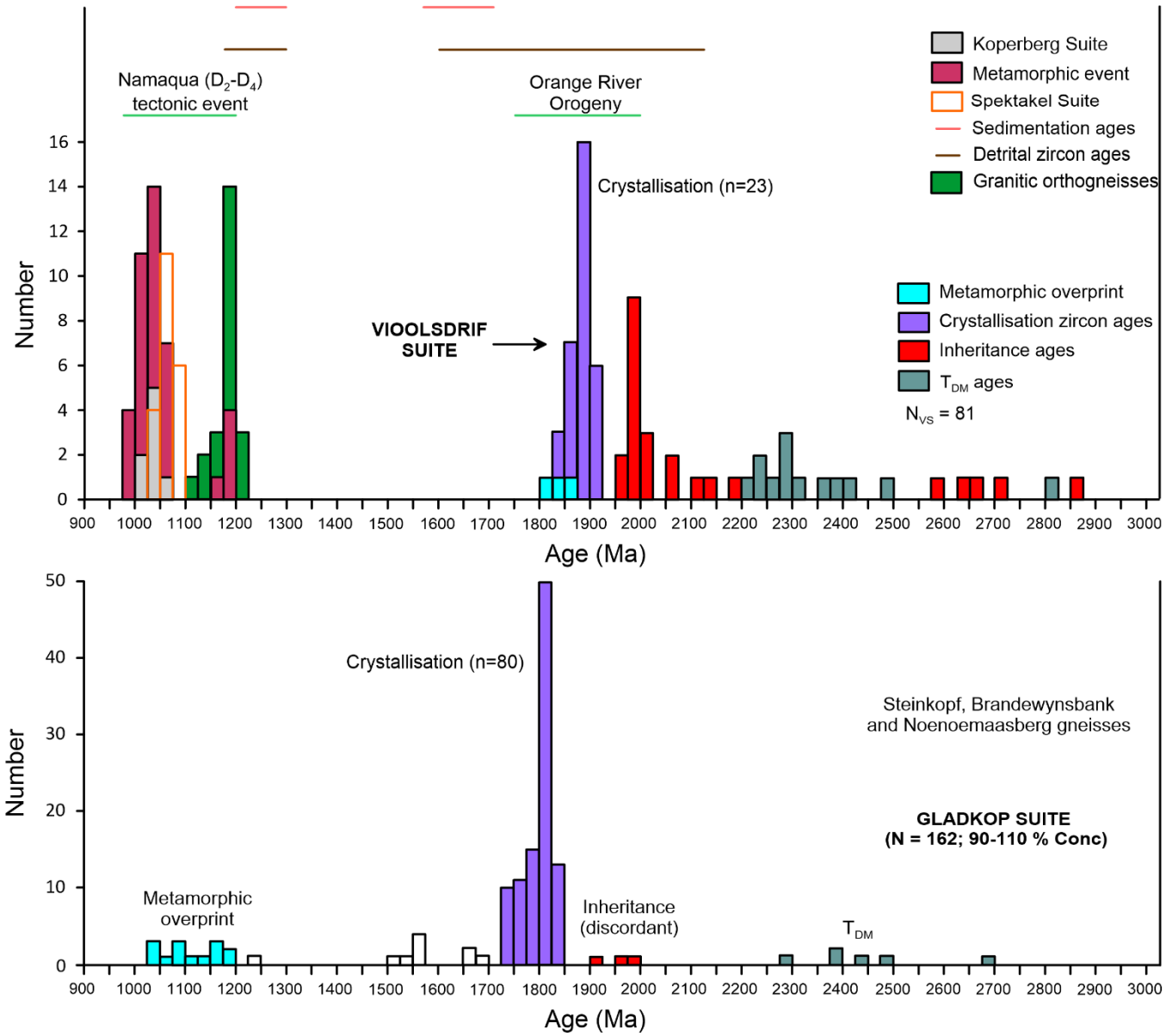

Fig. 7.6. *U-Pb zircon age data (90-110% concordant) of Gladkop Suite zircons compared to ages from the Vioolsdrif Suite rocks, as well as metamorphic, igneous and sedimentation ages from the Bushmanland Domain. The zircon crystallization and metamorphic overgrowth age data are sourced from Reid et al. (1987), Thomas et al. (1996), Reid (1997), Clifford et al. (1995, 2004), Ashwal et al. (1997), Robb et al. (1999), Grantham et al. (2000), De Beer et al. (2002), Eglington and Amstrong (2003), Raith et al. (2003), Eglington (2006), McClung (2006), Bailie et al. (2007a, b), Petterson (2008), Cornell et al. (2009), De Beer (2010), Macey et al. (2011, 2017, 2018). N represents the total number of ages.*

The extensional event reported by Cornell et al. (2015) and Bial et al. (2015b) can possibly explain the probability distribution curve at ~1.4 Ga recorded by the STK Gneiss (Fig. 6.6b, d). The events recorded at 1237 and 1654 Ma (Fig. 7.6) are interpreted as sedimentation ages in the BD, suggesting that the GS rocks acted as a supracrustal basement. Also, detrital zircon ages recorded

in supracrustal rocks in the BD correspond to emplacement ages of the GS (Fig. 7.6), supporting previous observations (e.g. McClung, 2006) that the GS rocks acted as a basement complex in the BD. The GS rocks acting as a basement would suggest that some of the U-Pb ages recorded between 1000 and 1200 Ma represent contractional or extensional events, or both. To date, no magmatic events have been recorded in the NS at ~1800-1700 and ~1500-1575 Ma. As a result, the peak probabilities at 1741 and 1557 Ma recorded by the GS rocks are considered geologically meaningless, and can be attributed to Pb-loss.

The STK, BWB and NNM gneisses have similar crystallization ages (1813-1825 Ma), possibly suggesting that they intruded penecontemporaneously, rather than at different times as previously suggested (Van Aswegen, 1983). The cross-cutting relationships described by Van Aswegen (1983) and from field evidence in this study, which suggest that the NNM Gneiss intruded the grey gneisses (also visible on a map scale, Figs. 4.1 and 4.2), could suggest magma injection occurred in three separate pulses, all from a single fractionating magma chamber. The age data, however, do not provide the resolution to distinguish the relative age relationships.

7.5. Relationship to the Vioolsdrif Suite, Richtersveld Magmatic Arc

The questions that need to be answered here are: (1) could the GS magmas be derived by partial melting of the VS intermediate to felsic rocks or by more extensive fractionation of the VS magmas? If the latter is the case, then the VS and the GS magmas could have a similar source, and (2) What was the maximum degree of melting allowed by such a source?

Both the GS and the VS have similar REE patterns (Fig. 5.8), as well as similar ε_{Nd} values (Table 6.2), T_{DM} and inheritance ages (Fig. 7.6). These suggest that both magmas were derived from slightly enriched fractionated sources which first separated at the same time from the mantle. The VS rocks are slightly more mafic than the GS rocks, the latter being more fractionated. The VS rocks have relatively lower incompatible element concentrations with respect to the GS rocks (Figs. 5.8, 5.9) and both suites have different chemical signatures, defining a completely different liquid-line-of-descent (Figs. 5.3, 5.4, 5.6a, c). These suggest that the GS rocks are more fractionated than the VS rocks. Also, emplacement ages in the GS correspond to metamorphism in the VS rocks (Macey et al., 2017; Fig. 7.6). This metamorphic overprint coincides with the Orange River Orogeny, and together with the age gap in the mean emplacement ages of the VS (~1885 Ma) and GS (~1813 Ma) rocks and evidence of a D_1 deformation event in xenoliths of the GS (Blignault, 1983;), suggests that the GS rocks were emplaced during the Orange River Orogeny and possibly during the later stages. The age and tectonomagmatic relationship between the GS and the VS could therefore suggest that magmatism lasted throughout the Orange River Orogeny.

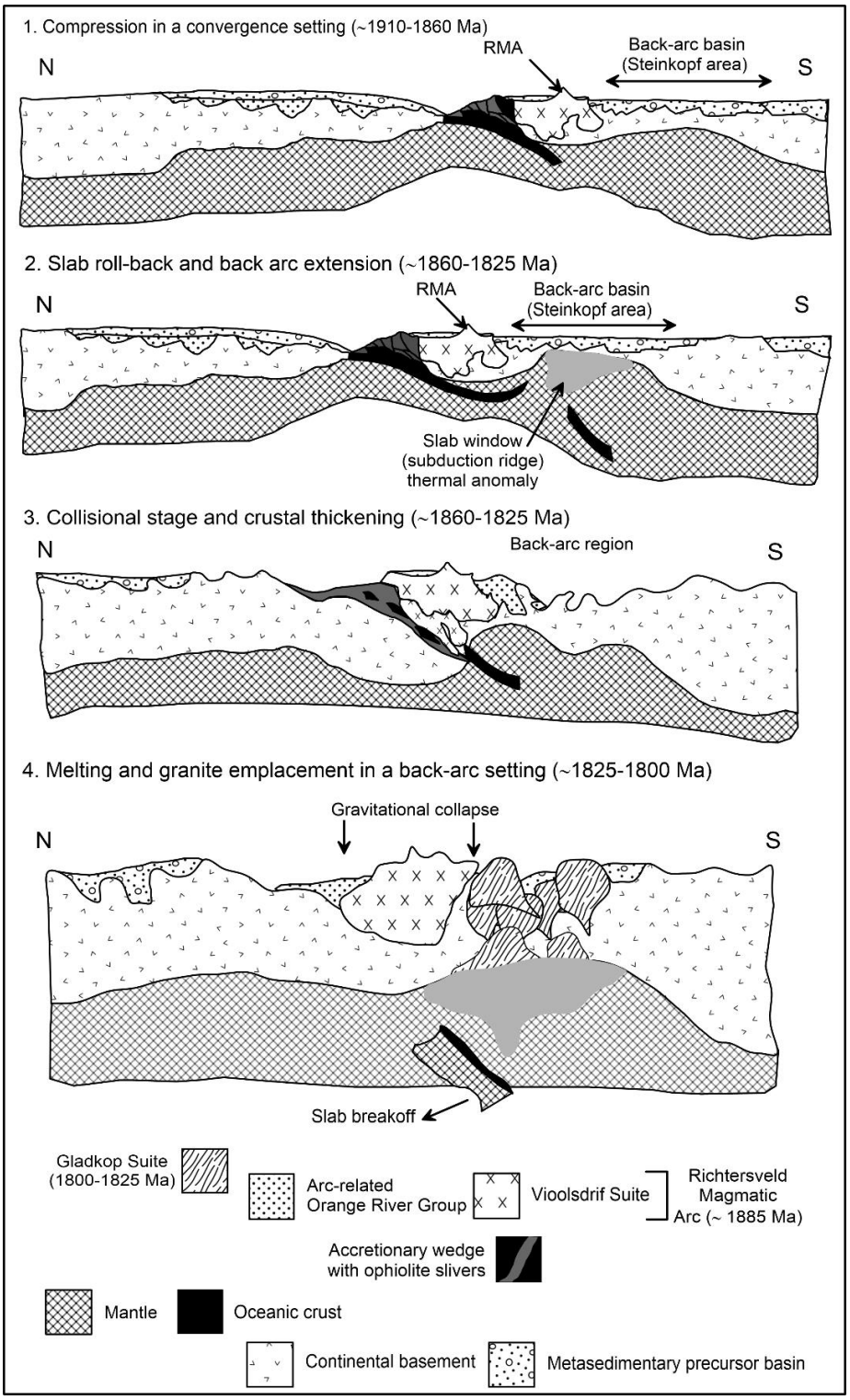

Fig. 7. 7. *Conceptual diagram illustrating the tectonic evolution of the Gladkop Suite rocks: (1) Northward convergence and compression between the RMA and a northern continental block; (2) Slab roll-back and back-arc extension; (3) Delamination, back-arc rifting and melting; (4) Emplacement of the Gladkop Suite plutons in a back-arc setting, the Steinkopf area; (5) End of emplacement of the Gladkop Suite plutons. GS-Gladkop Suite; RMA-Richtersveld Magmatic Arc. The positions of North and South are shown.*

7.6. A model for the evolution of the Gladkop Suite

In order to account for the formation of voluminous diversified syn- to post-tectonic magmatism involving reworking crustal material in a short period of geologic time, an adequate heat source is required, such as those generated by regional scale tectonic events. Researchers have proposed several models to explain how granitoid formation occurs as a result of a strong, short-lived external heat source in the final stages of the late-Archean tectonic cycle (e.g. Moyen et al., 2003; Van Hunen and Moyen, 2012; Laurent et al., 2014): (1) retreat ("roll-back") of the lithospheric mantle in the subducted slab; (2) break-off of the subducted slab which causes an inflow of mantle asthenosphere beneath the orogenic prism, resulting in a thermal anomaly and partial melting of the metasomatized lithospheric mantle; (3) amalgamation of pre-existing continents or arcs resulting in crustal thickening; or (4) delamination of the subcontinental lithospheric mantle beneath the upper plate.

We propose that the GS gneisses were emplaced towards the end of the Orange River Orogeny (which possibly evolved in atleast two stages) as shown in the cartoon representation in Fig. 7.7. In this model, the Palaeoproterozoic VS magmatic rocks were emplaced during the early stages (proposed stage 1) of the Orange River Orogeny in an arc setting, possibly volcanic island-arc setting (referred to as the RMA), adjacent to more continental material (possibly a magmatic arc to the north, the Sperrgebiet Arc; Thomas et al., 2016). The emplacement of the VS rocks was followed by sedimentation in the back-arc area. Subsequently, slab roll-back occurred, accompanied by extension in the back-arc region. The proposed stage 2 (Fig. 15) involved a collision between the northern continental material and the RMA, possibly converging in a southward migration, and subduction of the early intermediate (to mafic) VS rocks initiated due to crustal thickening. Subsequently, slab roll-back and tear off "behind" the arc (in the southward Steinkopf area) led to rifting and opening up of areas into which granites could intrude. Slab roll-back and delamination could add the necessary heat to melt the arc crust reworking it to produce granitic magmas, represented by the slightly younger more fractionated GS, which intruded during a collisional to post-collisional phase (within-plate setting).

CONCLUSIONS

This contribution provides whole-rock Sm-Nd, Lu-Hf isotope and comprehensive REE results for the first time, as well as new whole-rock geochemical and geochronological data of the GS gneisses from the northern BD, adjacent to the RMA. This study also provides new important constraints to understanding the formation of the GS orthogneisses by expanding the observed compositional heterogeneity and the temporal overlap of the STK, BWB and NNM gneisses in comparison to the VS rocks, RMA. The results lead to the following conclusions:

1. This study presents new petrographic and geochemical characterization of the GS gneisses. Geochemically, the precursor rocks to the GS gneisses are highly evolved rocks characterized as high-K (I-type) granitoids.
2. The GS rocks were generated by reworking of old continental crust as shown by Sm-Nd and Lu-Hf data.
3. Modelling using geochemical data shows that plagioclase, K-feldspar and biotite were fractionated during the GS magma ascend. Initially, K-feldspar was the dominant fractionated mineral, with minor plagioclase, producing the STK magmas. Then the fractionating pattern of the magma changed, fractionating more plagioclase, less K-feldspar, minor biotite as well as accessory and mafic minerals to produce the NNM and BWB magmas. These mafic and accessory minerals possibly include allanite, apatite, hornblende, clinopyroxene, magnetite, titanite and/or zircon.
4. The age of the GS gneisses (1813 ± 6 to 1825 ± 10 Ma) indicates that the protolith rocks to these gneisses intruded penecontemporaneously, and not at different times.
5. The GS rocks acted as a basement complex to the supracrustal rocks in the BD. This is evident from records of sedimentation events by the GS zircons, as well as detrital zircon ages corresponding to the emplacement of the GS rocks, hosted by the BD supracrustals.
6. The GS and VS possibly reveal an extended period of magmatism during the Orange River Orogeny as interpreted from the gap in their emplacement ages (1813 and 1885 Ma, respectively) which occurred during the same tectonic event, the Orange River Orogeny. The GS rocks formed from remelting of the early formed VS phases, as a result of crustal thickening.

Recommendations for further research

1. From the sample locations on the Gladkop Suite distribution map, it can be seen than most of the work done in this project focused on the west. We suggest further sampling more to the east and a comparison and/or integration of the data with the data obtained from this study.
2. More isotope data is required to confirm the relationship between both suites.

References

Abdallah, N., Liégeois, J., De Waele, B., Fezaa, N., Ouabadi, A. (2007). The Temaguessine Fe-cordierite orbicular granite (Central Hoggar, Algeria): U-Pb SHRIMP age, petrology, origin and geodynamical consequences for the late Pan-African magmatism of the Tuareg shield. Journal of African Earth Sciences 49, 153-178.

Agrawal, S., Guevara, M., Verma, S.P. (2008). Tectonic discrimination of basic and ultrabasic volcanic rocks through log-transformed ratios of immobile trace elements. International Geology Review 50, 1057-1079.

Aitchison, J. (1981). A new approach to null correlations of proportions. Math Geol 13, 175-189.

Aitchison, J. (1984). The statistical analysis of geochemical compositions. Math Geol 16, 531-564.

Aitchison, J. (1986). The Statistical Analysis of Compositional Data. Chapman and Hall, London, UK, 416 pp. ISBN:0-412-28060-4

Albat, H.M. (1979). The Kliprand area - a major charnockite province in Namaqualand. Annual Report, Precambrian Res. Unit, University of Cape Town 7, 49-64.

Albat, H.M. (1983). Garnet-cordierite thermometry/barometry and the temperature-pressure conditions of formation of granulite-facies metapelites in the Kliprand area. Annual Report, Precambrian Res. Unit, University of Cape Town 18-20, 105-115.

Albat, H.M. (1984). The Proterozoic granulite facies terrane around Kliprand, Namaqualand Metamorphic complex. Bulletin, Precambrian Res. Unit, University of Cape Town 33, 386.

Arndt, N.T. (2013). Formation and evolution of the continental crust. Geochemical Perspective 2, 405-533.

Arth, J.G. (1976). Behaviour of trace elements during magmatic processes - a summary of theoretical models and their applications. J. Res. U.S. Geol Surv. 4, 41-47.

Ashwal, L.D., Andreoli, M.A.G., Page, T., Armstrong, R.A., Tucker, R.D. (1997). Geology and geochronology of high temperature granulites, Vaalputs area, central Namaqualand, South Africa. Abstr 13th Conf Tectonic Division Geol Soc S Afr, Johannesburg, 1-3.

Bachmann, K., Schulz, B., Bailie, R., Gutzmer, J. (2015). Monazite geochronology and geothermobarometry in polymetamorphic host rocks of volcanic-hosted massive sulphide mineralizations in the Mesoproterozoic Areachap Terrane, South Africa, Journal of African Earth Sciences. Elsevier Ltd. 111, 258-272.

Bailie, R., Armstrong, R. Reid, D. (2007a). The Bushmanland Group supracrustal succession, Aggeneys, Bushmanland, South Africa: Provenance, age of deposition and metamorphism. South African Journal of Geology 110, 59-86.

Bailie, R., Armstrong, R., Reid, D. (2007b). Composition and single zircon U-Pb emplacement ages of the Aggeneys Granite Suite, Bushmanland, South Africa. South African Journal of Geology 110, 87-110.

Bailie, R., Macey, P.H., Nethenzheni, S., Frei, D., le Roux, P. (2017). The Keimoes Suite redefined: The geochronological and geochemical characteristics of the ferroan granites of the eastern Namaqua Sector, Mesoproterozoic Namaqua-Natal Metamorphic Province, southern Africa. Journal of African Earth Sciences 134, 737-765.

Bailie, R., Abrahams, G., Bokana, R., van Bever Donker, J., Frei, D., le Roux, P. (2019). The geochemistry and geochronology of the upper granulite facies Kliprand dome: Comparison of the southern and northern parts of the Bushmanland Domain of the Namaqua Metamorphic Province, southern Africa and clues to its evolution. Precambrian Res. 330, 58-100.

Barbarin, B. (1996). Genesis of the two main types of peraluminous granitoids. Geology 24, 295-298.

Barker, F. (1979). Trondhjemite: definition, environment and hypotheses of origin. In Trondhjemites, dacites, and related rocks. Edited by F. Barker. Elsevier, New York. 12 pp.

Barton, E. (1983). Reconnaissance isotopic investigations in the Namaqua mobile belt and implications for Proterozoic crustal evolution - Namaqua Geotraverse. In: Botha, B.J. V. (Ed.). Namaqualand Metamorphic Complex. Spec. Publ. Geol. Soc. South Africa 10, 45-66.

Bédard, J.H., Harris, L.B., Thurston, P.C. (2013). The hunting of the sn Arc. Precambrian Res. 229, 20-48.

Belousova, E.A., Griffin, W.l., O'Reilly, S.Y. (2006). Zircon crystal morphology, trace element signatures and Hf isotope composition as a tool for petrogenetic modelling: Examples from Eastern Australian Granitoids. Journal of Petrology 47, 329-353.

Beukes, G.J. (1973). 'n Geologiese ondersoek van die gebied suid van Warmbad, Suidwes-Afrika, met spesiale verwysing na die metamorf-magmatiese assosiasies van die Voorkambriese gesteentes D.Sc. Thesis. University of the Orange Free State, Bloemfontein. 333 pp.

Bhattacharya, S., Janwari, S. (2015). A short Review on Lu-Hf Isotope System in Zircon: Implications for Crustal Evolution. Journal of the Indian Institute of Science 95(2), 147-158.

Bial, J., Büttner, S. H., Frei, D. (2015a). Formation and emplacement of two contrasting late Mesoproterozoic magma types in the central Namaqua Metamorphic Complex (South Africa, Namibia): Evidence from geochemistry and geochronology. Lithos 224-225, 272-294.

Bial, J., Büttner, S.H., Schenk, V., Appel, P. (2015b). The long-term high-temperature history of the central Namaqua Metamorphic Complex: evidence for a Mesoproterozoic continental back-arc in southern Africa. Precambrian Res. 268, 243-278.

Bial, J., Büttner, S., Appel, P. (2016). Timing and conditions of regional metamorphism and crustal shearing in the granulite facies basement of south Namibia: Implications for the crustal evolution of the Namaqualand metamorphic basement in the Mesoproterozoic, Journal of African Earth Sciences 123, 145-176.

Blignault, H.J. (1974). Aspects of the Richtersveld province. In: Kröner, A. (Ed.), Contributions to the Precambrian geology of Southern Africa. Bulletin, Precambrian Res. Unit, Univ. Cape Town 15, 49-56.

Blignault, H.J. (1977). Structural-metamorphic imprint on part of the Namaqua mobile belt in South West Africa. Bulletin, Precambrian Res. Unit, Univ. Cape Town 23, 197 pp.

Blignault, H.J., Marais, J.A.H., van der Merwe, S.W., van Aswegen, G., Muller, J.A. (1980). The Namaqualand Geotraverse. A 1:250 000 Geological Map Sheet: contribution by the University of the Orange River Free State and the O'okiep Copper Company to the South African National geodynamics programme. Spec, Publ. of the Geol. Soc. S. Afri. 10, 29 pp.

Blignault, H.J., Van Aswegen, G., Van der Merwe, S.W., Colliston, W.P. (1983). The Namaqualand geotraverse and environs: part of the Proterozoic Namaqua mobile belt. In: Botha, B.J.V. (Ed.), Namaqualand Metamorphic Complex. Special Publication, Geological Society of South Africa 10, 29 pp.

Bonhomme, M. (1962). Contribution a l'étude géochronologique de la plate-forme de l'Ouest africain. Thèse. Ann. Fac. Sci. Univ. Clermond-Ferrand, Fr., Géol. Minéral 5, 62 pp.

Butler, J.C., Woronow, A. (1986). Discrimination among tectonic settings using trace element abundances of basalts. J Geophys Res 91, 10289-10300.

Büttner, S.H., Sherlock, S., Fryer, L., Lodge, J., Diale, T., Kazondunge, R., Macey, P. (2013). Controls of host rock mineralogy and H2O content on the nature of pseudotachylyte melts: evidence from Pan-African faulting in the foreland of the Gariep Belt, South Africa. Tectonophysics 608, 552-575.

Chappell, B.W., White, A.J.R. (1974). Two contrasting granite types. Pacific Geology 8, 173-174.

Chappell, B. W., White, A. J. R. (1992). I- and S-type granites in the Lachlan Fold Belt. Transactions of the Royal Society of Edinburgh: Earth Sciences 83, 1-26.

Chappell, B.W. (1996). Magma mixing and the production of compositional variation within granite suites: evidence from the granites of southeastern Australia. J. Petrol. 37, 449-470.

Cherniak, D.J., Hanchar, J.M., Watson, E.B. (1999). Diffusion of tetravalent cations in zircon. Contributions to Mineralogy and Petrology 127, 383-390.

Cilliers, B. (1989). 'n Petrogenetiese studie van 'n gedeelte van die Namakwalandse Metamorfe Kompleks langs die Oranjerivier tussen die Ramansdrif- en Homriviere, Warmbad distrik, suidelike Suidwes-Afrika/Namibia M.Sc. Thesis (Unpubl.). Univ. Orange Free State. 227 pp.

Clemens, J.D., Watkins, J.M. (2001). The fluid regime of high temperature metamorphism during granitoid magma genesis. Contribution to Mineralogy and Petrology 140, 600-606.

Clemens, J.D., Stevens, G., Farina, F. (2011). The enigmatic sources of I-type granites: the peritectic connexion. Lithos 126, 174-181.

Clemens, J.D., Stevens, G. (2012). What controls chemical variation in granitic magmas? Lithos 134-135, 317-329.

Clifford, T.N., Barton, E.A., Retief, E.A., Rex, D.C., Fanning, C.A. (1995). A crustal progenitor for the intrusive anorthosite-charnockite kindred of the cupriferous Koperberg Suite, O'okiep district, Namaqualand, South Africa; New isotope data for the country rocks and intrusives. Journal of Petrology 36, 231-258.

Clifford, T.N., Barton, E.S., Stern, R.A., Duchesne, J.C. (2004). U-Pb zircon calendar for Namaquan (Grenville) crustal events in the granulite-facies terrane of the O'okiep Copper District of South Africa. J. Petrol. 45, 669-691.

Colliston, W.P., Praekelt, H.E., Schoch, A.E. (1991). A progressive ductile shear model for the Proterozoic Aggeneys terrane, Namaqua mobile belt. Precambrian Res. 49, 205-215.

Colliston, W.P., Schoch, A.E. (1996). Proterozoic metavolcanic rocks and associated metasediments along the Orange River in the Pofadder Terrane, Namaqua Metamorphic Belt. S. Afr. J. Geol. 99 (1), 1-17.

Colliston, W.P., Schoch, A.E. (1998). Tectonostratigraphic features along the Orange River in the western part of the Mesoproterozoic Namaqua mobile belt. South African J. Geol. 101, 91-100.

Colliston, W.P., Schoch, A.E. (2000). Mid-Proterozoic tectonic evolution along the Orange River on the border between South Africa and Namibia. Communs geol. Surv. Namibia 12, 57-66.

Colliston, W.P., Schoch, A.E. (2002). The structural development of the Aggeneys Hills, Namaqua Metamorphic Complex. South African J. Geol. 105, 301-324.

Colliston, W.P., Schoch, A.E. (2013). Wrench-shearing during the Namaqua orogenesis - a Mesoproterozoic window on late-phase deformation during Rodinia assembly. Precambrian Res. 233, 44-58.

Colliston, W.P., Schoch, A.E., Cole, J. (2014). The Grenvillian Namaqua fold belt adjacent to the western Kaapvaal Craton: 1. Distribution of Mesoproterozoic collisional terranes deduced from results of regional surveys and selected profiles in the western and southern parts of the fold belt. J. African Earth Sci. 100, 7-19.

Colliston, W.P., Cornell, D.H., Schoch, A.E., Praekelt, H.E. (2015). Geochronological constraints on the Hartbees River Thrust and Augrabies Nappe: new insights into the assembly of the Mesoproterozoic Namaqua-Natal Province of Southern Africa. Precambrian Res. 265, 1-328.

Colliston, W.P., Schoch, A.E., Cole, J. (2017). The Grenvillian Namaqua fold belt adjacent to the western Kaapvaal Craton: 2. Archaean Craton and supercontinent connections. Precambrian Res. 300, 289-314.

Coney, P.J., Jones, D.L., Monger, J.W.H. (1980). Cordilleran suspect terranes. Nature 288, 329-333.

Conradie, J.A., Schoch, A.E. (1986). Petrographical characteristics of the koperberg suite, South Africa - an analogy to massif-type anorthosites? Precambrian Res. 31(2), 157-188.

Corfu, F., Hanchar, J.M., Hoskin, P.O.W., Kinny, P. (2003). Atlas of zircon textures. In Zircon (eds Hanchar, J. M. & Hoskin, P.W.O.). Reviews in Mineralogy & Geochemistry 53, 469-500.

Cornell, D.H., Armstrong, R.A., Walraven, F. (1998). Geochemistry of the Hartley Formation, South Africa: constraints on the Kheis tectogenesis and the Kaapvaal Craton's earliest Wilson cycle. J. African Earth Sci. 26, 5-27.

Cornell, D.H., Thomas, R.J., Moen, H.F.G., Reid, D.L., Moore, J.M., Gibson, R.L. (2006). The Namaqua-natal province. In: Johnson, M.R., Anhaeusser, C.R., Thomas, R.J. (Eds.), The Geology of South Africa. Geol. Soc. S. Africa and Council for Geoscience, South Africa, 325-379.

Cornell, D.H., Pettersson, A., Whitehouse, M.J. Schersten, A. (2009). A New Chronostratigraphic Paradigm for the Age and Tectonic History of the Mesoproterozoic Bushmanland Ore District, South Africa. Econ. Geo. 104, 385-404.

Cornell, D.H., van Schijndel, V., Simonsen, S.L., Frei, D. (2015). Geochronology of Mesoproterozoic hybrid intrusions in the Konkiep Terrane, Namibia, from passive to active continental margin in the Namaqua-Natal Wilson Cycle. Precambrian Res. 265, 166-188.

Cox, K.G., Bell, J.D., Pankhurst, R.J. (1979). The Interpretation of Igneous Rocks. George, Allen and Unwin, London, 450 pp.

Cox, K.G., Clifford, P. (1982). Correlation coefficient patterns and their interpretation in three basaltic suites. Contrib. Mineral. Petrol. 79, 268-278.

Cribb, J.W., Barton, M. (1996). Geochemical effects of decoupled fractional crystallization and crustal assimilation. Lithos 37, 293-307.

Dalziel, I.W., Mosher, S., Gahagan, L.M. (2000). Laurentia-Kalahari Collision and the assembly of Rodinia. J. Geol. 108, 499-513.

De Beer, C.H. (2010). The geology of the Garies area. 1:250 000 map sheet explanation 3017. Council for Geoscience, 110 pp.

De Beer, J.H., Meyer, R. (1983). Geoelectrical and gravitational characteristics of the Namaqua-Natal mobile belt and its boundaries. Spec. Publ. Geol. Soc. South Africa 10, 91-100.

De Beer, J.H., Meyer, R. (1984). Geophysical characteristics of the Namaqua-Natal Belt and its boundaries, South Africa. J. Geodyn. 1, 473-494.

De Beer, C.H., Gresse, P.G., Theron, J.N., Almond, J.E. (2002). The Geology of the Calvinia Area. Council for Geoscience South Africa, Explanation to the sheet 3118 Calvinia, 92 pp.

De la Roche, H., Leterrier, J. (1973). Transposition du tetraedre mineralogique de Yoder et Tilley dans un diagramme chimique de classification des roches basaltique. C.R. Acad. Sci. Paris, Ser. D. 276, 3115-3118.

De la Roche H., Leterrier J., Grandclaude P., Marchal M. (1980). A classification of volcanic and plutonic rocks using R_1-R_2 diagrams and major element analyses - its relationships and current nomenclature. Chemical Geology 29, 183-210.

Decrite, S., Gasquet, D., Marignac, C. (2002). Genesis of orbicular granitic rocks from the Ploumanac'h Plutonic Complex (Brittany, France): petrographical, mineralogical and geochemical constraints. European Journal of Mineralogy 14, 715-31.

DePaolo, D.J. (1981). A neodymium and strontium isotopic study of the Mesozoic calc-alkaline granitic batholiths of the Sierra Nevada and Peninsula Ranges, California. Journal of Geophysical Research 86, 10470-10488.

DePaolo, D.J. (1988). Neodymium isotope geochemistry': An introduction. Springer Verlag, New York, Minerals and rocks 20, 187 pp. ISBN: 0387186484.

Dickin, A. P. (2018). Radiogenic isotope geology (Third Edition). Cambridge University Press, Cambridge. 482 pp. ISBN: 9781316163009.

Doggart, S.W. (2019). Geochronology and Isotopic Characterization of LCT Pegmatites from the Orange River Pegmatite Province. M.Sc. thesis. Stellenbosch Univ. 234 pp.

Eglington, B.M. (2006). Evolution of the Namaqua-Natal Belt, Southern Africa – A geochronological and isotope geochemical review. J. Afr. Earth Sci. 46, 93-111.

Eglington, B.M., Armstrong, R.A. (2003). Geochronological and isotopic constraints on the Mesoproterozoic Namaqua-Natal Belt: evidence from deep borehole intersections in South Africa. Precambr. Res. 125, 179-189.

Eglington, B.M., Harmer, R.E., Kerr, A. (1989). Isotope and geochemical constraints on Proterozoic crustal evolution in south-eastern Africa. Precambrian Res. 45, 159-174.

Elliston, J.N. (1984). Orbicules: an indication of the crystallization of hydrosilicates, I. Earth Science Reviews 20, 265-344.

Ersoy, Y., Helvacı, C. (2010). FC–AFC–FCA and mixing modeler: A Microsoft® Excel© spreadsheet program for modeling geochemical differentiation of magma by crystal fractionation, crustal assimilation and mixing. Computers & Geosciences 36(3), 383-390.

Federal Geographic Data Committee [prepared for the Federal Geographic Data Committee by the U.S. Geological Survey] (2006). FGDC Digital Cartographic Standard for Geologic Map Symbolization: Reston, Va., Federal Geographic Data Committee Document Number FGDC-STD-013-2006, 290 p., 2 plates.

Fernández, C., Castro, A. (1999). Brittle behaviour of granitic magma: the example of Puente del congosto, Iberian massif, Spain. Geological Society, London, Special Publications 168, 191-206.

Fisher, C.M., Hanchar, J.M., Samson, S.D., Dhuime, B., Blichert-Toft, J., Vervoort, J.D., Lam, R. (2011). Synthetic zircon doped with hafnium and rare earth elements: a reference material for in situ hafnium isotope analysis. Chem. Geol. 286, 32–47.

Frei, D., Gerdes, A. (2009). Precise and accurate in situ U-Pb dating of zircon with high sample throughput by automated LA-SF-ICP-MS. Chemical Geology, 261, 261-270.

Frimmel, H.E., Zartman, R.E., Späth, A. (2001). The Richtersveld igneous complex, South Africa: U-Pb zircon and geochemical evidence for the beginning of Neoproterozoic continental breakup. J. Geol. 109 (4), 493-508.

Frost, B.R., Barnes, C.G., Collins, W.J., Arculus, R.J., Ellis, D.J., Frost, C.D. (2001). A geochemical classification for granitic rocks. Journal of Petrology 42, 2033-2048.

Frost, C.D., Frost, B.R. (2008). A Geochemical Classification for Feldspathic Igneous Rocks. Journal of Petrology 49(11), 1955-1969.

Gehrels, G.E., Valencia, V.A., Ruiz, J. (2008). Enhanced precision, accuracy, efficiency, and spatial resolution of U-Pb ages by laser ablation-multicollector-inductively coupled plasma-mass spectrometry. Geochemistry Geophysics Geosystems 9, Q03017, doi:10.1029/2007GC001805.

Gerdes, A., Zeh, A. (2006). Combined U-Pb and Hf isotope LA-(MC)-ICP-MS analysis of detrital zircons: comparison with SHRIMP and new constraints for the provenance and age of an Armorican metasediment in Central Germany. Earth and Planetary Science Letters 249, 47-61.

Glazner, A.F. (2007). Thermal limitations on incorporation of wall rock into magma. Geol 35(4), 319 pp. [Abstract].

Glazner, A. F., Coleman, D. S., Bartley, J. M., Wohletz, K. H. (2006). What plutons have to say about big eruptions. Eos Transactions of the AGU 87, Fall Meeting Supplement, Abstract V23G-05.

Goldstein, S. L., O'Nions, R. K., Hamilton, P. J. (1984). A Sm-Nd isotopic study of atmospheric dusts and particulates from major river systems. Earth and Planetary Science Letters 70, 221-36.

Grantham, G.H., Eglington, B.M., Armstrong, R.A. (2000). The geochronology of some lithologies from sheet 3018AC Leliefontein, Namaqua Metamorphic Province Internal Report, Council for Geoscience, 17 pp.

Green, T.H., Pearson, N.J. (1986). Rare-earth element partitioning between sphene and coexisting silicate liquid at high pressure and temperature. Chem. Geol. 55, 105-119.

Green, T.H., Sie, S.H., Ryan, C.G., Cousens, D.R. (1989). Proton microprobe-determined partitioning of Nb, Ta, Zr, Sr and Y between garnet, clinopyroxene and basaltic magma at high pressure and temperature. Chem. Geol. 74, 201-216.

Gresse, P.G., Von Veh, M.W., Frimmel, H.E. (2006). Namibian (Neoproterozoic) to Early Cambrian successions. In: Johnson, M.R., Anhaeusser, C.R., Thomas, R.J. (Eds.), The Geology of South Africa. Geol. Soc. S. Africa and Council for Geoscience, South Africa, 395-420.

Gresse, P.G., Macey, P.H., Smith, H., Hartnady, M.I., Frei, D. (2016). The Pre-Gariep geology east of Rosh Pinah, Karas Region, S. Namibia. Explanation to parts of 1:50 000 Geological Map Sheets 2716DA, 2716DB, 2716DC, 2716DD, 2717CC, 2816BB and 2817AA. Geol. Surv. Namibia, Council for Geoscience S.A., Min. Mines and Energy, Namibia. 193 pp.

Griffin, W. L., Pearson, N.J., Belousova, E., Jackson, S.E., van Achterbergh, E., O'Reilly, S., Shee, S.R. (2000). The Hf isotope composition of cratonic mantle: LAM-MC-ICPMS analysis of zircon megacrysts in kimberlites. Geochimica et Cosmochimica Acta 64(1), 133-147.

Griffn, W.L., Wang, X., Jackson, S.E., Pearson, N.J., O'Reilly, S. Y., Xu, X., Zhou, X. (2002). Zircon chemistry and magma mixing, SE China: In-situ analysis of Hf isotopes, Tonglu and Pingtan igneous complexes. Lithos 61, 237-269.

Grosse, P., Toselli, A., Rossi, J. (2010). Petrology and geochemistry of the orbicular granitoid of Sierra de Velasco (NW Argentina) and implications for the origin of orbicular rocks. Geological Magazine 147 (3), 451-468.

Gutiérrez, F., Payacán, I., Gelman, S.E., Bachmann, O., Parada, M.A. (2013). Late-stage magma flow in a shallow felsic reservoir: Merging the anisotropy of magnetic susceptibility record with numerical simulations in La Gloria Pluton, central Chile. JGR Solid Earth 118, 1984-1998.

Harley, S.L. (1989). The origins of granulites: a metamorphic perspective. Geological magazine 126 (3), 215-247.

Harris. N., Ayres, M., Massey, J. (1995). Geochemistry of granitic melts produced during the incongruent melting of muscovite: implications for the extraction of Himalayan leucogranite magmas. Journal of Geophysical Research 100, 15767-15777.

Hartnady, C.J.H., Joubert, P., Stowe, C.W. (1985). Proterozoic crustal evolution in southwestern Africa. Episodes 8, 236-244.

Hoaglin, D., Mosteller, F., Tukey, J. (1983). Understanding Robust and Exploratory Data Analysis. John Wiley and Sons, Inc., New York, 447 pp. ISBN-13: 978-0471384915.

Hoffman, P.F. (1991). Did the break-up of Laurentia Turn Gondwanaland inside-out? Science 252, 1409-1412.

Humphries, D. (1992). The preparation of thin sections of rocks, minerals and ceramics. Oxford Science Publications, Oxford, UK.

Irvine, T.N., Barager, W.R.A. (1971). A guide to the chemical classification of the common volcanic rocks. Canadian J. Earth Sci. 8, 523-548.

Jackson, C.J. (1998). The geology of the area east of Garies, Northern Cape. Sheet 3018CA Buffelsfontein. Internal report, Council for Geoscience, 1998-0315. (Unpublished).

Jacobs, J., Thomas, R.J., Weber, K. (1993). Accretion and indentation tectonics at the southern margin of the Kaapvaal Craton during the Kibaran (Grenville) Orogeny. Geology 21, 203-206.

Jacobs, J., Thomas, R.J. (1994). Oblique collision at about 1.1 Ga along the southern margin of the Kaapvaal continent, south-east Africa. Geol Rundsch 83, 322-333.

Jacobs, J., Falter, M., Thomas, R.J., Kunz, J., Jeßberger, E.K. (1997). $^{40}Ar/^{39}Ar$ thermochronological constraints on the structural evolution of the Mesoproterozoic Natal Metamorphic Province, SE Africa. Precambrian Res. 86, 71-92.

Jacobs, J., Pisarevsky, S., Thomas, R.J., Becker, T. (2008). The Kalahari Craton during the assembly and dispersal of Rodinia. Precambrian Res. 160, 142-158.

Jahn, B.M., Glikson, A.Y., Peucat, J.-J., Hickman, A.H. (1981). REE geochemistry and isotopic data of Archaean silicic volcanics and granitoids from the Pilbara block, Western Australia: implications for the early crustal evolution. Geochim Cosmochim Acta 45, 1633-1652.

Janoušek, V., Finger, F., Roberts, M., Frýda, J., Pin, C., Dolejš, D. (2004). Deciphering the petrogenesis of deeply buried granites: whole-rock geochemical constraints on the origin of largely undepleted felsic granulites from the Moldanubian Zone of the Bohemian Massif. Transactions of the Royal Society of Edinburgh: Earth Sciences 95, 141-159.

Janoušek, V., Farrow, C., Erban, V. (2006). Interpretation of whole-rock geochemical data in igneous geochemistry: Introducing Geochemical Data Toolkit (GCDkit). Journal of Petrology 47(6), 1255-1259. doi: 10.1093/petrology/egl013.

Janoušek, V., Moyen, J.-F., Martin, H., Erban, V., Farrow, C. (2016). Geochemical Modelling of Igneous Processes - Principles and Recipes in R Language. Bringing the Power of R to a Geochemical Community. Springer-Verlag, Berlin, Heidelberg, 346 pp. ISBN-13: 978-0471384915

Janoušek, V., Rogers, G., Bowes, D.R., Vaňková, V. (1997). Cryptic trace-element variation as an indicator of reverse zoning in a granitic pluton: the Říčany granite, Czech Republic. Journal of the Geological Society (London) 154, 807-815.

Jochum, K.P., Pfänder, J., Woodhead, J.D., Willbold, M., Stoll, B., Herwig, K., Amini, M., Abouchami, W., Hofmann, A.W. (2005). MPI-DING glasses: New geological reference materials for in situ Pb isotope analysis. Geochemistry Geophysics Geosystems 6(10), Q10008, doi:10.1029/2005GC000995, ISSN: 1525-2027.

Jochum, K.P., Weis, U., Schwager, B., Stoll, B., Wilson, S.A., Haug, G.H., Andreae, M.O., Enzweiler, H. (2016). Reference values following ISO guidelines for frequently requested rock reference materials. Geostand Geoanal Res 40, 333-350.

Joubert, P. (1971). The regional tectonism of the gneisses of part of Namaqualand Metamorphic Complex. Bulletin of the Precambrian Res. Unit, University of Cape Town 10, 220 pp.

Joubert, P. (1986). The Namaqualand metamorphic complex - A summary. In: Anhaeusser, C.R., Maske, S. (Eds.), Mineral Deposits of South Africa 1 & 2, Geol. Soc. S. Afr., 1395-1420.

Karlstrom, K.E., Åhäll, K.-I., Harlan, S.S., Williams, M.L., McLelland, J., Geissman, J.W. (2001). Long-lived (1.8-1.0 Ga) convergent orogen in southern Laurentia, its extension to Australia and Baltica, and implications for refining Rodinia. Precambrian Res. 111 (2001), 5-30.

Kisters, A.F.M., Potgieter, J.E., Charlesworth, E.G., Anhaeusser, C.R., Gibson, R.L., Watkeys, M.K. (1994). Emplacement features of cupriferous noritoids in the Okiep Copper District, Namaqualand, South Africa. Expl. Min. Geol. 3, 297-310.

Kisters, A.F.M., Gibson, R.L., Charlesworth, E.G., Anhaeusser, C.R. (1998). The role of strain localization in the segregation and ascent of anatectic melts, Namaqualand, South Africa. J. Struct. Geol. 20, 229-242.

Lake, E.T. (2013). Crystallization and saturation front propagation in silicic magma chambers, Earth and Planetary Science Letters 383, 182-193.

Lambert, C.W. (2013). Granitic melt transport and emplacement along transcurrent shear zones: Case study of the Pofadder Shear Zone in South Africa and Namibia. MSc. Dissertation (unpublished). Univ. Stellenbosch. 128 pp.

Latourrette, T.Z., Burnett, D.S., Bacon, C.R. (1991). Uranium and Minor-Element Partitioning in Fe-Ti Oxides and Zircon from Partially Melted Granodiorite, Crater Lake, Oregon. Geochimica et Cosmochimica Acta 55(2), 457-469.

Laurent, O., Martin, H., Moyen, J.F., Doucelance, R. (2014). The diversity and evolution of late-Archean granitoids: evidence for the onset of "modern-style" plate tectonics between 3.0 and 2.5 Ga. Lithos 205, 208-235.

Li, Z.X., Bogdanova, S.V., Collins, A.S., Davidson, A., De Waele, B., Ernst, R.E., FitzsiMons, I.C.W., Fuck, R.A., Gladkochub, D.P., Jacobs, J., Karlstrom, K.E., Lu, S., Natapov, L.M., Pease, V., Pisarevsky, S.A., Thrane, K., Vernikovsky, V. (2008). Assembly, configuration, and break-up history of Rodinia: a synthesis. Precambrian Res. 160, 179-210.

Liew, T. C., Hofmann, A. W. (1988). Precambrian crustal components, plutonic associations, plate environment of the Hercynian Fold Belt of Central Europe: indications from a Nd and Sr isotopic study. Contributions to Mineralogy and Petrology 98, 129-38.

Lombaard, A.F. and the Exploration Department Staff of the O'okiep Copper Company Limited (1986). The copper deposits of the Okiep Copper District. In: Anhaeusser, C.R. and Maske, S. (Eds.), Mineral Deposits of Southern Africa, Vol. II. Geol. Soc. S. Afr., 1421-1445.

Ludwig, K.R. (2003). Isoplot/Excel version 3.0: A Geochronological Toolkit for Microsoft Excel. Berkeley Geochronology Center, Berkeley, CA.

Macey, P.H. (2001). The geology of the region between Garies and Kliprand, southern Namaqualand. 1:50 000 sheets 3018 CA (Buffelsfontein), 3018 CB (Suurdam), 3018 DA (Kliprand) and 3018 DB (Oubees). Council for Geoscience internal report. (Unpublished).

Macey, P.H., Siegfried, H.P., Minnaar, H., Almond, J. (2011). The Geology of the Loeriesfontein Area. Explanation to Sheet 3018, Scale: 1:250 000. Council for Geoscience.

Macey, P.H., Minnaar, H., Miller, J.A., Lambert, C., Kisters, A.F.M., Diener, J., Thomas, R.J., Groenewald, C., Indongo, J., Angombe, M., Smith, H., Shifatoka, G., Le Roux, P., Frei D. (2015). The Precambrian geology of the Warmbad Region, southern Namibia. An interim explanation to 1:50 000 Geological Map Sheets of the 1:250 000 2818 Warmbad sheet. Geol. Surv. Namibia and Council for Geoscience of South Africa, 720 pp. Accompanied by twenty-four 1:50 000 geological maps.

Macey, P.H., Thomas, R.J., Minnaar, H.M., Gresse, P.G., Lambert, C.W., Groenewald, C.A., Miller, J.A., Indongo, J., Angombe, M., Shifotoka, G., Frei, D., Diener, J.F.A., Kisters, A.F.M., Dhansay, T. (2017). Origin and evolution of the ~1.9 Ga Richtersveld Magmatic Arc, SW Africa. Precambrian Res. 292, 417-451.

Macey, P.H., Bailie, R.H., Miller, J.A., Thomas, R.J., de Beer, C., Frei, D., le Roux, P.J. (2018). Implications of the distribution, age and origins of the granites of the Mesoproterozoic Spektakel Suite for the timing of the Namaqua Orogeny in the Bushmanland Subprovince of the Namaqua-Natal Metamorphic Province, South Africa. Precambrian Res. 312, 68-98.

Mahood, G., Hildreth, W. (1983). Large partition coefficients for trace elements in high-silica rhyolites. Geochim. Cosmochim. Acta 47, 11-30.

Marais, J.A.H., Agenbacht, A.L.D., Prinsloo, M., Basson, W.A. (2001). Geology of the 2916 Springbok sheet: Explanation, sheet 2916 Springbok (1: 250 000), Council for Geoscience, 103 pp.

Martin, H. (1987). Petrogenesis of Archaean trondhjemites, tonalites and granodiorites from eastern Finland; major and trace element geochemistry. Journal of Petrology 28, 921-953.

Martin, H., Smithies, R.H., Rapp, R., Moyen, J.-F., Champion, D. (2005). An overview of adakite, tonalite-trondhjemite-granodiorite (TTG), and sanukitoid: relationships and some implications for crustal evolution. Lithos 79, 1-24.

McCarthy, T.S., Robb, L.J. (1978). On the relationship between cumulus mineralogy and trace and alkali element chemistry in an Archean granite from the Barberton region, South Africa. Geochimica et Cosmochimica Acta, 42, 21-26. doi.org/10.1016/0016-7037(78)90212-0.

McClung, C.R. (2006). Basin analysis of the Mesoproterozoic Bushmanland Group of the Namaqua metamorphic province, South Africa: Ph.D. thesis, University of Johannesburg. (Unpublished).

McCulloch, M.T., Gamble, J.A. (1991). Geochemical and geodynaical constraints on subduction zone magmatism. Earth and Planetary Science Letters 102, 358-374.

McDonough, W.F., Sun, S-S. (1995). The composition of the earth. Chemical Geology 120, 223-253.

McMenamin, M. A., McMenamin, D. L. (1990). The emergence of animals: the Cambrian Breakthrough. Columbia University Press, New York. ISBN 978-0-231-06647-1.

McMillan, M.D. (1968). The geology of the Witputs-Sendelingsdrif area. Bull. Precambrian Res. Unit, vol. 4. Univ. Cape Town. 177 pp.

McStay, J. (1991). Granulite-facies metamorphism, fluid buffering and partial melting in the Buffels River area of the Namaqualand Metamorphic Complex, South Africa. Ph.D. thesis, University of Cape Town, 341 pp. (Unpublished).

Melcher, M., Graupner, T., Henjes-Kunst, F., Oberthür, T., Sitnikova, M., Gäbler, E., Gerdes, A., Brätz, H., Davis, D., Dewaele, S. (2008). Analytical fingerprint of columbite-tantalite (coltan) mineralization in pegmatites: focus on Africa. Proceedings, 9th ICAM, Brisbane. Australasian Institute Mining and Metallurgy, 615-624.

Melcher, F., Graupner, T., Gäbler, H.-E., Sitnikova, M., Henjes-Kunst, F., Oberthür, T., Gerdes, A., Dewaele, S. (2015). Tantalum–(niobium–tin) mineralisation in African pegmatites and rare metal granites: constraints from Ta–Nb oxide mineralogy, geochemistry and U–Pb geochronology. Ore Geol. Rev. 64, 667-719.

Middelburg, J.J., Van Der Weijden, C.H., Woittiez, J.R.W. (1988). Chemical processes affecting the mobility of major, minor and trace elements during weathering of granitic rocks. Chemical Geology 68, 253-273.

Miková, J., Denková, P. (2007). Modified chromatographic separation scheme for Sr and Nd isotope analysis in geological silicate samples. Journal of Geosciences 52, 221-226.

Miller, R.M.G. (2008). The geology of Namibia. Handbook, Geological Survey of Namibia, Vol. 3. ISBN: 9780869767313.

Miller, R.M.G. (2012). Review of Mesoproterozoic magmatism, sedimentation and terrane amalgamation in southwestern Africa. S. Afr. J. Geol. 115, 417-448.

Minnaar, H. (2012). Composition and evolution of the Proterozoic Vioolsdrif Batholith (including the Orange River Group), Northern Cape Province, South Africa Ph.D. thesis. Univ. Free State.

Moen, H.F.G., Toogood, D.J. (2007). The Geology of the Onseepkans area. Map and explanation, sheet 2818 Onseepkans (1:250 000), Council for Geoscience, 101 pp.

Moore, J.M. (1989). A comparative study of metamorphosed supracrustal rocks from Western Namaqualand Metamorphic Complex. Bulletin of the Precambrian Res. Unit, University of Cape Town 37, 370 pp.

Moore, J.M., Watkeys, M.K., Reid, D.L. (1990). The regional setting of the Aggeneys/Gamsberg base metal deposits, Namaqualand, South Africa. In: Spry, P.G. and Bryndzia, L.T. (Eds.), Regional Metamorphism of Ore Deposits and Genetic Implications. VSP, Utrecht, 77-95.

Moyen, J.-F. (2011). The composite Archaean grey gneisses: petrological significance, and evidence for a non-unique tectonic setting for Archaean crustal growth. Lithos 123, 21-36.

Moyen, J.F., Martin, H. (2012). Forty years of TTG research. Lithos 148, 312-336.

Nowell, G.M., Parrish, R.R. (2001). Simultaneous acquisition of isotope compositions and parent/daughter ratios by non-isotope dilution solution-mode Plasma ionisation Multi-collector Mass Spectrometry (PIMMS). In: Tanner, S.D., Holland, J.G. (Eds.), Plasma Source Mass Spectrometry. The New Millennium. Royal Society of Chemistry, London, 298-310.

O'Connor, J. T. (1965). A classification for quartz-rich igneous rocks based on feldspar ratios. US Geological Survey Professional Paper B525. USGS, 79-84.

Osbourn, E. F. (1959). Role of oxygen pressure in the crystallization and differentiation of basaltic magma. American Journal of Science 257, 609-647.

Patchett, P.J., Kouvo, O., Hedge, C.E., Tatsumoto, M. (1981). Evolution of Continental crust and mantle heterogeneity: Evidence from Hf isotopes, Contributions to Mineralogy and Petrology 778, 279-297.

Pandey, U.K., Bhattacharya, D., Sastry, D.V.L.N., Pandey, B.K. (2011). Geochronology Rb-Sr, Sm-Nd and Pb-Pb, isotope geochemistry and evolution of the granites and andesites hosting Mohar Cauldron, Bundelkhand Granite Complex, Shivpuri district, Central India. Explo. Res. Atom. Min. 21, 103-116.

Pearce, J.A. (1976). Statistical analysis of major element patterns in basalts. Journal of Petrology 17, 15-43.

Pearce, J.A. (1983). Role of the sub-continental lithosphere in magma genesis at active continental margins. In: Hawkesworth, C.J. and Norry, M.J. eds. Continental basalts and mantle xenoliths, Nantwich, Cheshire: Shiva Publications, 230-249.

Pearce, J.A. (1996). Sources and settings of granitic rocks. Episodes 19, 120-125.

Pearce, J.A. (2008). Geochemical fingerprinting of oceanic basalts with applications to ophiolite classification and the search for Archean oceanic crust. Lithos 100, 14-48.

Peccerillo, A., Taylor, S.R. (1976). Geochemistry of Eocene calc-alkaline volcanic rocks from the Kastamonu area, northern Turkey. Contrib. Mineral. Petrol. 58, 63-81.

Pettersson, Å. (2008). Mesoproterozoic Crustal Evolution in Southern Africa. PhD thesis. Gothenburg University, p. A117. http://gupea.ub.gu.se/handle/2077/17269.

Pitts, B.E., Maher, M.J., De Beer, J.H., Gough, D.I. (1992). Interpretation of magnetic, gravity and magnetotelluric data across the Cape fold belt and Karoo Basin, 27-32. In: De Wit, M.J., Ransome, I.G.D. (Eds.), Inversion Tectonics of the Cape fold belt, Karoo and Cretaceous Basins of Southern Africa. Balkema, Rotterdam.

Raith, J.G., Harley, S.L. (1998). Low-P high-T metamorphism in the Okiep Copper District, western Namaqualand, South Africa. Journal of Metamorphic Geology 16, 281-305.

Raith, J.G., Cornell, D.H., Frimmel, H.E.F., De Beer, C.H. (2003). New Insights into the Geology of the Namaqua Tectonic Province, South Africa, from Ion Probe Dating of Detrital and Metamorphic Zircon. The Journal of Geology 111, 347-366.

Reid, D.L. (1977). Geochemistry of Precambrian igneous rocks in the lower Orange River region. Bulletin (Ph.D. thesis), Precambrian Res. Unit, Univ. Cape Town 22, 397 pp.

Reid, D.L. (1982). Age relationships within the Vioolsdrif Batholith, lower Orange River region II. A two stage emplacement history and the extent of Kibaran overprinting. Trans. Geol. Soc. S. Afr. 85, 105-110.

Reid, D.L., Barton, E.S. (1983). Geochemical characterization of granitoids in the Namaqualand Geotraverse. In: Botha, B.J.V. (Ed.). Namaqualand Metamorphic Complex. Spec. Publ. Geol. Soc. South Africa 10, 67-82.

Reid, D.L., Welke, H.J., Erlank, A.J., Betton, P.J. (1987). Composition, age and tectonic setting of amphibolites in the central Bushmanland Group, Western Namaqua Province, southern Africa. Precambrian Research 36, 99-126.

Reid, D.L. (1997). Sm-Nd age and REE geochemistry of Proterozoic arc-related igneous rocks in the Richtersveld Subprovince, Namaqua Mobile Belt, Southern Africa. J. Afr. Earth Sci. 24 (4), 621-633.

Reid, D.L., Welke, H.J., Smith, C.B., Moore, J.M. (1997). Lead isotope patterns in Proterozoic stratiform mineralization in the Bushmanland Group, Namaqua Province, South Africa. Econ. Geol. 92, 248-258.

Ritter, U. (1980). The Precambrian evolution of the eastern Richtersveld. Precambrian Res. Unit, Univ. Cape Town Bull. 26, 1-276.

Robb, L.J., Armstrong, R.A., Waters, D.J. (1988). Nature and duration of mid-crustal granulite facies metamorphism: evidence from single zircon U-Pb geochronology in Namaqualand, South Africa. Inf. Circ. Economic Geol. Res. Unit, Univ. Witwatersrand 33, 38 pp.

Robb, L.J., Armstrong, R.A., Waters, D.J. (1999). Nature and duration of mid-crustal granulite-facies metamorphism and crustal growth: evidence from single zircon U-Pb geochronology in Namaqualand, South Africa. J. Petrol. 40, 1747-1770.

Roberts, M.P., Clemens, J.D. (1993). Origin of high potassium, calc-alkaline, I-type granitoids. Geology 21, 825-828.

Rogers, J.J.W., Santosh, M. (2002). Configuration of Columbia, a Mesoproterozoic Supercontinent. Gondwana Res. 5, 5-22.

Rollinson, H.R. (1992). Another look at the constant sum problem in geochemistry. Mineralogical magazine 56, 469-475.

Rollinson, H.R. (1993). Using Geochemical Data: Evaluation, Presentation, Interpretation. Mineralogical Magazine 58, 523 pp.

Rozendaal, A., Stumpfl, E.F. (1984). Mineral chemistry and genesis of Gamsberg zinc deposit, South Africa. Trans. Inst. Min. Metall. 93, 131-175.

Rudnick, R.L., Gao, S. (2003). 3.01 - Composition of the Continental Crust. In: Holland, H.D. and Turekian, K.K., Eds., Treatise on Geochemistry, Vol. 3, The Crust, Elsevier-Pergamon, Oxford, 64 pp.

Rudnick, R.L., McLennan, S.M., Taylor, S.R. (1985). Large ion lithophile elements in rocks from high-pressure granulites facies terrains. Geochimica et Cosmochimica Acta 49(7), 1645-1655.

Ryan, P.J., Lawrence, A.L., Lipson, R.D., Moore, J.M., Patterson, A., Stedman, D.P., Van Zyl, D. (1986). The Aggeneys base metal sulphide deposits, South Africa. In: Anhaeusser, C.R. and Maske, S. (Eds.), Mineral Deposits of Southern Africa Vol. 2. Geol. Soc. S. Afr., 1447-1474.

Schoch, A. E., Conradie, J. A. (1990). Petrochemical and mineralogical relationships in the Koperberg Suite, Namaqualand, South Africa. American mineralogist 75, 27-36.

Shaw, D. M. (1968). A review of K–Rb fractionation trends by covariance analysis. Geochimica et Cosmochimica Acta 32, 573-601.

Seewald, J.S., Seyfried, W.E. (1990). The effect of temperature on metal mobility in sub-seafloor hydrothermal systems: constraints from basalt alteration experiments. Earth Planet. Sci. Lett. 101, 388-403.

Shifotoka, G., Indongo, J.I., Thomas, R.J., Macey, P.H., Miller, J.A.M. (2016). 1:50 000 geological map of the Haib region. Portions of map sheets 2817DA, DB, DC, DD. Geol. Surv. Namibia and Council for Geoscience, South Africa.

Shirey, S.B., Hanson, G.N. (1984). Mantle-derived Archaean monzodiorites and trachyandesites. Nature 310, 222-224.

Sisson, T.W., Ratajeski, K., Hankins, W.B., Glazner, A.F. (2005). Voluminous granitic magmas from common basaltic sources. Contribution to Mineralogy and Petrology 148, 635-661.

Skjerlie, K.P., Johnston, A.D. (1996). Vapour-absent melting from 10 to 20 kbar of crustal rocks that contain multiple hydrous phases: implications for anatexis in the deep to very deep continental crust and active continental margins. Journal of Petrology 37 (3), 661-691.

Soesoo, A. (2000). Fractional crystallization of mantlederived melts as a mechanism for some I-type granite petrogenesis: an example from Lachlan Fold Belt, Australia. Journal of the Geological Society 157 (1), 135-149.

Spencer, C.J., Cawood, P.A., Hawkesworth, C.J., Prave, A.R., Roberts, N.M.W., Horstwood, M.S.A., Whitehouse, M.J., E.I.M.F. (2015). Generation and preservation of continental crust in the Grenville Orogeny. Geosci. Front. 6, 357-372.

Stacey, J. S., Kramers, J. D. (1975). Approximation of terrestrial lead isotope evolution by a two-stage model. Earth Plan. Sci. Lett. 26, 207-221.

Stevens, G., Clemens, J.D., Droop, G.T.R. (1997). Melt production during granulite-facies anatexis: experimental data from “primitive” metasedimentary protoliths. Contribution to Mineralogy and Petrology 128, 352-370.

Stevens, G., Villaros, A., Moyen, J.-F. (2007). Selective peritectic garnet entrainment as the origin of geochemical diversity in S-type granites. Geology 35 (1), 9-12.

Streckeisen, A. (1974). Classification and nomenclature of plutonic rocks: Recommendations of the IUGS subcommission on the systematics of igneous rocks. Geologische Rundschau 63, 773-786.

Strydom, D., Colliston, W.P., Praekelt, H.E., Schoch, A.E., Van Aswegen, G., Pretorius, J.J., Beukes, G.J., De Villiers, B., Watkeys, M.K., Botes, F.J. (1987). The tectonic units of parts of Namaqualand, Bushmanland and southern Namibia. Map (1:250 000), Bushmanland Research Project, Department of Geology, Univ. Orange Free State.

Sun, S.S., McDonough, W.F. (1989). Chemical and isotopic systematics of oceanic basalts: implications for mantle composition and processes. In Saunders, A.D., Norry, M.J. (Eds.), Magmatism in ocean basins. Geol. Soc. London. Spec. Pub. 42, 313-345.

Sylvester, P. J. (1989). Post-collisional alkaline granites. Journal of Geology 97, 261-280.

Sylvester, P. J. (1998). Post-collisional strongly peraluminous granites. Lithos 45, 29-44.

Tanaka, T., Togashi, S., Kamioka, H., Amakawa, H., Kagami, H., Hamamoto, T., Yuhara, M., Orihashi, Y., Yoneda, S., Shimizu, H., Kunimaru, T., Takahashi, K., Yanagi, T., Nakano, T., Fujimaki, H., Shinjo, R., Asahara, Y., Tanimizu, M. and Dragusanu, C. (2000). JNdi-1: a neodymium isotopic reference in consistency with LaJolla neodymium. Chemical Geology Short Communication 168, 279-281.

Taylor, H.P. (1980). The effects of assimilation of country rocks by magmas on $^{18}O/^{16}O$ and $^{87}Sr/^{86}Sr$ systematics in igneous rocks. Earth and Planetary Science Letters 47, 243-254.

Taylor, J., Nicoli, G, Stevens, G., Frei, D., Moyen, J.-F. (2014). The processes that control leucosome compositions in metasedimentary granulites: perspectives from the Southern Marginal Zone migmatites, Limpopo Belt, South Africa. Journal of Metamorphic Geology 32(7), 713-742.

Taylor, S.R., McLennan, S.M. (1985). The Continental Crust: Its Composition and Evolution. Blackwell Scientific, Oxford, 312 pp. ISBN: 0 632 01148 3.

Taylor, S.R., McLennan, S.M. (1995). The geochemical evolution of the continental crust. Reviews in Geophysics 33, 241-265.

Thomas, R.J., Agenbacht, A.L.D., Cornell, D.H., Moore, J.M. (1994). The Kibaran of Southern Africa: tectonic evolution and metallogeny. Ore Geol. Rev. 9, 131-160.

Thomas, R.J., De Beer, C.H., Bowring, S.A. (1996). A comparative study of the Mesoproterozoic late orogenic porphyritic granitoids of southwest Namaqualand and Natal, South Africa. Journal of African Earth Sciences 23(3), 485-508.

Thomas, R.J., Macey, P.H., Spencer, C., Dhansay, T., Diener, J.F.A., Lambert, C.W., Nguno, A. (2016). The Sperrgebiet Domain, Aurus Mountains, SW Namibia: a ~2020 to 850 Ma window within the Pan-African Gariep Orogen. Precambrian Res. 286, 35-58.

Toogood, D.J. (1976). Structural and metamorphic evolution of a gneiss terrain in the Namaqua Belt near Onseepkans, South West Africa. Bulletin, Precambrian Res. Unit, Univ. Cape Town, Vol. 19, 220 pp.

Van Aswegen, G. (1983). The Gladkop Suite - grey and pink gneisses of Steinkopf. In: Botha, B.J.V. (Ed.), Namaqualand Metamorphic Complex. Spec. Publ. Geol. Soc. South Africa 10, 31-44.

Van Aswegen, G., Strydom, D., Colliston, W.P., Praekelt, H.E., Blignault, H.J., Scoch, A. E., Botha, B.J.V., Van Der Merwe, S.W. (1987). The structural-stratigraphic development of part of the Namaqua Metamorphic Complex - an example of Proterozoic major thrust tectonics. In: Kröner, A. (Ed.), Proterozoic Lithosphere Evolution. American Geophysical Union, Geodynamics Service, 207-216.

Van Bever Donker, J.M. (1991). A synthesis of the structural geology of a major tectonic boundary between a 1000 m.y. mobile belt and a 3000 m.y. craton. Tectonophysics 196, 359-370.

van Hunen, J., Moyen, J.-F. (2012). Archean Subduction: Fact or Fiction. Annu. Rev. Earth Planet. Sci. 40, 195-219.

Van der Merwe, S.W., Botha, B.J.V. (1989). The Groothoek thrust belt in western Namaqualand: an example of a midcrustal structure. S. Afr. J. Geol. 92, 155-166.

Verma, S.P. (2005). Estadística Básica para el Manejo de Datos Experimentales: Aplicación en la Geoquímica (Geoquimiometría). Mexico City, Mexico: Universidad Nacional Autónoma de México, 186 pp.

Verma, S.P., Guevara, M., Agrawal, S. (2006). Discriminating four tectonic settings: Five new geochemical diagrams for basic and ultrabasic volcanic rocks based on log-ratio transformation of major-element data. Journal of Earth System Science 115, 485-528.

Verma, S.P., Agrawal, S. (2011). New tectonic discrimination diagrams for basic and ultrabasic volcanic rocks through log-transformed ratios of high field strength elements and implications for petrogenetic processes. Revista Mexicana de Ciencias Geologicas 28, 24-44.

Verma, S.K., Pandarinath, K., Verma, S.P. (2012). Statistical evaluation of tectonomagmatic discrimination diagrams for granitic rocks and proposal of new discriminant-function-based multi-dimensional diagrams for acid rocks. Int Geol Rev 54, 325-347.

Verma, S.P., Pandarinath, K., Verma, S.K., Agrawal, S. (2013). Fifteen new discriminant-function-based multi-dimensional robust diagrams for acid rocks and their application to Precambrian rocks. Lithos 168-169, 113-123.

Verma, S.P., Verma, S.K. (2013). First 15 probability-based multi-dimensional discrimination diagrams for intermediate magmas and their robustness against post-emplacement compositional changes and petrogenetic processes. Turkish J. Earth Sci. 22, 931-995.

Verma, S.P. (2015). Monte Carlo comparison of conventional ternary diagrams with new log-ratio bivariate diagrams and an example of tectonic discrimination. Geochem. J. 49, 393-412.

Verma, S.P., Verma, S.K., Oliveira, E.P. (2015). Application of 55 multi-dimensional tectonomagmatic discrimination diagrams to Precambrian belts. International Geology Review 57, 1365-1388.

Vernon, R.H. (2007). Problems in identifying restite in S-type granites of southeastern Australia, with speculations on sources of magma and enclaves. Canadian Mineralogist 45, 147-178.

Vervoort, J.D., Patchett, P.J. (1996). Behaviour of hafnium and neodymium isotopes in the crust: Constraints from Precambrian crustally-derived granites. Geochimica et Cosmochimica Acta 60, 3717-3733.

Vielzeuf, D., Montel, J.M. (1994). Partial melting of metagreywackes. Part I. Fluid-absent experiments and phase relationships. Contribution to Mineralogy and Petrology 117, 375-393.

Villaros, A., Stevens, G., Moyen, J.-F., Buick, I.S. (2009). The trace element compositions of S-type granites: evidence for disequilibrium melting and accessory phase entrainment in the source. Contributions to Mineralogy and Petrology 158, 543-561.

Waters, D.J. (1986). Metamorphic zonation and thermal history of pelitic gneisses from western Namaqualand, South Africa. Trans. Geol. Soc. South Africa 89, 97-102.

Waters, D.J. (1988). Partial melting and the formation of granulite facies assemblages in Namaqualand, South Africa. Journal of Metamorphic Geology 6, 87-404.

Waters, D.J. (1989). Metamorphic evidence for the heating and cooling path of Namaqualand granulites. In: Daly, J.S., Clift, R.A., Yardley, B.W.D. (Eds.). Evolution of metamorphic belts. Geol. Soc. London Spec. Publ. 4, 357-363.

Waters, D.J. (1990). Thermal history and tectonic setting of the Namaqualand granulites, southern Africa: clues to Proterozoic crustal development. In: Vielzeuf, D., Vidal, P. (Eds.), Granulites and Crustal Evolution. Kluver, Dordrecht, Netherlands, ASIC 311, 243-256.

Watkeys, M.K. (1986). The Achab gneiss: A “floor” in Bushmanland or a flaw in Namaqualand? Trans. Geol. Soc. South Africa 89, 103-116.

Weaver, B., Tarney J. (1984). Empirical approach to estimating the composition of the continental crust. Nature 310, 575-57.

Wedepohl, K. H. (1995). The composition of the continental crust. Geochimica et Cosmochimica Acta 59, 1217-1232.

Weis, D., Kieffer, B., Maerschalk, C., Barling, J., de Jong, J., Williams, G. A., Hanano, D., Pretorius, W., Mattielli, N., Scoates, J., Goolaerts, A., Friedman, R., Mahoney, J.B. (2006). High-precision isotopic characterization of USGS reference materials by TIMS and MC-ICP-MS. Geochemistry, Geophysics, Geosystems, 7(8), doi: 10.1029/2006GC001283.

Wells, P.R.A. (1980). Thermal models for the magmatic accretion and subsequent metamorphism of continental crust. Earth Planet. Sci. Lett. 46, 253-265.

Whalen, J.B., Currie, K.L., Chappell, B.W. (1987). A-type granites: geochemical characteristics, discriminations and petrogenesis. Contributions to Mineralogy and Petrology 95, 407-419.

White, A.J.R., Chappell, B.W. (1977). Ultra metamorphism and granitoid genesis. Tectonophisics 43, 7-22.

Willner, A., Schreyer, W., Moore, J.M. (1990). Peraluminous metamorphic rocks from the Namaqualand Metamorphic Complex (South Africa): Geochemical evidence for an exhalation-related, sedimentary origin in a Mid-Proterozoic rift system. Chemical Geology 81, 221-240.

Wilson, M. (1989). Igneous Petrogenesis. A Global Tectonic Approach. London, Boston, Sydney, Wellington: Unwin Hyman. 466 pp.

Winchester, J.A., Floyd, P.A. (1977). Geochemical discrimination of different magma series and their differentiation products using immobile elements. Chem. Geol. 20, 325-343.

Wood, D.A. (1978). Major and trace element variation in the Tertiary lavas of eastern Iceland and their significance with respect to the Iceland geochemical anomaly. J. Petrol. 19, 393-436.

Yurimoto, H., Duke, E.F., Papike, J.J., Shearer, C.K. (1990). Are discontinuous chondrite-normalized REE patterns in pegmatitic granite systems the results of monazite fractionation? Geochim. Cosmochim. Acta 54, 2141-2145.

Zorpi, M., Coulon, C., Orsini, J., Cocirta, C. (1989). Magma mingling, zoning and emplacement in calc-alkaline granitoid plutons. Tectonophysics 157(4), 315-329.

Appendices

Appendix A. Structural data

Table A1: Structural readings of the S_2 fabric in the GS gneisses

Latitude	Longitude	S_2	Latitude	Longitude	S_2	Latitude	Longitude	S_2	Latitude	Longitude	S_2
-29.4681	17.7658	144/54	-29.4361	17.7249	130/35	-29.4555	17.7674	146/36	-29.3869	17.7112	304/50
-29.4687	17.7643	160/38	-29.4396	17.7183	144/31	-29.4556	17.7675	158/46	-29.3874	17.7085	318/49
-29.4686	17.7629	160/40	-29.4314	17.7046	154/30	-29.4578	17.7675	132/39	-29.3872	17.7078	356/50
-29.4692	17.7621	150/32	-29.4308	17.7046	144/26	-29.4572	17.7699	152/52	-29.3936	17.7146	154/52
-29.4701	17.7617	144/38	-29.4294	17.7052	164/30	-29.4566	17.7704	154/72	-29.3923	17.7160	001/56
-29.4693	17.7611	154/36	-29.4291	17.7061	130/23	-29.4559	17.7703	188/44	-29.3899	17.7202	336/45
-29.4703	17.7594	174/40	-29.4269	17.7074	156/26	-29.4558	17.7721	173/50	-29.4475	17.7325	158/35
-29.4695	17.7585	158/34	-29.4258	17.7089	162/30	-29.4551	17.7748	317/40	-29.4488	17.7383	148/23
-29.4689	17.7576	134/44	-29.4261	17.7108	138/27	-29.4536	17.7784	348/32	-29.4316	17.7048	160/46
-29.4688	17.7573	150/40	-29.4229	17.7152	320/40	-29.4531	17.7795	124/56	-29.2501	17.7528	336/68
-29.4694	17.7566	146/44	-29.4229	17.7152	136/30	-29.4530	17.7805	161/42	-29.2508	17.7527	334/64
-29.4700	17.7571	147/42	-29.4225	17.7154	358/40	-29.4533	17.7803	154/75	-29.2521	17.7523	076/68
-29.4722	17.7579	166/40	-29.4208	17.7173	140/41	-29.4505	17.7838	160/65	-29.2536	17.7535	302/42
-29.4719	17.7592	174/36	-29.4198	17.7198	183/32	-29.4499	17.7850	153/55	-29.2517	17.7529	322/82
-29.4667	17.7710	138/52	-29.4193	17.7213	342/28	-29.4490	17.7856	148/52	-29.2513	17.7530	328/50
-29.4667	17.7714	154/46	-29.4192	17.7214	168/36	-29.4472	17.7869	162/30	-29.2512	17.7531	318/20
-29.4658	17.7721	122/50	-29.4183	17.7244	202/36	-29.4462	17.7875	166/65	-29.2533	17.7474	207/53
-29.4651	17.7718	102/36	-29.4181	17.7257	148/42	-29.4458	17.7878	144/59	-29.2534	17.7471	324/48
-29.4640	17.7721	103/52	-29.4245	17.7245	136/20	-29.4427	17.7889	138/42	-29.2558	17.7518	322/42
-29.4638	17.7725	103/36	-29.4277	17.7175	168/35	-29.4419	17.7889	172/55	-29.2744	17.7873	334/81
-29.4640	17.7728	146/46	-29.4165	17.7088	118/21	-29.4415	17.7891	158/45	-29.2738	17.7887	096/74
-29.4640	17.7730	156/40	-29.4188	17.7077	153/26	-29.4404	17.7905	173/45	-29.2737	17.7889	314/76
-29.4640	17.7731	123/36	-29.4203	17.7075	142/25	-29.4379	17.7908	178/40	-29.2770	17.7906	306/62
-29.4640	17.7731	126/32	-29.4204	17.7056	149/36	-29.4378	17.7908	168/39	-29.2783	17.7912	142/72
-29.4643	17.7734	146/34	-29.4206	17.7051	183/22	-29.4369	17.7905	162/37	-29.2696	17.7731	092/58
-29.4642	17.7735	174/50	-29.4223	17.7054	158/34	-29.4363	17.7903	164/31	-29.4341	17.7702	334/34
-29.4635	17.7751	098/36	-29.4226	17.7055	157/36	-29.4350	17.7893	152/37	-29.4311	17.7709	166/50
-29.4635	17.7754	162/38	-29.4231	17.7051	160/29	-29.4352	17.7876	167/38	-29.4302	17.7679	157/28
-29.4623	17.7751	136/36	-29.4245	17.7025	130/20	-29.4363	17.7830	146/38	-29.4324	17.7656	126/42
-29.4627	17.7782	202/27	-29.4245	17.7019	165/27	-29.4390	17.7819	131/40	-29.4566	17.7483	168/68
-29.4618	17.7780	140/50	-29.4247	17.7013	128/30	-29.4410	17.7809	158/36	-29.4523	17.7407	134/48
-29.4598	17.7727	142/72	-29.4248	17.7006	165/20	-29.4421	17.7790	189/25	-29.4518	17.7406	170/54
-29.4598	17.7726	148/84	-29.4245	17.6998	124/36	-29.4423	17.7788	200/39	-29.4492	17.7386	058/54
-29.4619	17.7703	154/32	-29.4247	17.7002	166/35	-29.4491	17.7733	148/30	-29.4452	17.7406	166/38
-29.4659	17.7691	156/44	-29.4249	17.7001	160/22	-29.4568	17.7621	178/40	-29.4363	17.7496	164/72
-29.4675	17.7700	142/40	-29.4246	17.7017	162/26	-29.4519	17.7577	138/31	-29.4236	17.8239	209/19
-29.4554	17.7836	152/50	-29.4252	17.7024	194/35	-29.4517	17.7578	170/42	-29.4231	17.8240	206/12
-29.4543	17.7848	150/80	-29.4223	17.7067	130/35	-29.4495	17.7588	132/45	-29.4231	17.8240	216/14
-29.4529	17.7879	162/35	-29.4208	17.7077	134/30	-29.4496	17.7557	152/40	-29.4231	17.8240	334/18
-29.4522	17.7903	131/42	-29.4147	17.7196	157/46	-29.4416	17.7534	148/39	-29.4231	17.8240	176/20
-29.4537	17.7953	140/45	-29.4141	17.7194	018/28	-29.4364	17.7496	156/31	-29.4236	17.8257	121/10
-29.4538	17.7954	146/50	-29.4121	17.7191	012/34	-29.4363	17.7602	140/26	-29.4306	17.8323	120/62
-29.4542	17.7954	143/50	-29.4116	17.7190	014/37	-29.4339	17.7597	314/41	-29.4342	17.8321	165/38
-29.4549	17.7956	135/36	-29.4117	17.7155	316/38	-29.4306	17.7646	170/34	-29.4344	17.8324	157/78
-29.4556	17.7952	140/38	-29.4130	17.7029	310/33	-29.4332	17.7692	120/26	-29.4338	17.8251	160/44
-29.4569	17.7936	183/50	-29.4133	17.7026	299/31	-29.4351	17.7664	338/50	-29.4340	17.8251	158/50
-29.4582	17.7906	142/43	-29.4146	17.7007	355/31	-29.4365	17.7629	144/31	-29.4343	17.8252	182/50
-29.4626	17.7812	158/34	-29.4147	17.7005	344/44	-29.4484	17.7640	160/48	-29.4329	17.8246	181/56
-29.4681	17.7435	164/30	-29.4148	17.6995	353/38	-29.4479	17.7638	162/48	-29.4286	17.8192	208/33
-29.4594	17.7410	152/25	-29.4159	17.6958	192/25	-29.4474	17.7630	159/41	-29.4283	17.8191	146/34
-29.4591	17.7396	144/38	-29.4162	17.6945	152/26	-29.4467	17.7628	158/46	-29.4200	17.8133	172/35
-29.4589	17.7390	186/25	-29.4188	17.6920	012/28	-29.4459	17.7619	152/42	-29.4156	17.8049	170/42
-29.4614	17.7352	182/70	-29.4212	17.6908	330/31	-29.4451	17.7618	150/35	-29.4139	17.8233	195/42
-29.4613	17.7351	172/45	-29.4206	17.6893	166/25	-29.4027	17.7619	150/41	-29.4100	17.8325	162/52
-29.4625	17.7331	183/25	-29.4186	17.6879	343/31	-29.4031	17.7611	146/42	-29.3561	17.7835	316/72
-29.4623	17.7351	156/35	-29.4179	17.6876	298/26	-29.4040	17.7606	136/25	-29.4616	17.7333	133/50
-29.4614	17.7393	160/30	-29.4163	17.6862	355/22	-29.4049	17.7606	162/33	-29.4620	17.7332	150/58
-29.4567	17.7483	164/32	-29.4152	17.6854	334/35	-29.4077	17.7598	138/30	-29.4562	17.7247	169/66
-29.4565	17.7478	132/35	-29.4134	17.6856	352/46	-29.4086	17.7582	143/36	-29.4544	17.7245	158/55
-29.4570	17.7470	130/40	-29.4123	17.6886	192/30	-29.4093	17.7567	146/41	-29.4483	17.7257	167/40
-29.4580	17.7457	154/32	-29.4111	17.6897	332/40	-29.4103	17.7554	163/40	-29.4478	17.7253	152/66
-29.4578	17.7447	160/32	-29.4107	17.6930	337/42	-29.4104	17.7543	142/30	-29.4409	17.7188	028/46
-29.4581	17.7435	110/28	-29.4103	17.6949	306/32	-29.4104	17.7532	164/46	-29.4312	17.7099	013/28
-29.4588	17.7426	132/30	-29.4102	17.6972	332/30	-29.4121	17.7501	182/49	-29.4141	17.7306	006/44
-29.4592	17.7417	138/34	-29.4117	17.7012	322/40	-29.4132	17.7512	162/51	-29.4075	17.7096	030/52
-29.4582	17.7453	176/36	-29.4078	17.7081	305/24	-29.4144	17.7518	172/40	-29.4477	17.7347	208/52
-29.4584	17.7464	138/44	-29.4070	17.7092	334/50	-29.4149	17.7570	164/59	-29.4477	17.7347	140/30
-29.4591	17.7469	162/32	-29.4063	17.7090	350/50	-29.4121	17.7605	168/47	-29.4476	17.7456	142/32
-29.4587	17.7481	156/40	-29.4059	17.7089	147/34	-29.4087	17.7634	150/55	-29.3109	17.7678	124/58
-29.4560	17.7523	124/44	-29.4045	17.7085	140/60	-29.4101	17.7665	151/60	-29.3119	17.7695	110/54
-29.4560	17.7530	148/45	-29.4038	17.7082	163/25	-29.4070	17.7668	178/36	-29.3113	17.7624	102/52
-29.4559	17.7513	154/55	-29.4026	17.7074	148/25	-29.4029	17.7664	155/46	-29.3110	17.7589	358/62
-29.4555	17.7384	136/35	-29.4032	17.7070	157/30	-29.4154	17.7347	154/44	-29.3100	17.7562	344/46
-29.4544	17.7371	163/31	-29.4036	17.7066	152/45	-29.4140	17.7354	156/50	-29.3441	17.7839	090/62
-29.4543	17.7362	144/50	-29.4052	17.7065	126/30	-29.4139	17.7355	152/55	-29.3345	17.7893	284/60
-29.4518	17.7356	170/64	-29.4029	17.6990	136/72	-29.4115	17.7397	114/50	-29.3839	17.8048	316/21
-29.4519	17.7337	144/48	-29.4042	17.6941	332/60	-29.4071	17.7407	318/46	-29.3781	17.8154	172/40
-29.4484	17.7293	192/50	-29.4041	17.6949	078/31	-29.4061	17.7426	332/49	-29.3882	17.8011	008/20
-29.4486	17.7361	144/42	-29.4044	17.6921	248/26	-29.4076	17.7450	342/50	-29.3941	17.7967	335/43
-29.4458	17.7368	142/10	-29.4061	17.6917	134/29	-29.4035	17.7524	132/30	-29.3834	17.7130	344/49
-29.4455	17.7367	177/12	-29.4049	17.6959	185/60	-29.4033	17.7534	160/47	-29.3839	17.7157	328/56
-29.4446	17.7380	157/28	-29.4037	17.6999	174/20	-29.4026	17.7545	177/50	-29.3817	17.7170	306/57
-29.4443	17.7397	148/35	-29.4014	17.7054	138/31	-29.4019	17.7562	124/52	-29.3813	17.7188	335/56
-29.4462	17.7409	162/25	-29.4013	17.7041	187/44	-29.4042	17.7427	003/63	-29.3864	17.7152	305/50
-29.4492	17.7377	145/30	-29.3996	17.6930	338/32	-29.4016	17.7374	336/37	-29.3866	17.7124	331/46

Table A1: Structural readings of the S_2 fabric in the GS gneisses (continued).

Latitude	Longitude	S_2	Latitude	Longitude	S_2	Latitude	Longitude	S_2	Latitude	Longitude	S_2
-29.4519	17.7395	145/28	-29.3981	17.6896	356/35	-29.4019	17.7268	164/41	-29.3929	17.6856	350/44
-29.4524	17.7401	156/25	-29.3995	17.6873	328/30	-29.4064	17.7243	332/50	-29.3936	17.6896	310/55
-29.4437	17.7261	168/52	-29.4022	17.6871	248/36	-29.4118	17.7320	152/39	-29.3933	17.6903	314/50
-29.4437	17.7258	152/35	-29.4031	17.6825	027/35	-29.4118	17.7320	166/50	-29.3923	17.6926	030/50
-29.4436	17.7255	148/76	-29.4043	17.6799	307/22	-29.3875	17.7082	326/50	-29.3936	17.6940	320/45
-29.4439	17.7224	143/33	-29.4049	17.6771	147/53	-29.3869	17.7085	298/66	-29.4548	17.7670	156/30
-29.4424	17.7242	161/36	-29.4009	17.6806	348/43	-29.3863	17.7091	356/60	-29.4316	17.7302	332/60
-29.4409	17.7259	330/51	-29.3997	17.6821	133/55	-29.3852	17.7097	340/52	-29.4348	17.7271	112/25
-29.4397	17.7277	100/27	-29.3979	17.6852	102/36	-29.3846	17.7107	338/65	-29.4551	17.7673	158/35
-29.4376	17.7323	130/33	-29.4314	17.7306	314/50	-29.4305	17.7338	138/26			

Table A2: Structural readings of the S_3 fabric in the GS gneisses.

Latitude	Longitude	S_3	Latitude	Longitude	S_3	Latitude	Longitude	S_3
-29.4698	17.7568	168/24	-29.4175	17.6933	334/43	-29.4160	17.6956	258/03
-29.4642	17.7740	140/57	-29.4071	17.7082	338/61	-29.4075	17.7082	159/80
-29.4626	17.7782	136/85	-29.4058	17.7071	102/42	-29.4058	17.7071	030/30
-29.4542	17.7954	173/35	-29.4058	17.6931	145/61	-29.4036	17.6773	026/26
-29.4681	17.7435	191/42	-29.3809	17.7204	137/46	-29.4535	17.7786	288/26
-29.4590	17.7389	210/40	-29.4544	17.7245	208/38	-29.4010	17.7368	300/36
-29.4591	17.7380	220/43	-29.4410	17.7188	342/62	-29.4154	17.7179	356/37
-29.4614	17.7337	214/48	-29.3839	17.8048	159/76	-29.4455	17.7367	162/25
-29.4565	17.7478	236/40	-29.3780	17.8153	284/85	-29.4428	17.7231	090/24
-29.4484	17.7293	132/35	-29.4338	17.7069	340/62	-29.4424	17.7242	304/34
-29.4226	17.7068	130/36	-29.4363	17.7239	282/45	-29.4415	17.7250	113/24
-29.4152	17.7198	008/39	-29.4338	17.7069	134/32			

Table A3: Structural readings of the lineations (L_2) encountered in the GS gneisses.

Latitude	Longitude	Lineation
-29.4686	17.7651	064/14
-29.4701	17.7617	234/14
-29.4564	17.7810	245/06
-29.4554	17.7836	010/25
-29.4536	17.7864	035/02
-29.4523	17.7899	051/05
-29.4552	17.7382	222/26
-29.4020	17.7661	082/02
-29.4070	17.7599	260/08
-29.4033	17.7532	253/05
-29.4016	17.7374	072/15

Table A4: Locations of shear zones encountered in the GS. Shear zone orientations could only be measured at certain locations as shown on the table. General trend of shear zones were recorded where the complete planar orientation could not be determined.

Latitude	Longitude	Sense of shear	Orientation	Latitude	Longitude	Sense of shear	Orientation	Latitude	Longitude	Sense of shear	Orientation
-29.4640	17.7731	Sinistral	x	-29.4363	17.7234	Sinistral	x	-29.4198	17.6919	Dextral	310/85
-29.4546	17.7848	Dextral	202/89	-29.4334	17.7075	Dextral	x	-29.3996	17.6930	Dextral	234/89
-29.4536	17.7868	Dextral	x	-29.4328	17.7053	Dextral	x	-29.4034	17.6808	Sinistral	x
-29.4573	17.7929	Dextral	174/37	-29.4316	17.7048	Dextral	x	-29.4014	17.6795	Sinistral	x
-29.4591	17.7381	Dextral	x	-29.4301	17.7046	Dextral	x	-29.4009	17.6807	Dextral	x
-29.4537	17.7358	Dextral	136/78	-29.4254	17.7120	Dextral	x	-29.4556	17.7675	Sinistral	x
-29.4513	17.7320	Dextral	x	-29.4229	17.7152	Dextral	186/66	-29.4571	17.7702	Sinistral	x
-29.4508	17.7320	Dextral	x	-29.4205	17.7179	Dextral	x	-29.4505	17.7838	Sinistral	x
-29.4509	17.7318	Sinistral	x	-29.4196	17.7205	Dextral	x	-29.4502	17.7848	Dextral	x
-29.4484	17.7292	Sinistral	x	-29.4183	17.7244	Dextral	x	-29.4456	17.7770	Dextral	x
-29.4476	17.7303	Sinistral	x	-29.4275	17.7187	Dextral	x	-29.4298	17.7633	Dextral	x
-29.4478	17.7321	Sinistral	x	-29.4216	17.7050	Sinistral	x	-29.4301	17.7637	Dextral	x
-29.4487	17.7355	Dextral	x	-29.4249	17.7009	Sinistral	x	-29.4107	17.7521	Sinistral	x
-29.4437	17.7261	Dextral	231/75	-29.4149	17.6991	Dextral	x	-29.4113	17.7505	Dextral	x
-29.4438	17.7253	Dextral	x	-29.4154	17.6976	Dextral	289/80	-29.4025	17.7554	Dextral	066/88
-29.4287	17.7381	Dextral	x	-29.4183	17.6928	Dextral	x	-29.3861	17.7092	Dextral	x
-29.4276	17.7367	Dextral	x	-29.4192	17.6921	Dextral	x	-29.4305	17.7322	Dextral	x

Appendix B. LA-ICP-MS data

Table B1: Complete LA-ICP-MS whole-rock geochemical data of the Brandewynsbank Gneiss. Major element data is reported in wt. % oxide and trace element concentrations in ppm.

Sample No.	GS1	GS2	GS6	GS11	GS28B	GS31	GS33A	GS35	GS36	GS37	GS30	GS21	GS23	GS18
Lithology	Brandewynsbank Gneiss													
SiO_2	76.51	76.29	74.16	74.66	65.36	72.97	74.93	74.78	70	69.64	72.28	71.91	73.48	73.1
TiO_2	0.29	0.27	0.34	0.29	0.71	0.38	0.38	0.38	0.65	0.57	0.49	0.54	0.24	0.34
Al_2O_3	11.84	11.66	12.85	12.9	15.11	13.85	12.55	12.05	14.08	14.1	13.47	13.27	13.07	13.55
Fe_2O_3	1.71	1.99	2.23	1.91	5.52	2.18	2.17	2.33	3.49	3.81	2.43	2.77	2.03	2.54
MnO	0.04	0.05	0.06	0.06	0.1	0.08	0.06	0.05	0.07	0.07	0.07	0.06	0.04	0.04
MgO	0.34	0.31	0.54	0.38	1.41	0.56	0.41	0.54	1.16	0.81	0.52	0.58	0.51	0.56
CaO	1.46	1.29	1.80	1.61	3.77	2.50	1.60	1.86	2.83	2.59	1.92	2.05	1.11	2.18
Cr_2O_3	0.01	0.02	0.02	0.02	0.04	0.02	0.01	0.03	0.01	0.06	0.01	0.02	0.02	0.02
Na_2O	2.66	2.53	2.98	2.90	3.45	3.25	3.26	2.70	3.23	3.36	2.88	2.89	2.45	3.54
K_2O	4.15	4.41	4.05	4.46	3.24	3.51	3.87	3.80	3.21	3.77	4.69	4.64	5.65	2.95
P_2O_5	0.06	0.07	0.07	0.05	0.18	0.08	0.08	0.08	0.15	0.13	0.10	0.11	0.04	0.07

Table B1: Complete LA-ICP-MS whole-rock geochemical data of the Brandewynsbank Gneiss (continued).

Sample No.	GS1	GS2	GS6	GS11	GS28B	GS31	GS33A	GS35	GS36	GS37	GS30	GS21	GS23	GS18
Lithology	Brandewynsbank Gneiss													
LOI	0.36	0.51	0.67	0.46	0.72	0.36	0.20	0.76	0.65	0.93	0.23	0.39	0.58	0.68
Sc	11.65	12.21	13.68	12.33	21.13	11.81	10.38	8.84	16.48	15.28	12.58	20.19	13.12	11.49
V	34.20	60.61	62.25	54.25	118.85	50.43	38.86	68.40	72.15	71.95	54.95	63.30	57.85	55.85
Cr	162.55	498.55	450.85	376.55	315.35	295.50	256.95	506.80	200.15	258.10	285.10	351.75	341.40	451.75
Co	2.30	2.75	3.55	3.67	11.62	3.37	2.32	3.85	6.71	6.09	4.45	4.26	5.05	3.67
Ni	11.60	16.40	18.35	14.5	14.44	7.85	7.65	12.9	12	11.7	9	9.75	11.55	25.7
Cu	49.7	56.45	71.65	34.2	21.1	20.43	80.15	32.75	60.5	37.75	35.14	25.41	36.15	150.7
Zn	32.4	26.55	242.1	30.25	145.55	44.35	45.95	38.35	62.05	120.5	47.3	119.5	38.7	57.15
Rb	142.95	157.15	157.45	169.1	124.65	137.6	177.45	146.55	130.8	153.45	177.25	166.1	219.25	112.8
Sr	134.55	117.05	164.8	178	213.65	272.2	118.8	202.4	298.8	141.925	177.9	168.35	213.55	142.4
Y	34.58	24.125	15.595	22.935	33.68	22.31	58.065	33.67	17.83	34.39	50.215	52.77	36.465	10.355
Zr	120.45	108.4	184.5	131.2	271.7	195.75	184.85	168.8	278.6	297.7	264.55	286.8	194.75	227.4
Nb	11.02	12.095	10.675	9.425	11.97	11.225	15.515	14.125	13.425	14.02	14.21	15.595	6.18	9.195
Mo	9.72	31.05	28.65	23.73	19.63	19.06	15.91	31.9	12.03	15.8	18.075	21.975	20.53	28.3
Cs	0.915	0.709	0.9505	1.335	0.955	1.1935	1.257	1.083	0.9605	1.505	1.288	0.908	1.194	0.819
Ba	598.5	523.45	689	996	832.7	1148.5	444.35	859	854	1044.5	1437	1421.5	1441.5	310.85
La	35.125	34.66	117.8	69.88	46.79	54.415	35.185	41.96	55.2	57.255	117.2	99.94	79.65	58.305
Ce	68.95	68.225	239.6	143.25	96.99	106.52	73.605	86.1	115.1	113.85	192.5	191.95	165.25	115.2
Pr	7.63	7.38	24.905	14.33	11.255	11.68	8.91	10.185	13.105	12.66	24.58	20.625	18.635	12.155
Nd	27.415	25.24	83.5	49.7	43.125	42.27	35.07	37.5	47.9	46.365	86.65	73.6	67.2	41.03
Sm	5.395	4.67	12.54	8.135	7.985	6.74	8.395	7.31	8.145	8.245	14.655	12.29	12.545	6.805
Eu	0.9215	0.907	1.29	1.3	1.805	1.548	0.9425	1.249	1.565	1.59	1.98	1.815	1.715	1.1395
Gd	5.275	3.975	7.645	5.68	7.34	5.36	8.345	6.525	6.06	6.985	11.385	10.8	10.265	4.5
Tb	0.764	0.576	0.854	0.744	1.07	0.7325	1.3855	0.9365	0.6615	1.035	1.533	1.5095	1.273	0.5005
Dy	5.705	3.725	4.21	4.125	6.275	4.11	9.295	5.945	3.6	6.2	9.14	9.8	7.36	2.51
Ho	1.242	0.831	0.5975	0.8205	1.225	0.785	1.959	1.205	0.653	1.3	1.7695	1.9335	1.3085	0.4085
Er	3.82	2.535	1.43	2.51	3.625	2.27	6.22	3.805	1.745	3.78	5.28	5.54	3.45	0.89
Tm	0.5235	0.416	0.1765	0.319	0.53	0.3095	0.908	0.503	0.244	0.51	0.7955	0.7805	0.423	0.095
Yb	3.26	2.905	0.975	2.51	3.125	2.09	6.215	3.295	1.39	3.615	5.05	5.365	2.74	0.57
Lu	0.4685	0.4415	0.1605	0.311	0.49	0.2985	0.8375	0.472	0.235	0.53	0.767	0.781	0.429	0.073
Hf	3.815	3.905	5.735	3.89	6.985	5.41	5.65	4.995	7.83	8.005	7.215	8.3	6.93	6.525
Ta	0.762	0.876	0.391	0.6985	0.78	0.6175	1.2885	1.2295	0.6215	0.905	0.9705	1.03	0.2195	0.288
Pb	26.15	23.17	28.455	21.885	20.92	25.63	23.26	19.9	19.23	18.99	27.305	20.62	43.165	30.37
Th	16.95	17.775	26.545	16.5	13.445	15.73	14.37	14.46	15.35	18.5	18.835	27.185	58.23	31.14
U	0.85	1.73	1.06	1.16	0.91	0.97	4.23	0.726	0.588	1.605	1.397	1.426	2.6	0.7925

Table B2: Complete LA-ICP-MS whole-rock geochemical data of the Noenoemaasberg and Steinkopf gneisses. Major element data is reported in wt. % oxide and trace element concentrations in ppm.

Sample No.	GS20	GS26	GS27	GS38	GS39	GS42	GS43	GS4	GS13	GS14	GS16	GS22	GS28A	GS32B	GS33B	GS34	GS41
Lithology	Noenoemaasberg Gneiss								Steinkopf Gneiss								
SiO_2	75.20	77.47	78.93	78.28	75.86	73.74	72.39	72.01	69.39	69.40	67.58	68.60	64.64	72.09	66.78	65.29	71.68
TiO_2	0.30	0.23	0.18	0.19	0.30	0.34	0.34	0.17	0.48	0.57	0.62	0.61	0.79	0.41	0.66	0.75	0.51
Al_2O_3	12.40	11.44	10.69	11.30	12.08	12.86	13.31	13.91	14.54	14.46	15.23	14.28	15.52	13.61	15.33	15.13	14.10
Fe_2O_3	1.67	1.24	1.29	0.91	1.78	2.25	2.40	1.73	3.57	3.94	4.63	4.25	5.85	2.41	4.90	5.45	2.57
MnO	0.03	0.03	0.01	0.02	0.03	0.06	0.14	0.03	0.09	0.13	0.10	0.10	0.10	0.06	0.12	0.10	0.05
MgO	0.36	0.11	0.11	0.12	0.32	0.49	1.05	0.42	0.77	0.89	1.08	1.26	1.53	0.54	0.84	1.50	0.68
CaO	0.80	0.47	0.39	0.35	1.26	1.74	2.87	0.78	1.99	2.66	3.57	3.36	4.58	2.14	3.27	3.82	2.63
Cr_2O_3	0.02	0.02	0.02	0.01	0.03	0.02	0.01	0.02	0.05	0.02	0.03	0.02	0.03	0.02	0.04	0.02	0.02
Na_2O	2.98	2.15	2.38	2.39	2.68	2.97	3.59	2.35	3.31	3.72	3.84	3.18	3.79	2.97	4.13	3.20	3.10
K_2O	5.24	5.99	5.24	5.77	4.16	4.38	2.76	6.91	4.27	2.79	1.76	2.78	1.54	4.29	2.19	3.59	3.53
P_2O_5	0.06	0.02	0.02	0.02	0.02	0.06	0.06	0.09	0.12	0.14	0.14	0.17	0.19	0.09	0.16	0.18	0.10
LOI	0.34	0.40	0.29	0.35	0.93	0.46	0.25	0.88	0.91	0.58	0.77	0.52	0.77	0.65	1.01	0.53	0.34
Sc	11.53	10.41	10.46	8.77	9.76	12.79	21.99	9.65	17.50	17.51	19.17	18.59	21.36	12.84	20.48	19.94	12.83
V	51.05	37.20	47.15	22.41	60.60	59.83	47.75	53.05	79.50	93.30	112.45	106.55	119.15	61.70	104.70	135.45	65.05
Cr	399.75	329.20	485.90	172.45	593.50	446.30	236.65	362.90	295.10	368.85	462.15	475.00	301.50	373.55	263.30	505.65	362.75
Co	2.58	1.09	1.24	1.04	2.36	3.26	4.56	3.92	7.38	8.18	9.56	8.99	12.07	4.13	9.56	12.87	4.18
Ni	11.55	8.80	12.60	10.50	14.80	13.25	18.35	18.15	27.60	23.55	21.60	17.80	15.60	11.25	12.18	18.45	11.35
Cu	46.10	19.84	35.55	11.08	36.70	32.65	35.70	98.15	37.00	167.35	194.50	34.55	385.25	53.85	46.47	30.74	19.76
Zn	23.30	15.10	12.55	18.45	27.95	30.15	65.05	30.60	76.35	65.75	77.55	62.95	82.75	38.95	66.70	146.65	43.25
Rb	176.65	212.65	249.60	227.05	142.25	166.10	98.65	209.65	210.45	126.15	118.25	116.75	58.77	158.40	155.00	161.75	126.90
Sr	118.65	34.40	33.50	33.80	145.85	154.95	113.50	283.60	187.05	332.00	162.83	251.20	207.79	255.10	209.88	216.70	251.05
Y	33.28	13.83	27.67	10.18	8.62	45.16	65.12	11.12	31.61	31.30	32.41	29.05	72.14	27.93	26.98	33.70	22.55
Zr	162.10	128.40	118.60	99.45	144.45	159.40	121.50	96.20	255.20	255.30	250.30	249.65	278.45	209.40	231.05	268.20	256.65
Nb	11.21	11.73	13.24	10.60	8.26	15.89	18.27	4.22	13.59	12.52	12.47	12.89	21.18	12.29	15.34	12.44	11.66
Mo	25.50	20.20	31.60	10.78	37.50	28.65	14.55	22.98	18.34	22.87	30.72	29.55	18.51	23.79	16.47	31.98	22.55
Cs	1.24	0.35	0.73	0.65	0.77	1.08	0.76	1.29	3.15	2.72	3.46	0.76	0.59	1.12	2.66	1.70	1.02
Ba	1036.00	241.70	179.50	291.50	571.50	754.50	249.20	1878.50	1518.50	1010.00	695.95	977.50	501.90	1381.00	716.40	947.50	930.50
La	52.47	44.30	35.59	44.10	49.24	47.84	34.21	48.54	55.14	52.46	46.39	50.81	48.79	55.35	41.64	49.19	60.24
Ce	107.45	92.50	80.65	87.20	100.95	92.80	71.31	96.40	111.95	104.50	99.47	100.54	107.69	110.95	84.70	100.88	120.29
Pr	11.66	9.78	8.09	9.91	11.14	11.13	8.79	10.44	12.67	11.74	10.82	11.38	13.40	12.01	9.52	11.65	13.17
Nd	42.40	33.85	29.05	34.75	40.55	41.05	34.05	36.78	47.65	45.50	40.90	41.86	56.20	43.93	36.50	44.16	49.15
Sm	7.54	6.50	5.56	6.66	7.07	7.70	8.12	7.15	8.27	8.40	7.98	7.34	13.34	7.64	6.95	8.56	8.07
Eu	1.44	0.50	0.41	0.55	1.31	1.24	0.85	1.70	2.03	1.92	1.80	1.58	1.99	1.49	1.57	1.74	1.67
Gd	6.45	4.39	4.48	4.43	4.91	7.23	8.01	5.50	7.13	7.08	6.47	6.09	12.48	6.21	6.01	7.50	6.52
Tb	0.89	0.59	0.76	0.54	0.53	1.07	1.29	0.63	0.94	0.96	0.97	0.85	2.06	0.85	0.83	1.04	0.79
Dy	5.90	3.24	4.87	2.71	2.53	7.28	9.09	2.93	5.87	5.72	6.03	5.49	13.46	4.94	5.36	6.26	4.40
Ho	1.19	0.55	1.08	0.39	0.34	1.52	2.08	0.42	1.15	1.13	1.21	1.03	2.68	1.03	0.96	1.27	0.82
Er	3.51	1.39	3.13	0.96	0.70	4.68	6.97	0.87	3.47	3.54	3.59	3.16	8.26	3.07	2.73	3.58	2.16
Tm	0.49	0.17	0.44	0.12	0.07	0.74	1.12	0.09	0.49	0.49	0.54	0.46	1.11	0.40	0.39	0.51	0.28
Yb	3.47	1.04	2.62	0.70	0.53	4.72	8.56	0.60	3.06	3.11	3.52	2.79	7.30	2.78	2.57	3.51	1.94
Lu	0.48	0.15	0.38	0.06	0.08	0.77	1.35	0.10	0.47	0.45	0.52	0.42	0.95	0.42	0.37	0.47	0.26
Hf	4.60	4.24	4.61	3.76	4.56	4.87	4.31	2.61	6.98	6.76	6.60	6.68	7.36	6.16	6.04	7.24	7.26
Ta	0.65	0.64	0.76	0.42	0.26	1.29	1.16	0.20	0.81	0.81	0.95	0.80	1.40	0.87	1.30	0.70	0.47
Pb	15.71	20.95	21.18	26.10	33.75	20.33	19.45	57.74	18.85	31.34	15.36	20.42	14.99	26.79	20.23	19.85	24.98
Th	21.00	22.99	24.62	25.32	27.92	17.10	17.92	28.87	16.62	15.31	13.11	16.74	6.85	17.32	12.96	11.72	20.72
U	2.09	1.56	2.16	1.98	0.67	1.55	1.16	1.31	1.62	1.59	1.63	0.96	0.52	1.00	2.59	0.86	1.27

Table B3: LA-ICP-MS whole-rock major element data of the Vioolsdrif Suite rocks (Macey et al., 2017). Concentrations are reported in wt. % oxide.

Sample No.	Lithology	SiO_2	TiO_2	Al_2O_3	Fe_2O_3	MnO	MgO	CaO	Cr_2O_3	Na_2O	K_2O	P_2O_5	LOI

CHM 271	Gaarseep Granodiorite	65.41	0.49	15.23	4.77	0.12	2.04	4.45	below detection	2.73	3.44	0.13	1.43
CHM 279	Gaarseep Granodiorite	69.96	0.42	14.39	2.94	0.06	0.94	2.55	below detection	3.02	5.17	0.12	0.48
CHM12	Gaarseep Granodiorite	68.37	0.47	15.10	1.97	0.07	1.38	2.91	0.00	3.63	4.34	0.17	
CHM25	Gaarseep Granodiorite	72.67	0.40	14.00	1.46	0.05	0.44	1.64	0.00	3.36	4.80	0.07	
CHM37	Gaarseep Granodiorite	65.28	0.83	15.81	2.68	0.10	1.61	4.33	0.00	2.57	3.76	0.24	
CHM45	Gaarseep Granodiorite	62.45	1.03	16.52	2.92	0.12	2.51	5.38	0.00	1.62	3.44	0.32	
CHM64	Gaarseep Granodiorite	62.95	0.68	15.92	2.90	0.12	2.91	5.91	0.00	1.27	3.17	0.15	
CHM74	Gaarseep Granodiorite	65.47	0.70	15.50	2.58	0.10	1.86	4.03	0.00	3.08	4.06	0.23	
CHM89	Gaarseep Granodiorite	66.99	0.66	14.89	2.42	0.08	1.60	3.49	0.00	3.38	4.17	0.19	
CHM99	Gaarseep Granodiorite	67.12	0.62	15.43	2.29	0.06	1.19	2.90	0.00	3.33	5.11	0.17	
CHM136	Gaarseep Granodiorite	70.73	0.35	14.21	1.74	0.07	1.05	2.80	0.00	3.43	4.01	0.14	
CHM139	Gaarseep Granodiorite	67.98	0.58	14.63	2.31	0.09	1.50	3.72	0.00	3.65	3.17	0.20	
CHM140	Gaarseep Granodiorite	68.17	0.46	14.92	2.23	0.08	1.47	3.53	0.00	3.29	3.61	0.15	
CHM146	Gaarseep Granodiorite	74.80	0.18	12.86	1.09	0.05	0.56	1.67	0.00	2.87	5.05	0.05	
CHM147	Gaarseep Granodiorite	75.26	0.10	13.30	0.71	0.04	0.34	1.50	0.00	3.31	4.86	0.05	
CHM150	Gaarseep Granodiorite	66.79	0.48	14.71	2.46	0.08	2.17	3.79	0.00	2.88	4.26	0.13	
CHM153	Gaarseep Granodiorite	55.37	0.78	17.25	3.40	0.15	5.17	8.12	0.00	2.80	1.74	0.37	
CHM159	Gaarseep Granodiorite	67.26	0.43	15.09	2.27	0.09	2.22	3.83	0.00	2.49	3.92	0.12	
CHM161	Gaarseep Granodiorite	67.44	0.51	14.73	2.36	0.10	2.43	4.08	0.00	2.39	3.18	0.12	
CHM163	Gaarseep Granodiorite	74.01	0.19	13.51	1.12	0.03	0.52	1.94	0.00	2.59	5.14	0.07	
CHM164	Gaarseep Granodiorite	69.42	0.56	14.07	2.41	0.07	1.11	3.04	0.00	2.98	3.89	0.21	
CHM166	Gaarseep Granodiorite	64.65	0.55	16.43	2.51	0.09	2.04	4.89	0.00	3.17	2.73	0.19	
CHM168	Gaarseep Granodiorite	70.38	0.36	14.58	1.95	0.07	1.27	3.07	0.00	2.90	3.35	0.13	
CHM169	Gaarseep Granodiorite	70.04	0.44	14.45	1.91	0.08	1.29	2.95	0.00	3.14	3.83	0.15	
CHM190	Gaarseep Granodiorite	74.62	0.23	13.59	1.12	0.06	0.56	1.77	0.00	2.02	4.97	0.07	
CHM192	Gaarseep Granodiorite	71.16	0.33	14.83	1.54	0.06	1.13	3.28	0.00	2.60	3.33	0.12	
CHM196	Gaarseep Granodiorite	69.90	0.48	14.61	1.96	0.07	1.26	2.56	0.00	3.13	4.18	0.15	
CHM202	Gaarseep Granodiorite	67.54	0.45	14.63	2.27	0.09	2.04	4.25	0.00	2.61	3.65	0.13	
CHM204	Gaarseep Granodiorite	68.26	0.41	14.60	2.20	0.09	1.87	3.81	0.00	2.40	4.03	0.13	
CHM205	Gaarseep Granodiorite	63.81	0.90	15.75	2.90	0.10	2.14	4.61	0.00	3.25	3.29	0.26	
CHM213	Gaarseep Granodiorite	62.27	0.85	16.82	3.32	0.09	2.30	3.33	0.00	4.75	3.18	0.28	
CHM216	Gaarseep Granodiorite	71.40	0.26	14.37	1.56	0.07	1.03	2.86	0.00	2.82	4.12	0.12	
CHM218	Gaarseep Granodiorite	64.20	0.62	16.41	2.64	0.11	2.26	4.91	0.00	2.76	2.92	0.18	
CHM220	Gaarseep Granodiorite	70.59	0.44	14.09	1.95	0.06	1.14	2.66	0.00	2.79	4.42	0.16	
DRL-107	Gaarseep Granodiorite	71.05	0.29	14.52	1.39	0.04	1.13	2.66	0.00	2.86	4.81	0.08	
DRV-21	Gaarseep Granodiorite	67.69	0.48	15.45	2.19	0.09	1.37	2.82	0.00	4.30	3.63	0.17	
DRV-01	Gaarseep Granodiorite	69.94	0.49	14.27	1.78	0.07	1.36	2.68	0.00	3.11	4.71	0.14	
DRV-03	Gaarseep Granodiorite	65.89	0.75	15.37	2.72	0.09	1.39	3.69	0.00	2.91	4.53	0.22	
DRV-06	Gaarseep Granodiorite	71.47	0.32	13.95	1.56	0.06	1.07	2.45	0.00	2.42	5.32	0.07	
DRV-09	Gaarseep Granodiorite	65.69	0.44	15.17	2.46	0.08	2.40	4.03	0.00	2.72	4.60	0.12	
DRV-33	Gaarseep Granodiorite	64.50	0.65	16.68	2.24	0.07	1.73	4.06	0.00	3.12	4.85	0.25	
DRV-51	Gaarseep Granodiorite	65.24	0.60	15.95	2.46	0.08	2.00	3.94	0.00	3.35	3.96	0.17	
DRV-55	Gaarseep Granodiorite	62.74	0.70	16.77	2.76	0.08	2.16	4.81	0.00	3.48	3.64	0.26	
DRV-62	Gaarseep Granodiorite	58.99	0.99	18.11	3.10	0.12	2.59	6.27	0.00	2.96	2.93	0.35	
DRV-C	Gaarseep Granodiorite	60.47	0.53	16.98	2.94	0.12	3.58	6.58	0.00	2.91	1.72	0.13	
PM15195	Gaarseep Granodiorite	67.48	0.43	15.04	3.93	0.07	1.77	3.35	0.01	2.91	4.16	0.15	0.89
RPGV2	Gaarseep Granodiorite	67.74	0.60	15.01	4.40	0.07	1.26	2.72	0.01	2.93	4.77	0.21	0.58
RPGG30	Gaarseep Granodiorite	62.52	0.63	15.45	6.12	0.12	2.96	5.28	0.01	2.29	3.38	0.21	1.10
PM15183	Gaarseep Granodiorite	68.72	0.59	14.49	4.24	0.08	1.53	2.27	0.01	3.13	3.46	0.28	1.12
RPGV15	Gaarseep Granodiorite	71.85	0.24	14.72	2.30	0.05	0.31	1.17	0.01	3.75	4.52	0.13	0.71
CHM225	undifferentiated	76.01	0.15	12.78	1.58	0.02	0.38	1.26	0.00	2.98	4.63	0.05	0.62
CHM228	undifferentiated	64.67	0.49	14.37	4.76	0.07	2.36	4.35	0.01	3.65	2.94	0.18	1.03
CHM230	undifferentiated	59.70	0.76	15.07	7.43	0.12	3.31	5.64	0.01	3.08	2.73	0.21	1.33
DRP-01	undifferentiated	68.58	0.45	15.42	2.00	0.05	1.68	3.14	0.00	2.81	3.79	0.13	
DRP-01A	undifferentiated	69.76	0.36	15.29	1.60	0.04	1.36	3.13	0.00	3.40	3.43	0.12	
DRP-09	undifferentiated	70.12	0.38	15.21	1.74	0.05	0.71	2.82	0.00	2.90	4.48	0.08	
DRV-13A	undifferentiated	61.87	0.95	16.04	3.43	0.17	2.32	4.99	0.00	3.29	2.85	0.33	
DRV-15	undifferentiated	66.23	0.55	15.23	2.45	0.08	1.82	3.87	0.00	3.02	4.38	0.18	
DRV-15A	undifferentiated	65.86	0.52	15.33	2.29	0.07	2.52	3.85	0.00	3.21	4.10	0.18	
DRV-15D	undifferentiated	65.78	0.58	15.25	2.43	0.07	2.28	3.94	0.00	3.08	4.15	0.20	
DRV-15F	undifferentiated	64.61	0.55	16.37	2.45	0.07	2.23	3.66	0.00	3.43	4.36	0.18	
DRV-44	undifferentiated	60.64	0.93	16.34	3.52	0.12	2.75	5.08	0.00	3.46	3.30	0.32	
DRV-54	undifferentiated	68.18	0.52	14.58	2.18	0.06	1.65	3.01	0.00	3.27	4.60	0.15	
CHM 286	undifferentiated	77.82	0.10	12.25	0.60	0.01	0.04	0.14	below detection	3.36	5.56	0.02	0.21
CHM 289	undifferentiated	75.34	0.21	12.86	1.34	0.05	0.29	0.97	below detection	3.70	4.66	0.04	0.76
GS15 031	undifferentiated	74.09	0.30	13.99	0.97	0.04	0.35	1.39	0.00	3.06	5.33	0.06	
CHM185	undifferentiated	78.94	0.10	11.50	0.46	0.01	0.04	0.37		2.48	5.76	0.01	
DRV-12	undifferentiated	74.08	0.27	13.74	1.09	0.04	0.38	1.32		2.88	5.37	0.05	
DRV-12B	undifferentiated	73.95	0.29	13.56	1.08	0.04	0.18	1.41		3.63	5.04	0.06	
DRV-12E	undifferentiated	73.70	0.25	13.63	1.00	0.04	0.41	1.31		3.39	5.55	0.04	
DRV-71	undifferentiated	77.41	0.13	12.14	0.48	0.03	0.13	0.62		3.58	5.13	0.02	
TD1353	undifferentiated	54.05	0.75	16.39	8.36	0.15	4.21	9.17	0.02	3.93	1.37	0.29	0.53
PM13225	undifferentiated	60.14	0.63	16.27	6.62	0.12	3.05	6.03	0.01	3.19	2.88	0.17	0.42
GS15 23	Khoromus porphyry	60.83	0.58	16.12	5.52	0.10	3.30	5.31	0.02	2.96	3.08	0.21	2.06
CHM 280	Khoromus porphyry	60.69	0.69	18.07	4.72	0.08	1.24	5.40	0.01	3.79	3.72	0.28	0.66
CHM2	Khoromus porphyry	67.54	0.68	15.46	2.17	0.08	1.11	3.46		3.11	4.30	0.18	
CHM14	Khoromus porphyry	66.63	0.50	14.64	2.55	0.10	2.63	3.83		2.73	3.70	0.12	
CHM123	Khoromus porphyry	60.49	0.72	17.69	2.75	0.11	2.34	6.41		3.04	3.20	0.23	
CHM125	Khoromus porphyry	64.22	0.52	17.95	1.82	0.07	1.24	5.30		3.54	3.46	0.14	
CHM129	Khoromus porphyry	63.48	0.72	16.96	2.47	0.09	1.85	5.02		2.91	3.74	0.24	
CHM131	Khoromus porphyry	63.46	0.73	16.55	2.48	0.09	1.85	5.35		3.11	3.69	0.23	
CHM133	Khoromus porphyry	63.73	0.62	17.21	2.34	0.10	1.72	5.13		3.07	3.49	0.19	
CHM148	Khoromus porphyry	65.38	0.71	15.69	2.36	0.08	1.68	4.53		3.53	3.61	0.24	
CHM92	Khoromus porphyry	68.43	0.32	16.08	1.69	0.06	1.05	2.98		3.83	4.01	0.15	
CHM94	Khoromus porphyry	63.04	0.64	16.88	2.81	0.09	2.64	3.75		3.46	3.66	0.35	
CHM100	Khoromus porphyry	63.69	0.57	18.08	2.14	0.07	1.80	4.26		4.38	2.87	0.14	
CHM26	Khoromus porphyry	69.80	0.53	14.60	1.83	0.06	0.84	2.79		3.25	4.69	0.13	
DRH-01	Khoromus porphyry	65.42	0.77	15.65	2.81	0.08	1.82	3.05		3.60	4.18	0.24	
DRV-08B	Khoromus porphyry	57.79	0.98	16.55	3.58	0.14	4.58	6.23		2.40	2.81	0.34	
DRV-32	Khoromus porphyry	66.90	0.47	15.02	2.30	0.09	2.59	4.06		2.45	3.51	0.11	
RT15_264	Weisserquartzkuppe	76.10	0.22	12.71	1.74	0.03	0.18	0.99	0.01	3.60	3.62	0.05	0.43
RT15_328	Weisserquartzkuppe	71.59	0.34	14.08	3.08	0.05	0.98	1.69	0.01	2.79	4.48	0.11	0.89
TD15_122	Weisserquartzkuppe	69.83	0.44	15.48	3.09	0.03	0.78	1.89	0.01	4.14	2.97	0.18	1.11
CG1391	Goabis Diorite	54.41	0.68	13.89	9.73	0.21	7.60	8.47	0.06	2.19	1.33	0.38	1.27
RT_15_591	Goabis Diorite	61.46	0.68	15.77	6.77	5.60	2.69	3.07		0.19	0.01	0.66	100.16
CHM 285	Goabis Diorite	55.83	0.77	18.83	6.96	0.13	2.96	7.20	0.01	3.27	2.79	0.32	0.96

Table B4: LA-ICP-MS whole-rock trace element data of the Vioolsdrif Suite rocks (Macey et al., 2017). Concentrations are reported in ppm. Not all samples were analysed for trace element concentrations.

Sample No.	CHM 271	CHM 279	PM15195	PM15183	CHM 286	TD1353	PM13225	CHM 280	RT15_264	CG1391	RT_15_591
Lithology	Gaarseep Granodiorite				undifferentiated Vioolsdrif Suite			Khoromus porphyry	Weisserquartzkuppe	Goabis Diorite	
Sc	14.01	4.19	8.24	8.71	2.48	18.88	15.87	8.42	1.96	21.68	15.51
V	100.40	50.42	78.91	62.63	2.69	179.70	125.50	89.43	8.16	212.90	125.40
Cr	24.88	13.57	36.93	30.71	1.76	124.70	56.37	7.71	7.63	390.30	59.10
Co	10.57	5.21	9.40	9.33	0.49	15.73	15.42	5.89	1.63	31.08	17.44
Ni	10.41	4.53	9.95	22.23	0.94	24.00	10.45	below detection	20.15	84.65	546.80
Cu	8.60	37.24	186.20	53.52	2.70	121.90	86.02	46.17	89.19	105.80	60.83
Zn	69.18	37.44	43.52	60.46	2.64	67.98	69.63	55.03	19.76	87.78	66.86
Rb	140.50	169.90	137.70	180.20	359.60	30.88	92.96	140.80	77.61	37.35	113.80
Sr	357.20	340.60	420.50	237.80	19.70	805.60	438.40	575.10	155.90	572.40	432.90
Y	21.31	26.39	13.09	13.29	26.32	14.74	21.04	18.26	9.96	13.25	20.61
Zr	113.60	155.50	78.58	120.40	78.19	26.54	131.90	149.20	124.70	54.35	121.20
Nb	8.36	11.32	9.09	15.98	20.84	5.67	9.26	9.20	4.95	3.96	9.76
Ba	747.50	1202.00	952.00	746.10	63.28	252.60	793.30	1136.00	4997.00	582.90	729.00
La	32.09	54.84	27.55	66.96	13.51	23.80	34.94	34.49	52.54	18.82	34.78
Ce	66.82	110.10	61.07	139.10	28.20	49.93	69.70	70.83	105.50	41.13	71.16
Pr	7.60	12.10	6.87	14.27	2.79	5.97	7.95	8.06	11.05	4.93	8.09
Nd	29.30	44.72	25.45	53.95	8.70	23.78	30.27	30.94	41.93	20.32	32.33
Sm	5.56	7.80	4.42	7.75	1.82	4.47	5.46	5.31	5.16	3.87	6.02
Eu	1.03	1.09	0.88	1.33	0.12	1.50	1.16	1.20	1.49	0.98	1.29
Gd	4.54	5.89	3.40	5.19	2.19	3.56	4.50	4.11	3.69	3.18	4.88
Tb	0.67	0.85	0.48	0.64	0.49	0.49	0.63	0.57	0.43	0.43	0.75
Dy	4.14	5.17	2.72	3.22	3.96	2.82	3.83	3.43	2.30	2.61	4.27
Ho	0.79	1.00	0.53	0.54	0.92	0.54	0.76	0.67	0.44	0.50	0.87
Er	2.25	2.77	1.51	1.26	3.27	1.52	2.25	1.89	1.25	1.41	2.47
Tm	0.32	0.40	0.23	0.15	0.56	0.21	0.32	0.27	0.18	0.20	0.38
Yb	2.02	2.52	1.52	0.84	4.20	1.40	2.11	1.82	1.39	1.30	2.38
Lu	0.29	0.35	0.24	0.13	0.67	0.21	0.32	0.27	0.24	0.19	0.40
Hf	3.29	4.25	2.70	3.26	3.74	0.95	3.66	3.88	3.72	1.62	3.40
Ta	0.40	1.23	1.10	1.78	2.38	0.40	0.82	0.65	0.38	0.31	1.11
Pb	16.55	27.17	18.93	14.11	20.10	13.04	18.64	24.86	11.40	8.63	21.53
Th	12.69	21.51	11.02	18.84	32.66	4.55	13.03	9.93	11.75	4.18	13.72
U	0.79	2.59	2.33	2.87	2.77	1.92	2.25	2.20	0.98	0.84	2.95

Appendix C. Correlation and covariance matrices

Table C1: Multivariate Spearman rank coefficient of correlation (r) matrices for the BWB, NNM and STK gneisses. n=number of samples. Significance levels of 10% (0.1), 1% (0.01) and 0.1% (0.001) correspond to confidence limits, at which the relationship observed in the sample can apply to the whole population, of 90%, 99% and 99.9% respectively. The aforementioned ratios represent the least significant correlation coefficient (r_s) value at the specified significance level; values are taken from Rollinson (1993).

Brandewynsbank (n = 14, 10%-0.367; 1%-0.626; 0.1%-0.771)

	Al_2O_3	CaO	Fe_2O_3	K_2O	MgO	MnO	Na_2O	P_2O_5	SiO_2	TiO_2
Al_2O_3	1									
CaO	**0.87****	1								
Fe_2O_3	**0.82****	**0.89****	1							
K_2O	**-0.64****	**-0.82****	**-0.69****	1						
MgO	**0.92****	**0.94****	**0.96****	**-0.69****	1					
MnO	**0.74****	**0.8****	**0.66****	-0.53*	**0.73****	1				
Na_2O	**0.75****	**0.8****	**0.71****	**-0.84****	**0.71****	**0.64****	1			
P_2O_5	**0.70****	**0.87****	**0.88****	**-0.67****	**0.85****	**0.81****	**0.65****	1		
SiO_2	**-0.97****	**-0.87****	**-0.89****	0.57*	**-0.96****	**-0.74****	**-0.67****	**-0.75****	1	
TiO_2	**0.76****	**0.91****	**0.89****	**-0.69****	**0.89****	**0.82****	**0.72****	**0.97****	**-0.79****	1

Noenoemaasberg (n = 8, 10%-0.524; 1%-0.833; 0.1%-0.952)

	Al_2O_3	CaO	Fe_2O_3	K_2O	MgO	MnO	Na_2O	P_2O_5	SiO_2	TiO_2
Al_2O_3	1									
CaO	0.71*	1								
Fe_2O_3	0.74*	**0.95****	1							
K_2O	-0.12	-0.73*	-0.71*	1						
MgO	**0.89****	**0.83****	**0.85****	-0.46	1					
MnO	0.79*	**0.91****	0.82*	-0.5	**0.84****	1				
Na_2O	0.36	0.71*	0.64*	-0.81*	0.69*	0.57*	1			
P_2O_5	**0.91****	0.52*	0.57*	0.046	0.81*	0.58*	0.33	1		
SiO_2	**-0.99****	-0.71*	-0.74*	0.12	**-0.89****	-0.79*	-0.36	**-0.91****	1	
TiO_2	0.31	0.82*	0.66*	-0.81*	0.58*	0.78*	0.8*	0.14	-0.31	1

Steinkopf (n = 9, 10%-0.483; 1%-0.783; 0.1%-0.917)

	Al_2O_3	CaO	Fe_2O_3	K_2O	MgO	MnO	Na_2O	P_2O_5	SiO_2	TiO_2
Al_2O_3	1									
CaO	0.67*	1								
Fe_2O_3	**0.87****	**0.87****	1							
K_2O	-0.72*	-0.72*	-0.68*	1						
MgO	0.65*	**0.92****	**0.87****	-0.63*	1					
MnO	0.68*	0.56*	0.73*	-0.63*	0.66*	1				
Na_2O	**0.93****	0.53*	0.73*	-0.78*	0.55*	0.78*	1			
P_2O_5	0.68*	**0.82****	**0.93****	-0.58*	**0.92****	0.74*	0.56*	1		
SiO_2	**-0.9****	**-0.85****	**-0.97****	0.65*	**-0.85****	-0.63*	-0.73*	**-0.88****	1	
TiO_2	0.73*	**0.88****	**0.95****	-0.68*	**0.8****	0.66*	0.6*	**0.88****	**-0.87****	1

******** *Correlation is significant at the 0.01 and 0.001 level*
** Correlation is significant at the 0.1 level*

The most significant correlations are highlighted in bold and the most significant correlations indicate two tails of which the number is either positive (elements vary together) or negative (elements vary in an inverse manner).

Table C2: Centered log-ratio covariance matrices for the BWB Gneiss calculated after the methods of Aitchison (1986), where SiO_2, etc. represents (natural) log [SiO_2 wt. % / g], etc. and where g is the geometric mean of the geometric mean.

	Al_2O_3	CaO	Fe_2O_3	K_2O	MgO	MnO	Na_2O	P_2O_5	SiO_2	TiO_2	Sc	V	Cr	Co	Ni	Cu	Zn	Rb	Sr	Y	Zr	Nb
Al_2O_3	0.0073	0.0300	0.0291	-0.0173	0.0393	0.0202	0.0091	0.0295	-0.0042	0.0264	0.0176	0.0220	-0.0059	0.0391	0.0019	0.0146	0.0316	-0.0158	0.0134	0.0065	0.0238	0.0074
CaO	0.0300	0.1593	0.1403	-0.1001	0.1818	0.1022	0.0454	0.1696	-0.0189	0.1411	0.0721	0.1038	-0.0264	0.1654	0.0129	0.0856	0.1428	-0.0959	0.0535	0.0327	0.0982	0.0711
Fe_2O_3	0.0291	0.1403	0.1501	-0.0842	0.1854	0.0923	0.0375	0.1663	-0.0199	0.1376	0.0827	0.1188	-0.0182	0.1868	0.0189	0.0849	0.1515	-0.0797	0.0395	0.0630	0.1025	0.0623
K_2O	-0.0173	-0.1001	-0.0842	0.0907	-0.1057	-0.0548	-0.0320	-0.0986	0.0111	-0.0788	-0.0335	-0.0601	0.0121	-0.0927	-0.0271	-0.1696	-0.0485	0.0883	-0.0210	-0.0263	-0.0453	-0.0551
MgO	0.0393	0.1818	0.1854	-0.1057	0.2539	0.1159	0.0471	0.2032	-0.0253	0.1745	0.1018	0.1480	-0.0353	0.2466	0.0170	0.0920	0.1970	-0.0981	0.0860	0.0503	0.1412	0.0633
MnO	0.0202	0.1022	0.0923	-0.0548	0.1159	0.0932	0.0274	0.1154	-0.0128	0.0953	0.0543	0.0731	-0.0171	0.1109	-0.0192	0.0055	0.1015	-0.0490	0.0402	0.0521	0.0568	0.0532
Na_2O	0.0091	0.0454	0.0375	-0.0320	0.0471	0.0274	0.0176	0.0445	-0.0050	0.0377	0.0160	0.0215	-0.0086	0.0376	0.0056	0.0468	0.0429	-0.0281	0.0074	0.0013	0.0303	0.0196
P_2O_5	0.0295	0.1696	0.1663	-0.0986	0.2032	0.1154	0.0445	0.2202	-0.0209	0.1759	0.0912	0.1195	-0.0405	0.1813	-0.0036	0.0760	0.1748	-0.0931	0.0414	0.0769	0.1150	0.1046
SiO_2	-0.0042	-0.0189	-0.0199	0.0111	-0.0253	-0.0128	-0.0050	-0.0209	0.0028	-0.0179	-0.0118	-0.0158	0.0032	-0.0261	-0.0018	-0.0099	-0.0197	0.0106	-0.0069	-0.0088	-0.0139	-0.0068
TiO_2	0.0264	0.1411	0.1376	-0.0788	0.1745	0.0953	0.0377	0.1759	-0.0179	0.1475	0.0784	0.0978	-0.0378	0.1580	-0.0091	0.0554	0.1525	-0.0731	0.0438	0.0704	0.1055	0.0813
Sc	0.0176	0.0721	0.0827	-0.0335	0.1018	0.0543	0.0160	0.0912	-0.0118	0.0784	0.0735	0.0673	-0.0199	0.1115	0.0061	0.0235	0.1139	-0.0365	0.0243	0.0461	0.0615	0.0286
V	0.0220	0.1038	0.1188	-0.0601	0.1480	0.0731	0.0215	0.1195	-0.0158	0.0978	0.0673	0.1195	0.0265	0.1671	0.0379	0.0480	0.1205	-0.0606	0.0434	0.0322	0.0706	0.0369
Cr	-0.0059	-0.0264	-0.0182	0.0121	-0.0353	-0.0171	-0.0086	-0.0405	0.0032	-0.0378	-0.0199	0.0265	0.1127	-0.0133	0.0552	0.0034	0.0090	0.0087	-0.0142	-0.0513	-0.0209	-0.0173
Co	0.0391	0.1654	0.1868	-0.0927	0.2466	0.1109	0.0376	0.1813	-0.0261	0.1580	0.1115	0.1671	-0.0133	0.2709	0.0334	0.0707	0.1754	-0.0904	0.0825	0.0665	0.1274	0.0437
Ni	0.0019	0.0129	0.0189	-0.0271	0.0170	-0.0192	0.0056	-0.0036	-0.0018	-0.0091	0.0061	0.0379	0.0552	0.0334	0.1043	0.1231	0.0371	-0.0350	-0.0170	-0.0951	-0.0072	-0.0199
Cu	0.0146	0.0856	0.0849	-0.1696	0.0920	0.0055	0.0468	0.0760	-0.0099	0.0554	0.0235	0.0480	0.0034	0.0707	0.1231	0.6374	0.0240	-0.1633	-0.0497	0.0238	0.0296	0.0803
Zn	0.0316	0.1428	0.1515	-0.0485	0.1970	0.1015	0.0429	0.1748	-0.0197	0.1525	0.1139	0.1205	0.0090	0.1754	0.0371	0.0240	0.4505	-0.0419	0.0227	0.0036	0.1549	0.0540
Rb	-0.0158	-0.0959	-0.0797	0.0883	-0.0981	-0.0490	-0.0281	-0.0931	0.0106	-0.0731	-0.0365	-0.0606	0.0087	-0.0904	-0.0350	-0.1633	-0.0419	0.0906	-0.0193	-0.0226	-0.0371	-0.0518
Sr	0.0134	0.0535	0.0395	-0.0210	0.0860	0.0402	0.0074	0.0414	-0.0069	0.0438	0.0243	0.0434	-0.0142	0.0825	-0.0170	-0.0497	0.0227	-0.0193	0.0833	-0.0138	0.0416	-0.0036
Y	0.0065	0.0327	0.0630	-0.0263	0.0503	0.0521	0.0013	0.0769	-0.0088	0.0704	0.0461	0.0322	-0.0513	0.0665	-0.0951	0.0238	0.0036	-0.0226	-0.0138	0.2818	0.0331	0.0846
Zr	0.0238	0.0982	0.1025	-0.0453	0.1412	0.0568	0.0303	0.1150	-0.0139	0.1055	0.0615	0.0706	-0.0209	0.1274	-0.0072	0.0296	0.1549	-0.0371	0.0416	0.0331	0.1131	0.0360
Nb	0.0074	0.0711	0.0623	-0.0551	0.0633	0.0532	0.0196	0.1046	-0.0068	0.0813	0.0286	0.0369	-0.0173	0.0437	-0.0199	0.0803	0.0540	-0.0518	-0.0036	0.0846	0.0360	0.0858
Mo	-0.0060	-0.0256	-0.0194	0.0120	-0.0371	-0.0155	-0.0081	-0.0413	0.0034	-0.0385	-0.0211	0.0268	0.1175	-0.0155	0.0558	-0.0004	0.0114	0.0087	-0.0139	-0.0546	-0.0216	-0.0170
Cs	-0.0029	-0.0303	-0.0305	0.0432	-0.0312	-0.0071	-0.0051	-0.0386	0.0037	-0.0225	-0.0252	-0.0328	-0.0149	-0.0324	-0.0413	-0.1250	-0.0111	0.0517	0.0034	-0.0057	-0.0002	-0.0253
Ba	0.0040	-0.0161	-0.0053	0.0664	0.0177	0.0204	-0.0217	-0.0140	-0.0015	0.0074	0.0285	0.0159	-0.0123	0.0441	-0.0740	-0.2668	0.0353	0.0631	0.0662	0.0489	0.0312	-0.0291
La	0.0068	-0.0050	-0.0023	0.0278	0.0190	0.0001	-0.0020	-0.0250	-0.0013	-0.0015	0.0331	0.0181	0.0363	0.0300	0.0199	-0.0414	0.1449	0.0257	0.0283	-0.0476	0.0439	-0.0336
Ce	0.0082	0.0009	0.0050	0.0215	0.0292	0.0049	-0.0002	-0.0191	-0.0023	0.0039	0.0355	0.0245	0.0352	0.0409	0.0209	-0.0260	0.1468	0.0206	0.0318	-0.0407	0.0469	-0.0308
Pr	0.0099	0.0109	0.0171	0.0121	0.0445	0.0119	0.0022	-0.0042	-0.0038	0.0157	0.0381	0.0318	0.0292	0.0538	0.0145	-0.0109	0.1471	0.0128	0.0348	-0.0194	0.0539	-0.0209
Nd	0.0126	0.0250	0.0322	0.0008	0.0627	0.0232	0.0061	0.0133	-0.0059	0.0307	0.0444	0.0408	0.0210	0.0711	0.0068	0.0042	0.1505	0.0031	0.0388	0.0059	0.0627	-0.0095
Sm	0.0131	0.0320	0.0460	-0.0160	0.0725	0.0288	0.0089	0.0290	-0.0075	0.0421	0.0446	0.0446	0.0083	0.0805	-0.0043	0.0549	0.1269	-0.0110	0.0290	0.0607	0.0625	0.0102
Eu	0.0185	0.0667	0.0715	-0.0259	0.1041	0.0496	0.0134	0.0663	-0.0109	0.0663	0.0539	0.0666	-0.0043	0.1152	-0.0079	-0.0199	0.0933	-0.0253	0.0530	0.0385	0.0696	0.0118
Gd	0.0129	0.0380	0.0582	-0.0214	0.0786	0.0366	0.0081	0.0498	-0.0089	0.0568	0.0489	0.0456	-0.0125	0.0869	-0.0308	0.0471	0.1038	-0.0162	0.0217	0.1263	0.0631	0.0309
Tb	0.0132	0.0472	0.0705	-0.0312	0.0805	0.0509	0.0103	0.0683	-0.0103	0.0696	0.0521	0.0498	-0.0208	0.0915	-0.0505	0.0526	0.0904	-0.0252	0.0090	0.1866	0.0607	0.0545
Dy	0.0102	0.0415	0.0684	-0.0313	0.0693	0.0489	0.0063	0.0733	-0.0098	0.0715	0.0516	0.0418	-0.0365	0.0812	-0.0681	0.0525	0.0622	-0.0271	-0.0030	0.2340	0.0507	0.0697
Ho	0.0080	0.0390	0.0687	-0.0303	0.0588	0.0520	0.0036	0.0811	-0.0095	0.0748	0.0497	0.0372	-0.0492	0.0746	-0.0862	0.0347	0.0201	-0.0271	-0.0128	0.2721	0.0400	0.0836
Er	0.0066	0.0402	0.0708	-0.0311	0.0546	0.0624	0.0013	0.0902	-0.0097	0.0808	0.0489	0.0373	-0.0587	0.0736	-0.1065	0.0153	-0.0070	-0.0279	-0.0154	0.3146	0.0301	0.0994
Tm	0.0053	0.0412	0.0752	-0.0286	0.0534	0.0732	-0.0011	0.1060	-0.0100	0.0891	0.0540	0.0402	-0.0658	0.0727	-0.1217	-0.0066	-0.0157	-0.0256	-0.0189	0.3390	0.0242	0.1131
Yb	0.0037	0.0319	0.0666	-0.0226	0.0349	0.0731	-0.0035	0.0952	-0.0089	0.0813	0.0495	0.0338	-0.0622	0.0615	-0.1322	-0.0214	-0.0465	-0.0198	-0.0265	0.3588	0.0150	0.1158
Lu	0.0035	0.0298	0.0695	-0.0137	0.0444	0.0746	-0.0071	0.1018	-0.0092	0.0850	0.0552	0.0393	-0.0660	0.0692	-0.1350	-0.0477	-0.0232	-0.0109	-0.0180	0.3498	0.0200	0.1114
Hf	0.0171	0.0618	0.0733	-0.0256	0.1029	0.0339	0.0189	0.0783	-0.0100	0.0733	0.0480	0.0518	-0.0124	0.0948	-0.0061	0.0253	0.1204	-0.0191	0.0297	0.0277	0.0890	0.0204
Ta	0.0012	0.0778	0.0676	-0.0580	0.0428	0.0804	0.0159	0.1384	-0.0064	0.1032	0.0215	0.0354	-0.0316	0.0270	-0.0679	0.0256	-0.0088	-0.0547	-0.0252	0.1924	0.0082	0.1419
Pb	-0.0083	-0.0696	-0.0614	0.0467	-0.0655	-0.0530	-0.0169	-0.0939	0.0071	-0.0743	-0.0290	-0.0450	0.0138	-0.0587	0.0069	-0.0413	-0.0351	0.0456	-0.0081	-0.0540	-0.0285	-0.0666
Th	-0.0136	-0.1263	-0.0958	0.1061	-0.1029	-0.1027	-0.0339	-0.1494	0.0116	-0.1115	-0.0288	-0.0626	0.0418	-0.0833	0.0184	-0.1192	0.0018	0.1020	-0.0171	-0.0986	-0.0123	-0.1143
U	-0.0190	-0.1412	-0.0924	0.1072	-0.1487	-0.0521	-0.0274	-0.1191	0.0125	-0.0972	-0.0433	-0.0915	0.0088	-0.1344	-0.0816	-0.1133	-0.0618	0.1231	-0.0853	0.0864	-0.0410	-0.0425

Table C2 (continued):

	Mo	Cs	Ba	La	Ce	Pr	Nd	Sm	Eu	Gd	Tb	Dy	Ho	Er	Tm	Yb	Lu	Hf	Ta	Pb	Th	U
Al_2O_3	-0.0060	-0.0029	0.0040	0.0068	0.0082	0.0099	0.0126	0.0131	0.0185	0.0129	0.0132	0.0102	0.0080	0.0066	0.0053	0.0037	0.0035	0.0171	0.0012	-0.0083	-0.0136	-0.0190
CaO	-0.0256	-0.0303	-0.0161	-0.0050	0.0009	0.0109	0.0250	0.0320	0.0667	0.0380	0.0472	0.0415	0.0390	0.0402	0.0412	0.0319	0.0298	0.0618	0.0778	-0.0696	-0.1263	-0.1412
Fe_2O_3	-0.0194	-0.0305	-0.0053	-0.0023	0.0050	0.0171	0.0322	0.0460	0.0715	0.0582	0.0705	0.0684	0.0687	0.0708	0.0752	0.0666	0.0695	0.0733	0.0676	-0.0614	-0.0958	-0.0924
K_2O	0.0120	0.0432	0.0664	0.0278	0.0215	0.0121	0.0008	-0.0160	-0.0259	-0.0214	-0.0312	-0.0313	-0.0303	-0.0311	-0.0286	-0.0226	-0.0137	-0.0256	-0.0580	0.0467	0.1061	0.1072
MgO	-0.0371	-0.0312	0.0177	0.0190	0.0292	0.0445	0.0627	0.0725	0.1041	0.0786	0.0805	0.0693	0.0588	0.0546	0.0534	0.0349	0.0444	0.1029	0.0428	-0.0655	-0.1029	-0.1487
MnO	-0.0155	-0.0071	0.0204	0.0001	0.0049	0.0119	0.0232	0.0288	0.0496	0.0366	0.0509	0.0489	0.0520	0.0624	0.0732	0.0731	0.0746	0.0339	0.0804	-0.0530	-0.1027	-0.0521
Na_2O	-0.0081	-0.0051	-0.0217	-0.0020	-0.0002	0.0022	0.0061	0.0089	0.0134	0.0081	0.0103	0.0063	0.0036	0.0013	-0.0011	-0.0035	-0.0071	0.0189	0.0159	-0.0169	-0.0339	-0.0274
P_2O_5	-0.0413	-0.0386	-0.0140	-0.0250	-0.0191	-0.0042	0.0133	0.0290	0.0663	0.0498	0.0683	0.0733	0.0811	0.0902	0.1060	0.0952	0.1018	0.0783	0.1384	-0.0939	-0.1494	-0.1191
SiO_2	0.0034	0.0037	-0.0015	-0.0013	-0.0023	-0.0038	-0.0059	-0.0075	-0.0109	-0.0089	-0.0103	-0.0098	-0.0095	-0.0097	-0.0100	-0.0089	-0.0092	-0.0100	-0.0064	0.0071	0.0116	0.0125

Table C2 (continued):

	Mo	Cs	Ba	La	Ce	Pr	Nd	Sm	Eu	Gd	Tb	Dy	Ho	Er	Tm	Yb	Lu	Hf	Ta	Pb	Th	U
TiO_2	-0.0385	-0.0225	0.0074	-0.0015	0.0039	0.0157	0.0307	0.0421	0.0663	0.0568	0.0696	0.0715	0.0748	0.0808	0.0891	0.0813	0.0850	0.0733	0.1032	-0.0743	-0.1115	-0.0972
Sc	-0.0211	-0.0252	0.0285	0.0331	0.0355	0.0381	0.0444	0.0446	0.0539	0.0489	0.0521	0.0516	0.0497	0.0489	0.0540	0.0495	0.0552	0.0480	0.0215	-0.0290	-0.0288	-0.0433
V	0.0268	-0.0328	0.0159	0.0181	0.0245	0.0318	0.0408	0.0446	0.0666	0.0456	0.0498	0.0418	0.0372	0.0373	0.0402	0.0338	0.0393	0.0518	0.0354	-0.0450	-0.0626	-0.0915
Cr	0.1175	-0.0149	-0.0123	0.0363	0.0352	0.0292	0.0210	0.0083	-0.0043	-0.0125	-0.0208	-0.0365	-0.0492	-0.0587	-0.0658	-0.0622	-0.0660	-0.0124	-0.0316	0.0138	0.0418	0.0088
Co	-0.0155	-0.0324	0.0441	0.0300	0.0409	0.0538	0.0711	0.0805	0.1152	0.0869	0.0915	0.0812	0.0746	0.0736	0.0727	0.0615	0.0692	0.0948	0.0270	-0.0587	-0.0833	-0.1344
Ni	0.0558	-0.0413	-0.0740	0.0199	0.0209	0.0145	0.0068	-0.0043	-0.0079	-0.0308	-0.0505	-0.0681	-0.0862	-0.1065	-0.1217	-0.1322	-0.1350	-0.0061	-0.0679	0.0069	0.0184	-0.0816
Cu	-0.0004	-0.1250	-0.2668	-0.0414	-0.0260	-0.0109	0.0042	0.0549	-0.0199	0.0471	0.0526	0.0525	0.0347	0.0153	-0.0066	-0.0214	-0.0477	0.0253	0.0256	-0.0413	-0.1192	-0.1133
Zn	0.0114	-0.0111	0.0353	0.1449	0.1468	0.1471	0.1505	0.1269	0.0933	0.1038	0.0904	0.0622	0.0201	-0.0070	-0.0157	-0.0465	-0.0232	0.1204	-0.0088	-0.0351	0.0018	-0.0618
Rb	0.0087	0.0517	0.0631	0.0257	0.0206	0.0128	0.0031	-0.0110	-0.0253	-0.0162	-0.0252	-0.0271	-0.0271	-0.0279	-0.0256	-0.0198	-0.0109	-0.0191	-0.0547	0.0456	0.1020	0.1231
Sr	-0.0139	0.0034	0.0662	0.0283	0.0318	0.0348	0.0388	0.0290	0.0530	0.0217	0.0090	-0.0030	-0.0128	-0.0154	-0.0189	-0.0265	-0.0180	0.0297	-0.0252	-0.0081	-0.0171	-0.0853
Y	-0.0546	-0.0057	0.0489	-0.0476	-0.0407	-0.0194	0.0059	0.0607	0.0385	0.1263	0.1866	0.2340	0.2721	0.3146	0.3390	0.3588	0.3498	0.0277	0.1924	-0.0540	-0.0986	0.0864
Zr	-0.0216	-0.0002	0.0312	0.0439	0.0469	0.0539	0.0627	0.0625	0.0696	0.0631	0.0607	0.0507	0.0400	0.0301	0.0242	0.0150	0.0200	0.0890	0.0082	-0.0285	-0.0123	-0.0410
Nb	-0.0170	-0.0253	-0.0291	-0.0336	-0.0308	-0.0209	-0.0095	0.0102	0.0118	0.0309	0.0545	0.0697	0.0836	0.0994	0.1131	0.1158	0.1114	0.0204	0.1419	-0.0666	-0.1143	-0.0425
Mo	0.1227	-0.0144	-0.0122	0.0383	0.0370	0.0306	0.0220	0.0080	-0.0044	-0.0140	-0.0225	-0.0391	-0.0526	-0.0624	-0.0696	-0.0656	-0.0700	-0.0136	-0.0308	0.0136	0.0409	0.0082
Cs	-0.0144	0.0640	0.0588	0.0144	0.0127	0.0095	0.0073	-0.0008	-0.0008	-0.0036	-0.0048	-0.0095	-0.0077	-0.0045	-0.0075	0.0009	0.0012	-0.0009	-0.0168	0.0152	0.0364	0.0704
Ba	-0.0122	0.0588	0.2037	0.0829	0.0798	0.0752	0.0733	0.0497	0.0691	0.0507	0.0460	0.0439	0.0463	0.0553	0.0603	0.0712	0.0865	0.0305	-0.0210	0.0097	0.0676	0.0330
La	0.0383	0.0144	0.0829	0.1433	0.1414	0.1295	0.1201	0.0864	0.0507	0.0499	0.0206	-0.0063	-0.0393	-0.0635	-0.0822	-0.0879	-0.0800	0.0430	-0.1039	0.0279	0.1032	-0.0011
Ce	0.0370	0.0127	0.0798	0.1414	0.1410	0.1304	0.1226	0.0919	0.0538	0.0562	0.0279	0.0009	-0.0324	-0.0558	-0.0747	-0.0808	-0.0731	0.0452	-0.1003	0.0251	0.0950	-0.0044
Pr	0.0306	0.0095	0.0752	0.1295	0.1304	0.1235	0.1189	0.0951	0.0571	0.0658	0.0424	0.0189	-0.0119	-0.0322	-0.0492	-0.0561	-0.0483	0.0506	-0.0835	0.0191	0.0797	-0.0053
Nd	0.0220	0.0073	0.0733	0.1201	0.1226	0.1189	0.1181	0.1011	0.0634	0.0782	0.0605	0.0405	0.0128	-0.0038	-0.0189	-0.0253	-0.0186	0.0565	-0.0634	0.0106	0.0599	-0.0074
Sm	0.0080	-0.0008	0.0497	0.0864	0.0919	0.0951	0.1011	0.1029	0.0591	0.0959	0.0925	0.0838	0.0652	0.0575	0.0469	0.0429	0.0455	0.0563	-0.0209	-0.0007	0.0261	0.0084
Eu	-0.0044	-0.0008	0.0691	0.0507	0.0538	0.0571	0.0634	0.0591	0.0703	0.0582	0.0567	0.0493	0.0422	0.0398	0.0361	0.0343	0.0385	0.0548	-0.0051	-0.0169	-0.0061	-0.0460
Gd	-0.0140	-0.0036	0.0507	0.0499	0.0562	0.0658	0.0782	0.0959	0.0582	0.1108	0.1245	0.1314	0.1272	0.1322	0.1307	0.1305	0.1316	0.0560	0.0336	-0.0138	-0.0052	0.0268
Tb	-0.0225	-0.0048	0.0460	0.0206	0.0279	0.0424	0.0605	0.0925	0.0567	0.1245	0.1564	0.1760	0.1845	0.2020	0.2083	0.2149	0.2111	0.0515	0.0928	-0.0307	-0.0445	0.0476
Dy	-0.0391	-0.0095	0.0439	-0.0063	0.0009	0.0189	0.0405	0.0838	0.0493	0.1314	0.1760	0.2090	0.2292	0.2569	0.2700	0.2806	0.2748	0.0433	0.1359	-0.0401	-0.0662	0.0602
Ho	-0.0526	-0.0077	0.0463	-0.0393	-0.0324	-0.0119	0.0128	0.0652	0.0422	0.1272	0.1845	0.2292	0.2640	0.3032	0.3247	0.3427	0.3337	0.0330	0.1829	-0.0538	-0.0940	0.0745
Er	-0.0624	-0.0045	0.0553	-0.0635	-0.0558	-0.0322	-0.0038	0.0575	0.0398	0.1322	0.2020	0.2569	0.3032	0.3546	0.3840	0.4081	0.3970	0.0227	0.2326	-0.0688	-0.1278	0.0842
Tm	-0.0696	-0.0075	0.0603	-0.0822	-0.0747	-0.0492	-0.0189	0.0469	0.0361	0.1307	0.2083	0.2700	0.3247	0.3840	0.4235	0.4499	0.4416	0.0178	0.2685	-0.0802	-0.1501	0.0976
Yb	-0.0656	0.0009	0.0712	-0.0879	-0.0808	-0.0561	-0.0253	0.0429	0.0343	0.1305	0.2149	0.2806	0.3427	0.4081	0.4499	0.4854	0.4716	0.0096	0.2896	-0.0853	-0.1567	0.1192
Lu	-0.0700	0.0012	0.0865	-0.0800	-0.0731	-0.0483	-0.0186	0.0455	0.0385	0.1316	0.2111	0.2748	0.3337	0.3970	0.4416	0.4716	0.4666	0.0165	0.2760	-0.0808	-0.1436	0.1196
Hf	-0.0136	-0.0009	0.0305	0.0430	0.0452	0.0506	0.0565	0.0563	0.0548	0.0560	0.0515	0.0433	0.0330	0.0227	0.0178	0.0096	0.0165	0.0750	-0.0116	-0.0121	0.0154	-0.0107
Ta	-0.0308	-0.0168	-0.0210	-0.1039	-0.1003	-0.0835	-0.0634	-0.0209	-0.0051	0.0336	0.0928	0.1359	0.1829	0.2326	0.2685	0.2896	0.2760	-0.0116	0.3040	-0.1195	-0.2185	-0.0208
Pb	0.0136	0.0152	0.0097	0.0279	0.0251	0.0191	0.0106	-0.0007	-0.0169	-0.0138	-0.0307	-0.0401	-0.0538	-0.0688	-0.0802	-0.0853	-0.0808	-0.0121	-0.1195	0.0647	0.1077	0.0627
Th	0.0409	0.0364	0.0676	0.1032	0.0950	0.0797	0.0599	0.0261	-0.0061	-0.0052	-0.0445	-0.0662	-0.0940	-0.1278	-0.1501	-0.1567	-0.1436	0.0154	-0.2185	0.1077	0.2433	0.1236
U	0.0082	0.0704	0.0330	-0.0011	-0.0044	-0.0053	-0.0074	0.0084	-0.0460	0.0268	0.0476	0.0602	0.0745	0.0842	0.0976	0.1192	0.1196	-0.0107	-0.0208	0.0627	0.1236	0.3309

Table C3: Centered log-ratio covariance matrices for the NNM Gneiss calculated after the methods of Aitchison (1986), where SiO_2, etc. represents (natural) log [SiO_2 wt. % / g], etc. and where g is the geometric mean of the geometric mean.

	Al_2O_3	CaO	Fe_2O_3	K_2O	MgO	MnO	Na_2O	P_2O_5	SiO_2	TiO_2	Sc	V	Cr	Co	Ni	Cu	Zn	Rb	Sr	Y	Zr	Nb
Al_2O_3	0.0079	0.0481	0.0216	-0.0061	0.0641	0.0495	0.0077	0.0523	-0.0031	0.0091	0.0115	0.0143	-0.0007	0.0486	0.0167	0.0372	0.0377	-0.0152	0.0667	0.0168	0.0002	-0.0121
CaO	0.0481	0.5578	0.2270	-0.1705	0.5778	0.5134	0.1083	0.2822	-0.0206	0.1766	0.1698	0.1525	0.0435	0.3806	0.1298	0.1755	0.3475	-0.2077	0.4218	0.3252	0.0617	0.0998
Fe_2O_3	0.0216	0.2270	0.1042	-0.0595	0.2429	0.1903	0.0419	0.1458	-0.0093	0.0675	0.0667	0.0863	0.0477	0.1734	0.0583	0.1242	0.1320	-0.0757	0.2059	0.1501	0.0302	0.0272
K_2O	-0.0061	-0.1705	-0.0595	0.0804	-0.1537	-0.1573	-0.0412	-0.0226	0.0034	-0.0636	-0.0697	-0.0284	0.0038	-0.0811	-0.0328	0.0086	-0.1030	0.0767	-0.0400	-0.1373	-0.0204	-0.0849
MgO	0.0641	0.5778	0.2429	-0.1537	0.6813	0.5426	0.1187	0.4256	-0.0264	0.1584	0.1765	0.1574	0.0126	0.4707	0.1663	0.2813	0.4028	-0.2103	0.5515	0.3442	0.0422	0.0360
MnO	0.0495	0.5134	0.1903	-0.1573	0.5426	0.5940	0.1009	0.2880	-0.0206	0.1668	0.1845	0.0731	-0.0739	0.3337	0.0941	0.0668	0.3562	-0.2043	0.3199	0.3240	0.0380	0.1230
Na_2O	0.0077	0.1083	0.0419	-0.0412	0.1187	0.1009	0.0285	0.0576	-0.0034	0.0399	0.0411	0.0222	-0.0033	0.0718	0.0230	0.0205	0.0702	-0.0441	0.0630	0.0977	0.0152	0.0401
P_2O_5	0.0523	0.2822	0.1458	-0.0226	0.4256	0.2880	0.0576	0.4290	-0.0206	0.0502	0.0853	0.1013	-0.0039	0.3335	0.1039	0.2911	0.2213	-0.0722	0.4329	0.2364	0.0094	-0.0536
SiO_2	-0.0031	-0.0206	-0.0093	0.0034	-0.0264	-0.0206	-0.0034	-0.0206	0.0012	-0.0041	-0.0056	-0.0063	-0.0002	-0.0198	-0.0070	-0.0150	-0.0154	0.0066	-0.0257	-0.0095	-0.0003	0.0032
TiO_2	0.0091	0.1766	0.0675	-0.0636	0.1584	0.1668	0.0399	0.0502	-0.0041	0.0848	0.0548	0.0447	0.0220	0.0879	0.0125	-0.0001	0.0902	-0.0715	0.0864	0.1275	0.0457	0.0760
Sc	0.0115	0.1698	0.0667	-0.0697	0.1765	0.1845	0.0411	0.0853	-0.0056	0.0548	0.0830	0.0280	-0.0218	0.1041	0.0351	0.0260	0.1119	-0.0711	0.0547	0.1836	0.0136	0.0812
V	0.0143	0.1525	0.0863	-0.0284	0.1574	0.0731	0.0222	0.1013	-0.0063	0.0447	0.0280	0.1057	0.1065	0.1317	0.0465	0.1593	0.0635	-0.0405	0.1941	0.0816	0.0359	-0.0117
Cr	-0.0007	0.0435	0.0477	0.0038	0.0126	-0.0739	-0.0033	-0.0039	-0.0002	0.0220	-0.0218	0.1065	0.1601	0.0395	0.0141	0.1334	-0.0358	0.0040	0.1151	-0.0085	0.0447	-0.0297
Co	0.0486	0.3806	0.1734	-0.0811	0.4707	0.3337	0.0718	0.3335	-0.0198	0.0879	0.1041	0.1317	0.0395	0.3477	0.1279	0.2682	0.2657	-0.1258	0.4426	0.2067	0.0227	-0.0259
Ni	0.0167	0.1298	0.0583	-0.0328	0.1663	0.0941	0.0230	0.1039	-0.0070	0.0125	0.0351	0.0465	0.0141	0.1279	0.0656	0.1134	0.1011	-0.0444	0.1601	0.0474	-0.0094	-0.0284
Cu	0.0372	0.1755	0.1242	0.0086	0.2813	0.0668	0.0205	0.2911	-0.0150	-0.0001	0.0260	0.1593	0.1334	0.2682	0.1134	0.3960	0.1171	-0.0321	0.4134	0.0672	0.0061	-0.1442
Zn	0.0377	0.3475	0.1320	-0.1030	0.4028	0.3562	0.0702	0.2213	-0.0154	0.0902	0.1119	0.0635	-0.0358	0.2657	0.1011	0.1171	0.2611	-0.1378	0.2929	0.1722	0.0081	0.0252
Rb	-0.0152	-0.2077	-0.0757	0.0767	-0.2103	-0.2043	-0.0441	-0.0722	0.0066	-0.0715	-0.0711	-0.0405	0.0040	-0.1258	-0.0444	-0.0321	-0.1378	0.0908	-0.1199	-0.1123	-0.0209	-0.0503
Sr	0.0667	0.4218	0.2059	-0.0400	0.5515	0.3199	0.0630	0.4329	-0.0257	0.0864	0.0547	0.1941	0.1151	0.4426	0.1601	0.4134	0.2929	-0.1199	0.6898	0.0691	0.0314	-0.1611

Table C3 (continued):

	Al_2O_3	CaO	Fe_2O_3	K_2O	MgO	MnO	Na_2O	P_2O_5	SiO_2	TiO_2	Sc	V	Cr	Co	Ni	Cu	Zn	Rb	Sr	Y	Zr	Nb
Y	0.0168	0.3252	0.1501	-0.1373	0.3442	0.3240	0.0977	0.2364	-0.0095	0.1275	0.1836	0.0816	-0.0085	0.2067	0.0474	0.0672	0.1722	-0.1123	0.0691	0.5787	0.0645	0.2542
Zr	0.0002	0.0617	0.0302	-0.0204	0.0422	0.0380	0.0152	0.0094	-0.0003	0.0457	0.0136	0.0359	0.0447	0.0227	-0.0094	0.0061	0.0081	-0.0209	0.0314	0.0645	0.0388	0.0417
Nb	-0.0121	0.0998	0.0272	-0.0849	0.0360	0.1230	0.0401	-0.0536	0.0032	0.0760	0.0812	-0.0117	-0.0297	-0.0259	-0.0284	-0.1442	0.0252	-0.0503	-0.1611	0.2542	0.0417	0.2043
Mo	-0.0010	0.0408	0.0480	0.0052	0.0105	-0.0822	-0.0036	-0.0028	-0.0001	0.0210	-0.0238	0.1092	0.1652	0.0396	0.0145	0.1379	-0.0395	0.0065	0.1175	-0.0068	0.0457	-0.0306
Cs	0.0233	0.1174	0.0692	-0.0017	0.2053	0.0465	0.0309	0.2108	-0.0090	0.0176	0.0106	0.0722	0.0453	0.1740	0.0657	0.1859	0.0878	-0.0198	0.2702	0.0827	0.0126	-0.0593
Ba	0.0527	0.1494	0.1020	0.0760	0.3055	0.0846	0.0117	0.3875	-0.0185	0.0143	-0.0494	0.1281	0.0976	0.2919	0.0822	0.3610	0.1248	-0.0060	0.5821	-0.0983	0.0207	-0.2454
La	0.0035	-0.0088	-0.0005	0.0214	0.0004	-0.0142	-0.0051	0.0210	-0.0008	0.0045	-0.0244	0.0097	0.0191	0.0082	-0.0079	0.0193	-0.0090	0.0089	0.0577	-0.0522	0.0106	-0.0369
Ce	0.0010	-0.0193	-0.0034	0.0200	-0.0141	-0.0297	-0.0063	0.0070	0.0001	0.0011	-0.0231	0.0106	0.0242	-0.0020	-0.0091	0.0200	-0.0187	0.0113	0.0372	-0.0461	0.0103	-0.0313
Pr	0.0045	0.0194	0.0089	0.0071	0.0266	0.0154	0.0022	0.0265	-0.0014	0.0141	-0.0103	0.0117	0.0134	0.0213	-0.0022	0.0148	0.0095	-0.0039	0.0590	-0.0227	0.0123	-0.0193
Nd	0.0059	0.0424	0.0180	-0.0023	0.0505	0.0355	0.0079	0.0363	-0.0020	0.0218	-0.0012	0.0170	0.0138	0.0359	0.0034	0.0197	0.0240	-0.0133	0.0705	-0.0021	0.0149	-0.0104
Sm	0.0087	0.0734	0.0278	-0.0176	0.0863	0.0812	0.0153	0.0549	-0.0034	0.0253	0.0205	0.0128	-0.0079	0.0560	0.0142	0.0192	0.0530	-0.0281	0.0691	0.0365	0.0079	0.0061
Eu	0.0402	0.2341	0.1143	-0.0097	0.3213	0.1758	0.0375	0.2644	-0.0149	0.0625	0.0137	0.1127	0.0733	0.2569	0.0790	0.2384	0.1627	-0.0668	0.4344	0.0074	0.0332	-0.1122
Gd	0.0156	0.1550	0.0663	-0.0445	0.1801	0.1541	0.0363	0.1227	-0.0066	0.0506	0.0561	0.0385	-0.0031	0.1196	0.0344	0.0574	0.1012	-0.0542	0.1224	0.1434	0.0192	0.0406
Tb	0.0128	0.1736	0.0780	-0.0636	0.1917	0.1737	0.0467	0.1325	-0.0062	0.0600	0.0849	0.0427	-0.0064	0.1216	0.0334	0.0502	0.1024	-0.0596	0.0773	0.2487	0.0257	0.0972
Dy	0.0129	0.2249	0.1023	-0.0909	0.2396	0.2234	0.0654	0.1625	-0.0069	0.0873	0.1197	0.0563	-0.0047	0.1455	0.0341	0.0487	0.1220	-0.0780	0.0649	0.3712	0.0433	0.1602
Ho	0.0122	0.2754	0.1299	-0.1208	0.2866	0.2706	0.0850	0.1977	-0.0075	0.1115	0.1625	0.0734	-0.0009	0.1704	0.0368	0.0565	0.1384	-0.0944	0.0392	0.5236	0.0598	0.2344
Er	0.0120	0.3258	0.1512	-0.1508	0.3341	0.3298	0.1051	0.2271	-0.0080	0.1383	0.2020	0.0776	-0.0140	0.1904	0.0359	0.0397	0.1615	-0.1139	0.0112	0.6567	0.0742	0.3068
Tm	0.0126	0.3753	0.1721	-0.1771	0.3808	0.3874	0.1229	0.2579	-0.0089	0.1627	0.2368	0.0822	-0.0257	0.2119	0.0362	0.0251	0.1847	-0.1312	-0.0064	0.7747	0.0868	0.3702
Yb	0.0177	0.4329	0.1947	-0.1966	0.4455	0.4380	0.1358	0.2853	-0.0109	0.1822	0.2545	0.0983	-0.0209	0.2536	0.0514	0.0492	0.2242	-0.1568	0.0415	0.8009	0.0938	0.3750
Lu	0.0266	0.5172	0.2439	-0.2111	0.5307	0.4973	0.1452	0.3494	-0.0150	0.2018	0.2792	0.1534	0.0274	0.3260	0.0760	0.1391	0.2614	-0.1785	0.1336	0.8616	0.1077	0.3738
Hf	-0.0080	0.0319	0.0108	-0.0303	-0.0065	0.0139	0.0132	-0.0489	0.0026	0.0379	0.0174	0.0118	0.0249	-0.0223	-0.0184	-0.0506	-0.0112	-0.0165	-0.0559	0.0734	0.0311	0.0743
Ta	-0.0066	0.1737	0.0703	-0.1056	0.1119	0.2115	0.0600	0.0389	0.0002	0.1062	0.1295	0.0141	-0.0281	0.0255	-0.0279	-0.1205	0.0515	-0.0624	-0.1484	0.4440	0.0628	0.2819
Pb	0.0138	-0.0264	-0.0056	0.0479	0.0140	-0.0511	-0.0287	0.0423	-0.0045	-0.0625	-0.0515	0.0131	0.0146	0.0503	0.0498	0.1147	0.0208	0.0227	0.1565	-0.2085	-0.0492	-0.1636
Th	-0.0039	-0.0846	-0.0338	0.0338	-0.0779	-0.0998	-0.0232	-0.0467	0.0021	-0.0409	-0.0426	-0.0112	0.0113	-0.0399	-0.0003	0.0175	-0.0424	0.0298	-0.0075	-0.1313	-0.0207	-0.0718
U	-0.0138	-0.1666	-0.0601	0.0468	-0.1444	-0.1244	-0.0148	0.0007	0.0055	-0.0433	-0.0174	-0.0583	-0.0506	-0.1001	-0.0515	-0.0625	-0.1050	0.0718	-0.1665	0.0815	-0.0084	0.0436

Table C3 (continued):

	Mo	Cs	Ba	La	Ce	Pr	Nd	Sm	Eu	Gd	Tb	Dy	Ho	Er	Tm	Yb	Lu	Hf	Ta	Pb	Th	U
Al_2O_3	-0.0010	0.0233	0.0527	0.0035	0.0010	0.0045	0.0059	0.0087	0.0402	0.0156	0.0128	0.0129	0.0122	0.0120	0.0126	0.0177	0.0266	-0.0080	-0.0066	0.0138	-0.0039	-0.0138
CaO	0.0408	0.1174	0.1494	-0.0088	-0.0193	0.0194	0.0424	0.0734	0.2341	0.1550	0.1736	0.2249	0.2754	0.3258	0.3753	0.4329	0.5172	0.0319	0.1737	-0.0264	-0.0846	-0.1666
Fe_2O_3	0.0480	0.0692	0.1020	-0.0005	-0.0034	0.0089	0.0180	0.0278	0.1143	0.0663	0.0780	0.1023	0.1299	0.1512	0.1721	0.1947	0.2439	0.0108	0.0703	-0.0056	-0.0338	-0.0601
K_2O	0.0052	-0.0017	0.0760	0.0214	0.0200	0.0071	-0.0023	-0.0176	-0.0097	-0.0445	-0.0636	-0.0909	-0.1208	-0.1508	-0.1771	-0.1966	-0.2111	-0.0303	-0.1056	0.0479	0.0338	0.0468
MgO	0.0105	0.2053	0.3055	0.0004	-0.0141	0.0266	0.0505	0.0863	0.3213	0.1801	0.1917	0.2396	0.2866	0.3341	0.3808	0.4455	0.5307	-0.0065	0.1119	0.0140	-0.0779	-0.1444
MnO	-0.0822	0.0465	0.0846	-0.0142	-0.0297	0.0154	0.0355	0.0812	0.1758	0.1541	0.1737	0.2234	0.2706	0.3298	0.3874	0.4380	0.4973	0.0139	0.2115	-0.0511	-0.0998	-0.1244
Na_2O	-0.0036	0.0309	0.0117	-0.0051	-0.0063	0.0022	0.0079	0.0153	0.0375	0.0363	0.0467	0.0654	0.0850	0.1051	0.1229	0.1358	0.1452	0.0132	0.0600	-0.0287	-0.0232	-0.0148
P_2O_5	-0.0028	0.2108	0.3875	0.0210	0.0070	0.0265	0.0363	0.0549	0.2644	0.1227	0.1325	0.1625	0.1977	0.2271	0.2579	0.2853	0.3494	-0.0489	0.0389	0.0423	-0.0467	0.0007
SiO_2	-0.0001	-0.0090	-0.0185	-0.0008	0.0001	-0.0014	-0.0020	-0.0034	-0.0149	-0.0066	-0.0062	-0.0069	-0.0075	-0.0080	-0.0089	-0.0109	-0.0150	0.0026	0.0002	-0.0045	0.0021	0.0055
TiO_2	0.0210	0.0176	0.0143	0.0045	0.0011	0.0141	0.0218	0.0253	0.0625	0.0506	0.0600	0.0873	0.1115	0.1383	0.1627	0.1822	0.2018	0.0379	0.1062	-0.0625	-0.0409	-0.0433
Sc	-0.0238	0.0106	-0.0494	-0.0244	-0.0231	-0.0103	-0.0012	0.0205	0.0137	0.0561	0.0849	0.1197	0.1625	0.2020	0.2368	0.2545	0.2792	0.0174	0.1295	-0.0515	-0.0426	-0.0174
V	0.1092	0.0722	0.1281	0.0097	0.0106	0.0117	0.0170	0.0128	0.1127	0.0385	0.0427	0.0563	0.0734	0.0776	0.0822	0.0983	0.1534	0.0118	0.0141	0.0131	-0.0112	-0.0583
Cr	0.1652	0.0453	0.0976	0.0191	0.0242	0.0134	0.0138	-0.0079	0.0733	-0.0031	-0.0064	-0.0047	-0.0009	-0.0140	-0.0257	-0.0209	0.0274	0.0249	-0.0281	0.0146	0.0113	-0.0506
Co	0.0396	0.1740	0.2919	0.0082	-0.0020	0.0213	0.0359	0.0560	0.2569	0.1196	0.1216	0.1455	0.1704	0.1904	0.2119	0.2536	0.3260	-0.0223	0.0255	0.0503	-0.0399	-0.1001
Ni	0.0145	0.0657	0.0822	-0.0079	-0.0091	-0.0022	0.0034	0.0142	0.0790	0.0344	0.0334	0.0341	0.0368	0.0359	0.0362	0.0514	0.0760	-0.0184	-0.0279	0.0498	-0.0003	-0.0515
Cu	0.1379	0.1859	0.3610	0.0193	0.0200	0.0148	0.0197	0.0192	0.2384	0.0574	0.0502	0.0487	0.0565	0.0397	0.0251	0.0492	0.1391	-0.0506	-0.1205	0.1147	0.0175	-0.0625
Zn	-0.0395	0.0878	0.1248	-0.0090	-0.0187	0.0095	0.0240	0.0530	0.1627	0.1012	0.1024	0.1220	0.1384	0.1615	0.1847	0.2242	0.2614	-0.0112	0.0515	0.0208	-0.0424	-0.1050
Rb	0.0065	-0.0198	-0.0060	0.0089	0.0113	-0.0039	-0.0133	-0.0281	-0.0668	-0.0542	-0.0596	-0.0780	-0.0944	-0.1139	-0.1312	-0.1568	-0.1785	-0.0165	-0.0624	0.0227	0.0298	0.0718
Sr	0.1175	0.2702	0.5821	0.0577	0.0372	0.0590	0.0705	0.0691	0.4344	0.1224	0.0773	0.0649	0.0392	0.0112	-0.0064	0.0415	0.1336	-0.0559	-0.1484	0.1565	-0.0075	-0.1665
Y	-0.0068	0.0827	-0.0983	-0.0522	-0.0461	-0.0227	-0.0021	0.0365	0.0074	0.1434	0.2487	0.3712	0.5236	0.6567	0.7747	0.8009	0.8616	0.0734	0.4440	-0.2085	-0.1313	0.0815
Zr	0.0457	0.0126	0.0207	0.0106	0.0103	0.0123	0.0149	0.0079	0.0332	0.0192	0.0257	0.0433	0.0598	0.0742	0.0868	0.0938	0.1077	0.0311	0.0628	-0.0492	-0.0207	-0.0084
Nb	-0.0306	-0.0593	-0.2454	-0.0369	-0.0313	-0.0193	-0.0104	0.0061	-0.1122	0.0406	0.0972	0.1602	0.2344	0.3068	0.3702	0.3750	0.3738	0.0743	0.2819	-0.1636	-0.0718	0.0436
Mo	0.1706	0.0502	0.1023	0.0196	0.0249	0.0136	0.0140	-0.0087	0.0750	-0.0033	-0.0060	-0.0038	0.0010	-0.0120	-0.0234	-0.0191	0.0298	0.0256	-0.0280	0.0147	0.0117	-0.0482
Cs	0.0502	0.1763	0.2725	0.0243	0.0172	0.0231	0.0281	0.0223	0.1793	0.0553	0.0502	0.0595	0.0673	0.0711	0.0768	0.0915	0.1135	-0.0202	-0.0382	0.0409	-0.0060	0.0013
Ba	0.1023	0.2725	0.6864	0.0993	0.0745	0.0796	0.0776	0.0481	0.4162	0.0634	-0.0065	-0.0460	-0.1068	-0.1639	-0.2079	-0.1880	-0.1397	-0.0797	-0.2558	0.1672	0.0269	-0.0586
La	0.0196	0.0243	0.0993	0.0241	0.0193	0.0185	0.0163	0.0050	0.0561	-0.0022	-0.0198	-0.0308	-0.0489	-0.0634	-0.0753	-0.0752	-0.0765	-0.0050	-0.0486	0.0163	0.0074	-0.0077
Ce	0.0249	0.0172	0.0745	0.0193	0.0169	0.0141	0.0120	0.0013	0.0401	-0.0059	-0.0194	-0.0281	-0.0418	-0.0542	-0.0650	-0.0654	-0.0653	-0.0020	-0.0425	0.0106	0.0086	-0.0041
Pr	0.0136	0.0231	0.0796	0.0185	0.0141	0.0158	0.0153	0.0079	0.0527	0.0062	-0.0065	-0.0116	-0.0228	-0.0304	-0.0363	-0.0333	-0.0328	-0.0005	-0.0248	0.0066	0.0003	-0.0120
Nd	0.0140	0.0281	0.0776	0.0163	0.0120	0.0153	0.0160	0.0105	0.0581	0.0132	0.0033	0.0021	-0.0047	-0.0081	-0.0103	-0.0047	-0.0015	0.0024	-0.0119	0.0014	-0.0042	-0.0163

Table C3 (continued):

	Mo	Cs	Ba	La	Ce	Pr	Nd	Sm	Eu	Gd	Tb	Dy	Ho	Er	Tm	Yb	Lu	Hf	Ta	Pb	Th	U
Sm	-0.0087	0.0223	0.0481	0.0050	0.0013	0.0079	0.0105	0.0140	0.0467	0.0239	0.0218	0.0266	0.0289	0.0343	0.0399	0.0482	0.0544	-0.0002	0.0147	-0.0030	-0.0123	-0.0174
Eu	0.0750	0.1793	0.4162	0.0561	0.0401	0.0527	0.0581	0.0467	0.3001	0.0720	0.0315	0.0193	-0.0082	-0.0318	-0.0489	-0.0184	0.0257	-0.0299	-0.1170	0.0836	-0.0016	-0.0940
Gd	-0.0033	0.0553	0.0634	-0.0022	-0.0059	0.0062	0.0132	0.0239	0.0720	0.0563	0.0707	0.0963	0.1242	0.1514	0.1769	0.1923	0.2145	0.0084	0.0832	-0.0278	-0.0351	-0.0122
Tb	-0.0060	0.0502	-0.0065	-0.0198	-0.0194	-0.0065	0.0033	0.0218	0.0315	0.0707	0.1114	0.1613	0.2225	0.2767	0.3256	0.3403	0.3707	0.0245	0.1775	-0.0739	-0.0569	0.0198
Dy	-0.0038	0.0595	-0.0460	-0.0308	-0.0281	-0.0116	0.0021	0.0266	0.0193	0.0963	0.1613	0.2391	0.3348	0.4191	0.4942	0.5129	0.5530	0.0464	0.2809	-0.1306	-0.0853	0.0449
Ho	0.0010	0.0673	-0.1068	-0.0489	-0.0418	-0.0228	-0.0047	0.0289	-0.0082	0.1242	0.2225	0.3348	0.4757	0.5972	0.7045	0.7262	0.7814	0.0701	0.4075	-0.1956	-0.1177	0.0811
Er	-0.0120	0.0711	-0.1639	-0.0634	-0.0542	-0.0304	-0.0081	0.0343	-0.0318	0.1514	0.2767	0.4191	0.5972	0.7525	0.8895	0.9144	0.9757	0.0918	0.5239	-0.2579	-0.1495	0.1129
Tm	-0.0234	0.0768	-0.2079	-0.0753	-0.0650	-0.0363	-0.0103	0.0399	-0.0489	0.1769	0.3256	0.4942	0.7045	0.8895	1.0529	1.0803	1.1476	0.1103	0.6280	-0.3101	-0.1788	0.1399
Yb	-0.0191	0.0915	-0.1880	-0.0752	-0.0654	-0.0333	-0.0047	0.0482	-0.0184	0.1923	0.3403	0.5129	0.7262	0.9144	1.0803	1.1165	1.1907	0.1132	0.6322	-0.3130	-0.1840	0.1181
Lu	0.0298	0.1135	-0.1397	-0.0765	-0.0653	-0.0328	-0.0015	0.0544	0.0257	0.2145	0.3707	0.5530	0.7814	0.9757	1.1476	1.1907	1.3020	0.1151	0.6572	-0.3065	-0.1941	0.0912
Hf	0.0256	-0.0202	-0.0797	-0.0050	-0.0020	-0.0005	0.0024	-0.0002	-0.0299	0.0084	0.0245	0.0464	0.0701	0.0918	0.1103	0.1132	0.1151	0.0402	0.0934	-0.0679	-0.0222	0.0039
Ta	-0.0280	-0.0382	-0.2558	-0.0486	-0.0425	-0.0248	-0.0119	0.0147	-0.1170	0.0832	0.1775	0.2809	0.4075	0.5239	0.6280	0.6322	0.6572	0.0934	0.4435	-0.2301	-0.1190	0.0955
Pb	0.0147	0.0409	0.1672	0.0163	0.0106	0.0066	0.0014	-0.0030	0.0836	-0.0278	-0.0739	-0.1306	-0.1956	-0.2579	-0.3101	-0.3130	-0.3065	-0.0679	-0.2301	0.1675	0.0582	-0.0724
Th	0.0117	-0.0060	0.0269	0.0074	0.0086	0.0003	-0.0042	-0.0123	-0.0016	-0.0351	-0.0569	-0.0853	-0.1177	-0.1495	-0.1788	-0.1840	-0.1941	-0.0222	-0.1190	0.0582	0.0373	-0.0160
U	-0.0482	0.0013	-0.0586	-0.0077	-0.0041	-0.0120	-0.0163	-0.0174	-0.0940	-0.0122	0.0198	0.0449	0.0811	0.1129	0.1399	0.1181	0.0912	0.0039	0.0955	-0.0724	-0.0160	0.1496

Table C4: Centered log-ratio covariance matrices for the STK Gneiss calculated after the methods of Aitchison (1986), where SiO_2, etc. represents (natural) log [SiO_2 wt. % / g], etc. and where g is the geometric mean of the geometric mean.

	Al_2O_3	CaO	Fe_2O_3	K_2O	MgO	MnO	Na_2O	P_2O_5	SiO_2	TiO_2	Sc	V	Cr	Co	Ni	Cu	Zn	Rb	Sr	Y	Zr	Nb
Al_2O_3	0.0022	0.0095	0.0136	-0.0115	0.0125	0.0103	0.0047	0.0093	-0.0015	0.0071	0.0086	0.0127	0.0025	0.0170	0.0098	0.0114	0.0141	-0.0016	-0.0023	-0.0026	0.0006	0.0007
CaO	0.0095	0.0682	0.0682	-0.0646	0.0821	0.0422	0.0168	0.0547	-0.0077	0.0435	0.0392	0.0720	0.0396	0.0852	0.0275	0.0394	0.0649	-0.0316	0.0009	-0.0172	0.0031	-0.0031
Fe_2O_3	0.0136	0.0682	0.0993	-0.0697	0.1016	0.0840	0.0268	0.0761	-0.0110	0.0530	0.0625	0.0953	0.0287	0.1304	0.0728	0.0735	0.1066	-0.0135	-0.0072	-0.0060	0.0059	0.0052
K_2O	-0.0115	-0.0646	-0.0697	0.1097	-0.0633	-0.0625	-0.0347	-0.0488	0.0068	-0.0375	-0.0450	-0.0677	-0.0209	-0.0814	-0.0410	-0.1555	-0.0356	0.0446	0.0063	0.0215	0.0015	-0.0021
MgO	0.0125	0.0821	0.1016	-0.0633	0.1305	0.0722	0.0170	0.0839	-0.0112	0.0582	0.0610	0.1061	0.0604	0.1368	0.0851	0.0421	0.1194	-0.0281	0.0019	-0.0108	0.0108	-0.0051
MnO	0.0103	0.0422	0.0840	-0.0625	0.0722	0.1020	0.0294	0.0657	-0.0084	0.0398	0.0564	0.0749	0.0069	0.1134	0.0761	0.1355	0.0796	-0.0085	0.0046	0.0098	0.0041	0.0110
Na_2O	0.0047	0.0168	0.0268	-0.0347	0.0170	0.0294	0.0152	0.0172	-0.0027	0.0124	0.0184	0.0231	-0.0033	0.0318	0.0202	0.0573	0.0168	-0.0071	-0.0010	-0.0073	-0.0009	0.0036
P_2O_5	0.0093	0.0547	0.0761	-0.0488	0.0839	0.0657	0.0172	0.0639	-0.0083	0.0434	0.0474	0.0739	0.0253	0.1011	0.0495	0.0313	0.0801	-0.0142	0.0011	-0.0027	0.0062	0.0043
SiO_2	-0.0015	-0.0077	-0.0110	0.0068	-0.0112	-0.0084	-0.0027	-0.0083	0.0013	-0.0060	-0.0067	-0.0106	-0.0032	-0.0144	-0.0069	-0.0050	-0.0126	0.0008	0.0013	0.0007	-0.0006	-0.0006
TiO_2	0.0071	0.0435	0.0530	-0.0375	0.0582	0.0398	0.0124	0.0434	-0.0060	0.0347	0.0308	0.0517	0.0185	0.0688	0.0222	0.0164	0.0591	-0.0122	-0.0036	-0.0006	0.0062	0.0022
Sc	0.0086	0.0392	0.0625	-0.0450	0.0610	0.0564	0.0184	0.0474	-0.0067	0.0308	0.0408	0.0587	0.0136	0.0820	0.0515	0.0521	0.0638	-0.0064	-0.0050	-0.0048	0.0027	0.0047
V	0.0127	0.0720	0.0953	-0.0677	0.1061	0.0749	0.0231	0.0739	-0.0106	0.0517	0.0587	0.0955	0.0407	0.1254	0.0718	0.0704	0.1038	-0.0203	-0.0017	-0.0106	0.0054	0.0003
Cr	0.0025	0.0396	0.0287	-0.0209	0.0604	0.0069	-0.0033	0.0253	-0.0032	0.0185	0.0136	0.0407	0.0556	0.0409	0.0324	0.0324	0.0407	-0.0275	0.0085	-0.0072	0.0033	-0.0141
Co	0.0170	0.0852	0.1304	-0.0814	0.1368	0.1134	0.0318	0.1011	-0.0144	0.0688	0.0820	0.1254	0.0409	0.1748	0.1043	0.0974	0.1483	-0.0130	-0.0102	0.0013	0.0098	0.0065
Ni	0.0098	0.0275	0.0728	-0.0410	0.0851	0.0761	0.0202	0.0495	-0.0069	0.0222	0.0515	0.0718	0.0324	0.1043	0.1519	0.1398	0.0942	-0.0047	0.0038	-0.0076	0.0089	-0.0061
Cu	0.0114	0.0394	0.0735	-0.1555	0.0421	0.1355	0.0573	0.0313	-0.0050	0.0164	0.0521	0.0704	0.0324	0.0974	0.1398	0.5955	0.0341	-0.0597	0.0076	0.0222	-0.0080	-0.0047
Zn	0.0141	0.0649	0.1066	-0.0356	0.1194	0.0796	0.0168	0.0801	-0.0126	0.0591	0.0638	0.1038	0.0407	0.1483	0.0942	0.0341	0.1562	0.0083	-0.0192	0.0134	0.0151	0.0016
Rb	-0.0016	-0.0316	-0.0135	0.0446	-0.0281	-0.0085	-0.0071	-0.0142	0.0008	-0.0122	-0.0064	-0.0203	-0.0275	-0.0130	-0.0047	-0.0597	0.0083	0.0408	-0.0173	0.0176	0.0001	0.0082
Sr	-0.0023	0.0009	-0.0072	0.0063	0.0019	0.0046	-0.0010	0.0011	0.0013	-0.0036	-0.0050	-0.0017	0.0085	-0.0102	0.0038	0.0076	-0.0192	-0.0173	0.0487	-0.0220	-0.0033	-0.0075
Y	-0.0026	-0.0172	-0.0060	0.0215	-0.0108	0.0098	-0.0073	-0.0027	0.0007	-0.0006	-0.0048	-0.0106	-0.0072	0.0013	-0.0076	0.0222	0.0134	0.0176	-0.0220	0.0472	0.0069	0.0070
Zr	0.0006	0.0031	0.0059	0.0015	0.0108	0.0041	-0.0009	0.0062	-0.0006	0.0062	0.0027	0.0054	0.0033	0.0098	0.0089	-0.0080	0.0151	0.0001	-0.0033	0.0069	0.0059	-0.0005
Nb	0.0007	-0.0031	0.0052	-0.0021	-0.0051	0.0110	0.0036	0.0043	-0.0006	0.0022	0.0047	0.0003	-0.0141	0.0065	-0.0061	-0.0047	0.0016	0.0082	-0.0075	0.0070	-0.0005	0.0072
Mo	0.0027	0.0411	0.0296	-0.0240	0.0611	0.0068	-0.0028	0.0251	-0.0033	0.0189	0.0140	0.0418	0.0573	0.0420	0.0325	0.0413	0.0418	-0.0284	0.0055	-0.0059	0.0031	-0.0144
Cs	0.0168	0.0145	0.0833	-0.0806	0.0311	0.1045	0.0508	0.0345	-0.0087	0.0258	0.0599	0.0624	-0.0321	0.1085	0.1256	0.2682	0.0974	0.0244	-0.0402	0.0137	0.0045	0.0144
Ba	-0.0102	-0.0646	-0.0592	0.0860	-0.0589	-0.0388	-0.0259	-0.0433	0.0064	-0.0394	-0.0345	-0.0595	-0.0216	-0.0668	-0.0115	-0.0735	-0.0372	0.0389	0.0022	0.0249	-0.0007	0.0003
La	-0.0107	-0.0526	-0.0656	0.0643	-0.0661	-0.0471	-0.0249	-0.0445	0.0072	-0.0268	-0.0437	-0.0675	-0.0245	-0.0786	-0.0605	-0.0673	-0.0506	0.0208	-0.0142	0.0452	0.0073	0.0032
Ce	-0.0082	-0.0411	-0.0520	0.0500	-0.0510	-0.0397	-0.0197	-0.0366	0.0057	-0.0219	-0.0347	-0.0527	-0.0167	-0.0624	-0.0433	-0.0488	-0.0385	0.0158	-0.0123	0.0339	0.0059	0.0010
Pr	-0.0090	-0.0455	-0.0549	0.0575	-0.0548	-0.0396	-0.0221	-0.0372	0.0059	-0.0217	-0.0369	-0.0569	-0.0206	-0.0646	-0.0498	-0.0598	-0.0376	0.0203	-0.0158	0.0431	0.0078	0.0031
Nd	-0.0080	-0.0415	-0.0487	0.0519	-0.0493	-0.0338	-0.0193	-0.0331	0.0053	-0.0189	-0.0328	-0.0510	-0.0197	-0.0570	-0.0428	-0.0504	-0.0318	0.0188	-0.0138	0.0399	0.0079	0.0029
Sm	-0.0055	-0.0295	-0.0317	0.0376	-0.0340	-0.0186	-0.0138	-0.0216	0.0034	-0.0101	-0.0224	-0.0347	-0.0145	-0.0348	-0.0321	-0.0221	-0.0136	0.0164	-0.0162	0.0407	0.0079	0.0037
Eu	-0.0001	-0.0109	-0.0008	0.0081	-0.0029	0.0069	-0.0002	-0.0019	0.0003	-0.0011	0.0001	-0.0039	-0.0064	0.0029	0.0180	0.0173	0.0110	0.0087	-0.0074	0.0148	0.0059	0.0014
Gd	-0.0042	-0.0250	-0.0225	0.0350	-0.0253	-0.0109	-0.0114	-0.0147	0.0023	-0.0060	-0.0163	-0.0261	-0.0137	-0.0227	-0.0233	-0.0232	-0.0023	0.0181	-0.0147	0.0378	0.0081	0.0043
Tb	-0.0030	-0.0180	-0.0124	0.0242	-0.0162	-0.0001	-0.0084	-0.0079	0.0012	-0.0018	-0.0098	-0.0162	-0.0086	-0.0089	-0.0163	0.0061	0.0069	0.0157	-0.0190	0.0419	0.0074	0.0052
Dy	-0.0018	-0.0130	-0.0019	0.0161	-0.0074	0.0114	-0.0052	0.0008	0.0002	0.0027	-0.0022	-0.0072	-0.0090	0.0052	-0.0089	0.0131	0.0150	0.0159	-0.0226	0.0434	0.0073	0.0079
Ho	-0.0022	-0.0153	-0.0041	0.0206	-0.0079	0.0096	-0.0071	-0.0023	0.0004	0.0001	-0.0039	-0.0080	-0.0041	0.0039	-0.0043	0.0272	0.0176	0.0175	-0.0225	0.0463	0.0067	0.0059
Er	-0.0026	-0.0180	-0.0024	0.0199	-0.0069	0.0180	-0.0066	-0.0005	0.0004	-0.0013	-0.0018	-0.0069	-0.0035	0.0079	0.0048	0.0498	0.0182	0.0176	-0.0212	0.0513	0.0065	0.0067
Tm	-0.0020	-0.0152	0.0040	0.0149	-0.0008	0.0259	-0.0055	0.0052	-0.0002	0.0027	0.0024	-0.0018	-0.0029	0.0175	0.0085	0.0592	0.0257	0.0178	-0.0282	0.0594	0.0083	0.0088
Yb	-0.0017	-0.0129	0.0025	0.0160	-0.0029	0.0193	-0.0058	0.0023	-0.0003	0.0029	0.0003	-0.0023	-0.0015	0.0142	0.0009	0.0535	0.0263	0.0183	-0.0278	0.0556	0.0072	0.0074
Lu	-0.0026	-0.0200	-0.0019	0.0183	-0.0096	0.0209	-0.0063	-0.0009	0.0004	-0.0018	-0.0011	-0.0077	-0.0057	0.0094	0.0030	0.0626	0.0189	0.0207	-0.0298	0.0597	0.0062	0.0090

Table C4 (continued):

	Al_2O_3	CaO	Fe_2O_3	K_2O	MgO	MnO	Na_2O	P_2O_5	SiO_2	TiO_2	Sc	V	Cr	Co	Ni	Cu	Zn	Rb	Sr	Y	Zr	Nb
Hf	-0.0006	-0.0024	-0.0033	0.0100	0.0026	-0.0062	-0.0042	-0.0013	0.0003	0.0009	-0.0033	-0.0026	0.0031	-0.0023	0.0025	-0.0198	0.0065	0.0018	-0.0017	0.0050	0.0046	-0.0020
Ta	0.0032	0.0017	0.0255	-0.0318	-0.0073	0.0488	0.0170	0.0159	-0.0025	0.0067	0.0208	0.0139	-0.0263	0.0327	-0.0058	0.0900	0.0058	0.0121	-0.0212	0.0231	-0.0080	0.0187
Pb	-0.0073	-0.0314	-0.0433	0.0383	-0.0456	-0.0195	-0.0107	-0.0276	0.0051	-0.0198	-0.0286	-0.0417	-0.0156	-0.0552	-0.0364	-0.0140	-0.0485	0.0010	0.0342	0.0044	-0.0019	-0.0024
Th	-0.0075	-0.0354	-0.0528	0.0354	-0.0481	-0.0445	-0.0149	-0.0368	0.0062	-0.0275	-0.0323	-0.0504	-0.0144	-0.0695	-0.0313	-0.0592	-0.0612	0.0014	0.0087	-0.0025	-0.0006	-0.0035
U	0.0062	-0.0072	0.0174	-0.0513	-0.0296	0.0415	0.0313	0.0027	-0.0012	0.0039	0.0177	-0.0006	-0.0575	0.0129	0.0057	0.0898	-0.0141	0.0079	-0.0185	-0.0032	-0.0028	0.0189

Table C4 (continued):

	Mo	Cs	Ba	La	Ce	Pr	Nd	Sm	Eu	Gd	Tb	Dy	Ho	Er	Tm	Yb	Lu	Hf	Ta	Pb	Th	U
Al_2O_3	0.0027	0.0168	-0.0102	-0.0107	-0.0082	-0.0090	-0.0080	-0.0055	-0.0001	-0.0042	-0.0030	-0.0018	-0.0022	-0.0026	-0.0020	-0.0017	-0.0026	-0.0006	0.0032	-0.0073	-0.0075	0.0062
CaO	0.0411	0.0145	-0.0646	-0.0526	-0.0411	-0.0455	-0.0415	-0.0295	-0.0109	-0.0250	-0.0180	-0.0130	-0.0153	-0.0180	-0.0152	-0.0129	-0.0200	-0.0024	0.0017	-0.0314	-0.0354	-0.0072
Fe_2O_3	0.0296	0.0833	-0.0592	-0.0656	-0.0520	-0.0549	-0.0487	-0.0317	-0.0008	-0.0225	-0.0124	-0.0019	-0.0041	-0.0024	0.0040	0.0025	-0.0019	-0.0033	0.0255	-0.0433	-0.0528	0.0174
K_2O	-0.0240	-0.0806	0.0860	0.0643	0.0500	0.0575	0.0519	0.0376	0.0081	0.0350	0.0242	0.0161	0.0206	0.0199	0.0149	0.0160	0.0183	0.0100	-0.0318	0.0383	0.0354	-0.0513
MgO	0.0611	0.0311	-0.0589	-0.0661	-0.0510	-0.0548	-0.0493	-0.0340	-0.0029	-0.0253	-0.0162	-0.0074	-0.0079	-0.0069	-0.0008	-0.0029	-0.0096	0.0026	-0.0073	-0.0456	-0.0481	-0.0296
MnO	0.0068	0.1045	-0.0388	-0.0471	-0.0397	-0.0396	-0.0338	-0.0186	0.0069	-0.0109	-0.0001	0.0114	0.0096	0.0180	0.0259	0.0193	0.0209	-0.0062	0.0488	-0.0195	-0.0445	0.0415
Na_2O	-0.0028	0.0508	-0.0259	-0.0249	-0.0197	-0.0221	-0.0193	-0.0138	-0.0002	-0.0114	-0.0084	-0.0052	-0.0071	-0.0066	-0.0055	-0.0058	-0.0063	-0.0042	0.0170	-0.0107	-0.0149	0.0313
P_2O_5	0.0251	0.0345	-0.0433	-0.0445	-0.0366	-0.0372	-0.0331	-0.0216	-0.0019	-0.0147	-0.0079	0.0008	-0.0023	-0.0005	0.0052	0.0023	-0.0009	-0.0013	0.0159	-0.0276	-0.0368	0.0027
SiO_2	-0.0033	-0.0087	0.0064	0.0072	0.0057	0.0059	0.0053	0.0034	0.0003	0.0023	0.0012	0.0002	0.0004	0.0004	-0.0002	-0.0003	0.0004	0.0003	-0.0025	0.0051	0.0062	-0.0012
TiO_2	0.0189	0.0258	-0.0394	-0.0268	-0.0219	-0.0217	-0.0189	-0.0101	-0.0011	-0.0060	-0.0018	0.0027	0.0001	-0.0013	0.0027	0.0029	-0.0018	0.0009	0.0067	-0.0198	-0.0275	0.0039
Sc	0.0140	0.0599	-0.0345	-0.0437	-0.0347	-0.0369	-0.0328	-0.0224	0.0001	-0.0163	-0.0098	-0.0022	-0.0039	-0.0018	0.0024	0.0003	-0.0011	-0.0033	0.0208	-0.0286	-0.0323	0.0177
V	0.0418	0.0624	-0.0595	-0.0675	-0.0527	-0.0569	-0.0510	-0.0347	-0.0039	-0.0261	-0.0162	-0.0072	-0.0080	-0.0069	-0.0018	-0.0023	-0.0077	-0.0026	0.0139	-0.0417	-0.0504	-0.0006
Cr	0.0573	-0.0321	-0.0216	-0.0245	-0.0167	-0.0206	-0.0197	-0.0145	-0.0064	-0.0137	-0.0086	-0.0090	-0.0041	-0.0035	-0.0029	-0.0015	-0.0057	0.0031	-0.0263	-0.0156	-0.0144	-0.0575
Co	0.0420	0.1085	-0.0668	-0.0786	-0.0624	-0.0646	-0.0570	-0.0348	0.0029	-0.0227	-0.0089	0.0052	0.0039	0.0079	0.0175	0.0142	0.0094	-0.0023	0.0327	-0.0552	-0.0695	0.0129
Ni	0.0325	0.1256	-0.0115	-0.0605	-0.0433	-0.0498	-0.0428	-0.0321	0.0180	-0.0233	-0.0163	-0.0089	-0.0043	0.0048	0.0085	0.0009	0.0030	0.0025	-0.0058	-0.0364	-0.0313	0.0057
Cu	0.0413	0.2682	-0.0735	-0.0673	-0.0488	-0.0598	-0.0504	-0.0221	0.0173	-0.0232	0.0061	0.0131	0.0272	0.0498	0.0592	0.0535	0.0626	-0.0198	0.0900	-0.0140	-0.0592	0.0898
Zn	0.0418	0.0974	-0.0372	-0.0506	-0.0385	-0.0376	-0.0318	-0.0136	0.0110	-0.0023	0.0069	0.0150	0.0176	0.0182	0.0257	0.0263	0.0189	0.0065	0.0058	-0.0485	-0.0612	-0.0141
Rb	-0.0284	0.0244	0.0389	0.0208	0.0158	0.0203	0.0188	0.0164	0.0087	0.0181	0.0157	0.0159	0.0175	0.0176	0.0178	0.0183	0.0207	0.0018	0.0121	0.0010	0.0014	0.0079
Sr	0.0055	-0.0402	0.0022	-0.0142	-0.0123	-0.0158	-0.0138	-0.0162	-0.0074	-0.0147	-0.0190	-0.0226	-0.0225	-0.0212	-0.0282	-0.0278	-0.0298	-0.0017	-0.0212	0.0342	0.0087	-0.0185
Y	-0.0059	0.0137	0.0249	0.0452	0.0339	0.0431	0.0399	0.0407	0.0148	0.0378	0.0419	0.0434	0.0463	0.0513	0.0594	0.0556	0.0597	0.0050	0.0231	0.0044	-0.0025	-0.0032
Zr	0.0031	0.0045	-0.0007	0.0073	0.0059	0.0078	0.0079	0.0079	0.0059	0.0081	0.0074	0.0073	0.0067	0.0065	0.0083	0.0072	0.0062	0.0046	-0.0080	-0.0019	-0.0006	-0.0028
Nb	-0.0144	0.0144	0.0003	0.0032	0.0010	0.0031	0.0029	0.0037	0.0014	0.0043	0.0052	0.0079	0.0059	0.0067	0.0088	0.0074	0.0090	-0.0020	0.0187	-0.0024	-0.0035	0.0189
Mo	0.0596	-0.0284	-0.0236	-0.0248	-0.0167	-0.0208	-0.0199	-0.0140	-0.0065	-0.0135	-0.0076	-0.0079	-0.0025	-0.0019	-0.0009	0.0008	-0.0034	0.0029	-0.0245	-0.0181	-0.0159	-0.0575
Cs	-0.0284	0.3075	-0.0417	-0.0582	-0.0420	-0.0461	-0.0362	-0.0148	0.0306	-0.0056	0.0064	0.0148	0.0175	0.0235	0.0302	0.0295	0.0312	-0.0066	0.0663	-0.0466	-0.0594	0.1292
Ba	-0.0236	-0.0417	0.0817	0.0535	0.0417	0.0477	0.0429	0.0313	0.0113	0.0286	0.0226	0.0184	0.0239	0.0285	0.0265	0.0233	0.0304	0.0055	-0.0106	0.0292	0.0306	-0.0318
La	-0.0248	-0.0582	0.0535	0.0881	0.0674	0.0792	0.0723	0.0608	0.0149	0.0524	0.0470	0.0413	0.0423	0.0433	0.0471	0.0442	0.0485	0.0105	-0.0071	0.0324	0.0346	-0.0155
Ce	-0.0167	-0.0420	0.0417	0.0674	0.0522	0.0608	0.0554	0.0465	0.0121	0.0398	0.0356	0.0306	0.0320	0.0325	0.0352	0.0333	0.0364	0.0087	-0.0093	0.0232	0.0272	-0.0141
Pr	-0.0208	-0.0461	0.0477	0.0792	0.0608	0.0718	0.0657	0.0560	0.0150	0.0488	0.0444	0.0396	0.0407	0.0417	0.0458	0.0431	0.0467	0.0103	-0.0064	0.0261	0.0286	-0.0145
Nd	-0.0199	-0.0362	0.0429	0.0723	0.0554	0.0657	0.0603	0.0518	0.0149	0.0455	0.0413	0.0367	0.0377	0.0386	0.0424	0.0399	0.0429	0.0098	-0.0062	0.0247	0.0254	-0.0108
Sm	-0.0140	-0.0148	0.0313	0.0608	0.0465	0.0560	0.0518	0.0472	0.0146	0.0422	0.0407	0.0377	0.0391	0.0405	0.0454	0.0434	0.0457	0.0084	0.0021	0.0176	0.0140	-0.0061
Eu	-0.0065	0.0306	0.0113	0.0149	0.0121	0.0150	0.0149	0.0146	0.0121	0.0144	0.0140	0.0139	0.0146	0.0164	0.0190	0.0165	0.0179	0.0046	-0.0009	0.0008	0.0013	0.0086
Gd	-0.0135	-0.0056	0.0286	0.0524	0.0398	0.0488	0.0455	0.0422	0.0144	0.0387	0.0375	0.0353	0.0366	0.0379	0.0425	0.0407	0.0424	0.0080	0.0031	0.0147	0.0090	-0.0045
Tb	-0.0076	0.0064	0.0226	0.0470	0.0356	0.0444	0.0413	0.0407	0.0140	0.0375	0.0393	0.0388	0.0410	0.0439	0.0502	0.0480	0.0503	0.0063	0.0133	0.0084	0.0016	-0.0032
Dy	-0.0079	0.0148	0.0184	0.0413	0.0306	0.0396	0.0367	0.0377	0.0139	0.0353	0.0388	0.0408	0.0422	0.0461	0.0542	0.0505	0.0538	0.0049	0.0226	0.0018	-0.0032	0.0025
Ho	-0.0025	0.0175	0.0239	0.0423	0.0320	0.0407	0.0377	0.0391	0.0146	0.0366	0.0410	0.0422	0.0459	0.0508	0.0585	0.0554	0.0590	0.0051	0.0215	0.0026	-0.0045	-0.0059
Er	-0.0019	0.0235	0.0285	0.0433	0.0325	0.0417	0.0386	0.0405	0.0164	0.0379	0.0439	0.0461	0.0508	0.0581	0.0670	0.0621	0.0676	0.0043	0.0281	0.0039	-0.0054	-0.0057
Tm	-0.0009	0.0302	0.0265	0.0471	0.0352	0.0458	0.0424	0.0454	0.0190	0.0425	0.0502	0.0542	0.0585	0.0670	0.0785	0.0721	0.0785	0.0048	0.0353	-0.0013	-0.0084	-0.0027
Yb	0.0008	0.0295	0.0233	0.0442	0.0333	0.0431	0.0399	0.0434	0.0165	0.0407	0.0480	0.0505	0.0554	0.0621	0.0721	0.0682	0.0728	0.0045	0.0320	-0.0007	-0.0104	-0.0052
Lu	-0.0034	0.0312	0.0304	0.0485	0.0364	0.0467	0.0429	0.0457	0.0179	0.0424	0.0503	0.0538	0.0590	0.0676	0.0785	0.0728	0.0798	0.0035	0.0388	-0.0003	-0.0075	-0.0018
Hf	0.0029	-0.0066	0.0055	0.0105	0.0087	0.0103	0.0098	0.0084	0.0046	0.0080	0.0063	0.0049	0.0051	0.0043	0.0048	0.0045	0.0035	0.0047	-0.0128	0.0015	0.0037	-0.0092
Ta	-0.0245	0.0663	-0.0106	-0.0071	-0.0093	-0.0064	-0.0062	0.0021	-0.0009	0.0031	0.0133	0.0226	0.0215	0.0281	0.0353	0.0320	0.0388	-0.0128	0.0767	-0.0121	-0.0236	0.0536
Pb	-0.0181	-0.0466	0.0292	0.0324	0.0232	0.0261	0.0247	0.0176	0.0008	0.0147	0.0084	0.0018	0.0026	0.0039	-0.0013	-0.0007	-0.0003	0.0015	-0.0121	0.0502	0.0228	-0.0099
Th	-0.0159	-0.0594	0.0306	0.0346	0.0272	0.0286	0.0254	0.0140	0.0013	0.0090	0.0016	-0.0032	-0.0045	-0.0054	-0.0084	-0.0104	-0.0075	0.0037	-0.0236	0.0228	0.0353	-0.0100
U	-0.0575	0.1292	-0.0318	-0.0155	-0.0141	-0.0145	-0.0108	-0.0061	0.0086	-0.0045	-0.0032	0.0025	-0.0059	-0.0057	-0.0027	-0.0052	-0.0018	-0.0092	0.0536	-0.0099	-0.0100	0.1170

Appendix D. Harker plots using molar concentrations

Fig. D1. Harker diagram of whole-rock major elements using molar concentrations for the GS and VS rocks.

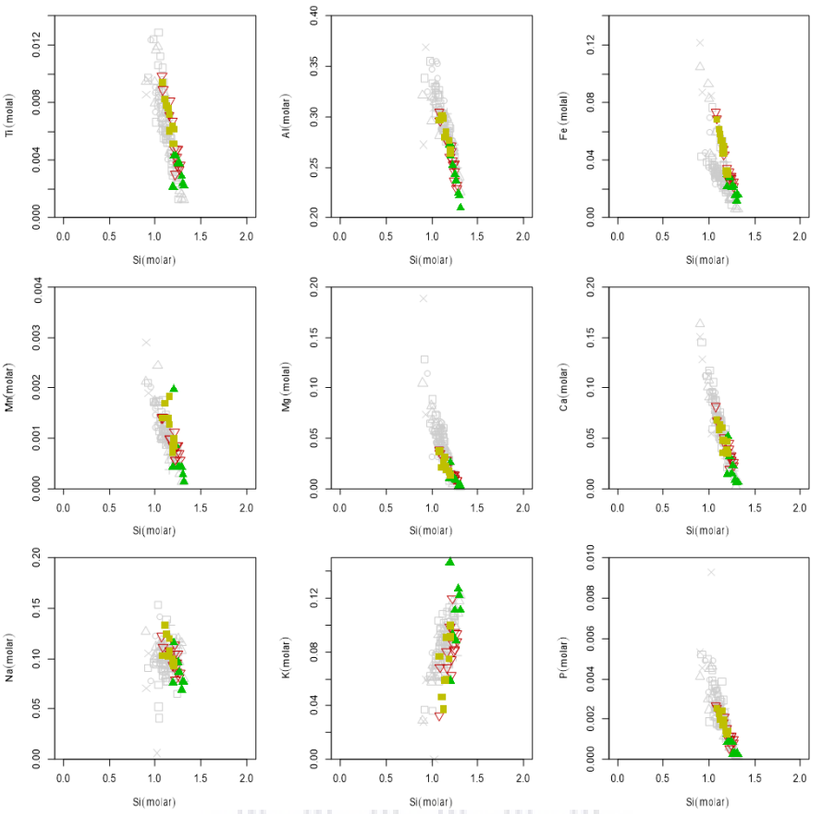

Fig. D2. Harker diagram of whole-rock trace element data using molar concentrations for the GS and VS rocks

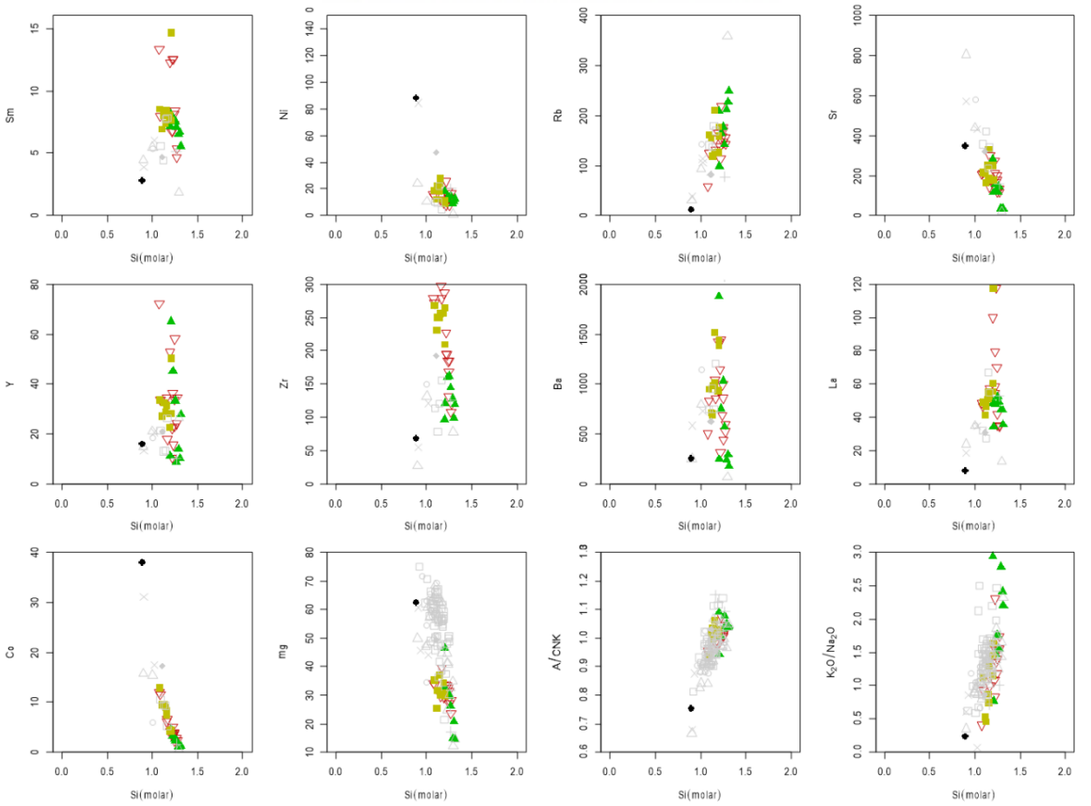

Appendix E. Using multivariate analyses to determine the Geotectonic environment in which the precursor rocks to the GS gneisses were deposited

Table E1. Application of multidimensional diagrams to Palaeoproterozoic (~1.8 Ga) felsic rocks of the NNM Gneiss, Gladkop Suite.

Magma type, Figure name	Figure type	Total number of samples	Number of discriminated samples				
			Arc			CR+OI [$\dot{x} \pm s$] [P_{CR+OI}] Θ	Col [$\dot{x} \pm s$] [P_{Col}] Θ
			IA+CA [$\dot{x} \pm s$] [P_{IA+CA}] Θ	IA [$\dot{x} \pm s$] [P_{IA}] Θ	CA [$\dot{x} \pm s$] [P_{CA}] Θ		
Acid; Verma et al. (2013); log-ratios of all major elements	(IA+CA-CR+OI-Col)	8	0 (0)	---	---	3 [0.6669±0.0121] (0.6549-0.6790)	5 [0.762±0.179] (0.5611-0.9808)
	(IA-CA-CR+OI)	8	---	1(0.5129)	0 (0)	7 [0.99812±0.00328] (0.9911-0.9999)	---
	(IA-CA-Col)	8	---	1(0.9199)	0 (0)	---	7 [0.9822±0.0301] (0.9219-1.0000)
	(IA-CR+OI-Col)	8	---	0 (0)	---	6 [0.759±0.121] (0.5506-0.8764)	2 [0.694±0.220] (0.5381, 0.8493)
	(CA-CR+OI-Col)	8	---	---	0 (0)	5 [0.718±0.108] (0.5802-0.8303)	3 [0.777±0.160] (0.6417-0.9537)
Diagrams based on log-ratios of major elements	***{Σn} {Σprob} [%prob]***	**40**	**{0} {0} [0%]**	**{2} {1.4328} [4%]**	**{0} {0} [0%]**	**{21} {17.1320} [52%]**	**{17} {14.4047} [44%]**
Acid; Verma et al. (2013); log-ratios of immobile major and trace elements	(IA+CA-CR+OI-Col)	8	0 (0)	---	---	7 [0.721±0.194] (0.4414-0.9030)	1(0.7635)
	(IA-CA-CR+OI)	8	---	0 (0)	1(0.5187)	7 [0.688±0.127] (0.4932-0.8780)	---
	(IA-CA-Col)	8	---	0 (0)	3 [0.696±0.160] (0.5678-0.8749)	---	5 [0.597±0.100] (0.5136-0.7677)
	(IA-CR+OI-Col)	8	---	0 (0)	---	7 [0.784±0.165] (0.5435-0.9334)	1(0.7799)
	(CA-CR+OI-Col)	8	---	---	1(0.3651)	6 [0.661±0.148] (0.4798-0.8063)	1(0.6729)
Diagrams based on log-ratios of immobile major and trace elements	***{Σn} {Σprob} [%prob]***	**40**	**{0} {0} [0%]**	**{0} {0} [0%]**	**{5} {2.9712} [11%]**	**{27} {19.3161} [70%]**	**{8} {5.1996} [19%]**
Acid; Verma et al. (2013); log-ratios of immobile trace elements	(IA+CA-CR+OI-Col)	8	0 (0)	---	---	1(0.6182)	7 [0.814±0.127] (0.6584-0.9553)
	(IA-CA-CR+OI)	8	---	0 (0)	6 [0.903±0.160] (0.6061-0.9999)	2 [0.907±0.080] (0.8507, 0.9632)	---
	(IA-CA-Col)	8	---	0 (0)	0 (0)	---	8 [0.871±0.065] (0.7577-0.9488)
	(IA-CR+OI-Col)	8	---	0 (0)	---	2 [0.618±0.053] (0.5806, 0.6550)	6 [0.888±0.173] (0.6429-1.0000)
	(CA-CR+OI-Col)	8	---	---	0 (0)	1(0.6048)	7 [0.740±0.174] (0.5531-0.9476)
Diagrams based on log-ratios of immobile trace elements	***{Σn} {Σprob} [%prob]***	**40**	**{0} {0} [0%]**	**{0} {0} [0%]**	**{6} {5.4198} [16%]**	**{6} {4.2724} [13%]**	**{28} {23.1768} [71%]**

IA−island arc; CA−continental arc; IA+CA–combined island and continental arcs, i.e., arc setting; CR−continental rift; OI−ocean island; CR+OI –combined continental rift and ocean island, i.e., within-plate (WP) setting; Col−collision; Θ the probability values for samples from a given locality are represented by (P_{IA+CA}) – probability for the combined island and continental arc setting in the first diagram; [P_{IA}] – probability for the island arc setting in the diagrams; [P_{CA}] – probability for the continental arc setting in the diagrams; [P_{CR+OI}] – probability for the combined continental rift and ocean island setting in all diagrams; [P_{Col}] – probability for the collision setting in the diagrams; [$\dot{x} \pm s$] − mean ± 1SD (standard deviation) of the probability estimates for all samples discriminated in a given tectonic setting; these are reported in [], the values are rounded mostly following the indications put forth by Verma (2005); the final rows give a synthesis of results as {Σn} {Σprob} [%prob], where {Σn} is the total number of samples or data points plotting in all five diagrams is reported in the column of total number of samples, whereas the sum of samples plotting in a given tectonic field is reported in the respective tectonic field column; {Σprob} is the sum of probability values for all samples plotting in a given tectonic field is reported in the respective tectonic field column; and [%prob] is the total probability of a given tectonic setting expressed in percent after assigning the probability of IA + CA to IA and CA (using weighing factors explained in Verma and Verma, 2013).

Table E2. Application of multidimensional diagrams to Palaeoproterozoic (~1.8 Ga) felsic rocks of the BWB Gneiss, Gladkop Suite.

Magma type, Figure name	Figure type	Total number of samples	Number of discriminated samples				
			Arc			CR+OI [$\dot{x} \pm s$]	Col [$\dot{x} \pm s$]
			IA+CA [$\dot{x} \pm s$]	IA [$\dot{x} \pm s$]	CA [$\dot{x} \pm s$]		
			[P_{IA+CA}] Θ	[P_{IA}] Θ	[P_{CA}] Θ	[P_{CR+OI}] Θ	[P_{Col}] Θ
Acid; Verma et al. (2012); log-ratios of all major elements	(IA+CA–CR–Col)	12	0 (0)	---	---	10 [0.744±0.079] (0.6330-0.8887)	2 [0.5321±0.0104] (0.5247, 0.5394)
	(IA–CA–CR)	12	---	0 (0)	0 (0)	12 [0.99836±0.00303] (0.9899-1.0000)	---
	(IA–CA–Col)	12	---	0 (0)	0 (0)	---	12 [0.919±0.085] (0.7430-0.9965)
	(IA–CR–Col)	12	---	0 (0)	---	7 [0.640±0.125] (0.5135-0.8496)	5 [0.552±0.082] (0.5059-0.6982)
	(CA–CR–Col)	12	---	---	3 [0.5050±0.0380] (0.4662-0.5422)	9 [0.636±0.102] (0.4634-0.7896)	0 (0)
Diagrams based on log-ratios of major elements	***{Σn} {Σprob} [%prob]***	**60**	**{0} {0} [0%]**	**{0} {0} [0%]**	**{3} {1.5149} [4%]**	**{38} {29.6189} [64%]**	**{19} {14.8579} [32%]**
Acid; Verma et al. (2013); log-ratios of all major elements	(IA+CA-CR+OI-Col)	12	0 (0)	---	---	0 (0)	12 [0.663±0.093] (0.5245-0.8204)
	(IA-CA-CR+OI)	12	---	0 (0)	0 (0)	12 [0.955±0.058] (0.8186-0.9994)	---
	(IA-CA-Col)	12	---	0 (0)	0 (0)	---	12 [0.857±0.124] (0.6679-0.9977)
	(IA-CR+OI-Col)	12	---	0 (0)	---	12 [0.698±0.077] (0.4883-0.7916)	0 (0)
	(CA-CR+OI-Col)	12	---	---	0 (0)	6 [0.6006±0.0423] (0.5497-0.6428)	6 [0.539±0.063] (0.4945-0.6550)
Diagrams based on log-ratios of major elements	***{Σn} {Σprob} [%prob]***	**60**	**{0} {0} [0%]**	**{0} {0} [0%]**	**{0} {0} [0%]**	**{30} {23.4316} [52%]**	**{30} {21.4696} [48%]**
Acid; Verma et al. (2013); log-ratios of immobile major and trace elements	(IA+CA-CR+OI-Col)	12	0 (0)	---	---	12 [0.476±0.060] (0.3468-0.5490)	0 (0)
	(IA-CA-CR+OI)	12	---	0 (0)	1(0.6287)	11 [0.565±0.046] (0.4837-0.6357)	---
	(IA-CA-Col)	12	---	1(0.3946)	2 [0.555±0.050] (0.5194, 0.5901)	---	9 [0.532±0.054] (0.4670-0.6570)
	(IA-CR+OI-Col)	12	---	0 (0)	---	11 [0.5747±0.0420] (0.5074-0.6643)	1(0.5109)
	(CA-CR+OI-Col)	12	---	---	2 [0.4015±0.0094] (0.3948, 0.4082)	9 [0.454±0.061] (0.3877-0.5664)	1(0.3498)
Diagrams based on log-ratios of immobile major and trace elements	***{Σn} {Σprob} [%prob]***	**60**	**{0} {0} [0%]**	**{1} {0.3946} [1%]**	**{5} {2.5411} [8%]**	**{43} {22.3298} [72%]**	**{11} {5.6527} [19%]**
Acid; Verma et al. (2013); log-ratios of immobile trace elements	(IA+CA-CR+OI-Col)	12	0 (0)	---	---	0 (0)	12 [0.650±0.132] (0.4392-0.8829)
	(IA-CA-CR+OI)	12	---	0 (0)	10 [0.916±0.139] (0.5642-0.9998)	2 [0.659±0.089] (0.5965, 0.7225)	---
	(IA-CA-Col)	12	---	0 (0)	2 [0.5729±0.0070] (0.5680, 0.5778)	---	10 [0.757±0.134] (0.5091-0.8990)
	(IA-CR+OI-Col)	12	---	0 (0)	---	1(0.5098)	11 [0.811±0.187] (0.4951-0.9998)
	(CA-CR+OI-Col)	12	---	---	3 [0.5454±0.0426] (0.4975-0.5792)	0 (0)	9 [0.611±0.124] (0.4536-0.8267)
Diagrams based on log-ratios of immobile trace elements	***{Σn} {Σprob} [%prob]***	**60**	**{0} {0} [0%]**	**{0} {0} [0%]**	**{15} {11.9435} [27%]**	**{3} {1.8288} [5%]**	**{42} {29.7920} [68%]**

Table E3. Application of multidimensional diagrams to Palaeoproterozoic (~1.8 Ga) felsic rocks of the STK Gneiss, Gladkop Suite.

Magma type, Figure name	Figure type	Total number of samples	Number of discriminated samples				
			Arc			CR+OI [$\dot{x} \pm s$] [P_{CR+OI}] Θ	Col [$\dot{x} \pm s$] [P_{Col}] Θ
			IA+CA [$\dot{x} \pm s$] [P_{IA+CA}] Θ	IA [$\dot{x} \pm s$] [P_{IA}] Θ	CA [$\dot{x} \pm s$] [P_{CA}] Θ		
Acid; Verma et al. (2012); log-ratios of all major elements	(IA+CA–CR–Col)	8	0 (0)	---	---	8 [0.820±0.123] (0.5775-0.9332)	0 (0)
	(IA–CA–CR)	8	---	0 (0)	0 (0)	8 [0.99819±0.00342] (0.9898-1.0000)	---
	(IA–CA–Col)	8	---	3 [0.630±0.223] (0.3905-0.8314)	0 (0)	---	5 [0.856±0.173] (0.5515-0.9570)
	(IA–CR–Col)	8	---	0 (0)	---	7 [0.797±0.136] (0.5568-0.9193)	1(0.5138)
	(CA–CR–Col)	8	---	---	5 [0.716±0.221] (0.4314-0.9828)	3 [0.746±0.112] (0.6278-0.8499)	0 (0)
Diagrams based on log-ratios of major elements	***{Σn} {Σprob} [%prob]***	**40**	**{0} {0} [0%]**	**{3} {1.8910} [6%]**	**{5} {3.5817} [11%]**	**{26} {22.3591} [68%]**	**{6} {4.7942} [15%]**
Acid; Verma et al. (2013); log-ratios of all major elements	(IA+CA-CR+OI-Col)	8	0 (0)	---	---	0 (0)	8 [0.679±0.077] (0.5611-0.7793)
	(IA-CA-CR+OI)	8	---	4 [0.716±0.234] (0.5136-0.9676)	0 (0)	4 [0.9761±0.0205] (0.9471-0.9931)	---
	(IA-CA-Col)	8	---	4 [0.864±0.147] (0.6470-0.9592)	0 (0)	---	4 [0.920±0.062] (0.8280-0.9590)
	(IA-CR+OI-Col)	8	---	2 [0.784±0.186] (0.6523, 0.9149)	---	6 [0.673±0.075] (0.5836-0.7853)	0 (0)
	(CA-CR+OI-Col)	8	---	---	1(0.3967)	4 [0.551±0.097] (0.4392-0.6336)	3 [0.5252±0.0420] (0.4940-0.5729)
Diagrams based on log-ratios of major elements	***{Σn} {Σprob} [%prob]***	**40**	**{0} {0} [0%]**	**{10} {7.8866} [27%]**	**{1} {0.3967} [1%]**	**{14} {10.1474} [35%]**	**{15} {10.6866} [37%]**
Acid; Verma et al. (2013); log-ratios of immobile major and trace elements	(IA+CA-CR+OI-Col)	8	3 [0.3827±0.0387] (0.3594-0.4274)	---	---	4 [0.4512±0.0417] (0.3913-0.4884)	1(0.4107)
	(IA-CA-CR+OI)	8	---	0 (0)	5 [0.557±0.046] (0.4997-0.6059)	3 [0.5529±0.0051] (0.5489-0.5586)	---
	(IA-CA-Col)	8	---	0 (0)	5 [0.5338±0.0419] (0.4847-0.5674)	---	3 [0.520±0.052] (0.4651-0.5693)
	(IA-CR+OI-Col)	8	---	0 (0)	---	7 [0.531±0.059] (0.4762-0.6145)	1(0.5532)
	(CA-CR+OI-Col)	8	---	---	4 [0.4640±0.0399] (0.4247-0.5063)	4 [0.4101±0.0240] (0.3787-0.4368)	0 (0)
Diagrams based on log-ratios of immobile major and trace elements	***{Σn} {Σprob} [%prob]***	**40**	**{3} {1.1482} [---]**	**{0} {0} [0%]**	**{14} {7.3094} [42%]**	**{18} {8.8233} [45%]**	**{5} {2.5230} [13%]**
Acid; Verma et al. (2013); log-ratios of immobile trace elements	(IA+CA-CR+OI-Col)	8	0 (0)	---	---	0 (0)	8 [0.513±0.069] (0.3960-0.6106)
	(IA-CA-CR+OI)	8	---	0 (0)	8 [0.9451±0.0327] (0.8969-0.9935)	0 (0)	---
	(IA-CA-Col)	8	---	0 (0)	6 [0.5604±0.0371] (0.5077-0.6046)	---	2 [0.591±0.057] (0.5505, 0.6317)
	(IA-CR+OI-Col)	8	---	0 (0)	---	1(0.5029)	7 [0.866±0.086] (0.7748-0.9942)
	(CA-CR+OI-Col)	8	---	---	6 [0.561±0.090] (0.4869-0.6991)	0 (0)	2 [0.4930±0.0076] (0.4876, 0.4984)
Diagrams based on log-ratios of immobile trace elements	***{Σn} {Σprob} [%prob]***	**40**	**{0} {0} [0%]**	**{0} {0} [0%]**	**{20} {14.2919} [53%]**	**{1} {0.5029} [2%]**	**{19} {12.3379} [45%]**

Appendix F. U-Pb and Lu-Hf zircon isotope data

Table F1. U-Pb zircon isotopic data (P. Macey, pers. comm., 2018)

Analysis	U [ppm][a]	Pb [ppm][a]	Th/U meas.	RATIOS					AGES [Ma]								LOCATION	U CONTENT	Concordance vs. Discordance
				$^{207}Pb/^{235}U$[b]	2 s[d]	$^{206}Pb/^{238}U$[b]	2 s[d]	rho[c]	$^{207}Pb/^{206}Pb$[e]	2 s[d]	$^{207}Pb/^{235}U$	2 s	$^{206}Pb/^{238}U$	2 s	$^{207}Pb/^{206}Pb$	2 s			
Brandewynsbank Gneiss (Sample RTB027)																			
RTB027 - 1	254	236	1.11	4.755	0.032	0.3098	0.0017	0.43	0.1110	0.0007	1777	6	1740	8	1814	11	Core	mod U	discordant
RTB027 - 2	62	60	1.14	4.970	0.110	0.3254	0.0054	0.82	0.1101	0.0014	1813	18	1816	26	1800	23	Core	low U	CONCORDANT
RTB027 - 3	167	169	1.23	4.824	0.055	0.3166	0.0024	0.69	0.1098	0.0009	1789	10	1773	12	1796	15	Core	mod U	discordant
RTB027 - 4	896	108	0.17	2.184	0.026	0.1989	0.0011	0.66	0.0791	0.0007	1176	8	1170	6	1174	17	Rim	high U	CONCORDANT
RTB027 - 5	2060	82	0.08	1.631	0.023	0.1615	0.0021	0.97	0.0728	0.0003	982	9	965	12	1008	8	Rim	mod U	discordant
RTB027 - 6	125	167	1.44	5.160	0.220	0.3028	0.0048	0.81	0.1229	0.0041	1844	37	1705	24	1994	59	Core	high U	discordant
RTB027 - 7	115	172	1.82	4.778	0.094	0.3151	0.0049	0.78	0.1095	0.0013	1780	16	1765	24	1789	22	Core - ign conc zoned	mod U	CONCORDANT
RTB027 - 8	1327	63	0.09	2.005	0.015	0.1894	0.0012	0.86	0.0763	0.0003	1117	5	1118	7	1103	8	Rim	high U	CONCORDANT
RTB027 - 9	103	107	1.20	4.970	0.073	0.3269	0.0042	0.78	0.1096	0.0010	1814	13	1823	21	1792	17	Core - ign conc zoned	low U	discordant
RTB027 - 10	1590	78	0.08	1.907	0.055	0.1805	0.0043	0.99	0.0761	0.0005	1083	19	1069	24	1097	14	Rim	high U	CONCORDANT
RTB027 - 11	319	442	1.67	4.821	0.064	0.3158	0.0040	0.91	0.1102	0.0006	1788	11	1769	19	1801	10			discordant
RTB027 - 12	119	154	1.45	5.400	0.120	0.3521	0.0080	0.93	0.1106	0.0011	1884	19	1944	38	1808	17			discordant
RTB027 - 13	192	182	1.11	4.900	0.046	0.3216	0.0031	0.86	0.1098	0.0007	1802	8	1797	15	1795	11	Core	mod U	CONCORDANT
RTB027 - 14	1260	65	0.10	2.143	0.019	0.1978	0.0015	0.92	0.0781	0.0003	1163	6	1163	8	1149	9	Rim	high U	CONCORDANT
RTB027 - 15	133	139	1.22	4.064	0.095	0.2689	0.0046	0.93	0.1089	0.0011	1646	19	1535	23	1780	19	Core - ign conc zoned	mod U	discordant
RTB027 - 16	1779	711	0.34	2.580	0.086	0.1796	0.0026	0.94	0.1035	0.0022	1294	24	1065	14	1685	39	Rim	high U	discordant
RTB027 - 17	1255	107	0.19	1.927	0.052	0.1725	0.0041	0.98	0.0806	0.0006	1090	18	1026	23	1211	14	Rim	high U	discordant
RTB027 - 18	105	121	1.38	4.535	0.083	0.3055	0.0062	0.93	0.1071	0.0008	1737	15	1718	31	1749	13	Core - ign conc zoned	mod U	CONCORDANT
RTB027 - 19	84	117	1.62	4.940	0.110	0.3209	0.0058	0.90	0.1109	0.0010	1808	18	1794	28	1813	16	Core		CONCORDANT
RTB027 - 20	1130	144	0.18	2.380	0.140	0.1891	0.0032	0.94	0.0905	0.0038	1233	40	1116	17	1426	76	Rim		discordant
RTB027 - 21	110	166	7.64	4.541	0.080	0.2733	0.0066	0.87	0.1199	0.0014	1738	15	1557	33	1953	21	Core - ign conc zoned		discordant
RTB027 - 22	501	298	0.53	4.210	0.220	0.2665	0.0027	0.94	0.1137	0.0048	1672	42	1523	14	1851	74	Core		discordant
RTB027 - 23	147	231	1.88	4.683	0.092	0.3112	0.0032	0.87	0.1084	0.0013	1764	17	1747	16	1772	22	Rim		discordant
RTB027 - 24	1566	108	0.12	2.200	0.015	0.2020	0.0014	0.88	0.0785	0.0002	1181	5	1186	8	1160	6	Core - ign conc zoned		CONCORDANT

RTB027 - 25	207	253	1.41	4.883	0.041	0.3199	0.0025	0.79	0.1101	0.0005	1799	7	1789	12	1801	9	Core - ign conc zoned		CONCORDANT
RTB027 - 26	1280	235	0.29	2.391	0.061	0.1940	0.0049	0.98	0.0889	0.0005	1239	18	1143	27	1400	10	Rim		discordant
RTB027 - 27	975	1100	1.27	5.008	0.034	0.3274	0.0030	0.94	0.1103	0.0003	1821	6	1826	15	1803	6	Core		discordant
RTB027 - 28	1467	81	0.10	2.158	0.012	0.1979	0.0015	0.77	0.0786	0.0003	1168	4	1164	8	1162	7	Rim		CONCORDANT
RTB027 - 29	3570	2540	0.05	3.680	0.220	0.0745	0.0027	0.98	0.3556	0.0098	1563	49	463	16	3728	43	Rim		discordant
RTB027 - 30	163	246	1.66	5.115	0.076	0.3140	0.0036	0.67	0.1176	0.0009	1838	13	1760	18	1919	13	Core - ign conc zoned		discordant
Steinkopf Gneiss (Sample RTB028)																			
RTB028 - 1	138	147	1.19	5.008	0.043	0.3265	0.0026	0.52	0.1106	0.0008	1821	7	1821	12	1808	14	Core - ign conc zoned	mod U	CONCORDANT
RTB028 - 2	129	167	1.51	4.893	0.054	0.3194	0.0024	0.76	0.1105	0.0008	1801	9	1787	12	1807	13	Core - ign conc zoned	mod U	discordant
RTB028 - 3	180	323	2.05	4.927	0.041	0.3227	0.0028	0.84	0.1101	0.0005	1807	7	1803	13	1800	9	Core - ign conc zoned	mod U	CONCORDANT
RTB028 - 4	188	215	1.29	4.953	0.070	0.3231	0.0030	0.87	0.1105	0.0009	1811	12	1805	15	1807	15	Core - ign conc zoned	mod U	CONCORDANT
RTB028 - 5	161	237	1.76	4.757	0.063	0.3126	0.0033	0.80	0.1097	0.0009	1777	11	1754	16	1793	14	Core - ign conc zoned	mod U	discordant
RTB028 - 6	258	322	1.46	4.691	0.038	0.3089	0.0019	0.80	0.1095	0.0005	1766	7	1735	10	1791	9	Core - ign conc zoned	mod U	discordant
RTB028 - 7	126	180	1.60	4.901	0.046	0.3220	0.0032	0.49	0.1097	0.0011	1802	8	1800	16	1794	17	Core - ign conc zoned	mod U	CONCORDANT
RTB028 - 8	99	101	1.12	5.003	0.061	0.3243	0.0057	0.88	0.1105	0.0010	1820	10	1810	28	1806	16	Core - ign conc zoned	low U	CONCORDANT
RTB028 - 9	148	211	1.66	4.823	0.049	0.3148	0.0027	0.77	0.1105	0.0007	1789	9	1764	13	1807	11	Core - ign conc zoned	mod U	discordant
RTB028 - 10	144	49	0.46	3.490	0.240	0.2590	0.0100	0.98	0.0965	0.0030	1519	54	1486	52	1552	59	core - inherited? !	mod U	CONCORDANT
RTB028 - 11	173	278	1.83	4.825	0.058	0.3121	0.0033	0.54	0.1115	0.0013	1789	10	1751	16	1823	21	Core	mod U	discordant
RTB028 - 12	212	226	1.32	3.675	0.052	0.2638	0.0021	0.79	0.1004	0.0009	1566	11	1509	11	1631	17	Core	mod U	discordant
RTB028 - 13	116	193	1.86	4.941	0.070	0.3246	0.0041	0.80	0.1097	0.0011	1809	12	1812	20	1794	18	Core - ign conc zoned	mod U	CONCORDANT
RTB028 - 14	85	84	1.07	4.934	0.056	0.3232	0.0032	0.73	0.1101	0.0009	1808	10	1805	16	1801	14	Core - ign conc zoned	low U	CONCORDANT
RTB028 - 15	289	296	1.21	4.870	0.065	0.3166	0.0031	0.90	0.1109	0.0007	1797	11	1773	15	1813	11	Core - ign conc zoned	mod U	discordant
RTB028 - 16	31	29	1.03	4.730	0.240	0.3160	0.0160	0.95	0.1079	0.0016	1788	28	1800	52	1762	26	Core - ign conc zoned	low U	CONCORDANT
RTB028 - 17	124	148	1.33	4.897	0.084	0.3202	0.0044	0.93	0.1103	0.0007	1801	14	1791	22	1804	11	Core - ign conc zoned	low U	CONCORDANT
RTB028 - 18	61	64	1.17	4.880	0.110	0.3224	0.0079	0.85	0.1092	0.0013	1798	20	1801	38	1785	23	Core - ign conc zoned	low U	CONCORDANT
RTB028 - 19	119	140	1.32	4.962	0.054	0.3256	0.0032	0.71	0.1099	0.0009	1813	9	1817	15	1796	14	Core	mod U	discordant
RTB028 - 20	86	113	1.51	4.633	0.072	0.3086	0.0038	0.66	0.1083	0.0013	1755	13	1733	19	1770	21	Core	low U	discordant

Table F2. Lu-Hf zircon isotopic data (P. Macey, pers. comm., 2018).

Analysis	$^{178}Hf/^{177}Hf^{c}$	2 s	$^{180}Hf/^{177}Hf^{c}$	2 s	$^{176}Yb/^{177}Hf$	2 s	$^{176}Lu/^{177}Hf$	2 s	Hf_{Total}	2 s	$^{176}Hf/^{177}Hfc$	2 s	εHf	2s	Age	2s	LOCATION	Concordance vs. Discordance
Brandewynsbank Gneiss (Sample RTB027)																		
RTB027 - 1	1.466840	0.000240	1.886710	0.000290	0.031400	0.002300	0.001038	0.000071	2.050000	0.100000	0.281557	0.000067	-5.49	0.67	1777	5.7	Core	discordant
RTB027 - 2	1.467090	0.000210	1.886840	0.000340	0.020600	0.001500	0.000670	0.000032	1.854000	0.079000	0.281573	0.000067	-2.78	0.67	1813	18	Core	CONCORDANT
RTB027 - 3	1.467250	0.000200	1.887050	0.000320	0.034390	0.000590	0.001099	0.000033	1.871000	0.047000	0.281580	0.000140	-4.00	1.4	1789	9.5	Core	discordant
RTB027 - 5	1.467040	0.000220	1.886870	0.000400	0.033650	0.000130	0.001183	0.000010	2.326000	0.088000	0.282006	0.000091	-6.17	0.91	965	12	Rim	discordant
RTB027 - 7	1.467190	0.000260	1.886960	0.000400	0.047270	0.000580	0.001442	0.000024	1.805000	0.048000	0.281615	0.000092	-3.35	0.92	1780	16	Core - ign conc zoned	CONCORDANT
RTB027 - 9	1.467290	0.000180	1.887120	0.000490	0.027810	0.000220	0.000839	0.000004	1.823000	0.068000	0.281580	0.000120	-2.59	1.2	1814	13	Core - ign conc zoned	discordant
RTB027 - 10	1.466950	0.000230	1.886680	0.000260	0.025200	0.001300	0.000970	0.000026	2.740000	0.120000	0.282014	0.000091	-3.56	0.91	1069	24	Rim	CONCORDANT
RTB027 - 11	1.466980	0.000210	1.887000	0.000320	0.039200	0.001800	0.001182	0.000039	1.880000	0.120000	0.281470	0.000100	-8.10	1	1788	11		discordant
RTB027 - 12	1.467080	0.000240	1.886780	0.000550	0.032330	0.000580	0.001043	0.000017	1.238000	0.016000	0.281670	0.000140	3.03	1.4	1884	19		discordant
RTB027 - 13	1.466460	0.000380	1.886800	0.000360	0.048700	0.001200	0.001630	0.000100	1.770000	0.200000	0.281566	0.000080	-4.62	0.8	1802	7.8	Core	CONCORDANT
RTB027 - 15	1.467020	0.000270	1.886980	0.000310	0.038700	0.000930	0.001171	0.000022	1.700000	0.088000	0.281520	0.000100	-11.42	1	1646	19	Core - ign conc zoned	discordant
RTB027 - 18	1.466880	0.000300	1.886960	0.000420	0.049800	0.001200	0.001568	0.000049	1.640000	0.063000	0.281570	0.000110	-6.11	1.1	1737	15	Core - ign conc zoned	CONCORDANT
RTB027 - 19	1.467010	0.000180	1.886830	0.000460	0.034940	0.000190	0.001060	0.000014	1.832000	0.065000	0.281510	0.000120	-5.98	1.2	1808	18	Core	CONCORDANT
RTB027 - 21	1.466920	0.000240	1.886750	0.000390	0.050500	0.001300	0.001473	0.000054	1.775000	0.058000	0.281653	0.000076	-6.54	0.76	1738	15	Core - ign conc zoned	discordant
RTB027 - 22	1.467140	0.000250	1.887030	0.000330	0.022090	0.000220	0.000738	0.000008	2.366000	0.097000	0.281851	0.000055	0.51	0.55	1672	42	Core	discordant
RTB027 - 23	1.466920	0.000210	1.887130	0.000270	0.051400	0.001200	0.001514	0.000033	1.716000	0.085000	0.281614	0.000080	-3.86	0.8	1764	17	Rim	discordant
RTB027 - 24	1.466860	0.000220	1.886800	0.000330	0.015410	0.000250	0.000656	0.000006	2.530000	0.140000	0.281888	0.000077	-5.65	0.77	1186	7.7	Core - ign conc zoned	CONCORDANT
RTB027 - 25	1.467160	0.000210	1.886860	0.000440	0.038350	0.000600	0.001159	0.000010	1.861000	0.091000	0.281538	0.000086	-5.22	0.86	1799	7.1	Core - ign conc zoned	CONCORDANT
RTB027 - 26	1.466890	0.000250	1.886650	0.000290	0.037270	0.000490	0.001258	0.000012	2.170000	0.120000	0.281697	0.000079	-11.64	0.79	1143	27	Rim	discordant
RTB027 - 27	1.467030	0.000180	1.887250	0.000210	0.068400	0.002100	0.002180	0.000042	2.311000	0.059000	0.281569	0.000058	-4.56	0.58	1821	5.8	Core	discordant
RTB027 - 29	1.467040	0.000210	1.886870	0.000260	0.016520	0.000650	0.000868	0.000012	2.890000	0.110000	0.281804	0.000052	-24.34	0.52	463	16	Rim	discordant
RTB027 - 30	1.466910	0.000230	1.886350	0.000410	0.046300	0.001400	0.001453	0.000029	1.564000	0.041000	0.281630	0.000120	-2.93	1.2	1838	13	Core - ign conc zoned	discordant
Steinkopf Gneiss (Sample RTB028)																		
RTB028 - 1	1.467210	0.000290	1.886500	0.000330	0.035350	0.000990	0.001089	0.000020	1.841000	0.049000	0.281690	0.000091	0.97	0.91	1821	7.3	Core - ign conc zoned	CONCORDANT

RTB028 - 2	1.467100	0.000260	1.886840	0.000410	0.041700	0.001400	0.001295	0.000061	1.766000	0.069000	0.281628	0.000096	-2.23	0.96	1801	9.3	Core - ign conc zoned	discordant
RTB028 - 3	1.467100	0.000210	1.886640	0.000420	0.054900	0.003200	0.001623	0.000072	1.714000	0.048000	0.281550	0.000110	-5.05	1.1	1807	7.1	Core - ign conc zoned	CONCORDANT
RTB028 - 4	1.467170	0.000270	1.886900	0.000230	0.036590	0.000920	0.001097	0.000039	1.973000	0.075000	0.281501	0.000089	-6.10	0.89	1811	12	Core - ign conc zoned	CONCORDANT
RTB028 - 5	1.467160	0.000270	1.886800	0.000430	0.041100	0.001000	0.001229	0.000018	1.652000	0.048000	0.281630	0.000100	-2.80	1	1777	11	Core - ign conc zoned	discordant
RTB028 - 6	1.467220	0.000270	1.886690	0.000350	0.049200	0.001500	0.001518	0.000043	1.950000	0.035000	0.281538	0.000092	-6.81	0.92	1766	6.7	Core - ign conc zoned	discordant
RTB028 - 7	1.467110	0.000300	1.887280	0.000390	0.050100	0.001900	0.001451	0.000063	1.796000	0.062000	0.281540	0.000110	-5.26	1.1	1802	7.9	Core - ign conc zoned	CONCORDANT
RTB028 - 8	1.467070	0.000220	1.886770	0.000280	0.046000	0.002300	0.001399	0.000055	1.634000	0.055000	0.281680	0.000120	-0.01	1.2	1820	10	Core - ign conc zoned	CONCORDANT
RTB028 - 9	1.467080	0.000240	1.887040	0.000320	0.049110	0.000790	0.001445	0.000033	1.794000	0.079000	0.281570	0.000110	-4.97	1.1	1789	8.6	Core - ign conc zoned	discordant
RTB028 - 10	1.466870	0.000170	1.886480	0.000410	0.037050	0.000970	0.001153	0.000010	2.047000	0.092000	0.281624	0.000093	-8.78	0.93	1486	52	core - inherited? !	CONCORDANT
RTB028 - 11	1.467200	0.000230	1.886720	0.000350	0.057600	0.001700	0.001656	0.000036	1.838000	0.053000	0.281610	0.000110	-4.08	1.1	1789	10	Core	discordant
RTB028 - 12	1.467170	0.000210	1.886860	0.000350	0.034700	0.001000	0.001080	0.000017	2.121000	0.033000	0.281474	0.000049	-13.53	0.49	1566	11	Core	discordant
RTB028 - 13	1.467110	0.000240	1.887170	0.000420	0.041800	0.002200	0.001232	0.000044	1.710000	0.062000	0.281540	0.000130	-4.73	1.3	1809	12	Core - ign conc zoned	CONCORDANT
RTB028 - 14	1.467170	0.000300	1.886870	0.000550	0.035080	0.000700	0.001077	0.000012	1.549000	0.056000	0.281600	0.000130	-2.56	1.3	1808	9.6	Core - ign conc zoned	CONCORDANT
RTB028 - 15	1.466920	0.000180	1.886540	0.000400	0.033210	0.000300	0.001000	0.000004	2.032000	0.076000	0.281567	0.000061	-4.35	0.61	1797	11	Core - ign conc zoned	discordant
RTB028 - 16	1.467140	0.000270	1.886540	0.000390	0.014940	0.000300	0.000455	0.000004	1.704000	0.044000	0.281610	0.000120	-1.56	1.2	1788	28	Core - ign conc zoned	CONCORDANT
RTB028 - 17	1.467060	0.000270	1.886720	0.000410	0.030270	0.000820	0.000900	0.000017	1.801000	0.075000	0.281469	0.000084	-7.31	0.84	1801	14	Core - ign conc zoned	CONCORDANT
RTB028 - 18	1.466890	0.000210	1.886360	0.000310	0.028800	0.001800	0.000877	0.000061	1.726000	0.084000	0.281725	0.000089	2.03	0.89	1798	20	Core - ign conc zoned	CONCORDANT
RTB028 - 19	1.467190	0.000260	1.887150	0.000350	0.052250	0.000890	0.001523	0.000017	1.831000	0.034000	0.281588	0.000086	-3.27	0.86	1813	9.1	Core	discordant
RTB028 - 20	1.466930	0.000250	1.886580	0.000480	0.036600	0.001400	0.001104	0.000023	1.446000	0.095000	0.281600	0.000130	-4.18	1.3	1755	13	Core	discordant

Appendix G. Regional geological map of the Namaqualand Geotraverse

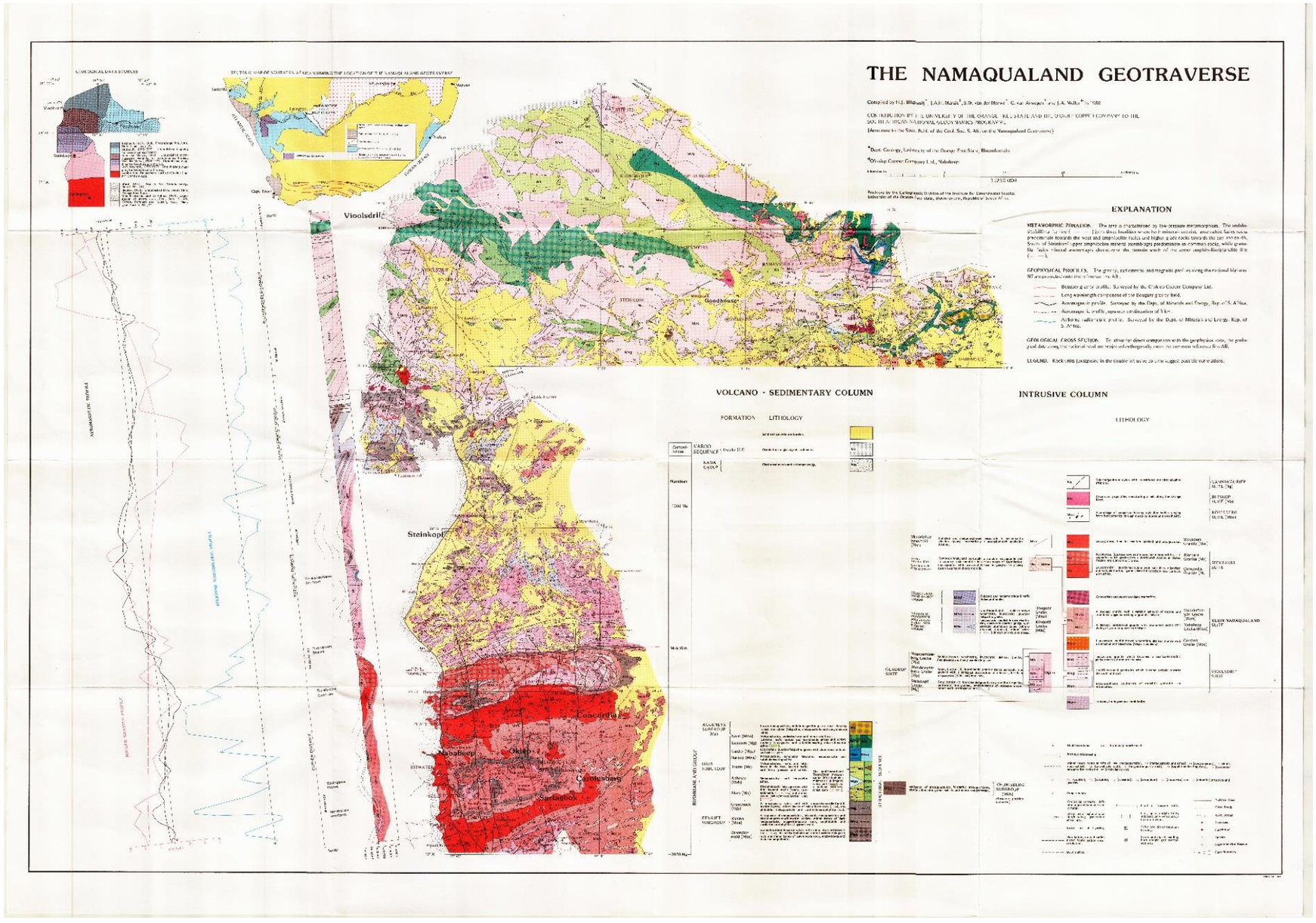

Appendix H. Locations of all samples collected during this project

Latitude	Longitude	Sample No.	Lithology
-29.4066	17.7079	GS-50	Steinkopf Gneiss
-29.3979	17.6852	GS-51	Brandewynsbank Gneiss
-29.4549	17.7670	GS-53	Steinkopf Gneiss
-29.4113	17.7365	GS-54	Orbicular granite
-29.4068	17.7093	GS-52	Steinkopf Gneiss
-29.4052	17.7065	GS-55	Steinkopf Gneiss
-29.4132	17.6852	GS-56	Steinkopf Gneiss
-29.2488	17.7521	GS-1	Brandewynsbank Gneiss
-29.2501	17.7528	GS-2	Brandewynsbank Gneiss
-29.2516	17.7525	GS-3	Amphibolite
-29.2521	17.7523	GS-4	Noenoemaasberg Gneiss
-29.2534	17.7531	GS-6	Brandewynsbank Gneiss
-29.2517	17.7529	GS-7	Amphibolite
-29.2512	17.7531	GS-8	Amphibolite
-29.2510	17.7534	GS-9	Amphibolite
-29.2531	17.7469	GS-11	Brandewynsbank Gneiss
-29.2742	17.7874	GS-13	Steinkopf Gneiss
-29.2737	17.7891	GS-14	Steinkopf Gneiss
-29.2772	17.7904	GS-15A	Metaquartzite
-29.2774	17.7900	GS-15B	Metaquartzite
-29.2773	17.7905	GS-16	Steinkopf Gneiss
-29.2698	17.7736	GS-17	Med-grained siliceous
-29.2694	17.7735	GS-18	Brandewynsbank Gneiss
-29.4360	17.7709	GS-19	Anorthosite
-29.4337	17.7702	GS-20	Noenoemaasberg Gneiss
-29.4298	17.7674	GS-21	Brandewynsbank Gneiss
-29.4523	17.7407	GS-22	Steinkopf Gneiss
-29.4518	17.7406	GS-23	Brandewynsbank Gneiss
-29.7406	17.4519	GS-24	Quartzofeldspathic sedimentary
-29.4492	17.7386	GS-25	Anorthosite
-29.4456	17.7410	GS-26	Noenoemaasberg Gneiss
-29.4233	17.8239	GS-27	Noenoemaasberg Gneiss
-29.4307	17.8322	Gs-28A	Steinkopf Gneiss
-29.4307	17.8325	GS-28B	Brandewynsbank Gneiss
-29.4343	17.8325	GS-29	Amphibolite
-29.4200	17.8133	GS-30	Brandewynsbank Gneiss
-29.4139	17.8233	GS-31	Brandewynsbank Gneiss
-29.3560	17.7834	GS-32A	Amphibolite
-29.3560	17.7833	GS-32B	Steinkopf Gneiss
-29.4616	17.7333	GS-33A	Brandewynsbank Gneiss
-29.4620	17.7331	GS-33B	Steinkopf Gneiss
-29.4544	17.7244	GS-34	Steinkopf Gneiss
-29.4312	17.7099	GS-35	Brandewynsbank Gneiss
-29.4256	17.7232	GS-36	Brandewynsbank Gneiss
-29.4076	17.7095	GS-37	Brandewynsbank Gneiss
-29.4477	17.7347	GS-38	Noenoemaasberg Gneiss
-29.3114	17.7673	GS-39	Noenoemaasberg Gneiss
-29.3100	17.7562	GS-40	Amphibolite
-29.3446	17.7834	GS-41	Steinkopf Gneiss
-29.3782	17.8153	GS-42	Noenoemaasberg Gneiss
-29.3916	17.7988	GS-43	Noenoemaasberg Gneiss
-29.4077	17.8136	RTB 027	Brandewynsbank Gneiss
-29.3222	17.7699	RTB 028	Steinkopf Gneiss